Global Imaging of Physiological and Pathophysiological Angiogenesis in Live Zebrafish using Optical Projection Tomography

Nicola Jayne Lockwood

A thesis submitted to University College London for the degree of
DOCTOR OF PHILOSOPHY

Division of Medicine / CoMPLEX
University College London

2016

Declaration

I, Nicola Lockwood confirm that the work presented in this thesis is my own. Where information has been derived from other sources, I confirm that this has been indicated in the thesis.

Abstract

Angiogenesis is found deregulated in many pathologies, including cancer where it is required for tumour progression and metastasis. Although much has been learnt from *in vitro* studies of angiogenesis, it is increasingly accepted that biological processes can differ significantly between *in vitro* and *in vivo* contexts, with whole-body responses determining phenotype.

I describe the development of a novel compressive sensing optical projection tomography (CS-OPT) platform using fluorescence microscopy, which enables live, whole organism imaging of adult zebrafish. Through incorporating contemporary compressive sensing algorithms the acquisition time is dramatically reduced, enabling decreased anaesthesia leading to improved zebrafish viability. The platform has been shown to provide accurate 3-dimensional quantifications of tumour volume and vascularisation using an adult zebrafish model of tumour progression. The model has a mCherry labelled vasculature and an inducible, liver specific cancer driven by the expression of oncogenic $kras^{V12}$ labelled with eGFP. This model recapitulates human hepatocellular carcinoma.

The platform is minimally invasive as zebrafish can be repeatedly imaged throughout development, from larvae to adult, without reducing viability. Therefore, CS-OPT should be beneficial for longitudinal mechanistic and drug development studies of tumour progression and angiogenesis.

With this in mind novel zebrafish models have been developed through genome editing techniques. The generation of an inducible knockout ptena zebrafish line that lacks functional ptenb was also attempted with the aim of creating a more metastatic cancer model to better reflect human disease. Furthermore, I performed studies to optimise both the anaesthetic regime and inducer treatment, which will be important for future studies.

Thus, the developed CS-OPT modality is a powerful imaging platform for longitudinal mechanistic and drug development studies within whole organisms. This has been shown in the context of tumour progression and angiogenesis, but has the potential for further developmental and pathophysiological applications.

Acknowledgements

I would like to take the opportunity to thank everyone who has helped me throughout the life changing experience that has been my PhD.

First and foremost, I want to thank my primary supervisor, Paul Frankel. Not only did he grant me the opportunity to contribute towards this rewarding project, but he has provided the most outstanding support in all aspects. He has enabled me to achieve so much, improving my research capabilities and confidence dramatically.

I also wish to extend thanks to my other two supervisors, Matilda Katan and Simon Arridge. They have provided great insight and direction into their fields allowing me to further understand and incorporate elements I would not have considered.

I would like to thank everyone on the zebrafish OPT project at both UCL and Imperial. In particular I would like to mention Marie-Christine Ramel and Teresa Correia who have always offered their help and assistance when needed. I also extend thanks to Sunil Kumar, James McGinty and Paul French for their insight, time and effort with regards to the design and assembly of the CS-OPT platform for imaging and analysing the zebrafish models.

I express my gratitude to the past and present members of the Cardiovascular Biology and Medicine lab at UCL; Tonya, Vanessa, Jenny, Caroline, Laura, Vedanta, Jorge, Katya, Ian, Marwa, Dan, Andy, Carla, Laura W, Rachel, Georgia and Ian. Thank you for your warm welcome into the lab, all the help and support you have provided as well as making it such an enjoyable environment to work in.

I would also like to thank Leo Valdivia Alvarez for sharing his novel TALEN and CRISPR concepts, as well as his invaluable help when troubleshooting problems I encountered. I would also like to extend my thanks to other members within the Steve Wilson group at UCL and the UCL fish facility for their insight, assistance and zebrafish care.

I am grateful to the UCL Division of Medicine and the School of Life and Medical Sciences for their support and advice throughout my PhD. I am also thankful for the opportunities they provided to both visit and present at conferences and research retreats, highlights I will not forget.

I thank CoMPLEX for selecting me for their interdisciplinary PhD programme. I learnt more than I could have ever imagined, I have had help and guidance throughout and also made some friends for life.

I wish to thank my funding bodies, in particular the BHF, who have enabled all of this to be possible whilst financially supporting me. Also, I thank NVIDIA Corporation for

kindly donating the Tesla K40 GPU card used for this research.

Finally, I send the biggest thank you to my friends and family, in particular my parents, sister and husband. If it were not for all the encouragement and support they have always provided, within all aspects of my life, I would have never succeeded. They have been instrumental throughout, always known how best to help and have consistently believed in me. Thank you.

Publications

A Frolov, IM Evans, N Li, K Sidlauskas, K Paliashvili, **N Lockwood**, A Barrett, S Brandner, IC Zachary, P Frankel. Imatinib and Nilotinib increase glioblastoma cell invasion via Abl-independent stimulation of p130Cas and FAK signalling. Scientific Reports, 6:27378. 2016.

S Kumar*, **N Lockwood***, MC Ramel, T Corriea, M Ellis, Y Alexandrov, N Andrews, R Patel, L Burgeon, MJ Dallman, S Brandner, SA Arridge, M Katan, J McGinty*, P Frankel*, PMW French*. Quantitative *in vivo* optical tomography of cancer progression & vasculature development in adult zebrafish. Oncotarget. 7(28):43939-43948. 2016.

N Andrews, MC Ramel, S Kumar, Y Alexandrov, J Mcginty, D Kelly, S Warren, L Kerry, **N Lockwood**, A Frolov, P Frankel, L Bugeon, J McGinty, MJ Dallman, PM French. Visualising apoptosis in live zebrafish using fluorescence lifetime imaging with optical projection tomography to map FRET biosensor activity in space and time. J Biophotonics, 9(4):414-24. 2016.

T Correia, **N Lockwood**, S Kumar, J Yin, MC Ramel, N Andrews, M Katan, L Bugeon, MJ Dallman, J McGinty, P Frankel, PM French, S Arridge. Accelerated Optical Projection Tomography Applied to In Vivo Imaging of Zebrafish. PloS One, 10(8): e0136213. 2015.

Contents

List of Figures

List of Tables

List of Videos

List of Abbreviations

fabp10	fatty acid binding protein 10
AMD	age-related macular degeneration
CRISPR	clustered regularly interspaced short palindromic repeat
CS	compressive sensing
CS-OPT	compressive sensing optical projection tomography
CT	computed tomography
DL	dictionary learning
dpf	days post fertilisation
dpi	days post induction
DSB	double strand break
dsDNA	double stranded DNA
ECM	extracellular matrix
eGFP	enhanced green fluorescent protein
EGFR	epidermal growth factor receptor
ES	embryonic stem
FAK	focal adhesion kinase
FBP	filtered back projection
FEP	fluorinated ethylene propylene
FFPE	formalin-fixed, paraffin-embedded
FGF	fibroblast growth factor
FLASH	fast ligation-based automatable solid-phase high-throughput
FLIM	Fluorescence Lifetime Imaging Microscopy
FRET	Förster Resonance Energy Transfer
gRNA	guide RNA
H&E	Hematoxylin and Eosin
HCC	hepatocellular carcinoma
HDR	homology directed repair
HGF	hepatocyte growth factor
HIF	hypoxia-inducible factor
hpf	hours post fertilisation
HRE	hypoxia-response element
HRMA	high resolution melting analysis
IHC	immunohistochemistry
indels	insertions or deletions
iRFP	infrared fluorescent protein
LB	Luria Bertani
LSM	light sheet microscopy

microCT	micro computed tomography
microMRI	micro magnetic resonance imaging
mLoxP	modified LoxP
MMP	matrix metalloprotease
MRI	magnetic resonance imaging
MSE	mean squared error
NA	numerical aperture
NHEJ	non-homologous end joining
OPT	optical projection tomography
PAM	protospacer adjacent motif
PCR	polymerase chain reaction
PDGF	platelet-derived growth factor
PI3K	phosphoinositide 3-kinase
PIP3	phosphatidylinositol (3,4,5)-trisphosphate
PLCγ	phospholipase C-γ
ppm	parts per million
PTEN	phosphatase and tensin homolog
qPCR	quantitative polymerase chain reaction
RasGAP	Ras GTPase activating protein
RO	reverse osmosis
RTK	receptor tyrosine kinase
rtTA	reverse tetracycline-dependent transactivator
RVDs	repeat-variable di-residues
SD	standard deviation
SH3	Src-homology 3
SNP	single nucleotide polymorphism
ssDNA	single stranded DNA
SSIM	structural similarity index measure
TALEN	transcription activator-like effector nuclease
TRE	tetracycline response element
TV	total variation
TwIST	two-step iterative shrinkage/thresholding
VEGF	vascular endothelial growth factor
VEGFR1/ Flt-1	VEGF receptor 1
VEGFR2/ KDR/ Flk-1	VEGF receptor 2
VHL	Von Hippel-Lindau
wpf	weeks post fertilisation
ZIRC	Zebrafish International Resource Center

CHAPTER 1

Introduction

1.1 Angiogenesis

The physiological process of angiogenesis is the formation of blood vessels from those pre-existing. During embryonic growth and organ development it establishes and remodels the primary vascular plexus created by vasculogenesis, the formation of new blood vessels from angioblasts. Furthermore angiogenesis is an essential process in the female reproductive system and in adult repair mechanisms such as wound healing (Risau and Flamme, 1995). Physiological angiogenesis provides all cells with an adequate supply of nutrients and metabolites, whilst removing waste products. Therefore, regulation is of importance to prevent inadequate or unrequired vascularisation, which lead to pathologies such as ischemia and cancer.

1.1.1 Modes of Physiological Vessel Formation

There are two forms of physiological angiogenesis, sprouting and non-sprouting (also known as intussusception). Sprouting of vessels occurs upon sensing an angiogenic stimulus. Firstly pericytes begin to detach, which usually ensheath endothelial cells, promote survival and prevent unnecessary proliferation. Subsequently the surrounding basement membrane and extracellular matrix (ECM) are degraded by matrix metalloproteases (MMPs). As this occurs the endothelial cells intercellular junctions begin to loosen allowing a provisional ECM scaffold to be formed from plasma proteins leaving the vessel. One endothelial cell is designated the tip cell, which can sense the angiogenic stimulus through filopodia on the protruding surface. Proximal endothelial neighbours, known as stalk cells, elongate and proliferate to create the sprout that can then migrate through the modified ECM. Functional vessels are formed once a lumen has been developed and the endothelium stabilised through pericyte recruitment and coverage (Papetti and Herman, 2002; Carmeliet and Jain, 2011).

Non-sprouting angiogenesis involves the splitting of a pre-existing vessel into two daughter vessels to expand the vascular network. The process commences with proliferation

of the endothelial cells within a vessel to create a large lumen (Risau, 1997). Endothelial cells from opposing sides of the vessel then protrude towards one another and form a cylindrical bridge, which becomes a perforated transvascular pillar of ECM. The pillar is stabilised internally through pericyte coverage and can then expand along the vessel to enable it to split entirely (Burri and Tarek, 1990). The mechanism is much faster and economical than sprouting angiogenesis, however it is not invasive so cannot penetrate new tissue or repair vessels during wound healing (Burri et al., 2004). Due to the differing benefits it is likely that the form of angiogenesis favoured differs between tissues and is dependent upon existing vessel number.

1.1.2 Angiogenic Regulation

Regulation of angiogenesis is important to maintain homeostasis and prevent pathologies. It is usually extensively controlled and coordinated through membrane bound proteins, diverse biomechanical forces and primarily the expression of soluble molecules known as pro and anti angiogenic factors (Papetti and Herman, 2002). These angiogenic factors include, but are not limited to, fibroblast growth factor (FGF), platelet-derived growth factor (PDGF), hepatocyte growth factor (HGF), angiogenin, angiostatin, endostatin and vascular endothelial growth factor (VEGF).

VEGF (also known as VEGF-A) is the principle driver of the angiogenic process. It is a part of a family of homodimeric glycoprotein growth factors, whereby there are 5 isoforms. Amongst other functions VEGF induces angiogenic sprouting, whilst stimulating ECM degradation and enabling vascular leakage. This leads to the production of the provisional ECM scaffold (Ferrara et al., 2003). The loss of a single allele of VEGF causes lethality with an evident lack of organised vasculature and a reduced number of blood vessels, emphasising its importance (Ferrara et al., 1996; Carmeliet et al., 1996). As a result it has been highly characterised since its discovery by Ferrara and Henzel (1989) and its signalling is now believed to be an essential rate-limiting step in coordinating angiogenic progression (Ferrara, 2002; Ferrara et al., 2003).

There are two receptor tyrosine kinases (RTKs) primarily located on endothelial cells to which VEGF is a ligand, these are VEGF receptor 1 (VEGFR1/ Flt-1) and VEGF receptor 2 (VEGFR2/ KDR/ Flk-1). Significant evidence indicates that VEGFR2 is the major mediator of the VEGF angiogenic response. It is lethal when homozygous deficient, resulting in a clear lack of both organised blood vessels and endothelial cell maturity (Shalaby et al., 1995). This is consistent with the *VEGF*$^{-/-}$ phenotype (Ferrara et al., 1996). Upon

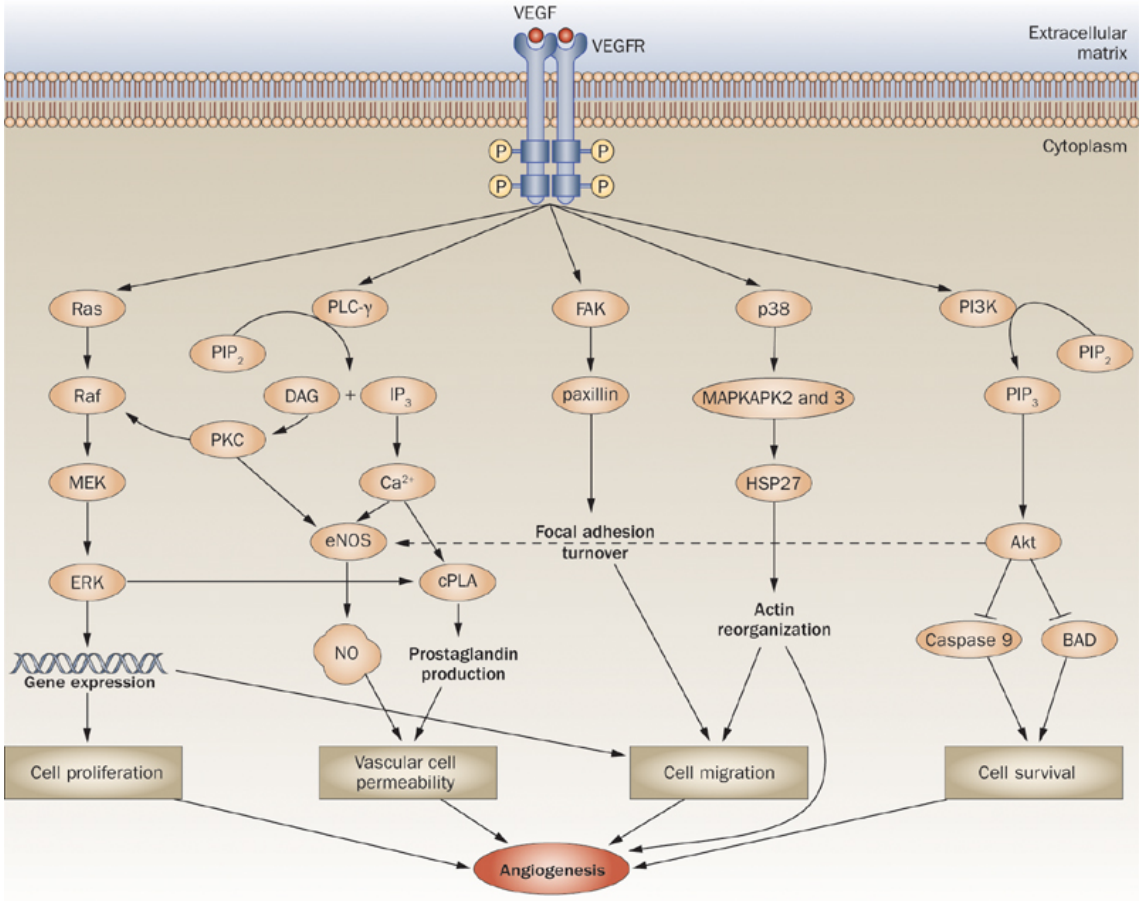

Figure 1.1: VEGF signalling in angiogenesis through VEGFR2. Ligand binding causes VEGFR2 dimerisation and autophosphorylation, resulting in subsequent phosphorylation of target proteins that promote cell survival, migration, proliferation and vascular permeability. Figure from (Ivy et al., 2009).

ligand binding VEGFR2 dimerises, autophosphorylates and then proceeds to phosphorylate target proteins. Its known targets include Ras GTPase activating protein (RasGAP), phospholipase C-γ (PLCγ), focal adhesion kinase (FAK) and phosphoinositide 3-kinase (PI3K) among others (Ferrara et al., 2003; Ivy et al., 2009). Figure 1.1 highlights the resulting downstream signalling events that promote cell survival, migration, proliferation and vascular permeability, ultimately all driving angiogenesis.

VEGFR1/ Flt-1 signalling is considerably different and not yet fully understood. VEGFR1 deficient organisms are also embryonic lethal, however they phenotypically have an excessive amount of endothelial precursor cell proliferation and lack of organisation (Fong et al., 1995). This differs from the *VEGFR*$^{-/-}$ phenotype. Furthermore, a kinase deficient mutant of VEGFR1 does not lead to any histological differences or defects in the vasculature during development, so it does not appear to propagate an angiogenic sig-

nal (Hiratsuka et al., 1998; Ferrara et al., 2003). Based upon these findings it has been speculated that VEGFR1 could act as a negative regulator of the VEGF signal through sequestering the ligand, preventing signal propagation through VEGFR2.

Due to the evident importance of the VEGF signal, and other angiogenic factors, tight spatial and temporal control is required. Tissue hypoxia is one of the major regulatory mechanisms. Oxygen sensitive transcription factors known as hypoxia-inducible factors (HIFs) independently regulate VEGF and other genes involved in different stages of the angiogenic process (see Table 1 in Pugh and Ratcliffe (2003) for greater detail). HIF-1 is the key mediator and is composed of two subunits, hypoxia dependent HIF-1α and constitutively expressed nuclear protein HIF-1β. In the presence of oxygen HIF-1α is prolyl hydroxylated and binds to the tumour suppressor protein Von Hippel-Lindau (VHL). This causes subsequent ubiquitination and proteosomal degradation, Figure 1.2 (Maxwell et al., 2001; Semenza, 2002). When tissues exceed the oxygen diffusion distance of approximately 100-200 μm from a blood vessel HIF-1α cannot be hydroxylated or subsequently degraded (Thomlinson and Gray, 1955; Semenza, 2000). As a result it dimerises with HIF-1β to create a functional HIF-1 transcription complex that is capable of binding hypoxia-response elements (HREs) in the promotors of pro-angiogenic genes (Semenza, 2002; Pugh and Ratcliffe, 2003). Once again the importance of these proteins within the angiogenic process is evident when analysing deficient systems. Reduced VEGF expression was observed under hypoxic conditions within $Hif1\alpha^{-/-}$ mice and embryonic stem (ES) cells, which resulted in histological similarities to VEGF deficient mice (Iyer et al., 1998).

HIF-1α degradation can also be inhibited in non-hypoxic conditions through particular growth factors and signalling pathways. These include the PI3K pathway upregulating HIF-1α protein expression and the MAPK pathway transactivating HIF-1α for functional activation. Both of these pathways involve growth factors, oncogenes and tumour suppressors, Figure 1.2 (Semenza, 2000, 2002; Sang et al., 2003).

1.1.3 Pathophysiological Angiogenesis

Angiogenic regulation is found disrupted in many pathologies, whereby the balance of pro and anti-angiogenic factors has been disturbed. When anti-angiogenic factors dominate, such as angiostatin and endostatin, the result can be vessel regression, endothelial cell dysfunction and lack of required revascularisation. As a consequence the vasculature does not sufficiently meet the requirements of the tissues, which can lead to ischemic

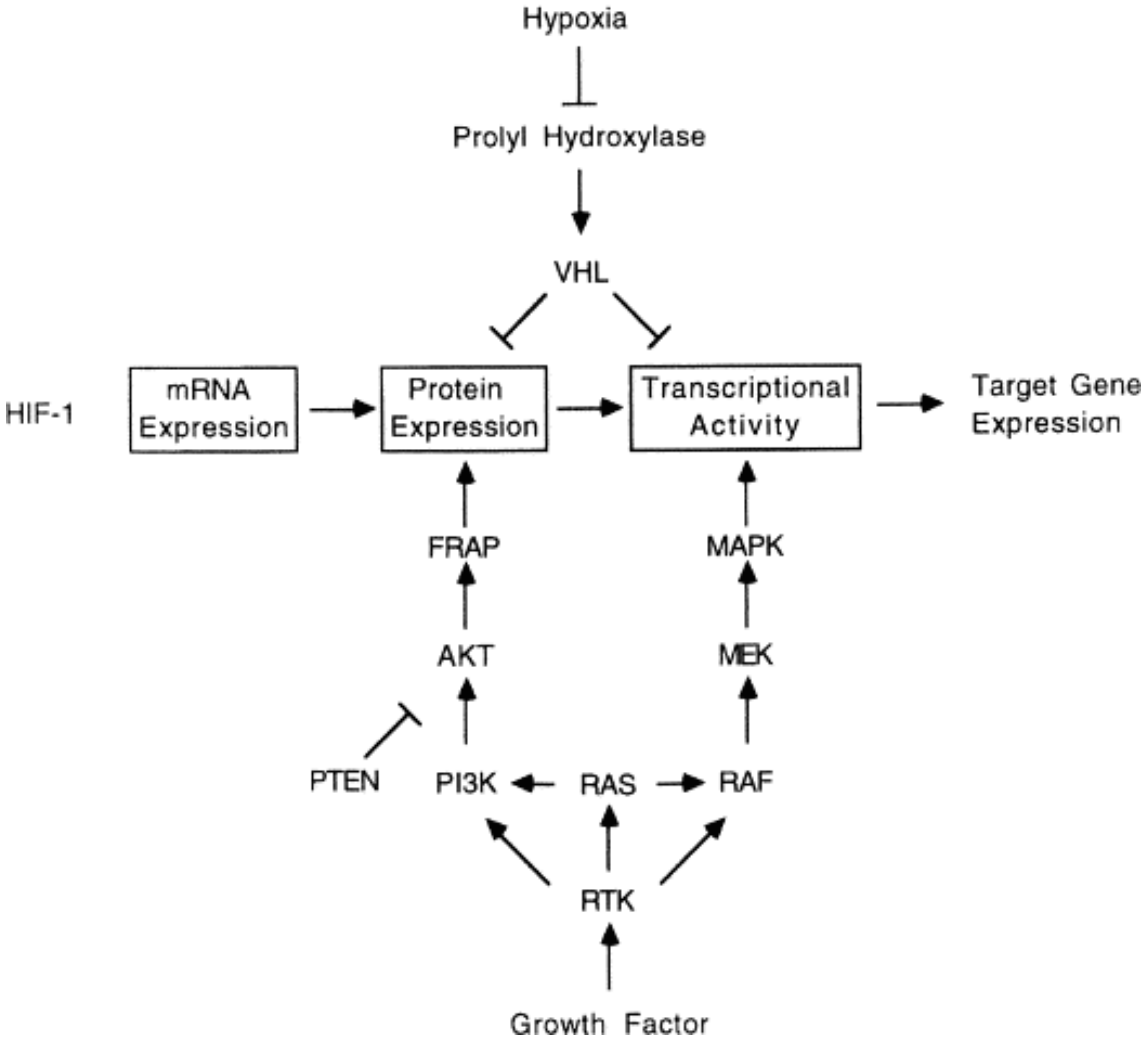

Figure 1.2: Oxygen dependent and independent regulatory mechanisms involved in the expression of the HIF-1 transcription factor complex. Figure adapted from Semenza (2002).

pathologies, such as cardiovascular diseases, neurodegenerative disorders and impaired wound healing, amongst others (Carmeliet, 2003, 2005).

However, when there is an inordinate amount of pro-angiogenic factors the "angiogenic switch" is said to be activated and subsequently excessive vascularisation occurs. Many pathologies are reliant on vascular development for progression of the disease state. This is so for age-related macular degeneration (AMD), the third most common cause of blindness worldwide (World Health Organisation, 2010). Unnecessary neovascularisation of the choroidal vessels into the sub retinal space results in damaging the surface of the retina (Witmer et al., 2003). The angiogenic stimulation is unknown, however an upregulation of several pro angiogenic factors, including VEGF, is consistently observed (Michalska-Małecka et al., 2015). A further example of excessive vascularisation is cancer, where the three most lethal cancers, lung, liver and stomach cancer respectively, were responsible for over 3 million deaths in 2012 alone (Ferlay et al., 2012).

1.1.4 Angiogenesis Assays

Quantitatively analysing angiogenesis is of interest to understand the underlying physiological and pathophysiological mechanisms as well as to determine therapeutic efficacy of anti-angiogenic drugs. Ideal assays would truly replicate the process and enable reliable and repeatable quantitative results in a robust and rapid manner. Typically key angiogenic measures include the number of vessels/outgrowths, vessel length, vessel diameter, vessel branching and vascular density (Staton et al., 2009). Currently a combination of *in vitro*, *ex vivo* and *in vivo* approaches are used.

The majority of *in vitro* approaches are rapid and reproducible but focus on endothelial cells alone, therefore the lack of support cells, ECM and the differing environment can cause limitations. These include cell proliferation studies that quantify changes in cell number, differentiation studies that look for formation of tubule structures and cell migration studies through 3-D transfilter assays or by 2-D scratch assays (Staton et al., 2009).

To overcome the limitations of *in vitro* studies tissue sections can be cultured in a 3D matrix, to provide *ex vivo* assays. Angiogenesis is analysed through the formation of microvessel outgrowths from the tissue sample and is quantified through vessel number, length and area. These studies are thought to better replicate *in vivo* angiogenesis due to being grown in a specific matrix and the explant containing support cells, such as smooth

muscle and pericytes (Auerbach et al., 2003; Staton et al., 2009). The aortic ring assay is used most frequently, although these large vessel fragments do not accurately represent the microvasculature that usually undergo the angiogenic process *in vivo* (Auerbach et al., 2003). The same is true for human explant models using placental or umbilical blood vessels for preclinical screening research (Staton et al., 2009). The chick aortic arch assay addresses this, where 12 day old chick explants have properties similar to microvasculature endothelial cells. However, being an embryonic explant the tissue was undergoing rapid proliferation prior to dissection, therefore this may misrepresent the stimulation of non-proliferative endothelial cells in adult angiogenesis (Auerbach et al., 2003; Staton et al., 2009).

Observing angiogenesis *in vivo* is essential to complement *in vitro* and *ex vivo* studies for a full understanding, whereby the environmental and global systems involved in the process are present.

1.2 Cancer

1.2.1 Tumour Angiogenesis

Angiogenesis has been studied in the context of cancer for the past 100 years, when it was first observed within tumours. It is a fundamental requirement of tumour progression, through neovascularisation providing oxygen and nutrients for tumour growth as well as a possible route for metastasis (Gimbrone et al., 1972; Hanahan and Weinberg, 2011). Metastasis is the primary cause of death through tumour malignancy, causing angiogenesis to be a key therapeutic target for cancer. Anti-VEGF drugs, such as the humanised monoclonal antibody Avastin, are used in combination with chemotherapy to prevent metastasis and tumour growth in many cancers, as well as other angiogenic diseases (Kim et al., 1993; Ferrara and Kerbel, 2005; Carmeliet and Jain, 2011).

Tumours can use additional modes of angiogenesis as well as the physiological approaches described in Section 1.1.1. The tumour cells can migrate along and hijack the existing vasculature in a process known as vascular co-option. Alternatively tumour vessels can be lined with either tumour cells through vascular mimicry or by endothelial cells derived from cancer stem-like cells (Carmeliet and Jain, 2011).

1.2.2 Tumour Biology

Tumours, both benign and malignant, are masses of abnormal tissue that disrupt essential processes and create unfavourable internal environments. This occurs through the breakdown of normal cell and tissue physiology, which proves fatal. Tumour acquisition is seen to be a multistep process whereby crucial defensive mechanisms are deregulated by the accumulation of genetic alterations (Hanahan and Weinberg, 2000). The defence mechanisms are signalling pathways that enable the cell to respond to extracellular signals, therefore producing desired characteristics when required to effectively maintain homeostasis. Consequently, cancer is thought of as a disease of cell signalling, whereby signalling networks are hijacked through gain of function mutations in oncogenes and loss of function mutations in tumour suppressors (Hanahan and Weinberg, 2000).

Ras proteins (HRas, KRas and NRas) are the most commonly activated oncogenes in human cancers and other members of their signalling pathways are also frequently found deregulated (Downward, 2003). Ras is a small GTPase protein that acts to stimulate both the ERK and PI3K signalling pathways, Figure 1.3. Therefore, their gain of function mutations drive cellular proliferation, growth, survival and invasion, Figure 1.3 (Semenza, 2000; Roberts and Der, 2007). A prime example of a tumour suppressor is phosphatase and tensin homolog (PTEN), which is the second most commonly mutated or deleted tumour suppressor within human cancers (Yin and Shen, 2008). PTEN is a phosphatase protein that negatively regulates PI3K through removing phosphates from its downstream target phosphatidylinositol (3,4,5)-trisphosphate (PIP3), Figure 1.3. PTEN loss of function mutations are shown to drive tumour formation by enhanced cell proliferation, growth and survival (Di Cristofano et al., 1998; Cully et al., 2006). It has been shown in numerous studies that a decrease in PTEN expression coupled with an increased Ras activity leads to more metastatic and aggressive tumours (Dankort et al., 2009; Nogueira et al., 2010; Wang et al., 2012).

The majority of examined human cancers are shown to have increased expression of the principle pro-angiogenic factor VEGF (see Table 1 in Ferrara and Davis-Smyth (1997)). Studies have shown inhibiting its action reduces both tumour size and vessel density (Kim et al., 1993; Ferrara and Davis-Smyth, 1997; Papetti and Herman, 2002). The upregulation of VEGF and other pro-angiogenic factors are a result of increased HIF-1 expression, which is found frequently overexpressed in human cancers (Talks et al., 2000). This arises through several key tumour characteristics. Firstly, as the tumour cells proliferate to form a mass the central cells become deprived and hypoxic, therefore stimulating the HIF path-

way shown in Figure 1.2 (Thomlinson and Gray, 1955; Maxwell et al., 2001). In addition the genetic regulation of HIF-1 can be implicated through activating and inhibiting mutations of oncogenes and tumour suppressors, respectively, that have arisen through tumour procurement (Semenza, 2000). Such examples include the upregulation of Ras and the loss of PTEN that have previously been discussed. A further example is loss of VHL protein function, leading to constitutive activation of the HIF pathway through transcription (Maxwell et al., 1999; Zhong et al., 2000). Figure 1.2 highlights how the functional changes of these proteins would result in oxygen independent expression and transcriptional activity of HIF-1.

1.2.3 Tumour Vasculature Properties

Due to the deregulation of angiogenesis, tumour vasculature is seen to have key characteristics that differ from physiological vessels. The vascular network is seen to be aberrant and chaotic with an abnormal branching pattern, lacking the hierarchal structure of healthy physiological vasculature (Semela and Dufour, 2004). The tumour vessels are also seen to have a greater variation in diameter and are more permeable, a likely cause of immaturity, which further facilitates metastasis (Konerding et al., 1999; Papetti and Herman, 2002). During tumour progression angiogenic measures show an increase in vessel number, vessel branching and vascular density (McMahon et al., 2001; Semela and Dufour, 2004; Vakoc et al., 2009).

1.3 Zebrafish

Recently zebrafish, *Danio rerio*, have become a popular model organism for a variety of biological studies, including development, angiogenic disease and cancer (Serbedzija et al., 1999; Stoletov and Klemke, 2008). This is a result of their many beneficial features, including a fully sequenced, highly conserved genome, ability to easily perform large scale, *in vivo* research and high number of offspring (Amatruda et al., 2002; Lieschke and Currie, 2007; Stoletov and Klemke, 2008). Furthermore, the external fertilisation and development of the zebrafish embryo, coupled with its transparent nature, enables high-resolution optical imaging and ease of genetic manipulation (Barriuso et al., 2015). As a result large scale forward genetics and mutagenesis based studies can be researched in a vertebrate system (Lieschke and Currie, 2007; Lu et al., 2015).

Zebrafish also have a rapid generation time. By 72 hours post fertilisation (hpf) they hatch from the chorion and reach the larvae stage (Kimmel et al., 1995). When zebrafish

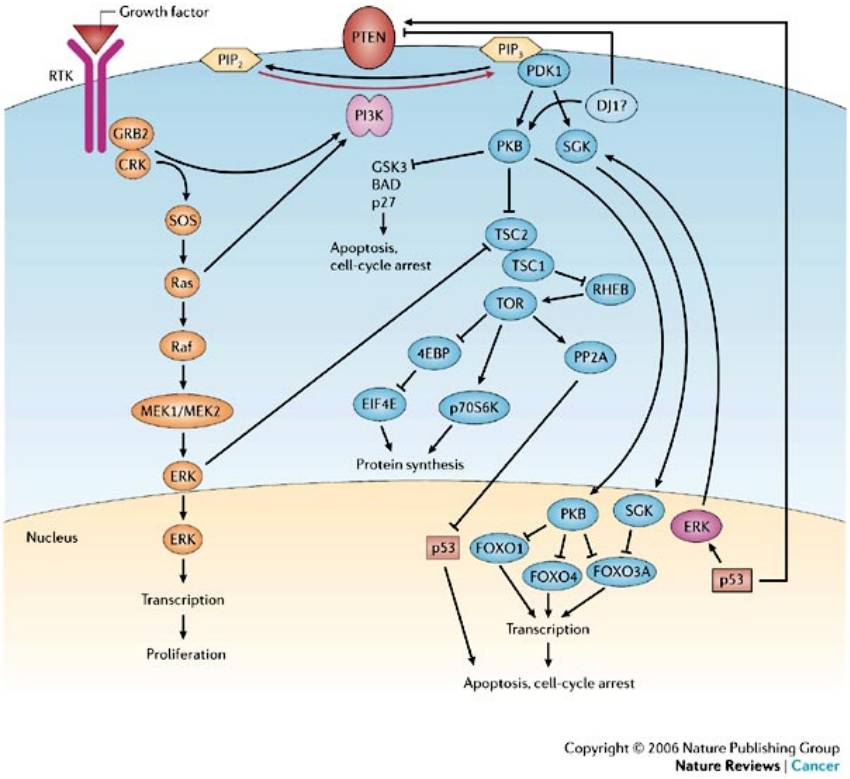

Figure 1.3: A schematic of the oncogene Ras and tumour suppressor PTEN signalling pathways. Ras promotes typical cancer cell characteristics, including transcription, cell survival, protein synthesis and proliferation. PTEN is the negative regulator of PI3K and suppresses these typical cancer cell characteristics when functioning correctly. Figure taken from Cully et al. (2006).

larvae reach 5 days post fertilisation (dpf) they are capable of independent feeding and have an inflated swim bladder (Kimmel et al., 1995; Sprague et al., 2006). At 30 dpf zebrafish reach the juvenile life stage, which is followed by adult life stage when they have reached sexual maturity (Sprague et al., 2006). This is usually at 90 dpf.

1.3.1 Mutant Non-Pigmented Lines

Due to their optical transparency zebrafish embryos are often a chosen model (Lieschke and Currie, 2007). However, this has severe limitations due to the immaturity of key biological processes implicated in disease pathophysiology, such as the vasculature and immune systems within cancer models. Zebrafish have three different types of chromatophore that contribute to their pigmentation and striped appearance. These are melanophores that create the black pigmented stripes, reflective iridophores and yellow coloured xanthophores. Early pigmentation begins to appear from 24 hpf, which progressively fills in throughout development (Kimmel et al., 1995; Sprague et al., 2006).

Casper is a transgenic zebrafish line developed by White et al. (2008) that remains optically transparent throughout its entire lifetime, Figure 1.4d. Its lack in pigmentation is a result of homozygous expression for two mutants, *nacre* and *roy*. The *nacre* mutant is a single base change mutation in the *mitfa* gene that consequently produces a truncated transcription factor, resulting in a complete lack of melanophores, Figure 1.4b (Lister, 1999). The *roy* mutant is a spontaneous mutation that has not yet been mapped, but its homozygous expression results in a total deficiency of iridophores and fewer melanophores, Figure 1.4c (White et al., 2008). Despite being ideal for fluorescence studies casper a low viability (approximately 50%) has been observed by the UCL fish facility that limit their breeding capabilities and this could potentially cause inaccuracy in disease studies. As a result a different mutant line with greater viability has been introduced. These fish are called TraNac and they physically identical to those with the casper phenotype, Figure 1.5. The difference is due to TraNac fish being homozygous recessive for a mitochondrial gene called *transparent (tra)* alongside *nacre*, opposed to *roy* (Krauss et al., 2013). The mutation present in the *tra* gene results in a truncated form of the mitochondrial protein mpv17, which leads to a loss of iridophores alongside a strong reduction in melanophores. This is shown in Figure 1.5a, which mimics the *roy* mutant in Figure 1.4c.

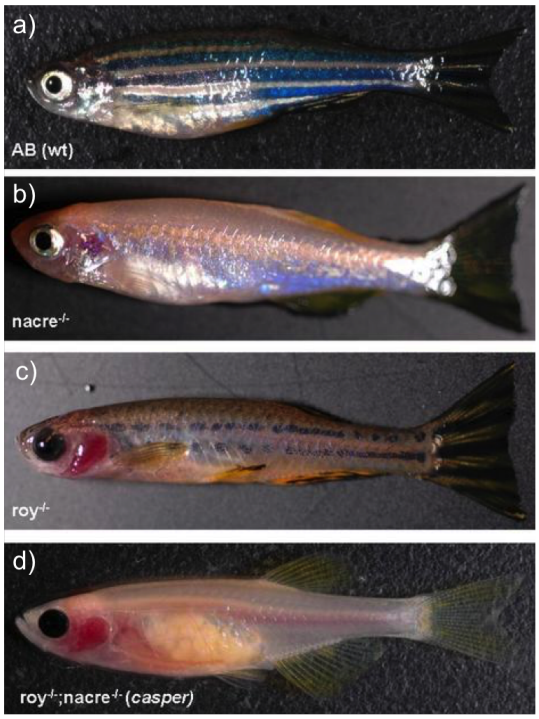

Figure 1.4: Pigmented wild type (a) and pigmentation mutant (b-d) zebrafish. b) shows the *nacre* mutant with a lack of melanophores, c) the *roy* mutant with lack of iridophores and reduction of melanophores and d) shows the optically clear double mutant casper zebrafish that lacks both melanophores and iridophores. Figure adapted from White et al. (2008).

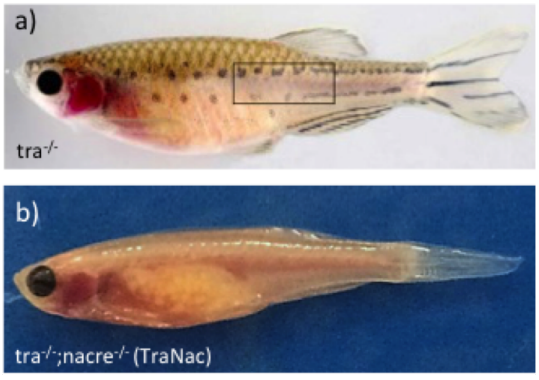

Figure 1.5: The *transparent (tra)* pigmentation mutant causes a lack of iridophores and reduction of melanophores in adult zebrafish (a) and combining this with the *nacre* mutant results in the non-pigmented, optically clear double mutant TraNac zebrafish, which completely lack melanophores and iridophores (b). Figure (a) adapted from Krauss et al. (2013).

1.3.2 Zebrafish Cancer Models

Zebrafish are proven to be important model organisms for researching cancer biology and they are seen to be very similar to humans with respect to their genome, gene expression and histology (Amatruda et al., 2002; Lieschke and Currie, 2007; White et al., 2013). Cancer models in zebrafish can be generated in several ways. Initially carcinogen treatment was used to spontaneously form tumours. This was advantageous due to the tumour being analysed within the true microenvironment. However, the spontaneity results in tumours that were difficult to identify in particular tissues, low incidence rates and late onset (Stoletov and Klemke, 2008). Zebrafish have also been widely used for xenograft models where human cancer cells are transplanted into the fish. This enables studies of human cancer cell progression, angiogenesis and metastasis within a whole vertebrate organism that is amenable for high throughput screens, pharmacological studies and high resolution imaging (Stoletov et al., 2007; Stoletov and Klemke, 2008; Konantz et al., 2012; Barriuso et al., 2015). To prevent rejection and successfully engraft the cancerous cells the zebrafish must be immunocompromised or under 30 dpf, where they lack an intact immune system (Stoletov and Klemke, 2008; White et al., 2013; Barriuso et al., 2015). Consequently the human pathology cannot be fully recapitulated as the immune system is known to closely interact with tumours in the progression of the disease state (Hanahan and Weinberg, 2011). This could heavily bias results. For these reasons transgenic zebrafish models of cancer can be favourable (Nguyen et al., 2012; White et al., 2013).

1.3.2.1 Existing Transgenic Cancer Models

Transgenic cancer models usually involve the overexpression of an oncogene to drive tumour formation. One such zebrafish model is the $BRAF^{V600E}$ driven melanoma (Patton et al., 2005). $BRAF^{V600E}$ is the most common oncogenic mutant of B-Raf, which is from the Raf family of serine kinases that are downstream effectors of Ras (Figure 1.3). Single base substitution mutations that activate BRAF are present within 66% of malignant melanomas and 80% of these are $BRAF^{V600E}$ (Davies et al., 2002). Only when expressed with a loss of p53 tumour suppressor function did this oncogene driven model produce malignant melanoma, which had great histological similarities to human pathology (Patton et al., 2005). However, this system is inefficient as only 6% of transgenic fish lead to malignant melanoma phenotypes. An alternate zebrafish melanoma model is driven by melanocyte expression of oncogenic $HRAS^{G12V}$ alone. This model produces neoplasia with spreading lesions and expansile nodules within 90% of animals by 12 weeks post fertilisation (wpf) (Michailidou et al., 2009). Within this model it was shown

that the Raf-Mek-Erk pathway was required and sufficient for neoplasia initiation but the PI3K pathway was essential for malignant progression (Michailidou et al., 2009). Both of the described melanoma models lack temporal control due to the spontaneity of tumour formation, so early tumour development stages may be missed. Furthermore, as these models are dependent upon melanocyte function and pigmentation, non-pigmented transparent lines cannot be used and the opportunity for optical imaging is not possible after the embryo life stage.

An alternative transgenic cancer model is the hepatocellular carcinoma (HCC) model developed by Nguyen et al. (2012). HCC is the most prevalent and malignant form of liver cancer within humans, where Ras is active approximately 50% of the time and its downstream signalling pathways (shown in Figure 1.3) are always found upregulated (Villanueva and Llovet, 2011; Nguyen et al., 2011, 2012). For example, this upregulation can occur through mutational activation of the upstream RTK epidermal growth factor receptor (EGFR) or inactivation of RasGAP that negatively regulates Ras activity (Baines et al., 2011; Nguyen et al., 2011, 2012). Furthermore, approximately 85% of Ras mutations within human cancer are within KRAS, the essential member of the Ras family (Downward, 2003). For these reasons the model is comprised of the zebrafish kras gene oncogenic mutant $kras^{V12}$ and it is N-terminally labelled with enhanced green fluorescent protein (eGFP). The expression of this oncogenic mutant is under spatial and temporal control through an inducible system utilising the liver specific promoter fatty acid binding protein 10 (*fabp10)*. Induction of tumour progression is dosage-dependent, whereby the level of $kras^{V12}$ expression is dependent on inducer concentration. Interestingly, removal of the inducer results in liver tumour regression and increased apoptosis, indicating 'oncogene addiction' is required for tumour maintenance (Nguyen et al., 2012). This HCC zebrafish model recapitulates the human disease as molecular hallmarks, signalling pathways and gene signatures are shown to be conserved (Nguyen et al., 2011).

1.3.2.2 Zebrafish Model of Tumour Angiogenesis

The HCC model zebrafish by Nguyen et al. (2012) has been adapted for studying angiogenesis within tumour development and progression. This tumour angiogenesis model zebrafish, TraNac *Tg (KDR:mCherry:Fabp10-rtTA:TREeGFPKRAS^{V12})*, inducibly expresses the eGFP-tagged oncogenic $kras^{V12}$ transgene specifically in hepatocytes through the Tet-On system. The Tet-On system uses two elements to control gene expression, a reverse tetracycline-dependent transactivator (rtTA) protein and a tetracycline response element (TRE) promoter sequence. The rtTA protein recognises and binds the TRE sequence

to elicit downstream effector protein expression only when tetracycline, or a derivative such as doxycycline, is bound (Bockamp et al., 2002). Within this zebrafish model the rtTA element is downstream of the *fabp10* liver specific promoter and the TRE sequence is upstream of the *eGFPKRAS*^{V12} transgene. Therefore oncogenic kras^{V12} is specifically expressed within hepatocytes and is dependent upon the presence and concentration of the inducer, doxycycline. Consequently tumours can be initiated when desired through the simple addition of doxycycline. This model is non-pigmented throughout its entire life span as a consequence of the TraNac mutant background. Also, the zebrafish have a red fluorescent vasculature due to mCherry fluorophore expression under the control of the endothelial specific promoter for KDR (VEGFR2). As a result fluorescent read-outs regarding tumour and vasculature physiology can be acquired throughout the entire lifespan of the zebrafish using optical imaging techniques. Figure 1.6 shows this tumour angiogenesis zebrafish model in the embryo and adult. The liver tissue is fluorescing green and the vessels are fluorescing red, where within the embryo individual primitive vessels are visible including the dorsal aorta (DA), the posterior cardinal vein (PCV) and the intersegmental vessels (SV) (Isogai et al., 2001).

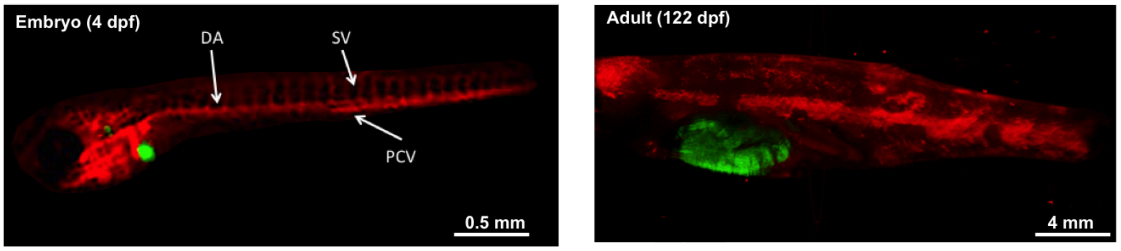

Figure 1.6: The tumour angiogenesis zebrafish model, TraNac *Tg (KDR:mCherry:Fabp10-rtTA:TRE-eGFPKRAS^{V12})*, with a red fluorescent vasculature and a green fluorescent liver tumour driven by the presence of doxycycline. a) shows the embryo at 4 dpf with 4 days of doxycycline treatment, highlighting the dorsal aorta (DA), posterior cardinal vein (PCV) and the intersegmental vessels (SV). b) shows the adult at 122 dpf after 2 weeks of doxycycline treatment. The embryo image was acquired using widefield microscopy and the adult image is a single maximum intensity projection using optical projection tomography.

1.3.3 Genomic Editing Techniques

Genetic analysis is an important approach to understanding the regulation of biological processes at the molecular level and zebrafish are prime model organisms for this type of research (Amatruda et al., 2002; Lieschke and Currie, 2007). Within the past few years novel genome editing techniques have been characterised to readily study gene function in zebrafish with ease, where it was previously difficult to implement loss of function mutations (Auer and Del Bene, 2014). These recent techniques include transcription activator-like effector nucleases (TALENs) and clustered regularly interspaced short palindromic repeats (CRISPRs). Both of these are able to modify particular genes of interest through introducing double strand breaks (DSBs) in targeted regions of DNA, Figure 1.7 (Dahlem et al., 2012; Hisano et al., 2014). This results in the induction of DNA repair mechanisms, such as non-homologous end joining (NHEJ) or homology directed repair (HDR), Figure 1.8. NHEJ repairs the DSB by fixing the two ends back together, but in doing so insertions or deletions (indels) are incorporated into the sequence resulting in frameshift mutations and defective proteins. Conversely, HDR uses a template of double stranded DNA to repair the break, therefore inserting precise sequences of DNA that have been designed and supplied (Sander and Joung, 2014; Hisano et al., 2014).

TALENs elicit their DSB through protein "arms". These arms are comprised of a DNA binding domain, designed to target the specific DNA sequence of interest, fused to a homodimeric FokI nuclease domain, Figure 1.7a. The specific DNA binding is achievable through approximately 20 highly conserved TALE repeats of 33-35 amino acids in length. These repeats recognise particular DNA bases through hypervariable residues called repeat-variable di-residues (RVDs) (Dahlem et al., 2012; Joung and Sander, 2013). Only when two arms are approximately 10-20 nucleotides apart can they bring the FokI nuclease domains together and elicit the DSB. The region of DNA between the two specific arm targets is called the spacer and this is where DSB occurs. This technique is precise and unlikely to elicit off target effects through cleavage being dependent on orientation and sequence of two specific 20 nucleotide DNA sequences (Miller et al., 2011; Joung and Sander, 2013).

Alternatively, CRISPRs function through the use of a single guide RNA (gRNA) and an accompanying Cas9 nuclease. The gRNA is composed of a 20 nucleotide DNA binding region, where Watson-Crick pairing occurs to complementary DNA. Following this is a 3 nucleotide protospacer adjacent motif (PAM) and a downstream region that can recruit the nuclease Cas9 (Auer and Del Bene, 2014). Through customising the DNA

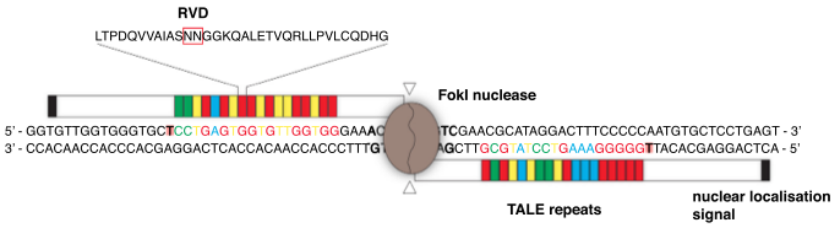

(a) TALEN

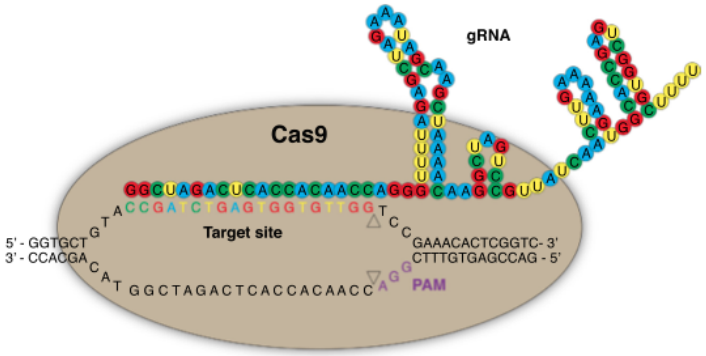

(b) CRISPR

Figure 1.7: Schematics of the two genome editing techniques, TALENs and CRISPRs. a) TALENs function through two protein arms containing DNA binding domains that bind approximately 10-20 nucleotides apart bringing homodimeric *FokI* nuclease domains together to elicit a DSB. DNA binding occurs through TALE arrays that contain repeat-variable di-residues (RVDs) that recognise particular nucleotides. b) CRISPR gRNA binds to target DNA regions, followed by the required PAM sequence, through complementary base pairing and recruits a Cas9 nuclease to cleave the desired target. Figure adapted from Auer and Del Bene (2014).

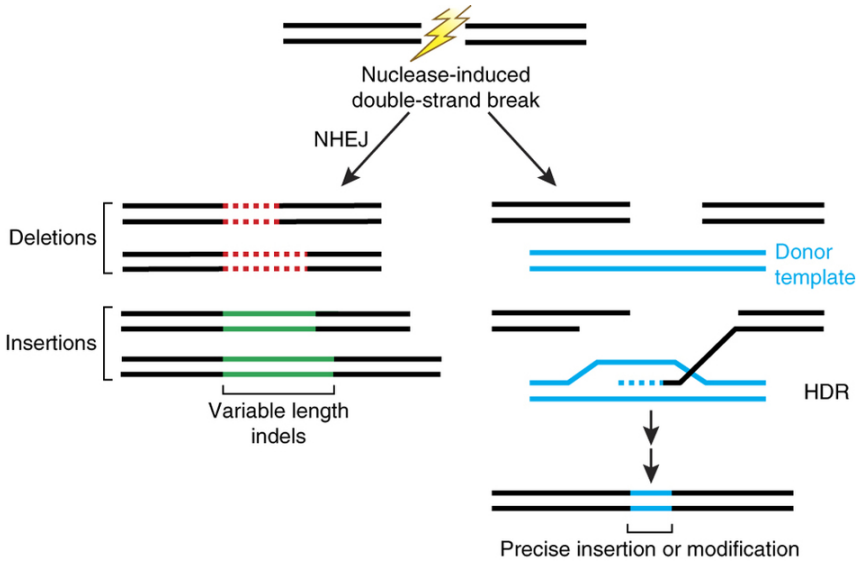

Figure 1.8: DNA repair mechanisms used to fix double strand breaks. The left hand side illustrates Non-Homologous End Joining (NHEJ), whereby the two ends are brought back together incorporating insertion or deletion mutations. The alternate mechanism, on the right, is Homology Directed Repair (HDR) that uses template DNA to fix the break, which can be used to incorporate precise modifications. Figure from Sander and Joung (2014).

binding nucleotides within the gRNA CRISPRs can target and bind specific loci, recruit Cas9 and produce a DSB 3 nucleotides upstream of the PAM domain (Jao et al., 2013; Hwang et al., 2013; Sander and Joung, 2014), Figure 1.7b. This causes more efficient and robust modification of gene sequence than the aforementioned TALENs, where the mutagenesis rate is consistently greater than 75% (Jao et al., 2013; Sander and Joung, 2014). It is also far less complex to design and produce the elements for CRISPR mutagenesis compared to synthesising and assembling an array of TALE protein repeats. However, there is a greater risk of off-target effects as it is reliant on a single 20 nucleotide stretch of DNA opposed to two that require correct spacing to elicit a response. There are now numerous tools available to help prevent this (Hsu et al., 2013; Auer and Del Bene, 2014).

Recently both TALENs and CRISPRs have also been used in zebrafish to perform precise knock-in mutations at DSBs through HDR (Bedell et al., 2012; Chang et al., 2013; Auer and Del Bene, 2014). This is achieved through using donor DNA that has sequence homology to the regions either side of the produced DSB. The optimal structure of the donor DNA is unknown and debatable, where different research groups are using DNA in circular, linear, single stranded or double stranded forms with relatively low efficiency (Genome Editing Session Workshop- Zebrafish Platform, The Allied Genetics Confer-

ence 2016). Bedell et al. (2012) have shown a TALEN mediated knock-in using a single stranded DNA (ssDNA) donor template containing a 34bp modified LoxP (mLoxP) site. This knock-in was targeted to an exon and had 10.3% insertion efficiency, where half of these were precise insertions with no additional indels. The mLoxP insertion was designed to disrupt the TALEN recognition sequence within the DNA, therefore the insertion will not be prone to further gene editing once incorporated. A CRISPR mediated approach has been described by Chang et al. (2013) where the same mLoxP sequence has been fully incorporated into the targeted exon in 1 of 12 tested embryos. However this was not precise and indels were seen around the insertion site. The donor template used here was also ssDNA and the insertion was targeted within the CRISPR recognition sequence, once again to prevent additional gene editing.

1.4 Imaging Modalities

Although much has been learnt from *in vitro* studies, the absence of integrative organ systems and true cellular environments limits their relevance and utility when studying disease and aiding drug development. *In vivo* studies can overcome this. Performing live global imaging of model organisms can provide spatial and temporal information of dynamic interactions at the molecular and signalling level (Ntziachristos et al., 2005).

1.4.1 The "Imaging Gap"

Whole model organism imaging at a reasonable resolution has been problematic due to the "mesoscopic imaging gap" that has become apparent between available imaging modalities (Sharpe, 2003; McDonald and Choyke, 2003). At one end of the imaging scale whole human, macroscopic, imaging techniques are available, such as magnetic resonance imaging (MRI) and computed tomography (CT) scans. These provide non-invasive 3-dimensional (3-D) imaging of internal structures within large specimens, however their achievable resolution is low (McDonald and Choyke, 2003). At the other end of the scale high resolution is achievable through microscopy techniques. One such example is 2-photon confocal microscopy, which also enable fluorescence readouts due to being an optical technique. Confocal images are gradually constructed through scanning the focal point of a laser along the sample to create optical sections, which is time consuming. This technique requires whole sample illumination and as a result the samples are prone to phototoxicity and photobleaching from prolonged exposure.

Intravital imaging can be achieved utilising 2-photon confocal microscopy or other mi-

croscopy techniques, but the maximal penetration depth is < 1mm (Potter et al., 1996; Vakoc et al., 2009; Conway et al., 2014). Therefore 3-D imaging of model organisms is reliant upon sacrifice, serial sectioning and subsequent digital reconstruction or is limited to the surface of optically clear specimens or those that have been prepared with a chronic-transparent window (Jain et al., 2002). The implantation of transparent window chambers is an invasive procedure that has significant disadvantages. The surgery disrupts the tissue being observed and this could bias results. For example, when studying angiogenesis the window is likely to disrupt the existing vasculature and physiological angiogenesis could occur for wound healing. Additionally, only subcutaneous tissues can be studied and the size of tumours and duration of the study are restricted due to the limited space and window degradation (Palmer et al., 2011; Moy et al., 2011).

1.4.2 Mesoscopic Imaging Techniques

There have been two different approaches to developing imaging modalities capable of whole organism mesoscopic imaging, spanning the micrometer to centimetre size range. The first has been to adapt the larger scale medical imaging techniques to image smaller specimens with higher resolution, such as micro computed tomography (microCT) and micro magnetic resonance imaging (microMRI). MicroCT can achieve cellular resolution of whole organisms comparable to the resolution and information achievable through histological analysis, if the specimen is not too large and is also imaged in segments (Betz et al., 2007; Cheng et al., 2011). The achievable resolution of microMRI, which is often insufficient for distinguishing particular tissues, is dependent upon the strength of the magnet and subsequently the modality is costly (Sharpe, 2003). Furthermore, neither of the aforementioned imaging techniques are able to image coloured dyes or fluorescent markers that are frequently used in biological assays. As a result sacrifice is often required for specific tissue imaging.

The second approach was to develop novel photonics based imaging techniques. One example is light sheet microscopy (LSM), which has reduced photobleaching and phototoxicity compared to 2-photon confocal microscopy. Only a thin, 2-dimensional (2-D) sheet of tissue selected for imaging is illuminated at any one time, creating optical sections. Numerous optical sections can be acquired throughout the specimen and can be used to create 3-D images. It is a fast imaging modality compared to other tomographic techniques, such as MRI and CT, and can achieve deep tissue penetration with subcellular resolution (Huisken and Stainier, 2009). Optically clear organisms up to 1 cm in size can be imaged, using multiple acquisitions and 3-D image stitching to overcome the mm size

field of view (Mayer et al., 2014). However, this is at the expense of resolution. Larger light sheets are required for uniform illumination within larger samples, therefore resulting in high lateral resolution but low axial resolution (Mayer et al., 2014). Additionally, LSM is only capable of fluorescence imaging and so brightfield (transmission) information that is important for many studies is not achievable (Mayer et al., 2014). It is also expensive as cost of implementation is approximately $30,000 (Santi, 2011).

1.4.3 Optical Projection Tomography

Optical projection tomography (OPT) is a mesoscopic imaging modality developed by Sharpe et al. (2002) that is analogous to the optical version of X-ray CT. Like LSM, OPT provides the advantages of fluorescence imaging and low phototoxicity associated with the widefield illumination. However, it also enables brightfield imaging, ease of scaling to image larger samples in a single acquisition and the cost of implementation is relatively low, comparable to that of a widefield microscope (Sharpe et al., 2002; Sharpe, 2003). OPT also offers the opportunity to reduce light dose and acquisition time using compressive sensing (CS) iterative reconstruction algorithms previously developed for X-ray CT (Correia et al., 2015). Due to its fluorescence and transmission imaging capability the system can take advantage of the numerous fluorescent dyes and markers that are readily available and have been frequently used to study tissues and genes (Sharpe et al., 2002). Using OPT high resolution images of whole specimens up to 15 mm in depth can be achieved (Sharpe et al., 2002). However, OPT is not capable of the subcellular resolution achievable by LSM (Santi, 2011; Mayer et al., 2014).

Specimens for imaging are placed within an index matched chamber and are subjected to widefield illumination. Transmitted light travels through two lenses positioned to maximise the depth of focus and subsequently 2-D projections are captured on a camera imaging chip (CIC). Within the projection each row of pixels represent an approximate line integral through the specimen. As the imaging chamber rotates multiple projections are acquired at different angles, therefore depth information can be rendered for each line integral to reconstruct 2-D transverse images (Sharpe, 2003). These 2-D images can be stacked to produce a 3-D image. A schematic of the OPT imaging apparatus is shown in Figure 1.9.

The crucial disadvantage to the system is the requirement of a transparent specimen with a homogenous refractive index. Previously OPT imaging has been performed using specimens that have been sacrificed and optically cleared (Sharpe et al., 2002; McGinty et al.,

2008) or those that are naturally transparent, such as the zebrafish embryo (McGinty et al., 2011; Correia et al., 2015; Andrews et al., 2016). Zebrafish embryos have been beneficial for many studies, however they have considerable limitations when studying some biological processes due to development of the animal being key. This is true when studying cancer where a mature vasculature and immune system are required to provide accurate representations of the human disease (Hanahan and Weinberg, 2011). Non-pigmented mutant lines of zebrafish, such as TraNac described in Section 1.3.1, that remain sufficiently transparent throughout their entire lifespan could enable live, adult imaging using OPT (Bassi et al., 2011; Fieramonti et al., 2012). However, due to internal organs the organisms do lack a consistent refractive index and so light scatter could cause unwanted artefacts during reconstruction.

To enable accurate live, adult imaging it is important that the non-pigmented zebrafish reach a deep level of anaesthesia where there is no response to external stimuli, Table 1.1. Furthermore, this level of anaesthesia needs to be maintained for prolonged periods of time without resulting in detrimental or lethal side effects. This is required as the 3-D reconstruction algorithms are reliant upon motionless specimens (Kak and Slaney, 1988; Sharpe et al., 2002).

1.5 Tomographic Reconstruction

1.5.1 Filtered Back Projection

3-D reconstruction of OPT images is conventionally performed using filtered back projection (FBP):

$$I(x,z) = \int_0^{\pi} \Big[\int_{-\infty}^{\infty} S_\theta(w)|w| e^{2\pi i w r} dw \Big] d\theta. \tag{1.1}$$

Every x row of pixels within the acquired 2-D (r,y) projection, P, is treated as a 1-dimensional (1-D) projection of the transverse slice through the specimen, where r is the polar co-ordinate $(x\cos(\theta) + z\sin(\theta))$ for the $x-z$ plane. This is indicated by the red ellipse and line in Figure 1.9 and illustrated within Figure 1.10. Observing these 1-D projections over all captured angles, $P_\theta(r)$, produces the fluorescence intensity sinogram (r,θ), where θ is the acquisition angle. The signal is subjected to deconvolution to account for the spatial frequency when sampling through filtering in the Fourier domain. The Fourier transform of $P_\theta(r)$, $S_\theta(w)$, is multiplied by a frequency filter function, such

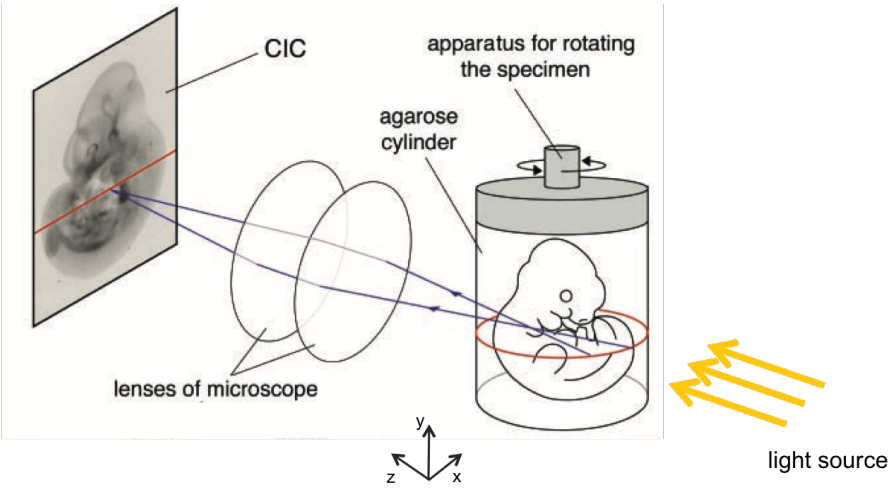

Figure 1.9: A diagrammatic representation of the OPT setup up for imaging whole organisms. The specimen is placed within the index matched chamber that rotates during image acquisition. The specimen is subjected to widefield illumination (yellow arrows) and transmitted light from the specimen (blue lines) is captured on the camera imaging chip (CIC) through two lenses that maximise the depth of focus, forming a projection. Each row of pixels within the projection corresponds to a transverse *(x-z)* section of the imaged organism (red ellipse and line). These can be observed over all acquired angles to reconstruct 2-D transverse images. Figure adapted from Sharpe et al. (2002).

Level	Movement	Opercula	Reaction to Stimuli
Light Anaesthesia	Equilibrium Loss Erratic Swimming	Increase	Only to substantial
Deep Anaesthesia	None	Decrease	None
Medullary Collapse (death)	None	Ceases	None

Table 1.1: Definitions of the levels of anaesthesia experienced in the zebrafish, with corresponding physical movement and reaction to external stimuli. Table adapted from McFarland (1959) and Ross and Ross (2008).

as the ramp filter $|w|$, and then the inverse transform is taken to produce the filtered sinogram. These sinograms are then back-projected at the acquisition angle to reconstruct the corresponding $(x-z)$ image I. The 3-D image can be produced by stacking the $(x-z)$ images for all r (Kak and Slaney, 1988; McGinty et al., 2008).

The filter is an essential aspect of the reconstructions that controls both unwanted blurring and high intensity central regions that result when overlapping the reconstructed $(x-z)$ slices. A ramp filter is used to enhance the high frequencies and reduce the lower ones in a linear manner, therefore enhancing contrasting features and minimising blurring. Statistical noise is often found as high frequency components in the Fourier domain and so applying the Ramp filter over a Hanning window, $H(w) = 1 + \cos(\pi w/w_n)$ where w_n is the Nyquist frequency, can further reduce aliasing (Chesler and Riederer, 1975).

A key principle of OPT is that parallel beam projection is assumed, defining projections 180° apart as identical. However, due to the inconsistent refractive index of the zebrafish and resultant scattering this is not so. As a result projections are captured over $0 < \theta < 2\pi$ to maximise the depth information acquired (McGinty et al., 2008).

1.5.2 Compressive Sensing

In many applications it is advantageous to acquire images in the minimal time possible. This is the case when imaging zebrafish through OPT, whereby their viability upon recovery is dramatically reduced under prolonged anaesthesia (Sun et al., 2009; Matthews and Varga, 2012). In order to accurately reconstruct an OPT dataset using FBP the number of angular projections obtained over 180° must be sampled at a rate equal to or better than the Nyquist frequency along the circumference of the zebrafish (Kak and Slaney, 1988; Phelps, 2006). However, acquiring a full dataset is time intensive and undersampling the data would result in a degradation in image quality and an increase in aliasing.

CS has been successfully incorporated in applications similar to OPT, such as CT and MRI reconstruction (Sidky and Pan, 2008; Sidky et al., 2009; Lustig et al., 2007; Chakraborty, 2008). It has also been used to successfully reconstruct high quality images from undersampled OPT datasets in zebrafish embryos (Correia et al., 2015). It can account for low sampling and computationally reconstruct a high quality image from an incomplete set of measured signals by exploiting redundancy. This is achieved through attempting to solve

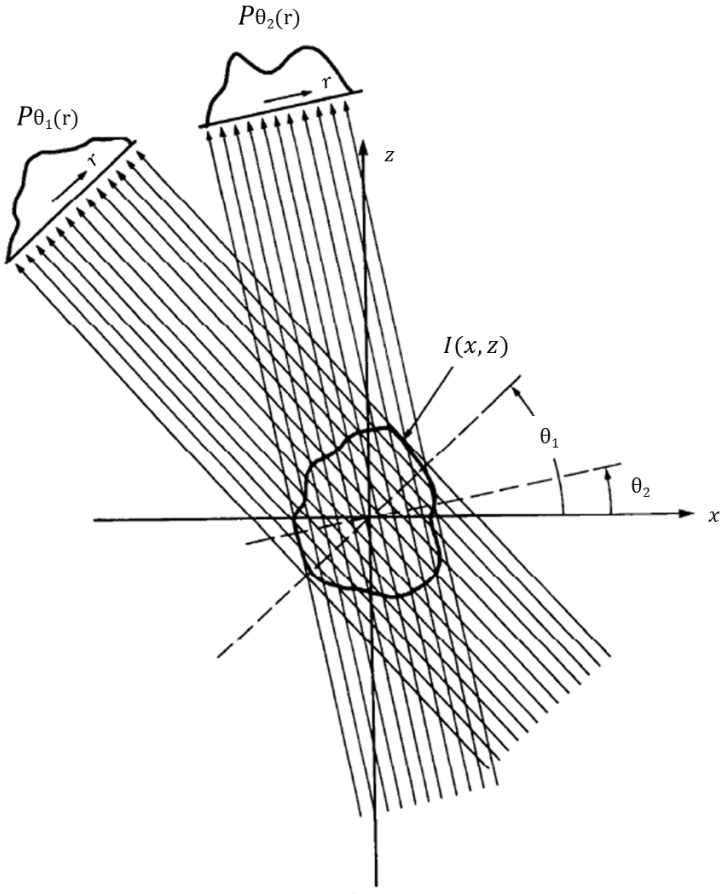

Figure 1.10: A schematic explaining the geometry and notation used in filtered back projection (FBP) reconstruction of OPT images, Equation 1.1. The 2-D transverse slice, *I(x-z)*, of the 3-D specimen is shown, where the projections, P, are being captured for the polar coordinate *r* at different angles, θ. Figure adapted from Kak and Slaney (1988).

the underdetermined linear problem;

$$P_\theta(r) = KI + \varepsilon, \tag{1.2}$$

under the constraint of sparsity, where the measured sinogram is comprised of the Radon transformation, K, of the unknown fluorescence signal with the addition of noise, ε (Donoho, 2006; Candès and Wakin, 2008). Sparsity is defined as having very few non-zero components, therefore observing the image within a sparsifying domain would result in little information. For example, Figure 1.11 shows a phantom image and its sparse representation in the gradient domain, where only neighbouring pixels that differ in intensity are represented. The original image has 32412 non-zero components and the gradient domain has only 2949, therefore is sparse. Hence, the objective function most commonly used for signal restoration can be minimised to recover I whilst exploiting this sparsity through regularisation, where $\phi(I)$ is the regulariser and τ is the regularisation parameter:

$$f(I) = ||P_\theta(r) - KI||_2^2 + \tau\phi(I). \tag{1.3}$$

The first element in the objective function is a data fidelity term that measures the residual error between the acquired and estimated data through the l_2 norm. The regularisation terms are chosen to reflect prior knowledge of the images, where the regulariser is the measure of sparsity and the parameter determines the degree of regularisation compared to data fidelity.

(a) **(b)**

Figure 1.11: An example of sparse representation of an image, where a) is a phantom in the image domain with 32412 non-zero components and b) is its sparse representation in the gradient domain with only 2949 non-zero components.

The l_0-norm is usually used to assess sparsity through computing the number of non-zero entries. However, it is non-convex and therefore becomes computationally difficult to minimise the objective function of Equation 1.3. The l_1-norm can provide a good approximation of the sparsest solution through calculating the sum of the coefficients and it is convex, so is often used an alternative. However, it has been found that for many images the TV-norm is more appropriate as a regulariser, where the total variation (TV) of the images is minimised instead. The TV of the image is defined as;

$$\phi_{TV}(I) = \sum_i \sqrt{(D_H I)_i^2 + (D_V I)_i^2}, \tag{1.4}$$

where D_H and D_V are the gradients of pixel i in the horizontal and vertical direction, respectively, (Rudin et al., 1992; Candes et al., 2005). Due to OPT images being piece-wise constant with sharp defining edges it is appropriate to assess sparsity of the gradient coefficients through TV, as they are compressible in this domain.

Aims of Thesis

Angiogenesis is found deregulated in many pathologies, including cancer where it is required for tumour progression and metastasis. Due to the absence of integrative organ systems and true *in vivo* microenvironments it is increasingly accepted that biological processes differ significantly when observed *in vitro*. Therefore, it is essential that *in vivo* research of whole organisms is performed to complement *in vitro* investigation. Live, global imaging of model organisms should achieve this, where longitudinal studies can be performed to provide additional information and increased accuracy. Furthermore, it is preferable to research tumour progression and angiogenesis within adult organisms. This is due to the requirement of a mature immune system and fully formed vasculature, which are not present within developing organisms, to accurately represent the human pathology.

The overarching aim of the research project was to develop a quantitative, global imaging platform that enables longitudinal studies of tumour progression and angiogenesis within adult zebrafish. OPT imaging and the tumour angiogenesis zebrafish model, TraNac *Tg (KDR:mCherry:Fabp10-rtTA:TREeGFPKRAS^{V12})*, could provide this and enable mechanistic and drug development studies. However, system optimisation was required and changes to the model organism could be desirable to better reflect the human disease. These became my main research objectives, which were to:

- Reduce the OPT imaging acquisition time when imaging adult zebrafish with inducible eGFP-tagged liver tumours and mCherry labelled vasculature
- Accurately quantify tumour progression and vascularisation from the resulting OPT images
- Perform and optimise longitudinal imaging of tumour progression and vascularisation
- Perform mechanistic studies of tumour progression by developing novel zebrafish models.

CHAPTER 2

Materials and Methods

2.1 Zebrafish

2.1.1 Husbandry and Breeding

All fish were kept in the Fish Facility at UCL in 28°C system water on a photoperiod of 14 hours light followed by 10 hours dark. The system water comprises of Tropin Marin® marine salts added to reverse osmosis (RO) water to a conductivity of 420 MicroSiemens. The products of fish metabolism and the addition of food increase the conductivity, which is monitored to run between 420 and 520 MicroSiemens. The pH is automatically adjusted to 7.0 through the addition of sodium bicarbonate. Fish were fed twice daily with a mix of live brineshrimp, blended krill and Hikari protein pellets. When breeding, a male and female fish of choice were placed within breeding tanks that contain a specialist insert to separate the fish from the eggs laid. Embryos were collected and kept in system water with 0.003% (w/v) methylene blue to prevent fungal infection, and were incubated at 28°C. They enter the UCL Fish Facility nursery at 4 days post fertilisation (dpf) and reach sexual maturity within 60 dpf.

2.1.2 Anaesthesia Preparations

Unless otherwise stated, tricaine methanesulfonate (MS-222) (Sigma) was used to anaesthetise zebrafish. 400 mg tricaine methanesulfonate powder was dissolved in 97.9 ml deionised water with 2.1 ml 1M Tris and adjusted to pH 7. This was stored at -20°C. For embryos 1 ml was used per petri dish and for adults a 4.2% (168 parts per million (ppm)) solution within system water totalling 100 ml.

In some instances isoflurane (Abbott) was used as an anaesthetic. Isoflurane was dissolved in ethanol to create a 100,000 ppm stock solution and stored at 4°C. The desired amounts of anaesthetic were added to fish water immediately prior to use.

2.1.3 Testing Anaesthesia

Zebrafish were placed into 100 ml of water containing the prescribed anaesthesia concentrations. Deep anaesthesia (Table 1.1) was determined by the loss of righting reflex and response to external stimuli, through both tapping the bench and pinching the caudal fin. Once deep anaesthesia was achieved the fish were placed into a fluorinated ethylene propylene (FEP) tube used for OPT imaging containing the same anaesthetic solution. Whilst in the tube the fish were closely monitored for movement, opercula movement and response to external stimuli through tapping the bench. The external stimuli of tapping on the bench is a greater stimulus than what would be experienced during OPT acquisition. The fish were removed from the tube and placed in a recovery tank, when they either awoke or as opercula movement ceased prior to encountering medullary collapse. Their recovery was monitored and a Pasteur pipette was used to gently squirt oxygenated water over the gills. Recovery was defined as the ability for the fish to swim once the righting reflex had returned.

2.1.4 Transgenic and Mutant Lines

The tumour angiogenesis zebrafish model used throughout was the TraNac *Tg(KDR:mCherry:Fabp10-rtTA:TRE-eGFPKRAS^{V12})*. These fish are an inducible, eGFP labelled genetic model of liver cancer that also present mCherry labelled vasculature. They also remain transparent throughout all life stages. The line was generated through the breeding of non-pigmented TraNac zebrafish (gift from Julian Lewis, Cancer Research Institute), a double mutant for the *mitfa/nacre* and the *mpv17/transparent* genes, to both *Tg(KDR:mCherry)* fish (gift from Steve Wilson, University College London) and *Tg (Fabp10-rtTA:TRE-eGFPKRAS^{V12})* fish (gift from Zhiyuan Gong, National University of Singapore). The resultant TraNac *Tg(KDR:mCherry)* and TraNac *Tg(Fabp10-rtTA:TRE-eGFPKRAS^{V12})* were crossed to generate the line.

Other zebrafish lines used included wild-type (AB), the non-pigmented mutant line Casper (*roy-/roy-; nacre-/nacre-* double mutant) gifted by Leonard Zon (Harvard Medical School) and the transgenic line *Tg (KDRmCherry:cmlc2GFP)* gifted by Ian Zachary (UCL). The *Tg (KDRmCherry:cmlc2GFP)* zebrafish were on a wild-type background with mCherry and GFP labelled vasculature and cardiomyocytes, respectively.

2.1.5 Embryonic Microinjection

Embryos were injected with 1 nl of solution at the one-cell stage of development, within the first 15 minutes of fertilisation for the greatest efficiency of germ cell integration. Glass capillary needles were loaded with the required solution before inserting into the microinjector, where the liquid was then forced out through applying air pressure. The volume injected was calibrated using a graticule. The needle was positioned in the blastodisc of the embryo for injection.

2.1.6 Fluorescent Zebrafish Larvae Selection

Embryos with fluorescent markers were selected under a widefield microscope from 2 dpf under anaesthesia.

2.1.7 Tumour Expression

Tumour induction of zebrafish containing the *Fabp10-rtTA:TREeGFPKRAS*^{V12} transgene were performed through the addition of doxycycline (Sigma D-9891) to the fish water at a concentration of 10 mg/L, unless otherwise stated. The eGFP signal was usually seen at approximately 4 days post induction (dpi) when using 10 mg/L. Tumour reduction was achievable through removing the doxycycline stimulant, which was used for zebrafish larvae selection.

2.1.8 DNA Extraction

2.1.8.1 Single Embryo DNA Extraction

The HotSHOT method was used for single embryo DNA extraction. Individual embryos were placed in separate wells of a 96 well plate with the excess water removed. 25 μl of base lysis buffer (25 mM KOH, 0.2 mM EDTA) was added to the individual embryos and the plate incubated at 95°C for 30 minutes. Once cooled to room temperature 25 μl of neutralisation solution (40 mM Tris-HCl at pH 5.0) was added to the wells and the plate was centrifuged to pellet the remaining tissue. The concentration of extracted DNA allowed for 1 μl of this solution to be used in subsequent polymerase chain reactions (PCRs).

2.1.8.2 Fin Clipping

DNA samples were acquired from adult zebrafish through fin clipping. The fish were anaesthetised in 4.2% MS-222 until they lost the tail pinch response. At this point less than 50% of the caudal fin was clipped using a sterile razor blade. The fish were transferred to a recovery tank, monitored to regain consciousness and then returned to storage tanks in isolation. The fin clip was placed into 140 μl of DNA extraction buffer (made with 50 μl 1 M Tris pH 8.0, 20 μl 0.5 M EDTA, 50 μl 20% Triton X-100 and 4.88 ml nuclease free H_2O) with 10 μl of 20 mg/ml Proteinase K. The reactions were then incubated at 57°C overnight in a waterbath followed by incubation for 10 minutes at 100°C before being centrifuged to pellet the remaining tissue. The concentration of extracted DNA solution required 3 μl to be used in subsequent PCRs.

2.2 Molecular Biology

2.2.1 Materials

2.2.1.1 LB Broth

Luria Bertani (LB) broth medium was made through adding 20 g of LB Broth Base (Invitrogen) to 1 L of deionised water and autoclaving. Ampicillin antibiotic was added as a selective agent once the broth had cooled to room temperature at a concentration of 100 μg/ml.

2.2.1.2 LB Agar Plates

LB agar medium was made through adding one LB Agar Tablet (Sigma-Aldrich) per 50 ml of deionised water and autoclaving. Once the solution had begun to cool ampicillin antibiotic was added at a concentration 100 μg/ml before the medium was poured into 10 cm petri dishes (approximately 20ml per dish) and left to solidify through cooling to room temperature. LB agar plates were stored at 4°C.

2.2.2 Molecular Cloning

2.2.2.1 Bacterial Transformation

Bacterial transformation was performed through the heat shock protocol. Unless otherwise stated the competent cells used were Stellar^{TM} (Clontech), which were were thawed on ice. 4 μl of plasmid DNA was added to 50 μl of the cells. This was left on ice for 20

minutes before performing heat shock at 42°C for 45 seconds. The cells were then placed on ice for a further 2 minutes before adding 250 μl of SOC media and were then left to recover at 37°C for 1 hour. The transformation can then be plated on LB agar plates with the appropriate antibiotic and left at 37°C overnight.

2.2.2.2 Expanding Bacterial Cultures

A single colony grown on a LB agar plate with the appropriate selective agent was isolated and added to 5 ml volume of LB broth with the appropriate antibiotic. This was then incubated for 16 hours at 37°C, shaking at 300 rpm.

2.2.2.3 Plasmid Isolation and Purification

Plasmids were isolated from bacterial cultures using the QIAGEN QIAprep Spin Miniprep Kit according to manufacturers instructions.

2.2.3 Polymerase Chain Reaction

All PCRs were performed with either Phusion® High-Fidelity DNA Polymerase (New England Biolabs) or Taq PCR Master Mix Kit (QIAGEN). Primer details, including sequences, annealing temperatures and the PCR enzyme used, are described in Table 2.1.

PCR with Phusion® High-Fidelity DNA Polymerase:

Per 50 μl reaction:

10μl	5x Phusion HF Buffer
1μl	10 mM dNTPs
2.5μl	10 μM forward primer
2.5μl	10 μM reverse primer
1.5μl	DMSO
0.5μl	Phusion DNA Polymerase
3μl	Extracted DNA
29μl	Nuclease Free Water

Cycling Conditions:

98°C	30*sec*	
98°C	10*sec*	} 35*cycles*
X°C	30*sec*	
72°C	30*sec*	
72°C	10*min*	

where X corresponds to the annealing temperature (Table 2.1).

PCR with Taq PCR Master Mix Kit:

Per 20 μl reaction:

$10\mu l$	2x Taq PCR Master Mix
$0.5\mu l$	100 μM forward primer
$0.5\mu l$	100 μM reverse primer
$3\mu l$	Extracted DNA
$6\mu l$	Nuclease Free Water

Cycling Conditions:

95°C	10*min*	
95°C	30*sec*	} 30*cycles*
X °C	30*sec*	
72°C	1*m*30*sec*	
72°C	10*min*	

where X corresponds to the annealing temperature (Table 2.1).

Gene of Interest	Polymerase used	Annealing Temperature	Primer	Sequence ($5' \rightarrow 3'$)
bcar1	Taq	60°C	Forward	AGTCTCCAGACGAGTTGTCC
			Reverse	TGCCAACGAGAATCTTCA
ptenb	Taq	52°C	Forward	TGTTGAGCTTTTGTTGGATGAA
			Reverse	CGATCAAACAGCCGCCTTAA
ptenb-LHS	Phusion	60°C	Forward	GACCAATGCTGATGATGTTCCA
			Reverse	AACCGATATCACAGAACTGAAGT
ptenb-RHS	Phusion	58°C	Forward	AAGGGAAGAACGGGTGTCAT
			Reverse	AGCCACCATCATTTGCAATCT
TREeGFPKRAS^{V12}	Taq	59°C	Forward	TATATCATGGCCGACAAGCA
			Reverse	GTGAGAGCGCTTTTGCCTAC

Table 2.1: Primer sequences and annealing temperatures used for PCRs and subsequent Sanger sequencing

2.2.4 Gel Electrophoresis

1.6% agarose gels were made using molecular grade agarose powder (Bioline) and 1x TAE Buffer (5PRIME), with the addition of 6 μl GelRed Nucleic Acid Gel Stain (Cambridge Bioscience) per 100 ml. All gels were run at 110 V in 1x TAE Buffer.

2.3 Genome Editing

2.3.1 Determining the Target Region

Ensembl genome browser (`http://www.ensembl.org`) was used to analyse the genes of interest within the zebrafish. The target region was determined and then primers were designed to confirm the sequence within the zebrafish using Primer3 (`http://primer3.ut.ee`) and UCSC In-Silico PCR (`http://genome.ucsc.edu`). PCR was then performed to enable Sanger sequencing by Source Bioscience (UK). Primers used can be found in Table 2.1.

2.3.2 TALENs

2.3.2.1 Design

The TALEN arms were created using the fast ligation-based automatable solid-phase high-throughput (FLASH) protocol published by Reyon et al. (2012). The sequenced, conserved DNA regions of interest were used to design TALENs using the online ZiFiT Targeter Software Version 4.2 (`http://zifit.partners.org/ZiFiT/`). The output from this included a sequence of TALE repeats and FLASH-IDs, the latter being a plasmid encoding one, two, three or four particular TALE repeats (detailed information regarding DNA sequence is available in Supplementary Tables 1 and 2 of Reyon et al. (2012)). Expansion of the desired FLASH plasmids (generously donated by Wilson group (UCL)) was performed before use.

2.3.2.2 Construction

For more detailed methodology see Supplementary Document 1 in Reyon et al. (2012). When purification and quantification are stated with respect to TALEN construction it refers to using QIAGEN QIAquick PCR Purification Kit according to the manufacturers instructions followed by the Nanodrop spectrophotometer, unless otherwise stated.

The FLASH plasmid containing the initial TALE fragment required amplification and 5'- biotinylation through PCR. This was performed using Phusion DNA Polymerase with the biotinylated forward primer (5' - Biotin - TCTAGAGAAGACAAGAACCTGACC - 3'), and was subsequently digested with BsaI-HF for 15 minutes at 50 °C before purification and quantification.

Each extension or termination FLASH plasmid was then prepared through a series of digestions at 37°C with BbsI, XbaI, BamHI-HF and SalI-HF for 2 hours, 5 minutes, 5 minutes and 5 minutes, respectively, to remove the backbone. This was followed by purification and quantification.

The FLASH units were then assembled through serial, solid-phase ligations and digestions on streptavidin coated magnetic beads (Dynabeads, Life Technologies) using BsaI-HF and T4 DNA ligase. They were then released from the beads through BbsI digestion. The resulting DNA of TALE repeats was then purified once again before cloning into the required JDS TALEN expression plasmid (gift from Wilson Group (UCL)) that had been digested by BsmBI for 8 hours at 55°C. The JDS plasmid used was dependent upon the final base in the TALEN binding site, shown in Table 2.2. These plasmids were then transformed into XL10-Gold Ultracompetent Cells through heat-shock and were left to grow on an ampicillin LB agar plates. The colonies that grew were then verified through colony PCR as follows:

Per 20μl reaction:

12.5μl	QIAGEN Taq Polymerase mastermix
1μl	2μM forward primer (5'- GACGGTGGCTGTCAAATACCAAGATATG)
1μl	2μM reverse primer (5'- TCTCCTCCAGTTCACTTTTGACTAGTTGGG)
5μl	colony sample

Cycling Conditions:

95°C	10*min*	
95°C	30*sec*	} 35*cycles*
62°C	30*sec*	
72°C	2*min*40*sec*	
72°C	10*min*	

The PCR products were examined through gel electrophoresis, where positive samples were expected to be 2.1 kb. Potential candidates were subsequently purified and sequenced by Source BioScience (Cambridge, UK).

JDS Plasmid	Final Base of TALEN Target Site
JDS70	A
JDS71	C
JDS74	G
JDS78	T

Table 2.2: JDS TALEN expression plasmids used for cloning TALE repeats from serial ligations. JDS plasmid used was dependent upon final base of TALEN binding site.

2.3.2.3 Transcription

The positive colonies were cultured for expansion and the TALEN plasmids were then isolated. The plasmids were linearised using PmeI (NEB) in CutSmart buffer at 37°C for one hour and subsequently purified using the QIAquick PCR Purification Kit. Transcription was then performed using the T7 Polymerase mMESSAGE mMACHINE^{TM} kit (Ambion) following manufacturers instructions and the TurboDNase step to remove the residual DNA template was included. The TALEN mRNA required a polyA tail for improved translational efficiency *in vivo*, which was achieved through the Poly(A) Tailing Kit (Ambion) following manufacturer instructions. The resulting RNA was purified using RNA Clean & Concentrator^{TM}-5 by Zymo Research and eluted in 25 μl of nuclease free water, before being quantified by Nanodrop.

2.3.3 CRISPRs

2.3.3.1 Design

The online CRISPR design tool (`http://crispr.mit.edu`) developed by Hsu et al. (2013) was used to generate possible guide RNAs (gRNAs) to target desired regions, of which the highest scored sequences were chosen as they are most unlikely to have off-target effects.

2.3.3.2 Construction

The gRNAs were created through transcription from a synthesised double stranded DNA (dsDNA). The dsDNA was created through annealing and extending two custom DNA oligonucleotides, as previously shown in Gagnon et al. (2014). The gene specific forward oligonucleotide consisted of the T7 promoter, the 20 nucleotide gRNA sequence identified and a complementary region to the reverse oligonucleotide that contained the Cas9 recruitment sequence. These oligonucleotides were synthesised by Eurofins Genomics (Germany).

Forward oligonucleotide template:
5'-TAATACGACTCACTATAAGG-N_{20}-GTTTTAGAGCTAGAAATAGCAAG-3'

Reverse oligonucleotide sequence:
5'- AAAAGCACCGACTCGGTGCCACTTTTTCAAGTTGATAACGGACTAGCCTTA
TTTTAACTTGCTATTTCTAGCTCTAAAAC-3'

The annealing reaction was performed with 10 μM of each oligo in a 10 μl reaction under the following conditions:

95°C	5 min
95°C $\rightarrow$ 85°C	-2°/sec
85°C $\rightarrow$ 25°C	-0.1°/sec
4°C	Hold

This was then immediately followed by the extension phase, which ensured the entire sequence was double stranded, through incubating at 12°C for 20 minutes after the addition of the following reagents from NEB:

2.5μl	dNTPs (10mM)
2μl	10x NEB Buffer 2
0.2μl	100x NEB BSA
0.5μl	T4 NEB DNA polymerase
4.8μl	Nuclease Free Water

The reaction was then purified using QIAGEN QIAquick PCR Purification Kit according to the manufacturers instructions, verified through gel electrophoresis and subsequently quantified using the Nanodrop.

2.3.3.3 Transcription

CRISPR transcription was achieved through the NEB HiScribe^{TM} T7 High Yield RNA Synthesis kit, following manufacturers directions. The QIAGEN RNeasy Mini kit was used to purify the RNA and remove remaining DNA template, where it was eluted in 30μl of nuclease free water. Concentration was then determined by Nanodrop.

2.3.3.4 Cas9 transcription

Cas9 mRNA was also required for CRISPR functioning. This was transcribed from a plasmid generously donated by the Wilson group (UCL) using the T3 Polymerase mMESSAGE mMACHINE^{TM}, TurboDNase and Poly(A) Tailing kits (Ambion), all following manufacturers instructions. The resulting RNA was purified through RNA Clean & Concentrator ^{TM}-5 by Zymo Research and quantified using the Nanodrop.

2.4 Genotyping

2.4.1 Sanger Sequencing

Sanger sequencing was performed by Source BioScience (Cambridge, UK) where PCR products at a concentration of 1 ng/μl per 100bp were analysed using 3.2 pmol/μl of supplied sequencing primers (as shown in Table 2.1).

2.4.2 Deep Sequencing

Primers surrounding the expected TALEN or CRISPR cleavage site were designed so they produced approximately a 200bp amplicon, had a melting temperature of approximately 60°C to 65°C and had no secondary structure or primer dimers. The primers had overhangs that were universal tags for the forward and reverse primers. This is schematically shown in Figure 2.1 and all MiSeq primers used and their corresponding annealing temperatures are shown in Table 2.3. These primers were then used to amplify the DNA region of interest through a PCR with Phusion® High-Fidelity DNA Polymerase, as described in Section 2.2.3. Gel electrophoresis was performed on the PCR products to confirm a single product and then the amplicons were cleaned using the QIAGEN QIAquick PCR Purification Kit according to the manufacturers instructions. The resulting DNA was quantified by the Nanodrop spectrophotometer and diluted to 15-25 ng/μl before being passed to the Wilson Group (UCL) to perform deep sequencing using the Illumina MiSeq based upon the protocol published within Gagnon et al. (2014).

Figure 2.1: A schematic of the primer design for deep sequencing using the Illumina MiSeq. Amplicon specific primers are designed with universal tags, where the blue indicates the universal tag for the forward primer and the red for the reverse primer.

Target	MiSeq Primer	Gene Specific Sequence ($5' \rightarrow 3'$)	Annealing Temperature
ptenaL	MiSeq-Forward 1	ACGCAGCGCTAGTTTCTTGTTTA	68°C
	MiSeq-Reverse 1	TACTTACCGGACAACGTCATCAA	
	MiSeq-Forward 2	TCTTGCTTGTCTCTTCTCTCACA	66°C
	MiSeq-Reverse 2	TGTCTCACAGAATGGTGCAATAAAA	
ptenaR	MiSeq-Forward 1	CAGCCGTGTCTAAAATAAAACTCAA	67°C
	MiSeq-Reverse 1	TACGTACGGAAGAAACAAGAACG	
	MiSeq-Forward 2	CTGAAGCCGCGCCACCG	72°C
	MiSeq-Reverse 2	CTTCGGGTTCATGCCGTTATCCTC	
bcar1	MiSeq-Forward 1	ATGTGTTGGCAAAAGCCCTG	66°C
	MiSeq-Reverse 1	GCCAACGAGAATCTTCAGCC	

Table 2.3: Primers used for Deep Sequencing with MiSeq to detect TALEN and CRISPR mediated genome editing. Annealing temperatures shown were for PCR with Phusion® High-Fidelity DNA Polymerase

After sequencing the files were analysed using Geneious R9 (`www.geneious.com`, Kearse et al. (2012)) to determine the insertions or deletions (indels) that had occurred.

2.4.3 HRMA

High resolution melting analysis (HRMA) was used to determine TALEN or CRISPR mediated genome editing using DNA from single embryo extraction and the Precision Melt Supermix kit (Bio-Rad). Initially multiple primers were designed for the target region and tested on control, uninjected DNA to identify those that elicited a single peak melting profile. Those that functioned effectively are shown in Table 2.4. Once proven these were used on the injected embryos. The HRMA reaction was performed according to the manufacturers instructions below.

Per 10μl reaction:

5 μl	1x Precision Melt Supermix
1 μl	200 nM primer mix of forward and reverse primer
1 μl	extracted DNA
3 μl	Nuclease Free Water

PCR Cycling Conditions:

$$\begin{array}{ll} 95^{\circ}\text{C} & 2min \\ 95^{\circ}\text{C} & 10sec \\ 60^{\circ}\text{C} & 30sec \\ 72^{\circ}\text{C} & 30sec \end{array} \Big\} 35cycles$$

High Resolution Melting Analysis:

95°C	30sec
60°C	1min
65°C $\rightarrow$ 95°C	0.2°/10sec

The HRMA reactions were performed on the BioRad CFX96 Touch® machine and analysed using the Bio-Rad CFX Manager® software, unless otherwise stated. Melting curves of TALENs/CRISPRs injected samples were compared to uninjected controls.

Gene of Interest	HRMA Primer	Sequence ($5' \rightarrow 3'$)
bcar1	Forward 1	CCCTCTATTTTGAGTTACACTCTTC
	Reverse 1	GTTGGTTCGCTAACTGCTGTA
	Forward 2	AGTCTCCAGACGAGTTGTCC
	Reverse 2	TGCCAACGAGAATCTTCA
ptena-L	Forward 1	TTTAATAAGACGCAGCGCTAG
	Reverse 1	GCCCATGGCAATGATGTTAGG
	Forward 2	CACTATAGCTTTACTTGCTCTAGCC
	Reverse 2	TCAACCGGGACCTTACTTTCTGT
	Forward 3	CTTGCTCTAGCCAGTAGCATTGT
	Reverse 3	ATTTGAGTAATCAACCGGGACCT
ptena-R	Forward 1	AGAACCAGGGATAAAAAGGTACAAT
	Reverse 1	ATGGAAGTGCAATTGAGCTGTG
	Forward 2	GGTGTATGGTTGTGCTGATA
	Reverse 2	CATTAATGCAAAACGAGCTA
	Forward 3	GGGTGTGTTGCTTCACATGA
	Reverse 3	GATATCTTTGCCTATCGTCG
ptena	Forward 1	ATGAGAACCATGTGGCTGCC
	Reverse 1	GCGATGCAGCAGATAGGCAC
	Forward 2	GATGAGAACCATGTGGCTG
	Reverse 2	CGATGCAGCAGATAGGCACA

Table 2.4: Primers used for High Resolution Melt Analysis to detect TALEN and CRISPR mediated genome editing.

2.4.4 Poly Peak Parser

The online tool Poly Peak Parser (`http://yosttools.genetics.utah.edu/PolyPeakParser/`) developed by Hill et al. (2014) was used to determine indels within DNA sequences from the chromatogram data received from Sanger sequencing from PCR samples. The chromatogram is compared to a provided reference sequence, from which the alternate sequence, if present, can be deduced and indels can then be identified. In all cases the signal ratio cut off was 0.33.

2.5 Histopathology and Immunohistochemistry

2.5.1 Sample Preparation

Liver tissue was dissected from euthanised zebrafish and fixed in 10% formalin (Fischer Scientific, P/0840/53), before being dehydrated in graded ethanols, paraffin embedded and sagittal sectioned at 5 μm. Formalin-fixed, paraffin-embedded (FFPE) sections were then mounted onto Superfrost Plus® slides (Thermo Scientific).

2.5.2 Staining

For immunohistochemistry (IHC) the slides were de-waxed with xylene treatment followed by rehydration in graded ethanols of decreasing concentration. Antigen retrieval was performed through either 10 mg/ml Pronase enzymatic digestion for 15 minutes or through boiling in citrate buffer (2.94 g Trisodium citrate dehydrate, 5.4 ml 1M HCl in 1 L dH_2O) for 10 minutes. Sections were subsequently blocked in 3% hydrogen peroxide for 15 minutes, Avidin and Biotin (Vectastain) for 15 minutes and 10% serum matching the secondary antibody host species for at least an hour. Primary antibody incubation was for 8 hours in a humidified chamber at 4°C. Slides were incubated with secondary antibody for an hour and then incubated with Avidin-Biotin complex (ABC) solution (Vectastain) for 30 minutes. DAB (3,3'-Diaminobenzidine) solution (SIGMAFAST) was then applied until optimum levels of staining occurred. Haematoxylin (Sigma-Aldrich) was used as a counterstain and the slides were subsequently dehydrated and mounted onto glass coverslips, before being digitally imaged using a NanoZoomer 2.0-HT (Hamamatsu, UK). All primary antibodies used are listed within Table 2.5.

Immunohistochemistry (IHC) for validation of CS-OPT quantification after antibody optimisation and all Hematoxylin and Eosin (H&E) stains were performed by IQPath (In-

stitute of Neurology, UCL). Staining was performed using the Ventana Discovery XT instrument, using the Ventana DAB Map detection kit (760-124). Heat mediated epitope demasking was performed on the Ventana instruments, using a citrate based buffer (Ventana Ribo CC, 760-107). Anti-mCherry (Novus Biologicals, 1C51) primary antibody incubation was for 8 hours using a 1:100 dilution. Rabbit anti-Mouse (Dako E0354) secondary antibody incubation was for 32 minutes, using a 1:200 dilution. Slides were haematoxylin counterstained. Digital images of the stained sections were generated using a Leica SCN400F at x40 magnification.

2.6 Immunohistochemistry Quantification

Immunohistochemistry quantification was achieved through collaboration with Sebastian Brandner (Institute of Neurology, UCL). Analysis of the digital IHC images was performed at x20 magnification. Manually selected regions of interest (ROI) corresponding to segmented vasculature in the CS-OPT data were analysed using Definiens Developer XD v2.4.2 (Munich, Germany). Initial identification of the tissue, background and vessels within these ROI was performed by Dr. Matthew Ellis (Institute of Neurology, UCL) based on the level of blue and brown staining, calculated from the RGB image using the HSD model (van Der Laak et al., 2000). The combined level of brown and blue staining was used to identify the tissue and background; background $\leq 0.5 >$ Tissue (value range 0-3 a.u.). The threshold used to identify vessels (Th_V) was calculated using percentiles decreasing from 99 in increments of 1, searching for a change in value greater than 0.01au; a percentile of 99 describes the threshold that separates the lowest stained 99% of tissue from the highest 1%. A lower threshold (Th_L) was then calculated at Th_V-4. Following identification of all areas with brown staining greater than Th_V, any object with blue staining equal to or greater than the level of brown staining was removed. The remaining brown areas were then grown into surrounding pixels with brown staining greater than Th_L. Vessel lumen were then incorporated and vessel diameters calculated. Percent tumour vascularisation was based on the vessel stain plus lumen for the area of tissue plus enclosed background.

Primary Antibody	Host	Source	Secondary Antibody	Host	Source
vWF	Rabbit	Dako	Biotinylated anti- rabbit IgG	Goat	Dako
CD31	Rat	BD Biosciences	Biotinylated anti- rat IgG	Goat	Vector Labs
eNOS	Mouse	BD Biosciences	Biotinylated anti- mouse IgG	Goat	Dako
ERG	Rabbit	Abcam	Biotinylated anti- rabbit IgG	Goat	Dako
mCherry	Mouse	Novus Biologicals	Biotinylated anti- mouse IgG	Horse	Dako

Table 2.5: Details of Primary and Secondary Antibodies used for Immunohistochemistry staining

2.7 Widefield Microscopy

Zebrafish were deeply anaesthetised (Table 1.1) in system water containing 4.2% MS-222, unless otherwise stated, prior to imaging. Widefield imaging was performed on a OLYMPUS MVX10 fluorescent microscope using a OLYMPUS U-HGLGPS light source at 561 nm and 488 nm for mCherry and eGFP excitation, respectively. The exposure time for both mCherry and eGFP channels was 175 ms, with additional images with 25 ms or 10 ms for particularly intense eGFP signals. Images were captured on a OLYMPUS XM10 CCD camera and were 1376 x 1038 pixels, where each pixel was 20.48 μm^2.

For quantification of tumour progression the eGFP signal area was calculated using ImageJ (`http://imagej.nih.gov`). A threshold was applied to segment the eGFP tumour region and then the area could be extracted.

2.8 Optical Projection Tomography

2.8.1 Instrumentation

Instrumentation was performed by the Photonics Group at Imperial College London. The angularly multiplexed (Chen et al., 2013) two channel OPT instrument represented in Figure 2.2 was designed to accommodate juvenile and adult zebrafish up to 5 cm in length and 1 cm in diameter and provide a field of view of 33.8 x 28.5 mm. In each channel the optical imaging system provided a magnification of 0.49x with images acquired using sCMOS cameras (Zyla 5.5 sCMOS, Andor Technology Ltd) with an imaging sensor of 16.6 x 14.0 mm with 2560 x 2160 pixels of 6.5 μm. The effective numerical aperture (NA) of each imaging arm was adjusted using the adjustable iris in the back focal plane of the "objective" lenses L1 to provide a depth of field of 2.5 mm with a diffraction limited point spread function of 18-22 μm depending on the wavelength. This is close to the Nyquist limit of 26 μm determined by the system magnification and the pixel size of the camera. One imaging arm was focused to 1.25 mm and the other to 3.75 mm from the axis of rotation. These imaging arms were optimised using WinLens (www.winlens.de) for minimum aberrations and field curvature across the field of view.

For imaging zebrafish larvae a single armed system was used comprising of a 200 mm focal length tube lens (ITL200, Thorlabs Inc), a sCMOS camera and a Nikon objective (N4X-PF) providing a magnification of 4x, Figure 2.3. The NA of the system was 0.04

and the depth of field was 0.6 mm.

2.8.2 Acquisition

For imaging, fish were deeply anaesthetised (Table 1.1) in system water containing 4.2% MS-222, unless otherwise stated, and transferred into a clear FEP tube with a refractive index of 1.3 (EW-06406-12, Cole Parmer Instrument Co Ltd) with care taken to minimise any bubbles within the tube. For juvenile and adult zebrafish the FEP tubing was 9.5 mm internal diameter (11 mm outside diameter) and for larvae (< 30 dpf) it was 794 μm internal diameter (1.58 mm outside diameter). These tubes were then sealed with a plug and mounted under a rotation stepper motor (T-NM17A200, Zaber Technologies Inc.) set to run using a sufficiently low level of acceleration to prevent 'slipping' of the fish within the tube. Typically, the acceleration used was 10 microsteps/s^2 for a motor with 12800 microsteps/revolution (T-NM17A200), corresponding to an angular acceleration of 1.6 deg/s^2. The tube was suspended in a custom-built imaging chamber of octagonal cross-section filled with water to provide index matching of the tube and with glass windows normal to the imaging and excitation axes. This chamber allowed for the sample to be illuminated from multiple directions simultaneously in order to improve uniformity of fluorescence excitation. Samples were illuminated at 561 nm for mCherry excitation and 488 nm for eGFP excitation.

Because adult zebrafish typically present an aspect ratio > 4:1 (i.e. > 4 cm length and 1 cm diameter), it is possible to more efficiently utilise this excitation light by dividing it into three sub-beams with similar aspect ratio to the fish. The OPT image projection data was acquired by the two sCMOS cameras running in parallel interfaced with separate computers and the acquisition process was controlled by custom software written in LabVIEW (National Instruments) by Dr. Sunil Kumar (Imperial College London) such that one computer was slaved to the other, which also controlled the rotation stage motor, and the projection images were acquired synchronously.

2.8.3 Data Management

Following the data acquisition, each series of angular projections was manipulated computationally to ensure that the rotation axis was centred in the adjusted dataset and the two multiplexed camera datasets were then co-registered using a calibration process incorporating magnification, translation and rotation with rigid body transforms. The co-registered angular projections were then saved as OME-TIFF files on an OMERO (Allan

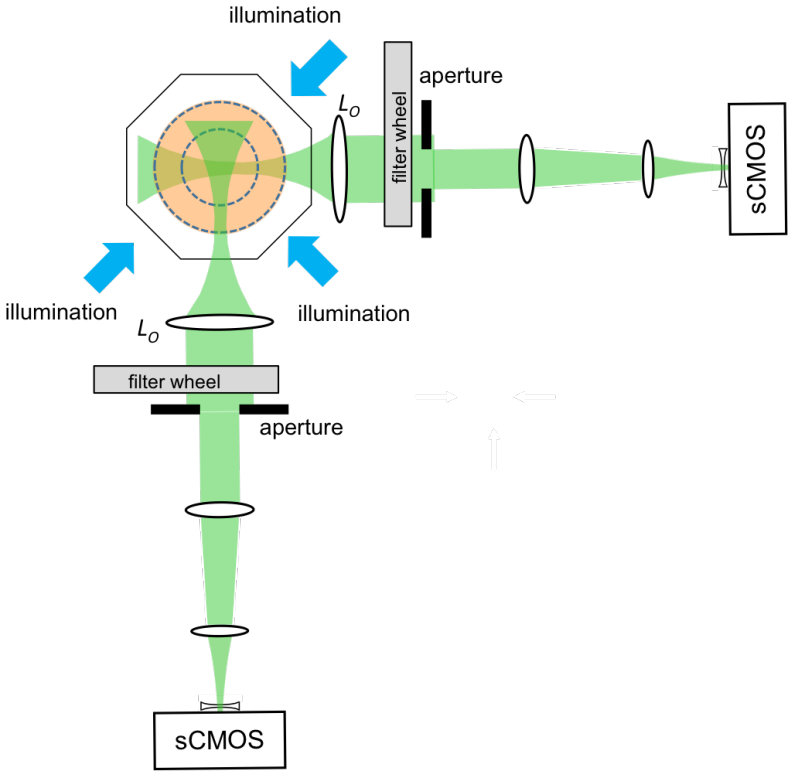

Figure 2.2: Schematic of dual projection channel multispectral OPT system used for imaging juvenile and adult zebrafish.

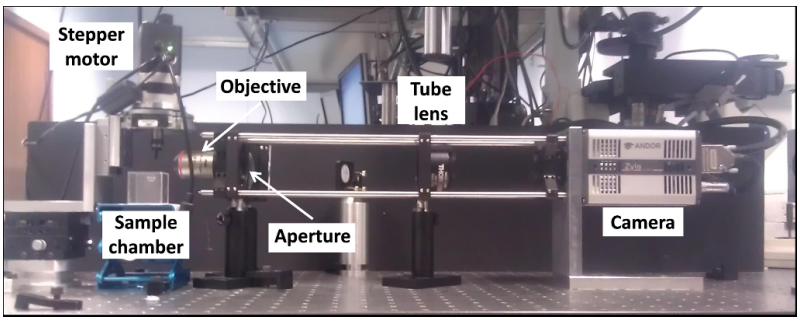

Figure 2.3: Schematic of the OPT system for imaging zebrafish larvae, mounted in a horizontal manner using a single sCMOS camera. Figure taken from Correia et al. (2015).

et al., 2012) server to enable sharing of these large datasets with remote access across the internet. This angular projection dataset requires much less storage capacity than the 3-D reconstructed image stacks. The projection data can subsequently be downloaded and the 3-D image stacks reconstructed on demand. Figure A.1 presents an overview of the data workflow.

2.8.4 Reconstruction

2.8.4.1 Filtered Back Projection

OPT datasets comprising co-registered sets of angular projections from each sCMOS camera saved as OME-TIFF files could be directly reconstructed using Filtered Back Projection (FBP) via a MATLAB (The MathWorks Inc) programme written in-house using the standard iradon library function, Equation 1.1. The iradon function was performed using the Hann filter (ramp filter multiplied over the Hann window). FBP reconstruction ideally requires several 100 angular projections to reconstruct 3-D images without loss of information using the imaging system reported here. When implemented on a personal computer with a graphics processing unit (NVIDIA Tesla K40 GPU), this typically takes a few minutes for a data set with 200 projections that reconstructs to a z-stack of 2000 image planes.

2.8.4.2 Compressive Sensing

For compressive sensing (CS) reconstruction an adapted version of the TwIST algorithm by Bioucas-Dias and Figueiredo (2007) is used, which is available as a MATLAB code from `http://www.lx.it.pt/~bioucas/TwIST/TwIST.htm`. All parameters we defaulted as in Bioucas-Dias and Figueiredo (2007), unless otherwise mentioned or optimised.

2.8.4.3 Similarity Measures

Structural similarity index measure (SSIM) is used to determine the correlation between two images, g and h, rather than traditional methods like mean squared error (MSE) where the result isn't seen to concur with the visual quality of the perceived image. SSIM compares the luminance, contrast and structure of two images, through the equation;

$$SSIM(g,h) = \frac{(2\mu_g\mu_h + c_1)(2\sigma_{gh} + c_2)}{(\mu_g^2 + \mu_h^2 + c_1)(\sigma_g^2 + \sigma_h^2 + c_2)} \tag{2.1}$$

where $\mu_g, \mu_h, \sigma_g, \sigma_h$ and σ_{gh} are the means, standard deviations and covariances for the images and c_1 and c_2 are regularisation constants. There is a built-in Matlab function, ssim, that calculates this using default values for regularisation constants, based upon the work in Wang et al. (2004). It provides an output value between -1 and 1, where 1 represents identical images. The images were converted and scaled to 8-bit grayscale with a dynamic range of 0-255, for optimal performance with this measure.

2.8.5 Segmentation

A percentile threshold based upon the cumulative frequency graph was applied to both tumour and vasculature reconstructions. A median filter was applied over a neighborhood of 5 pixels to the vasculature, before using a multiscale Hessian-based method in MATLAB for vessel enhancement (Frangi et al., 2006; Correia et al., 2015). This determines the "vesselness", i.e. the likelihood of each voxel belonging to a vessel, by analysing local image structure through a Hessian matrix (H), a square matrix of second order partial derivatives for a given voxel (I):

$$H(I) = \begin{vmatrix} \frac{d^2I}{dx^2} & \frac{d^2I}{dxdy} & \frac{d^2I}{dxdz} \\ \frac{d^2I}{dydx} & \frac{d^2I}{dy^2} & \frac{d^2I}{dydz} \\ \frac{d^2I}{dzdx} & \frac{d^2I}{dzdy} & \frac{d^2I}{dz^2} \end{vmatrix}.$$

Subsequently, the "vesselness" (likelihood of belonging to a vessel) can be resolved through calculating the Hessian eigenvalues (λ), which represent intensity variations for particular directions (eigenvectors). The three eigenvalues are ordered by magnitude, therefore $|\lambda_1| \leq |\lambda_2| \leq |\lambda_3|$. If the voxel has one eigenvalue of approximately 0 and the other two similarly large and negative it is likely a vessel. This is as it is presumed there will be little or no intensity change along the direction of the vessel but will be in the other directions, whilst incorporating prior knowledge that vessels are bright structures on a dark background.

The assessment of these eigenvalues is based upon a series of probabilities. Firstly, the following two ratios:

$$R_A = \frac{|\lambda_2|}{|\lambda_3|} \qquad R_B = \frac{|\lambda_1|}{\sqrt{|\lambda_2\lambda_3|}}, \tag{2.2}$$

that determine the relative relationships between each eigenvalue. If the voxel belongs to a vessel you would expect a value close to 1 for R_A and a low value for R_B. Furthermore,

background noise can be eliminated through the expression:

$$S = \sqrt{\sum_{j \leq D} \lambda_j^2}, \tag{2.3}$$

as low values would indicate no secondary structure, where D is the image dimension. These are all applied within the following expression to determine the likeliness that the voxel analysed belongs to a vessel:

$$V(s) = \begin{cases} 0, & \text{if } \lambda_2 > 0 \text{ or } \lambda_3 > 0 \\ (1 - exp(\frac{-R_A^2}{2\alpha^2}))exp(\frac{-R_B^2}{2\beta^2})(1 - exp(\frac{-S^2}{2c^2})), & \end{cases} \tag{2.4}$$

where α, β and c are chosen to determine the contribution of each element and were used as previously described in Correia et al. (2015). Importantly, the vesselness is observed over a range of scales, $V(s)$, to identify different sized vessels. This range is determined based upon the variation of expected vessel diameters and implemented in calculating the Hessian matrix. In line with Correia et al. (2015) a scale of 5 was used.

2.8.6 Skeletonisation

Following Hessian- based analysis the vasculature was subjected to a threshold before being imported into the Amira (FEI) software package. In Amira a 3-D median filter with a neighbourhood of 6 was used before applying the auto-skeleton tool with no threshold, 10 iterations and "smooth" and "attach to data" coefficients of 0.5 and 0.25, respectively.

2.8.7 Quantification and Visualisation

The tumour volume was quantified through extracting the number of non-zero voxels in the image within MATLAB. For the vasculature vessel length, volume, diameter and branching were analysed for the tumour region from the resultant skeleton within Amira. Vessels with diameter smaller than 26 μm were excluded from the analysis. For visualisation the final CS-OPT images are presented with the skeletonised and dilated vasculature to present a binary image with appropriate vessel diameters.

2.9 Statistical Analysis

Statistical analysis of data was performed using InStat (GraphPad) and a 95% significance level was used for all tests. The Kolmogorov and Smirnov test was used to test for Gaus-

sian distributions within the sample datasets and the Bartlett test was used to confirm that the datasets for comparison had equal standard deviations (SDs).

For comparing datasets proven to have a Gaussian distribution and equal SDs one-way ANOVA followed by the Student Newman Keuls test was used. If datasets for comparison were proven to differ from a Gaussian distribution or have significantly different SDs then the non-parametric ANOVA Kruskal-Wallis test was applied, followed by the Dunn's multiple comparison test.

When analysing rates of change linear regression analysis can be performed through Prism (GraphPad) if the linear function suitably fits the data, which is when $r^2 > 0.95$. The slopes of each fitted linear regression line are then compared through a two tail unpaired t test, where $P<0.05$ was considered significantly different.

CHAPTER 3

Reducing OPT Acquisition Time

3.1 Introduction

As described in Section 1.4.3, optical projection tomography (OPT) is a 3-D fluorescence microscopy technique that can provide whole-body mesoscopic imaging of live, transparent organisms such as zebrafish embryos (McGinty et al., 2011; Andrews et al., 2016). When researching biological processes and pathologies such as cancer progression and tumour angiogenesis the use of embryos has considerable limitations. This is due to their immature body systems, including the vasculature and immune system. Adult zebrafish are usually pigmented, however the mutant zebrafish described in Section 1.3.1 are non-pigmented throughout their lifespan and are sufficiently transparent to permit optical readouts (White et al., 2008; Heilmann et al., 2015). Therefore OPT has the potential to globally image live, adult zebrafish.

It is important for live, *in vivo* imaging that the acquisition period is minimal. The acquisition period required to obtain a sufficient number of projections for FBP reconstruction of both the tumour and vasculature channels would be greater than 15 minutes. During image acquisition the organisms require anaesthesia to prevent movement and stress. However, prolonged periods of anaesthesia cause respiratory and cardiac failure, as well as increased mortality rates (Sun et al., 2009; Matthews and Varga, 2012). Furthermore, shorter acquisition periods would result in lower light doses, subsequently reducing phototoxicity and the chance of fluorescent protein photobleaching. Reducing the number of projections during imaging would reduce the acquisition period, however the image quality would be degraded when reconstructing using the conventional filtered back projection (FBP) algorithm (as described in Section 1.5.1).

It has been shown in Correia et al. (2015) that incorporating compressive sensing (CS) iterative algorithms (as described in Section 1.5.2) can reconstruct 3-dimensional (3-D) images of zebrafish embryos with fewer angular projections, whilst retaining the image quality for quantitative analysis. The CS algorithm two-step iterative shrinkage/thresholding (TwIST) was used, which had been shown to efficiently converge to

minimise an objective function in the form of that in Equation 1.3 (Bioucas-Dias and Figueiredo, 2007). This approach can be used with various denoising problems and has been shown to work competently with total variation (TV) regularisation (Bioucas-Dias and Figueiredo, 2007). Using TwIST and TV regularisation as few as 50 projections could be used for image reconstruction opposed to the densely sampled dataset required for conventional FBP (Correia et al., 2015). Therefore the acquisition time for embryo imaging would be significantly reduced.

For these reasons I wanted to incorporate CS iterative algorithms into OPT reconstruction of adult zebrafish with inducible eGFP-tagged liver tumours and mCherry labelled vasculature. This would enable minimisation of the acquisition period whilst maintaining the image quality. Consequently readouts of tumour progression and angiogenesis could be achieved from live adult zebrafish.

3.2 Experimental Summary

To investigate whether CS reconstruction using the TwIST algorithm could be incorporated an adult (81 dpf) TraNac *Tg(KDR:mCherry:Fabp10-rtTA:TRE-eGFPKRAS^{V12})* zebrafish, as described in Section 1.3.2.2, was induced with 10 mg/L of doxycycline for 3 weeks. I performed OPT imaging of the zebrafish with Dr. Sunil Kumar (Photonics Group, Imperial College London), where 512 angular projections were acquired. I then reconstructed the oversampled 512 projection dataset with FBP to provide a "ground truth" reference image, as described in Section 2.8.4.1. This dataset was also undersampled to produce datasets of 160, 120, 80, 70, 64, 50, 40, 30 and 20 evenly spaced projections, for which CS reconstruction was applied and investigated through the TwIST algorithm, described in Section 2.8.4.2. Following CS reconstruction I segmented both tumour and vasculature images as described within Section 2.8.5 and I skeletonised the vasculature as described in 2.8.6. The similarity between reconstructions and the reference images was quantified using the structural similarity index measure (SSIM), Section 2.8.4.3.

3.3 Results

3.3.1 Algorithm parameters

Within the CS TwIST algorithm there are two key parameters that require optimisation. These are the number of TV minimisation iterations (TV_{it}), to minimise Equation 1.4, and the regularisation parameter, which controls the level of TV regularisation within the main algorithm (τ in Equation 1.3). It is important to determine the optimal parameters that will result in a high quality reconstruction, which preserves detail and minimises the loss of information, within a reasonable amount of time.

Previously 64 projections were sufficient for 3-D CS reconstruction of an OPT imaged TraNac *Tg(KDR:mCherry)* zebrafish embryo, producing high vascular detail for quantitative analysis (Correia et al., 2015). Therefore, the undersampled 64 projection dataset of the adult zebrafish was used to optimise TV_{it} and τ. As the image would only improve with the number of TV_{it} the highest value used in Correia et al. (2015), 40, was firstly used to optimise τ through assessing the SSIM value when compared to the 512 FBP reference image. Once the value for τ had been established optimisation of TV_{it} was performed to determine the lowest number of iterations required without introducing noise.

Cross-sectional $x-z$ reconstructions of the vasculature channel can be seen in Figure 3.1. The FBP reconstructions for the reference 512 projection dataset and the undersampled 64 projection dataset are shown within Figure 3.1a, where the white arrowheads highlight the level of noise that results when the sample rate of projections is lower than the Nyquist limit. Within the 512 FBP reference image key vascular detail to be retained during CS reconstruction can be observed, including the lateral cutaneous vessel (LCV) and unidentified vessels (UI). Figure 3.1b shows the same cross-sectional reconstruction with 64 projections using CS reconstruction with varying values of τ, when TV_{it} set to 40. As expected, increasing the value of τ caused an increased smoothing through denoising. The level of smoothing required would remove noise but retain important vasculature detail evident in the reference image. When using τ of 0.001 streak artefacts are present within the reconstruction, which are absent at higher tested values. Values of $\tau \geq 0.008$ show a loss of contrast within the zebrafish cross-section and a loss in key vasculature detail. This is reflected within the SSIM values, shown in the top right hand corners within Figure 3.1b, where individual reconstructions are compared to the 512 FBP reference image. The SSIM value is largest when $\tau = 0.004$ with a

value of 0.9594. Therefore $\tau = 0.004$ was considered optimal and was used to determine the lowest value of TV_{it}, Figure 3.1c. All reconstructions resulted in high SSIM values greater than 0.95, where only small increases occurred with higher values of TV_{it}. No discernible differences were seen between reconstructions using $TV_{it} \geq 10$ and above, however reconstructing with the lower value of $TV_{it} = 5$ noise and streak artefacts were introduced, as indicated by the white arrows in Figure 3.1c. Therefore, the optimal values for vasculature reconstruction were $\tau = 0.004$ and $TV_{it} = 10$, where reconstruction took 754 ms for this cross-section.

Optimisation was performed on the tumour channel reconstructions using the same tested values for τ and TV_{it}, Figure 3.2. Once again Figure 3.2a shows the FBP reconstructions for the reference 512 projection dataset and the noisy undersampled 64 projection dataset. The 512 FBP image shows the known lobed structure of the liver, where the right lobe (RL), central lobe (CL) and left lobe (LL) are annotated. However, some scatter artefacts are also seen despite utilising the oversampled dataset (white arrowhead). Figure 3.2b shows reconstructions with various τ when TV_{it} was set to 40. A value of τ =0.015 was considered optimal due to having the highest SSIM value. Once again this reflected the images as τ =0.004 had a reduced background compared to τ =0.008 and maintained detail lost in τ =0.02. When reconstructing with τ set to 0.015 a value of 25 for TV_{it} was optimal, as the streaks were reduced and further iterations did not introduce discernible differences or significantly increase the SSIM value, Figure 3.2c. Reconstructions of this tumour cross-section with the optimised parameters took 942 ms.

The reconstructions completed in Figures 3.1 and 3.2 had the maximum number of TwIST iterations (MaxiterA) within the main algorithm set to a value of 10. This was to ensure the reconstructions were not too time consuming. To confirm that 10 iterations were an adequate number to allow convergence the same vasculature and tumour cross-sections were reconstructed using the default value of MaxiterA = 1000 for comparison. In both cases there were no differences between the two images, Figure A.2. Therefore we can accept that a value of 10 for MaxiterA is adequate to enable convergence of both the vasculature and tumour channels when using the optimised τ and TV_{it} values.

3.3.2 Analysing the number of projections

Once the algorithm parameters were optimised CS reconstruction using TwIST could be applied to the evenly spaced undersampled datasets consisting of 120, 80, 70, 64, 50, 40,

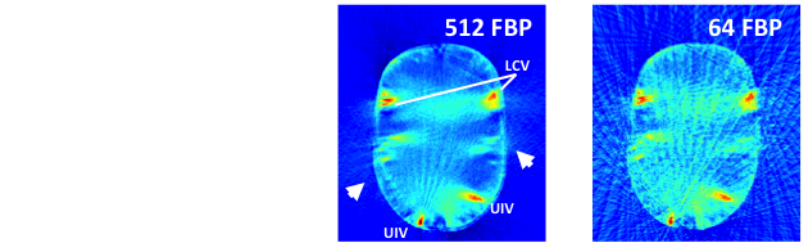

(a)

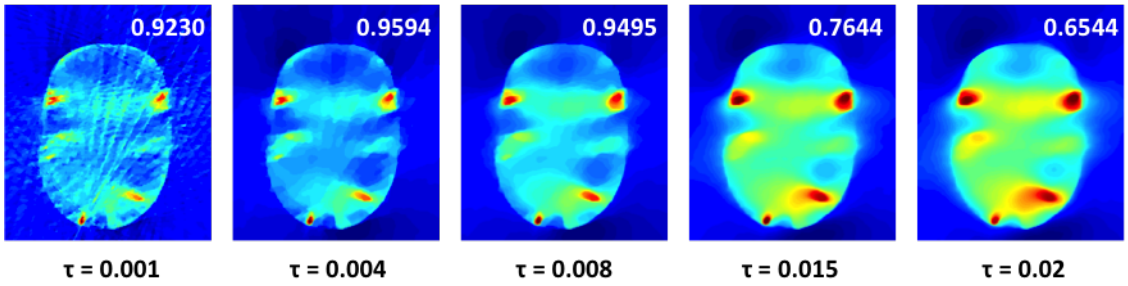

(b)

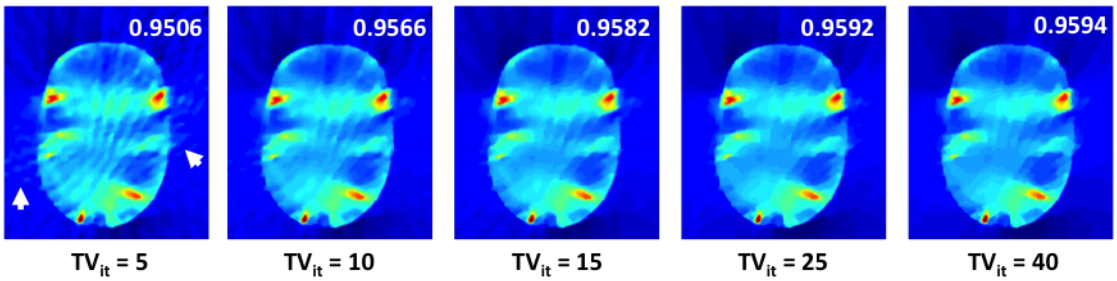

(c)

Figure 3.1: Optimising the TwIST parameters τ and TV$_{it}$ for the vasculature channel (561nm) using cross-sectional reconstructions of an adult TraNac *Tg (KDR:mCherry:Fabp10-rtTA:TRE-eGFPKRAS^{V12})* zebrafish. Images are represented as heat maps, where red indicates high fluorescence intensity and blue low. (a) shows the FBP reconstructions with the over sampled 512 projections, acting as a reference image, and the under sampled 64 projections (as indicated in the top right hand corner of the images). Key vascular features have been annotated including the lateral cutaneous vessels (LCV) and unidentified vessels (UI). (b) shows optimisation of τ when the value of TV$_{it}$ is set to the high value of 40 and (c) shows optimisation of TV$_{it}$ with the optimised value of τ = 0.004, when reconstructing the undersampled 64 projections using the TwIST algorithm. SSIM values of the images compared to the reference 512 FBP image are shown in the top right hand corner in (b) and (c). Arrows indicate scatter artefacts. Scale bar 1 mm.

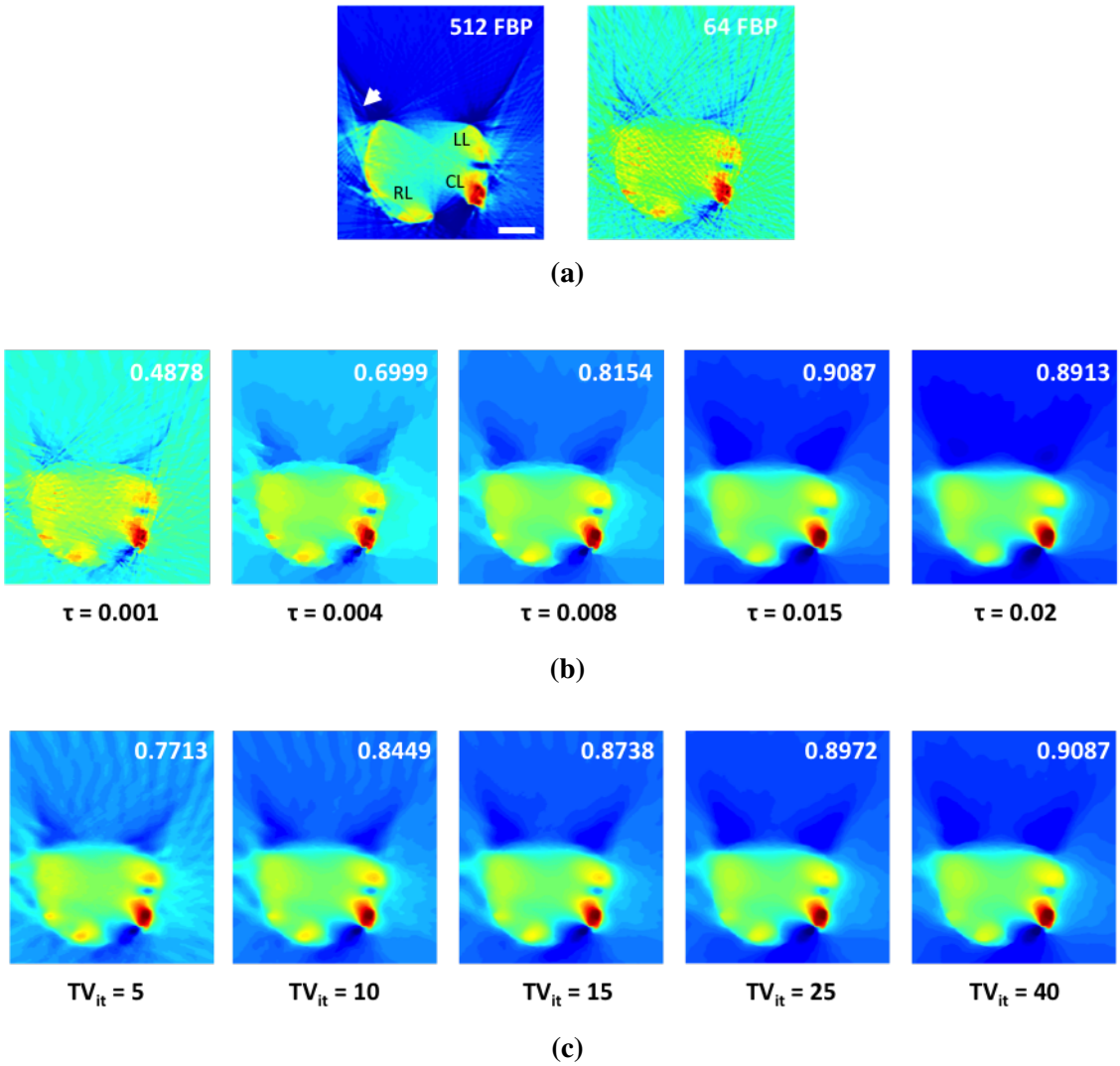

Figure 3.2: Optimising the TwIST parameters τ and TV$_{it}$ for the tumour channel (488nm) using cross-sectional reconstructions of an adult TraNac *Tg (KDR:mCherry:Fabp10-rtTA:TRE- eGFPKRAS^{V12})* zebrafish. Images are represented as heat maps, where red indicates high fluorescence intensity and blue low. (a) shows the FBP reconstructions with the over sampled 512 projections, acting as a reference image, and the under sampled 64 projections (as indicated in the top right hand corner of the images). The lobed structure of the zebrafish liver can be seen, where the right lobe (RL), central lobe (CL) and left lobe (LL) have been annotated. (b) shows optimisation of τ when the value of TV$_{it}$ is set to the high value of 40 and (c) shows optimisation of TV$_{it}$ with the optimised value of τ = 0.015, when reconstructing the undersampled 64 projections using the TwIST algorithm. SSIM values of the images compared to the reference 512 FBP image are shown in the top right hand corner in (b) and (c). Arrows indicate scatter artefacts. Scale bar 1 mm.

30 and 20 projections. Therefore, the trade-off between the reconstructed image quality and number of angular projections acquired could be investigated in order to reduce the acquisition time of OPT.

Initially the same 2-dimensional cross-sections for the vasculature and tumour channels as previously used for parameter optimisation were analysed and compared to the corresponding 512 FBP reference reconstructions. As expected it was clear that the fewer projections used the greater the streaking artefacts and the CS reconstructions with the greatest number of projections were the most similar to the reference images, Figure 3.3. Discernible differences were seen with 30 projections or fewer for the vasculature images and with 20 projections for the tumour images, where blocky effects were strongly depicted. Although streak artefacts and noise were seen within the other reconstructions with various projection numbers it was unclear as to whether these could influence the final processed images and subsequent conclusions. Therefore it was important to quantify this in the context of a processed 3-D reconstruction of the tumour burdened zebrafish to determine the level of undersampling achievable for our purposes.

The 3-D CS reconstructions of the undersampled datasets were segmented and the tumour regions were analysed. The quantification SSIM was used to determine the fidelity of the reconstructions to the full 512 projection FBP reconstruction reference image. The relationship between the SSIM and the number of projections differed slightly between the tumour and the vasculature channels, Figure 3.4. The SSIM for the tumour channel was consistently higher, which was to be expected considering the detail was less intricate. It is also a simple, smooth relationship where the SSIM always increased with projection number. This was unlike the vasculature where particular reconstructions had slightly greater similarity to the reference image than those reconstructed with a greater projection number. For example, 70 projections yielded a greater SSIM of 0.8599 than 80 projections with 0.8562. It is possible this was a result of selecting evenly spaced projections when undersampling, where different projections were incorporated in the different undersampled reconstructions. Particular projection angles could have captured greater vascular detail than others to produce this effect, which wouldn't be seen within the tumour channel due to being a more consistent, larger entity.

The SSIM as a function of projection number did not plateau to unity, Figure 3.4. This is a result of both artefacts being present within the reference images and denoising loosing the finer image details. Both reference cross-sectional images within Figure

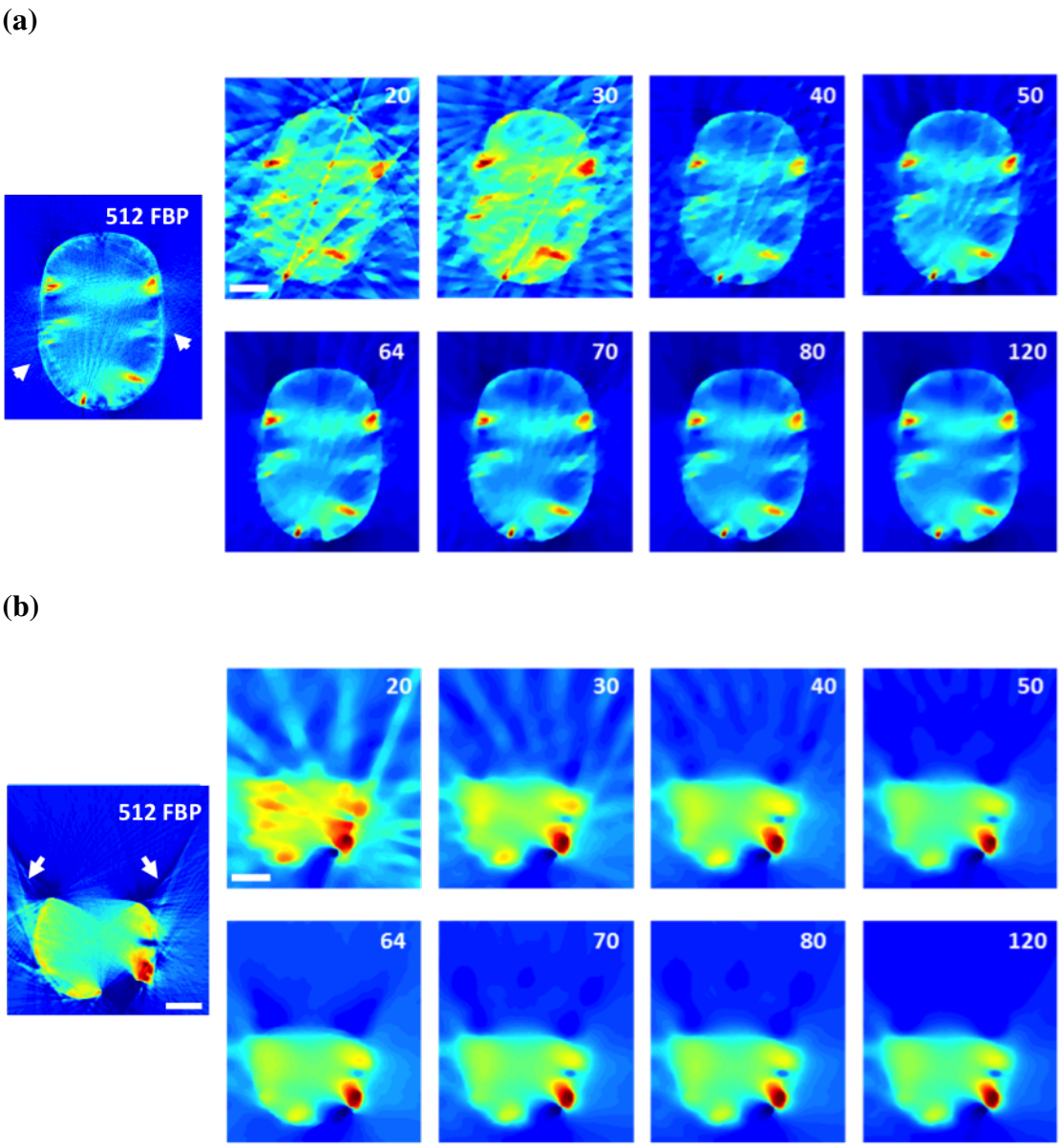

Figure 3.3: Cross-sectional reconstructions of an adult TraNac *Tg (KDR:mCherry:Fabp10-rtTA:TRE- eGFPKRAS^{V12})* using FBP for 512 projections (512 FBP) as a reference image or the TwIST algorithm with a different number of angular projections (as indicated in the top right hand corner) for (a) the vasculature channel and (b) the tumour channel. Images are represented as heat maps. Arrowheads indicate scatter artefacts. Scale bar 1 mm.

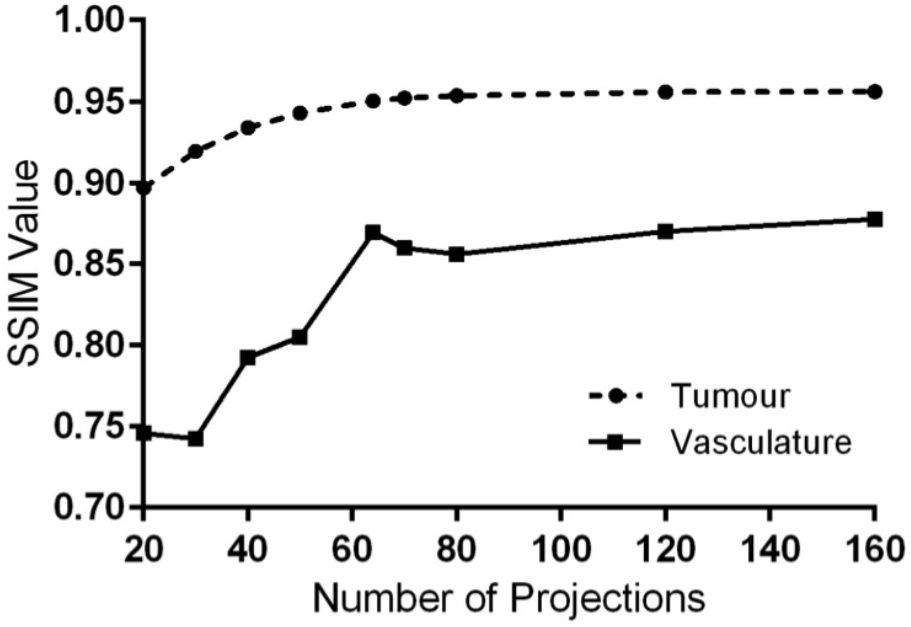

Figure 3.4: Quantitative analysis of fidelity for TwIST reconstructed images from undersampled datasets to the reference 512 FBP image. The SSIM is used as a function of the number of angular projections for tumour and vasculature channels.

3.3 have artefacts, as indicated by the white arrowheads. As a consequence of CS reconstruction the artefacts are removed during image denoising, therefore the images will never be identical. Denoising smooths the images in order to reduce the artefacts within the images, which results in finer details being lost that are unable to be recovered, independent of projection number. Due to the vasculature channel comprising of finer detail, compared to the tumour channel, this is more heavily affected, which is likely why the SSIM plateau occurs at a lower SSIM.

Despite the difference in SSIM values both channels plateaued at approximately 60 projections, Figure 3.4. This was seen to be in accordance to the cross-sectional reconstructions of Figure 3.3, where upon closer inspection the introduction of streak artefacts did progressively increase when fewer than 64 projections were used. For these reasons it was believed that reconstructing 64 projections with the TwIST algorithm would be the minimal number of projections sufficient to provide a true representation of the reference image. The tumour region reconstruction for the reference image and 64 projection CS reconstruction can be seen in Figure 3.5. The images are highly similar and have SSIM values of 0.8695 and 0.9503 for the vasculature and the tumour channels, respectively. Therefore it could be accepted that this level of undersampling is adequate

to provide a true representation of the tumour region.

To further highlight the capabilities of CS reconstruction recovering the loss of information when using only 64 projections, the fluorescence intensity images for the whole adult tumour burdened zebrafish were analysed, Figure 3.6. The reference FBP reconstruction with the full 512 projections is shown in Figure 3.6a. It is evident how this image is degraded when only 64 projections are used to reconstruct with FBP in Figure 3.6b. When utilising the TwIST algorithm in CS reconstruction for the same 64 projections the loss of information due to noise in the image was minimised, Figure 3.6c. Following reconstruction, the 3-D image stacks were segmented and skeletonised to produce binary images of the vasculature. Figure 3.6d shows the "vesselness" of this 3-D dataset visualised after the Hessian-based analysis and Figure 3.6e shows the "final" segmented image following skeletonisation and dilation of the vasculature. Rendered 3-D images of these corresponding figures are shown in Video 1. Therefore, acquiring as few as 64 projections using OPT was sufficient for whole organism imaging when using CS reconstruction, which would reduce the acquisition time to less than 3.5 minutes.

3.4 Discussion

It was important to reduce the acquisition time of OPT when performing live, *in vivo* imaging to reduce both the anaesthesia period and light dose experienced by adult zebrafish. This has been achieved through applying the CS algorithm TwIST, which was previously used to reconstruct a zebrafish embryo from undersampled datasets (Correia et al., 2015). As a result far fewer projections can be acquired and the undersampled dataset can be reconstructed to an adequate quality where there is a minimal loss of information.

In order to reconstruct using the TwIST algorithm optimisation of key parameters was required. Firstly the optimal level of denoising was determined to ensure artefacts were removed but detail was retained. This was achieved through optimising the regularisation parameter τ to be 0.004 and 0.015 for the vasculature and tumour reconstructions, respectively. It was beneficial to find the minimal number of TV minimisation iterations during denoising where no reduction in image quality was seen, as this is a computationally time intensive element. For the vasculature and tumour channels, respectively, I found 10 and 25 iterations sufficient taking 754 ms and 942 ms. Furthermore, 10 TwIST iterations were confirmed sufficient for algorithm convergence. OPT projections of adult

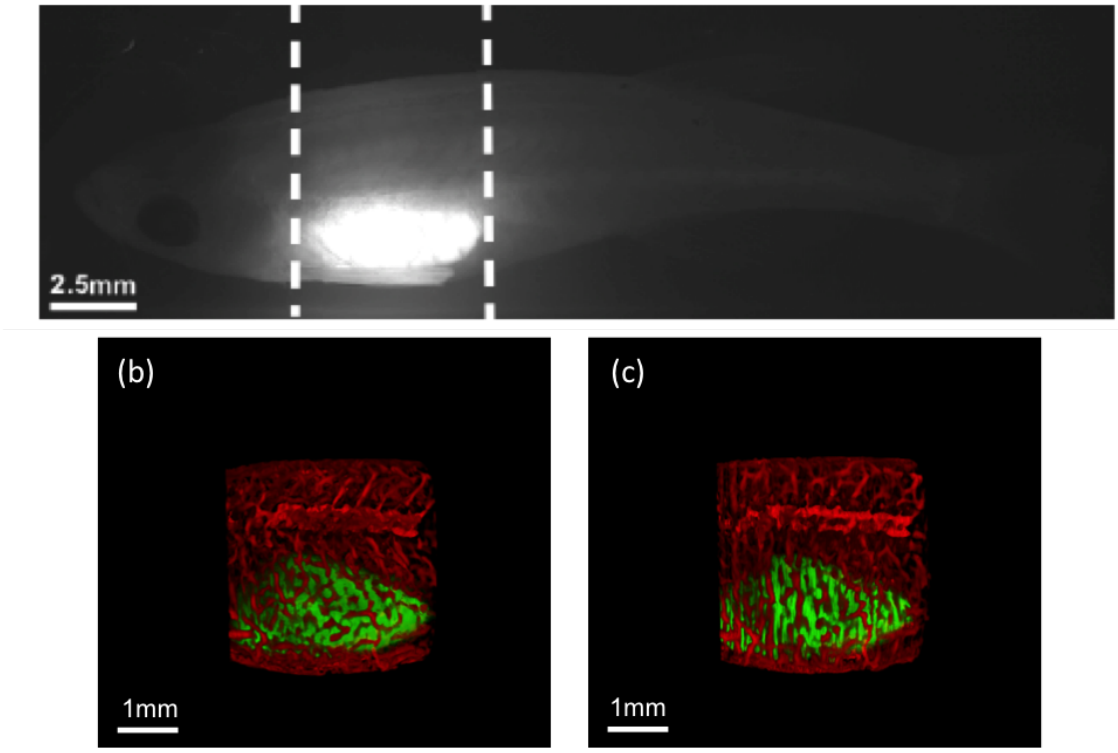

Figure 3.5: 3-D reconstructions of adult TraNac *Tg (KDR:mCherry:Fabp10-rtTA:TRE- eGFPKRAS^{V12})* zebrafish after tumour induction using FBP and CS. (a) An individual OPT projection fluorescence intensity image of the tumour excited at 488 nm. (b,c) Reconstructions of the tumour and vasculature (post segmentation) in the region indicated by dotted lines using (b) FBP with 512 Projections and (c) CS with 64 projections respectively.

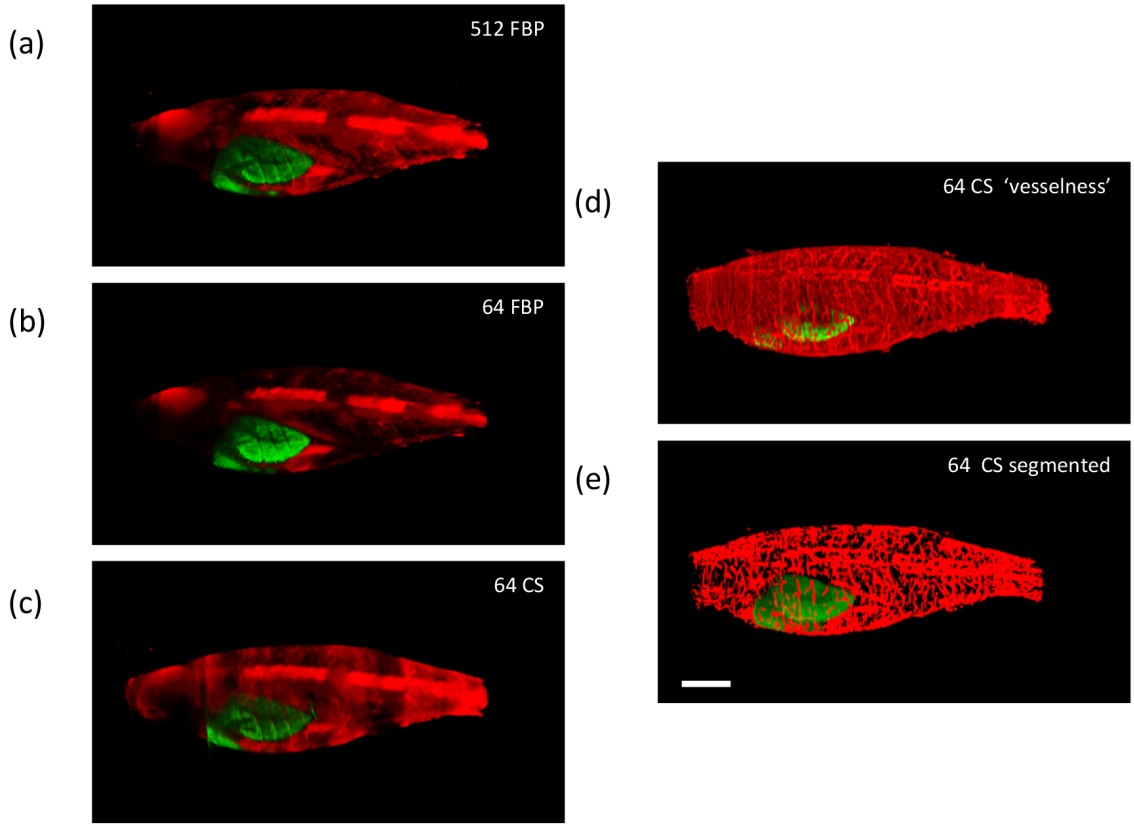

Figure 3.6: Reconstructed OPT images of adult TraNac *Tg (KDR:mCherry:Fabp10-rtTA:TRE- eGFPKRAS^{V12})* zebrafish expressing liver specific eGFP-labelled tumour and mCherry-labelled vasculature showing maximum intensity projections of eGFP (green) and mCherry (red) fluorescence. (a) and (b) show FBP reconstructed images computed with 512 and 64 projections respectively, (c) shows the corresponding image reconstructed from 64 projections using the CS-OPT approach, (d) shows the "vesselness" of the same reconstruction and (e) shows the "final" segmented image of the vasculature. Scale bar = 2.5 mm. See Video 1 for corresponding 3-D animations.

fish are approximately 2000 pixels along the y-axis. As a result TwIST reconstruction of the whole adult, tumour burdened zebrafish with these optimised parameters would be performed in under 30 mins per channel, which is an acceptable computational time.

Consequently, I analysed TwIST reconstruction with undersampled datasets to investigate image quality and number of angular projections through assessing both cross-sectional and 3-D reconstructions. The cross-sectional images highlighted the finer detail that would not be seen through 3-D reconstruction. It is clear that the fewer projections used to reconstruct the greater the block effects in the images. This is as TV regularisation tends to lead to blocky effects, known as the staircasing effect (Chan et al., 2005). The quantification SSIM was used to further determine where the undersampling limit lies through analysing the correlation between the undersampled and reference 3-D images. This measure accounts for luminance, contrast and structure of the image and results in a value that concurs with the visual quality of the perceived image, opposed to traditional measures such as mean squared error (MSE) (Wang et al., 2004). The SSIM and image quality both fall when using less than 60 projections, which is seen to a greater extent in the vasculature reconstructions. The sudden decline in SSIM value is likely due to a loss of the finer vasculature detail within the images, where it becomes more difficult to distinguish them from the residual noise once a certain level of undersampling is encountered. As a result denoising does not work efficiently at these levels with our chosen, optimised parameters. The decline does not occur as strongly within the tumour channel. The tumour fluorescence signal is a simple structure in comparison to the vasculature, consisting of a single solid element. Consequently, the tumour signals would be sparser than the vasculature within the compressible gradient domain used for denoising. As a result they would be less prone to image degradation with a greater degree of undersampling. For these reasons 64 projections were chosen for CS reconstruction using the TwIST algorithm with the chosen parameters. I proved this was sufficient for a true representation of the reference image through providing SSIM values greater than 0.85 in the tumour region for each channel and highlighted its capabilities for the entire fish. Therefore, the total number of angular projections required for compressive sensing optical projection tomography (CS-OPT) would be reduced 8-fold compared to the reference FBP image. Subsequently the imaging period would be reduced to less than 3.5 minutes and drastically improve zebrafish viability.

Reducing the acquisition time to such a degree provides the opportunity for further imaging avenues as well as improving zebrafish viability. For example, additional

fluorophores or Förster Resonance Energy Transfer (FRET) biosensors could be incorporated into the zebrafish tumour model and imaged using CS-OPT. FRET biosensors are devices that enable physiological interactions to be determined, indicating specific cellular physiology, through providing a readout based upon the proximity of two or more fluorophores (Clegg, 1995; Kiyokawa et al., 2006). FRET interactions can be measured through Fluorescence Lifetime Imaging Microscopy (FLIM), where the fluorescence lifetime of one of the fluorophores is measured to provide ratiometric, robust readouts. We have previously shown the ability to quantitatively image FRET biosensor activity within live zebrafish embryos using FLIM-OPT (McGinty et al., 2011; Andrews et al., 2016). It is possible that the additional time resulting from CS-OPT could enable FLIM imaging within the whole, live adult organism. However, greater image detail may be required to detect this.

The CS-OPT system is not limited to a minimal number of 64 projections and if required the number of projections could be further reduced. Greater regularisation and further optimisation of the parameters τ, TV_{it} and MaxiterA, could help maintain the desired image quality at the expense of reconstruction time. However, the image quality would be limited, due to missing information with a reduced projection number. It is also possible that different sets of projections could result in better reconstructions. This is a property that could explain the relationship between the number of angular projections and the SSIM value within the vasculature channel. Throughout the performed experiments the undersampled datasets consisted of evenly spaced projections throughout the entire 360° of the zebrafish. It is possible that particular projections could have captured greater vasculature detail. Therefore, it is plausible that the acquired projections could be chosen dependent upon the area of interest. For example, if tumour physiology alone was of interest it may be beneficial to have a greater proportion of the projections acquired at angles on the side of the zebrafish encompassing the tumour.

Decreasing acquisition time through utilising compressive sensing will always result in a loss of information that cannot be recovered. Therefore, other methods could be considered. Additional arms could be implemented within the OPT imaging instrumentation, which would enable multiple images to be captured simultaneously. However, this may be impractical due to spatial availability and would increase the cost of the system. Another option would be to increase in the imaging speed of the OPT system. During acquisition the imaging chamber containing the zebrafish is rotated to enable multiple images to be captured at different angles. The rotational speed of the chamber

could be increased, however the rotational pull would increase and this would result in the zebrafish moving within the imaging chamber during acquisition, subsequently introducing motion artefacts into the reconstructions. A possible option to overcome this would be to mount the zebrafish within the imaging tube and prevent any possible movement. Previous studies using OPT imaging have embedded samples within agarose to prevent this issue, however the samples were sacrificed prior to imaging (Sharpe et al., 2002; Sharpe, 2003; McGinty et al., 2011; Correia et al., 2015). To enable live adult zebrafish imaging this is not a feasible option, crucially as the gills are essential for oxygen uptake and ionoregulation and agarose would prevent these from functioning (Rombough, 2002). It is possible that, with substantial research to ensure health is not affected, one part of the zebrafish could be embedded within agarose to hold it in place, such as the tail fin. In practice mounting the fish prior to imaging and then removing the agarose afterwards are likely to be timely procedures and consequently the anaesthesia period required may be increased rather than reduced. A further possibility would be to adjust the water within the imaging capsule so that it is more viscous, therefore reducing the rotational pull. There are no known agents that can be used with live zebrafish and so if this were to be implemented it is once again critical that extensive research is performed to ensure the chemical agent used is not toxic and does not affect the imaging performance.

Using CS reconstruction for OPT imaging of an adult zebrafish is a novel application and zebrafish differ significantly between embryonic and adult lifeforms. One of the most crucial differences is the difference in their optical properties, where there is increased light scatter within the adult organism. This is a result of their internal pigmented organs, increased size and the remaining chromatophore development. Furthermore, the embryonic physiology is significantly different to the fully developed adult organism. The previous implementation of CS reconstruction of the zebrafish embryo in Correia et al. (2015) also used mCherry labelled vasculature. As shown within Figure 1.6 the vasculature is far more complex within the adult organism. With these significant physiological differences it was unknown as to whether undersampling would result in a too greater loss of information for recovery through CS reconstruction and if it did not to what extent it could be achieved.

Through optimisation of the parameters of the TwIST algorithm and the number of projections used for reconstruction I have shown that this CS-OPT approach using the TwIST algorithm is attractive for *in vivo* imaging. I have shown that 64 projections

of both vasculature and tumour fluorescence are sufficient when using CS-OPT. This reduction in the number of projections is 8-fold compared to our reference image and 5-fold compared to the previous 360 projections used in McGinty et al. (2008, 2011). Consequently, the acquisition time is reduced to less than 3.5 minutes and the zebrafish receive lower light doses and are anaesthetised for reduced periods of time. This increases their viability and reduces their chances of respiratory and cardiac failure (Sun et al., 2009; Matthews and Varga, 2012). Therefore, CS-OPT can enable the use of longitudinal studies of tumour progression and angiogenesis within adult organisms with improved accuracy through live, whole organism, 3-D imaging.

CHAPTER 4

Quantitative Analysis of Tumorigenesis and Angiogenesis using CS-OPT

4.1 Introduction

Deregulation of angiogenesis results in many pathologies, particularly cancer where it is crucial for tumour progression and provides a possible route for metastasis. Therefore, this is a potential therapeutic target and understanding the underlying physiology and mechanisms *in vivo* is of interest.

The developed compressive sensing optical projection tomography (CS-OPT) platform described in Chapter 3 is capable of globally imaging fluorescent reporters of vascularisation and tumour growth in live adult zebrafish. It has the potential for longitudinal applications to study physiological and pathophysiological events. When studying tumorigenesis and angiogenesis it is desirable to achieve quantitative readouts as well as qualitative 3-dimensional (3-D) images. Quantifications enable accurate analysis and statistical testing to understand relationships and confirm hypotheses. This is crucial when determining drug efficacy and for performing mechanistical studies on gene function.

The tumour angiogenesis zebrafish model TraNac *Tg (KDR:mCherry:Fabp10-rtTA:TREeGFPKRAS^{V12})*, described in Section 1.3.2.2, has an inducible, eGFP tagged liver tumour and a mCherry labelled vasculature. Consequently this model zebrafish provides fluorescent readouts of both tumour progression and regression, with the corresponding vasculature changes. Therefore, using the novel CS-OPT platform in combination with this model could enable 3-D quantifications of tumour progression and angiogenesis within a whole, adult organism.

During tumour growth and progression angiogenesis is stimulated through both hypoxic and non-hypoxic mechanisms, as described in Section 1.2.2. Additional modes of angiogenesis are used within the context of cancer and the resulting tumour vasculature

differs from physiological vessels, as mentioned in Section 1.2.3. Quantitative measures of angiogenesis previously used within other angiogenic assays (Section 1.1.4) such as vessel number, branching, length, diameter and density could be analysed from CS-OPT images.

It is important to determine that the extracted CS-OPT quantifications are accurate for future studies and they truly represent the biological processes occurring *in vivo* within the model zebrafish. Using histopathology the inducible liver specific eGFPKRAS^{V12} driven tumour model has previously been shown to produce liver hyperplasia that progresses to hepatocellular carcinoma (HCC) with inducer treatment and tumour shrinkage upon inducer withdrawal (Nguyen et al., 2012). Therefore, histopathological analysis can be performed to confirm tumour growth and progression. However, in order to validate the extracted angiogenic measures a well established technique is required for comparison, such as immunohistochemistry (IHC). From corresponding 2-dimensional (2-D) sections IHC can be used to specifically stain for the tumour vasculature. Comparing the two analyses will provide validation.

Within this Chapter I analyse the overall performance of the CS-OPT system with regards to image quality and the zebrafish model organism. I have extracted quantifications that can be used for measuring tumour progression and vascularisation, which I have also confirmed and validated using histopathology and IHC. Therefore, I demonstrate that the CS-OPT platform would be suitable for both mechanistic and drug development studies.

4.2 Experimental Summary

I performed all CS-OPT imaging with Dr. Paul Frankel and Dr. Sunil Kumar (Photonics Group, Imperial College London). Acquired images were then reconstructed using the TwIST algorithm, segmented, skeletonised and analysed by myself. For methods details see Section 2.8.

In initial preliminary studies 8 adult (122 days post fertilisation (dpf)) TraNac *Tg (KDR:mCherry:Fabp10-rtTA:TREeGFPKRAS^{V12})* zebrafish (Section 1.3.2.2) were treated for 1 week with 10 mg/L of doxycycline. These were then imaged using CS-OPT to determine the performance of the platform. 5 female and 3 male zebrafish were used.

Once the requirements for optimal CS-OPT imaging of adult tumour burdened zebrafish were determined from the preliminary study an *in vivo* cross-sectional study of tumour and vasculature development was performed. Adult (145 dpf) TraNac *Tg (KDR:mCherry:Fabp10-rtTA:TREeGFPKRAS^{V12})* zebrafish were housed within fish water comprising of 68 mg/L of Tropic Marin® Sea Salts dissolved in deionised water with the addition of 10 mg/L doxycycline. Images were acquired after 1, 2 and 3 weeks of treatment and after a 4th week where the doxycycline had been withdrawn. Each group contained at least 8 zebrafish and CS-OPT was performed with the acquisition of 64 projections.

MATLAB was used for segmentation, tumour quantification and vasculature skeletonisation. Amira (FEI) was also used for vasculature skeletonisation, subsequent quantification and all image visualisation. For tumour quantifications $n \geq 8$ and for vasculature quantifications $n \geq 5$ for each study group. To confirm tumour progression and validate CS-OPT derived quantifications the zebrafish were sacrificed after imaging and the tumours were removed, formalin-fixed, paraffin-embedded (FFPE) and subjected to histological analysis (Section 2.5). Hematoxylin and Eosin (H&E) staining of $n \geq 6$ FFPE tumour tissues for each study group was performed by IQPath (Institute of Neurology, UCL) and used to confirm what was previously reported by Nguyen et al. (2012). IHC was performed on $n \geq 3$ FFPE tumour tissues for each group using the antibodies within Table 2.5. I optimised IHC staining and subsequent IHC stains were performed by IQPath (Institute of Neurology, UCL). The resultant stained slides were quantified by myself and Dr. Matthew Ellis (Institute of Neurology, UCL) as described in Section 2.6.

4.3 Results

4.3.1 Preliminary acquisitions of adult zebrafish

In initial studies TraNac *Tg (KDR:mCherry:Fabp10-rtTA:TREeGFPKRAS^{V12})* zebrafish were imaged using CS-OPT to ascertain the performance of the platform with regards to image quality. The fish were immersed in 0.75x MS-222 solution for 2 minutes prior to imaging, when they were then immersed in 1x MS-222 solution. During the acquisitions this was altered to 2 minutes prior to acquisition in 1x MS-222 due to the fish recovering from anaesthesia and moving within the imaging chamber. Despite this alteration the zebrafish were still seen to move over the acquisition period, either through incomplete

anaesthesia, slipping within the imaging capsule or being affected by the speed of rotation whilst capturing the projections. Any movement within acquisition results in inaccurate image reconstructions, rendering the projection set useless. The fluorinated ethylene propylene (FEP) tubing was altered so that the base of the tube was angled. This restricted zebrafish placement within the tubing and prevented rotational movement and slippage during image acquisition.

When observing the acquired projections key requirements were determined. Firstly, strong auto fluorescent signals were observed in the gut of fed zebrafish when excited at both 488nm and 561nm, Figure 4.1a. Different food sources were trialled, including the sole use of brine shrimp or hikari protein pellets, but none reduced the fluorescence signal observed. Only when the zebrafish had been starved 24 hours prior to imaging was this problem rectified, Figure 4.1a.

It was also clear that the individual eggs within the female zebrafish were visible at both excitation wavelengths, as highlighted with the red arrow in Figure 4.1b. The eggs are visible within the non-pigmented female zebrafish by eye (Figure 1.5) and therefore have a different refractive index to the rest of the body, FEP tubing and water. This would lead to an increase of scattering. The fluorescence signal within this region of the fish appears greater than in the males, this also indicates the eggs have a level of auto-fluorescence.

Zebrafish with homozygous KDR:mCherry vasculature, *KDR:mCherry*$^{+/+}$, have a more intense fluorescence signal compared to the heterozygotes, *KDR:mCherry*$^{+/-}$, Figure 4.1c. Due to the increased signal intensity of the vessels the *KDR:mCherry*$^{+/+}$ zebrafish would be faster to image and reconstructions would have better accuracy and detail. Therefore, for future OPT imaging male, *KDR:mCherry*$^{+/+}$ zebrafish, that have been starved for 24 hours prior to acquisition, will be used.

4.3.2 Quantifying tumour growth and vascularisation with CS-OPT

Analysis of tumour progression and angiogenesis with CS-OPT was determined through an *in vivo* cross-sectional study. The groups imaged after 1, 2 and 3 weeks of doxycycline induction showed tumour progression and the final group of 3 weeks induction followed by one week of no inducer showed the tumour regression known of this model, Figure 4.2 and Video 2. Qualitative changes in tumour vasculature are also observed, where there is a greater tumour coverage and an increased amount of branching after 3 weeks of tumour

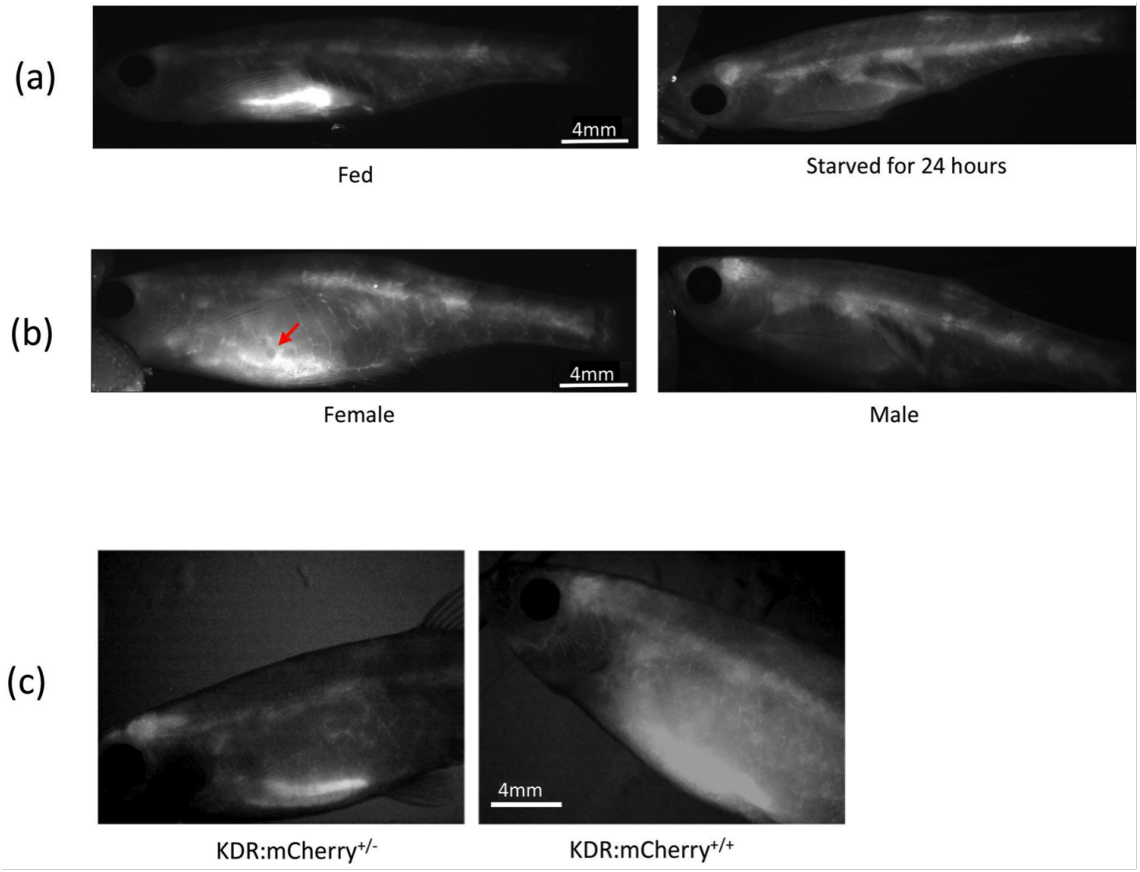

Figure 4.1: Fluorescent properties of adult TraNac *Tg (KDR:mCherry:Fabp10-rtTA:TRE- eGFPKRAS^{V12})* zebrafish excited at 561nm. (a) Individual OPT projections of fed and starved zebrafish indicating auto fluorescence in the gut of fed zebrafish. (b) Individual OPT projections of female and male zebrafish indicating light scattering in abdomen due to eggs within the female (indicated by arrow). (c) Widefield fluorescence microscopy images of heterozygous (KDR:mCherry$^{(+/-)}$) and homozygous (KDR:mCherry$^{(+/+)}$) zebrafish.

induction, which is subsequently lost upon tumour regression, Figure 4.2c and Video 3. The vasculature extending up to $\sim$1.7 mm into the fish has been reconstructed, as seen within in Figure 4.3 and Video 4 where the vasculature colocalised with the tumour is coloured orange.

To quantify tumorigenesis the tumour volume was calculated for all fish within each of the study groups. I calculated the number of non-zero voxels within the tumour channel image after reconstruction and segmentation. A significant increase in tumour volume was observed between 1 and 3 weeks of tumour induction, as well as a significant decrease between 3 weeks treatment and the 1 week of inducer removal, Figure 4.4. A degree of variability was observed within each study group due to genetic variation between the individual zebrafish.

In order to determine angiogenic measures skeletonisation of the segmented vasculature was required to extract information for analysis. Skeletonisation and the subsequent analysis was initially performed using modified versions of the MATLAB functions Skeleton3D and Skel2Graph3D written by Philip Kollmannsberger (available on the MATLAB file exchange (urlhttp://uk.mathworks.com/matlabcentral/fileexchange/authors/382138) (Kerschnitzki et al., 2013). The skeletonisation functioned used an iterative thinning approach, whereby the boundary points of the object are repeatedly removed until only single connected voxels remain. Skel2Graph3D was used to produce an adjacency matrix of all the branch points of this skeleton and the distance between them. The skeleton produced mapped well to the segmented vasculature, Figure A.3a, however Skel2Graph3D did not accurately depict the correct vessels and branch points as some regions lacked connection and others had incorrect nodes, Figure A.3b. To create a cleaner skeleton iterations of Graph2Skel3D (also written by Philip Kollmannsberger) were performed along with Skel2Graph3D. The stopping criteria for these iterations was when all branch points identified had greater than 2 emanating branches, therefore only true branches were depicted. This worked well for a subregion of vasculature shown in Figure A.3c, where the resulting image mimicked the original image in Figure A.3a. However, when analysing the entire tumour region the algorithm did not complete, even when left to compute for several days. Due to its time intensive nature this approach was not suitable for vasculature analysis.

The software package Amira (FEI) was subsequently used to skeletonise and extract quantifications of vascular properties from the CS-OPT images. Once the segmented

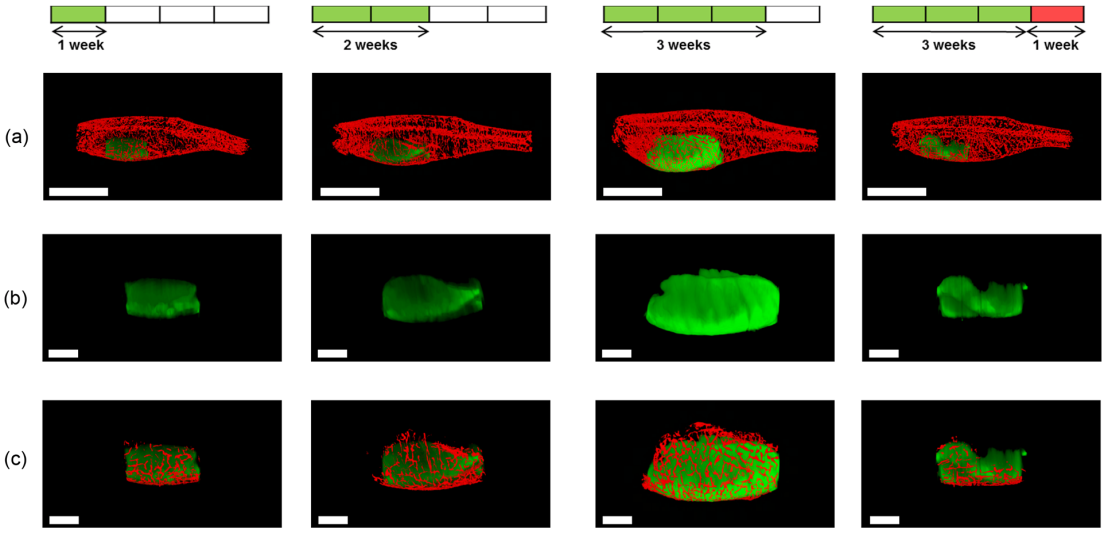

Figure 4.2: Representative CS-OPT reconstructions of the eGFP-labelled tumour and mCherry-labelled vasculature in adult TraNac *Tg (KDR:mCherry:Fabp10-rtTA:TRE- eGFPKRAS^{V12})* zebrafish. Data was acquired following 10 mg/L doxycycline treatment at 145 dpf after one, two and three weeks of treatment and after three weeks of doxycycline treatment plus a further week with no treatment. (a) shows whole zebrafish (scale bar = 5 mm); (b) the tumour alone and (c) with the segmented tumour vasculature (scale bar = 2 mm). See Videos 2 and 3 for corresponding 3-D animations.

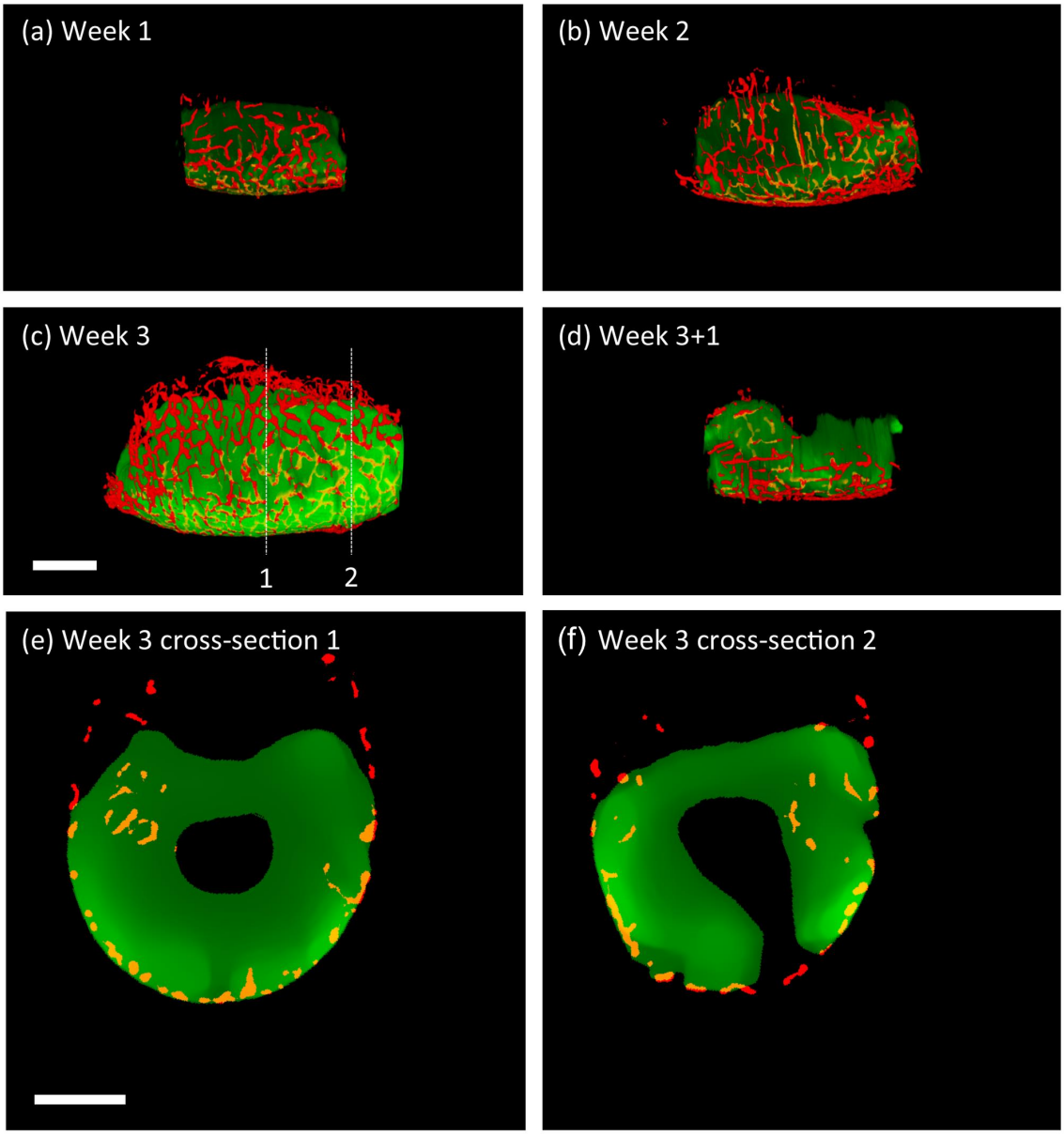

Figure 4.3: Representative CS-OPT reconstructions of eGFP-labelled tumour and the colocalised mCherry-labelled vasculature in adult (145 dpf) TraNac *Tg (KDR:mCherry:Fabp10-rtTA:TRE- eGFPKRAS^{V12})* zebrafish. Data has been acquired following doxycycline treatment after (a) one, (b) two, (c) three weeks of treatment and (d) after three weeks of doxycycline treatment plus a further week with no treatment. (e) and (f) are representative cross-sections showing tumour and vasculature from the reconstructed volume shown in (c) indicated by dotted lines 1 and 2 respectively. Red indicates vasculature 'outside' the tumour, orange indicates vascular 'inside' the tumour and green is the tumour. Scale bar 2 mm. See Video 4 for fly-through animations corresponding to the images in (a)-(d).

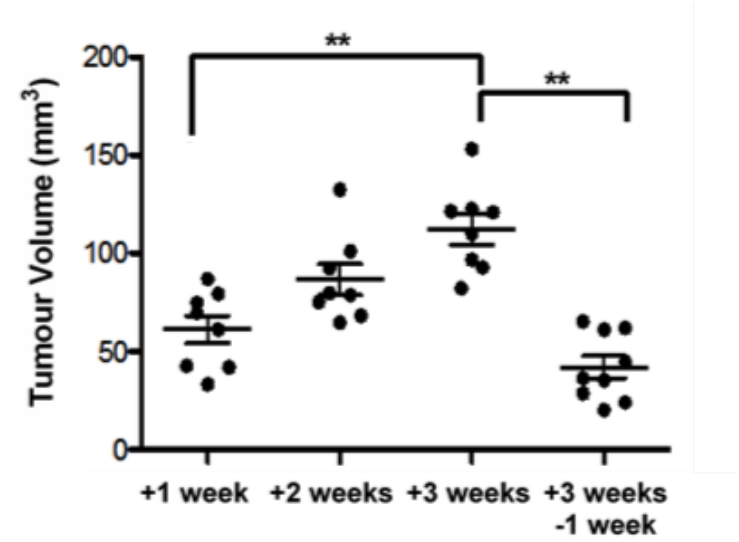

Figure 4.4: CS-OPT quantifications of tumour volume from the *in vivo* cross-sectional study using adult (145 dpf) TraNac *Tg (KDR:mCherry:Fabp10-rtTA:TRE-eGFPKRAS^{V12})* zebrafish. Data was acquired following doxycycline treatment after one, two and three weeks of treatment and after three weeks of doxycycline treatment plus a further week with no treatment. Graph plots the corresponding variation of the mean tumour volume, for which n$\geq$8 at each condition and the error bars represent the standard error of the mean (SEM). **p<0.01 as indicated by lines.

CS-OPT images were imported into Amira a 3-D median filter with a neighbourhood of 6 was applied to remove residual noise, Figures A.4a and A.4b. The auto-skeleton tool was then applied to produce a skeleton using no threshold, 10 iterations and "smooth" and "attach to data" coefficients of 0.5 and 0.25, respectively. From this skeleton the location, length, diameter and branching information for every individual vessel can be extracted. The resultant skeletons clearly mapped to the CS-OPT images well and with the chosen parameters there were no incorrect nodes or connections, Figure A.4c. Expanding the extracted skeleton to correspond to the calculated diameter for each voxel of the vessel shows its accuracy, Figure A.4d. The time taken for these processes to be accurately completed for the entire adult zebrafish was within 15 minutes.

Key markers of angiogenesis include vessel branching, length, diameter and percent tissue vascularisation. I analysed these for the tumour region of 5 CS-OPT images from each group of the *in vivo* cross-sectional study. Any vessels with a diameter or length less than 26μm, the known resolution of the CS-OPT platform, were excluded as noise. The mean angiogenic branching and percent tumour vascularisation for the tumour region, Figures 4.5a and 4.5b respectively, showed a significant increase during

the tumour progression period from 1 week to 3 weeks of treatment with doxycycline. Both also had a significant reduction during tumour regression once the inducer was removed. No significant differences were seen in mean vessel length or diameter, Figures 4.5c and d. Once again variability was observed for all angiogenic markers between individual fish within each of the study groups due to genetic variation.

4.3.3 Validating CS-OPT quantifications

It is important to determine that the quantifications drawn from CS-OPT truly represent the physiology of both the tumour and the vasculature. Therefore, validation with previously established techniques was required.

To assess tumour progression FFPE tissue sections from each of the study groups were analysed in collaboration with pathologist Professor Sebastian Brandner (Institute of Neurology, UCL) using H&E staining, Figure 4.6. The tumours are seen to be progressing from a hyperplastic liver, where there has been an increase in cell proliferation, towards a HCC phenotype. This is characterised by densely packed cells with high nuclear to cytoplasmic ratio, prominent nucleoli, reduced area of glycogen and lipid storage, increased mitosis and rosette like structures surrounding dilated bile canaliculi, Figure 4.6c. The samples taken after removing the inducer show a proportion of shrunken cells with intense eosinophilic cytoplasm and dense purple nuclear staining indicating chromatin condensation, which are features indicative of apoptosis, Figure 4.6d. This confirms what has been previously described for this eGFPKRAS^{V12} driven tumour model within the zebrafish by Nguyen et al. (2012).

For analysing the vasculature within the zebrafish liver tumours IHC was performed, however specific staining of zebrafish endothelial cells had not previously been possible. Numerous different endothelial markers (vWF, eNOS, CD31 and ERG) were trialled with different antigen retrieval techniques. This was without success as non-specific staining was seen in all cases, as summarised and shown within Table 4.1 and Figure A.5. Through discussions with Roberto Mayor (UCL) an mCherry antibody was identified that had been used previously and did not cross-react with the eGFP fluorophore, which is highly similar in protein structure to mCherry with a Protein BLAST E-value of 9e-20 (`https://blast.ncbi.nlm.nih.gov/Blast.cgi`). When using citrate buffer antigen retrieval and the mCherry antibody at 1:200 concentration specific staining of the zebrafish endothelial cells within the tumour was achieved. There was no background or cross reaction with the eGFP fluorophore within the zebrafish liver tumour, Figure 4.7.

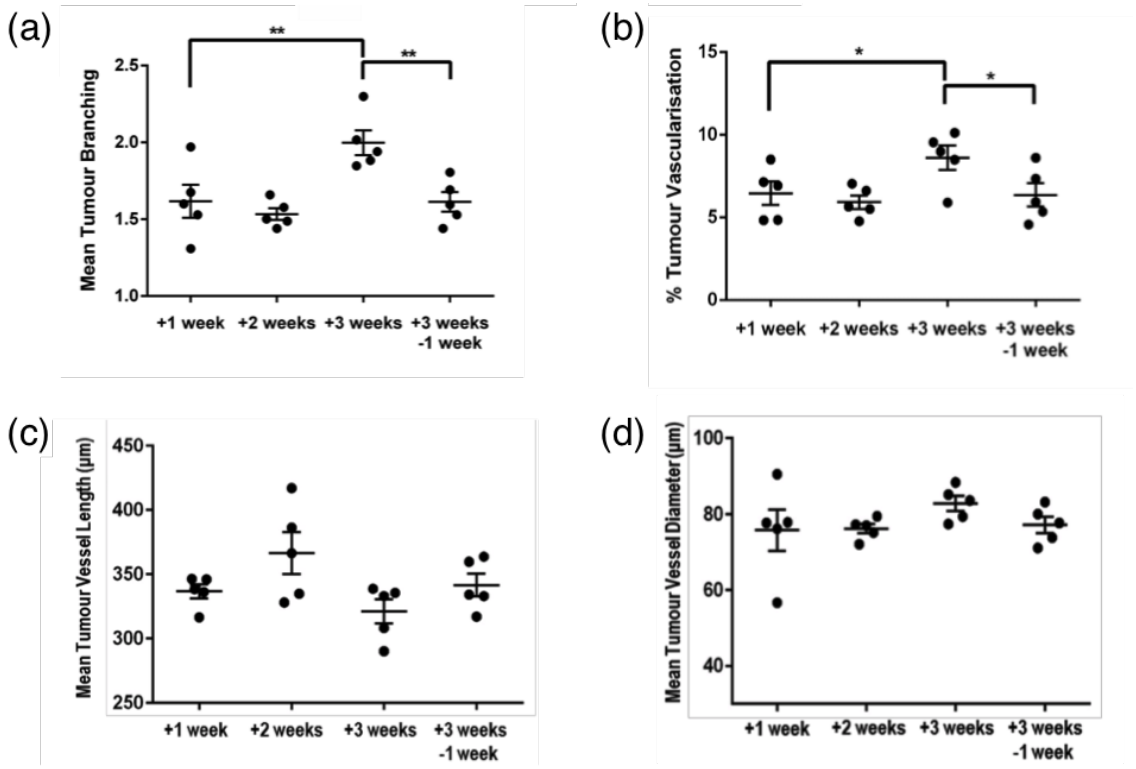

Figure 4.5: CS-OPT quantifications of vascular properties from the *in vivo* cross-sectional study using adult (145 dpf) TraNac *Tg (KDR:mCherry:Fabp10-rtTA:TRE-eGFPKRAS^{V12})* zebrafish. Data was acquired following doxycycline treatment after one, two and three weeks and also after three weeks of doxycycline treatment plus a further week with no treatment. Graphs plot the (a) mean number of tumour vessel branch points, (b) percent tumour vascularisation (proportion of vasculature volume within tumour volume), (c) mean tumour vessel length and (d) mean tumour vessel diameter, for which n$\geq$5 at each condition and the error bars represent the standard error of the mean (SEM). *p<0.05, **p<0.01 as indicated by lines.

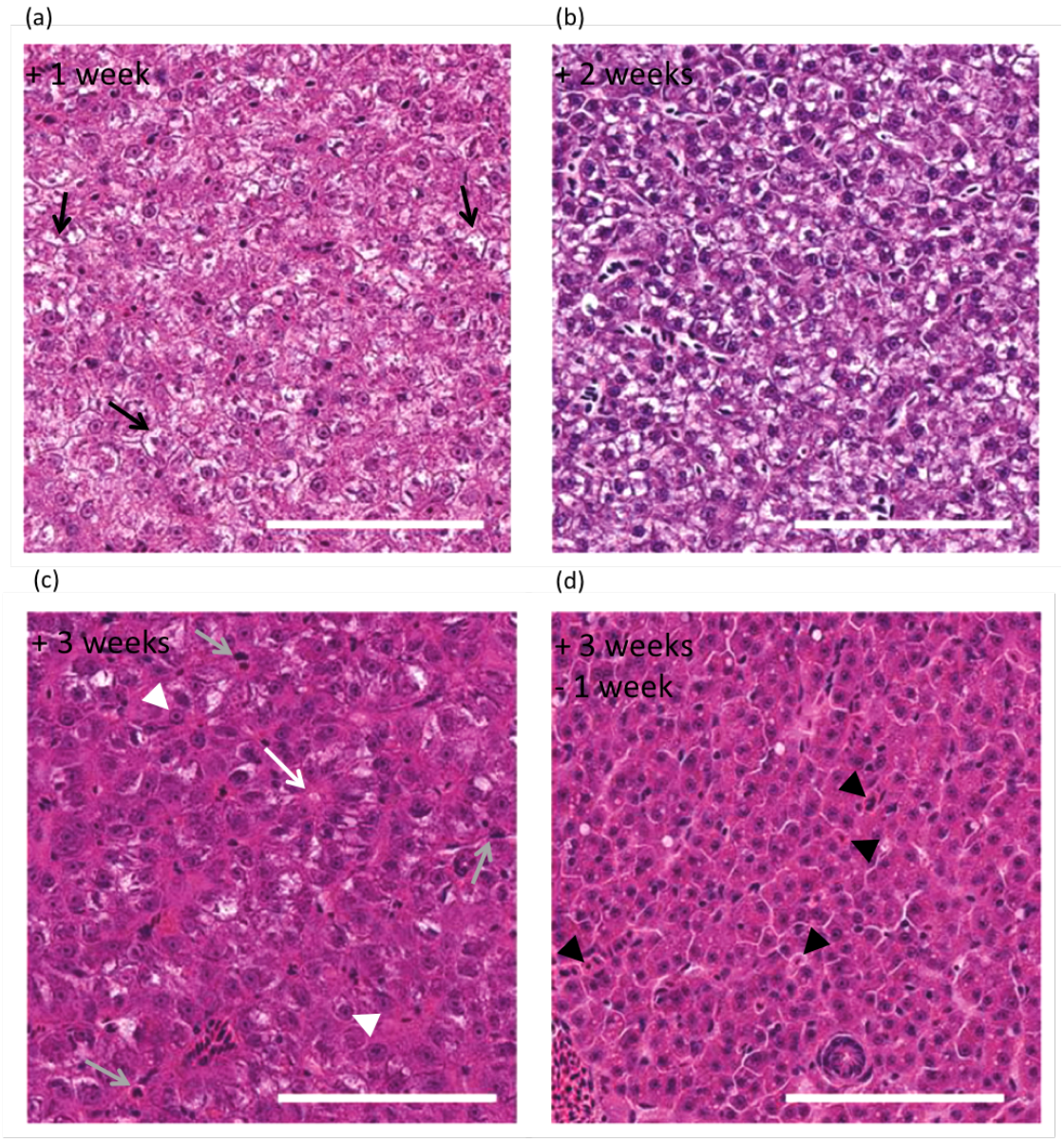

Figure 4.6: Induction and progression of HCC in adult (145 dpf) TraNac *Tg (KDR:mCherry:Fabp10-rtTA:TRE- eGFPKRAS^{V12})* zebrafish from the *in vivo* cross-sectional study. Images of H&E stained representative tumour sections following tumour induction for (a) one week, (b) two weeks, (c) three weeks and (d) three weeks of tumour induction plus a further week after removal of inducer treatment. White arrowheads highlight the cells with high nuclear to cytoplasmic ratio and prominent nuclei, grey arrows mitotic cells and white arrows rosette like structures with dilated bile canaliculi, all features of HCC. Black arrowheads indicate apoptotic cells that are shrunken with intense eosinophilic staining and condensed chromatin and black arrows indicate glycogen and lipid storage. Each group n=6-8. Scale bars 100 μm.

Antibody	Antigen Retrieval	Tissue Sample	Outcome
vWF	Pronase	Healthy Liver	Low level of non-specific staining
	Citrate Buffer	Healthy Liver	High level of non-specific staining
eNOS	Pronase	Healthy Liver	Low level of non-specific staining
	Citrate Buffer	Healthy Liver	Intermediate level of non-specific staining
CD31	Pronase	Liver Tumour	Low level of non-specific staining
	Citrate Buffer	Liver Tumour	Low level of non-specific staining
ERG	Pronase	Liver Tumour	Low level of non-specific staining
	Citrate Buffer	Liver Tumour	Low level of non-specific staining

Table 4.1: Summary of trialled antibodies for endothelial cell markers to detect vascularisation within zebrafish liver tissue sections. All sections were from TraNac *Tg (KDR:mCherry:Fabp10-rtTA:TRE- eGFPKRAS^{V12})* zebrafish, either when uninduced (healthy liver) or after 3 weeks of tumour induction with 10 mg/L doxycycline. Staining was performed at 1:100 antibody concentration.

Furthermore, the evidence of complete endothelial cell staining highlights the thorough expression of the KDR:mCherry transgene.

Once IHC with the mCherry antibody had been established it was used to stain FFPE tissue sections from numerous fish within each of the *in vivo* study groups. The resultant IHC stained sections could then be quantified. Regions of the mCherry stained liver tumour sections that correspond to the segmented vasculature in the CS-OPT data (as highlighted in Figure 4.3e and f) were selected for analysis. Due to the IHC data being 2-D and the CS-OPT data 3-D the quantification percent tumour vascularisation was analysed to enable comparison between datasets for validation.

The brown stained vessels were identified from the blue stained background of the tissue and surrounding slide area. The vessel lumen were incorporated into the identified areas to correspond to the CS-OPT signal and the vessel diameters were calculated. As previously mentioned the CS-OPT resolution limit is 26 μm and it is also well known that during the IHC process tissue and vessel morphology is likely to change, for example with collapsed vessels and tissue shrinkage. Furthermore, as IHC is a 2-D approach the vessels may be observed in different orientations and this must be considered. For these reasons vessels with a diameter lower than 5 μm or lower than 10 μm with a width/length ratio over 3 were excluded from the analysis. Based upon zebrafish physiology the upper vessel diameter limit analysis was 100 μm.

The percent tumour vascularisation was calculated through the vessel area detected within the selected tissue region of interest, for all of the *in vivo* cross-sectional study groups. It was seen to significantly increase during 1 to 3 weeks of tumour induction and also significantly reduce during tumour regression upon removal of the doxycycline inducer, Figure 4.8. Both the level and trend of vascularisation seen with IHC mimic the quantifications extracted from CS-OPT in Figure 4.5b. Therefore, the IHC quantifications validate the information extracted from CS-OPT images.

4.4 Discussion

4.4.1 Requirements of imaging adult zebrafish with CS-OPT

To acquire accurate images for subsequent analysis it was crucial to determine the performance of the CS-OPT platform when imaging whole, adult zebrafish. It was clear that the zebrafish gut was fluorescent when feeding had occurred within 24 hours of imaging. Several different foods were trialled to prevent this, but none resolved the problem. This issue could be a result of the food substances themselves, as they often contain nutrients and compounds to enhance fish colour (including shrimp and krill), or alternatively it could be elements of the zebrafish digestive system involved in metabolism. I have shown that depriving the zebrafish from food for 24 hours allows for emptying of the gut. Importantly, this did not impact the viability of the zebrafish.

The female zebrafish anatomy caused both vasculature and tumour signals to be inaccurate and unreliable, due to the eggs causing both auto-fluorescence and refraction. Such a finding restricts CS-OPT analysis to male zebrafish only. It is important to note that sexual dimorphism is present within the zebrafish liver, with respect to histology, sensitivity to sex hormone perturbation, regulatory networks and subsequent functions, (Zheng et al., 2013). This requirement is not a significant concern as single sexes are used for many studies, including the use of three previous zebrafish liver cancer models (Zheng et al., 2014) and mammalian models of physiology and pharmacology where there is a male bias, for example (Beery and Zucker, 2011).

It was apparent that fish homozygous for the *KDR:mCherry* transgene were advantageous for CS-OPT analysis due to their increased signal intensity. This would enable faster acquisition times and finer vascular detail to be detected. Homozygosity of zebrafish can be easily determined through out-crossing to a wild type fish and observing

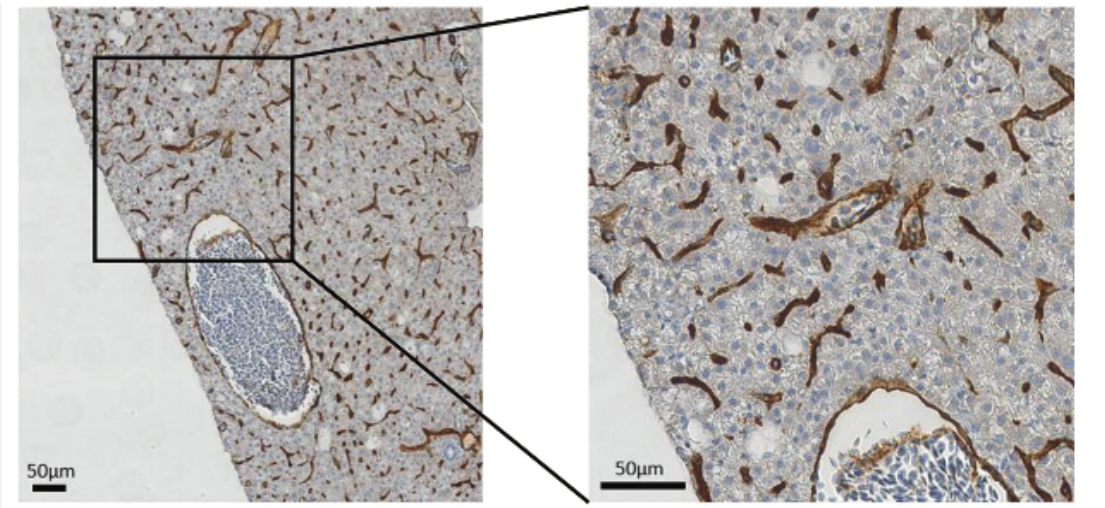

Figure 4.7: Immunohistochemical staining of tumour vasculature using the mCherry antibody. Representative images show staining of vessels (brown) from three week induced adult (145 dpf) TraNac *Tg (KDR:mCherry:Fabp10-rtTA:TRE-eGFPKRAS^{V12})* zebrafish from the *in vivo* cross-sectional study. Scale bar 50 μm.

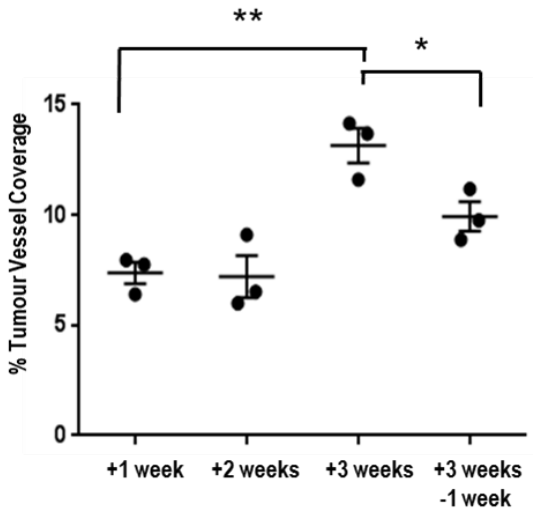

Figure 4.8: Validating CS-OPT vascular quantifications from the *in vivo* cross-sectional study through IHC quantification. Graph shows analysis of percent vessel coverage performed over regions of interest on mCherry stained sections from (145 dpf) TraNac *Tg (KDR:mCherry:Fabp10-rtTA:TRE- eGFPKRAS^{V12})* zebrafish. Data follows doxycycline treatment after one, two and three weeks and after three weeks of doxycycline treatment plus a further week with no treatment. Each group (n=3) and error bars represent the SEM. *p<0.05, **p<0.01 as indicated by lines.

fluorescence within 100% of offspring.

Movement of the zebrafish during acquisition poses a crucial problem, due to introducing artefacts in the reconstructions and rendering them unreliable. The anaesthesia protocol was altered to prevent the fish from gaining consciousness and moving, where 1x cold MS-222 was used throughout, with no impact on the viability of recovery. However, incomplete deep anaesthesia was still observed.

The movement of the rotating chamber within the CS-OPT apparatus results in the zebrafish slipping or slightly rotating within the FEP tubing overtime. The apparatus was modified so that the zebrafish were more restricted within the FEP tubing during acquisition to limit the chance of movement. This restriction could be further improved through using smaller FEP tubing or by using an index-matched material to hold the fish in place, such as agarose or beads. In order to apply either of these additional options substantial research would be required to ensure the health and viability of the zebrafish are not impacted, whilst ensuring the clarity of subsequent reconstructions remains.

4.4.2 Accurate quantifications for studying tumour progression and angiogenesis with CS-OPT

Quantitative analysis alongside qualitative information is beneficial when studying biological processes. The developed CS-OPT platform can provide 3-D whole organism images of live adult zebrafish, however its ability to provide accurate quantifications was unknown. Within this chapter I have quantified tumour growth and vascularisation within adult zebrafish using CS-OPT. I confirmed tumour growth with what has previously been reported by Nguyen et al. (2012) and have validated the vasculature measures with IHC to ensure the true biology is accurately represented. As a result these can be used as measures of tumour progression and angiogenesis.

4.4.2.1 Quantifications of tumour progression

It was previously reported that this zebrafish model driven by inducible, liver specific expression of eGFP tagged oncogenic krasV12 recapitulated the genetic and molecular hallmarks of human HCC (Nguyen et al., 2011). The eGFP fluorescence was also shown to correspond to tumour volume, which increased during tumour progression (Nguyen et al., 2012). These traits were replicated in the *in vivo* cross-sectional study with CS-OPT imaging. During the 3 weeks of inducer treatment histopathology revealed an increase in

densely packed cells with high nucleocytoplasmic ratio and rounded, prominent nuclei indicative of HCC. CS-OPT analysis also clearly showed a significant increase in tumour volume. Furthermore, tumours are known to regress upon removal of the inducer within this oncogene driven model zebrafish (Nguyen et al., 2012). This was also observed with CS-OPT imaging and analysis where a significant reduction in tumour volume was quantified and the histopathology of the regression group indicated signs of apoptosis causing the reduction in tissue size. Therefore, the CS-OPT quantifications of tumour progression and regression were confirmed.

4.4.2.2 Methods of extracting measures of angiogenesis from CS-OPT images

It was of interest to analyse tumour vascularisation and I initially encountered difficulties when trying to extract quantifications from the segmented CS-OPT 3-D images using MATLAB (MathWorks). This was overcome through using the software Amira (FEI). Amira successfully detected the vessels and branch points from the identified skeleton within a reasonable time frame and the the subsequent quantifications were proven to be accurate when mapped to the original image. Despite the MATLAB process described working effectively for small tumour subregions, it did not complete the entire tumour vasculature over a period of several days. This indicates that the process itself is correct and able to extract the information desired, but was not efficient. The images in Amira are filtered before the skeleton is extracted. The lack of this step in MATLAB may play a part in the extended computational time, however this was not seen to affect the subregion that was successfully analysed, so is unlikely to be the primary cause.

The iterations performed in attempt to clean the initial extracted skeleton had the stopping criteria of all branch points having greater than two protruding vessels, which was chosen as a vessel would only be branching if this were true. The stopping criteria could be relaxed, however this would lead to inaccuracies within quantifications. Not only would the number of vessels and their corresponding lengths be incorrect, but other properties reliant on these would also be affected, for example the mean vessel diameter. Due to these reasons, and the time required to address them, it was not beneficial to pursue this further when it became apparent Amira was efficient and accurate for the required purposes. Furthermore, it is possible to export the Amira skeleton into a format that is compatible with MATLAB. As a result using Amira will not limit any possible future analysis that requires in-house written codes.

4.4.2.3 Quantifications of angiogenesis

Angiogenesis is a key requirement of tumour progression and is usually quantified through assessing vessel length, vessel diameter, vessel branching and the vascular density (Staton et al., 2009). These measures were analysed for CS-OPT images from the *in vivo* cross-sectional study after vessels with an average length or diameter less than 26 μm were excluded. These vessels were removed as they had values lower than the known resolution of the CS-OPT platform, and therefore cannot be definitively proven to be vessels rather than noise. As a result the initial angiogenic sprouts may not be included in quantifications.

It is known that as tumours increase in size they become centrally oxygen deprived, as the central cells exceed the oxygen diffusion distance from the established vasculature (Thomlinson and Gray, 1955; Maxwell et al., 2001). Furthermore the tumour model zebrafish used is driven by the over expression of a constitutively active form of Ras, kras^{V12}. Both Ras signalling and hypoxia drive the expression and activity of HIF-1, the transcription factor that independently regulates VEGF and other genes involved in driving angiogenesis, Figure 1.2 (Pugh and Ratcliffe, 2003; Semenza, 2002). Therefore, the tumours being analysed, which are increasing in volume through the expression of oncogenic kras, should show an increased level of angiogenesis. The CS-OPT analysis revealed significant increases in both mean tumour vessel branching and percent tumour vascularisation during tumour progression and the vasculature appeared more aberrant and chaotic within the 3-D images. This is what would be expected if angiogenesis were occurring as described in Section 1.2.3 (McMahon et al., 2001; Semela and Dufour, 2004; Vakoc et al., 2009). These properties also decreased upon tumour regression. VEGF expression through hypoxic and non-hypoxic mechanisms is known to inhibit apoptosis, Figures 1.1 and 1.3. Therefore, when oncogenic Ras is no longer expressed and the tumours begin to regress endothelial apoptosis could be initiated. No significant differences were apparent in mean vessel length or mean vessel diameter within the CS-OPT images, which is what has previously been reported during tumour progression (Vakoc et al., 2009).

In attempt to validate the CS-OPT vascular quantifications the well established technique IHC was performed and, to the best of my knowledge, this is the first report of specific endothelial cell staining within the zebrafish. The mCherry antibody used did not produce any background staining or cross-react with the eGFP fluorophore expressed within the liver tumours. Therefore IHC can be used to accurately quantify the vascular

properties. As previously discussed the current limitation of CS-OPT is the ability to image the vasculature up to 1.7 mm into the zebrafish. For unbiased comparison the regions corresponding to the CS-OPT imaging capability were analysed from the IHC stains. Comparative analysis of percent tumour vascularisation was used for validation, as IHC is a 2-D technique and CS-OPT provided 3-D quantifications. The result showed that CS-OPT was truthfully representing the physiological changes occurring during tumour progression and regression.

4.4.3 TraNac *Tg (KDR:mCherry:Fabp10-rtTA:TRE-eGFPKRAS^{V12})* zebrafish as a model for HCC

As previously described in Section 1.3.2.2, the TraNac *Tg (KDR:mCherry:Fabp10-rtTA:TREeGFPKRAS^{V12})* zebrafish used are an adaptation of the previously developed and studied HCC model zebrafish by Nguyen et al. (2011, 2012). Through histopathological and transcriptomic analyses these zebrafish were shown to progress from a hyperplasia liver to a neoplastic, malignant HCC phenotype (Nguyen et al., 2011). It would be of interest to confirm that the progression being observed within the aforementioned studies was in agreement with the previous research and the observations were not purely hyperplasia. In order to so several approaches could be considered to determine the molecular hallmarks and gene signatures of the tumour samples. This could include quantitative PCR of genes and immunohistochemical staining or western blot analysis of proteins that are known to change in expression between hyperplasia and neoplasia. For example, the reduction in expression of gene *tp53* or the loss of the protein E-cadherin, which were both previously identified by Nguyen et al. (2011).

No metastases were observed using CS-OPT, however malignancy and metastasis were not studied by other means. The HCC model has previously been shown to be malignant, where tumour cells were found in surrounding vessels and nearby tissues (Nguyen et al., 2011). It would be of interest to determine whether the tumours within the performed research were malignant but too few cells had metastasised for detection using CS-OPT. This could easily be analysed through histological analysis of key surrounding tissues and vessels, either using H&E staining or immunostaining for GFP expression.

It is unknown whether tumour growth, vascularisation and regression are dependent purely on oncogene expression within this zebrafish model or whether hypoxia is a contributing factor. The commercial chemical Hypoxyprobe has previously been used to detect hypoxia within adult zebrafish both *in vitro* and *in vivo* (Jopling et al., 2012).

The Hypoxyprobe contains Pimonidazole that, at a low oxygen tension, can bind to thiol groups and therefore enable subsequent analyses, such as immunohistochemistry, to detect hypoxia. Incorporating this chemical into studies can provide additional information into the mechanisms involved within the zebrafish tumour model used, the similarity to the human pathology and the reliability of further studies.

One addition to the performed research that could enhance the qualitative and quantitative information achieved would be to include a data point prior to tumour induction. CS-OPT imaging was performed on Day 0 to confirm that the eGFPkras^{V12} expression was not leaky and a vasculature baseline was achieved. However, due to the healthy liver lacking fluorescence no liver volume can be extracted and subsequently the vascularisation of the healthy liver is also unknown. This information could be provided through the addition of a further fluorophore, that does not interfere with eGFP or mCherry, that is specifically expressed in the zebrafish liver. For example, infrared fluorescent protein (iRFP) expression downstream of the liver specific *fabp10* promoter. Consequently, the fate of healthy liver vasculature could be monitored within longitudinal studies and provide both a greater understanding of the tumorigenic and angiogenic processes and improved quantifications for mechanistic and drug development studies.

4.4.4 CS-OPT mesoscopic imaging capability

CS-OPT 3-D reconstructions of the tumour burdened zebrafish from the *in vivo* cross-sectional study clearly showed qualitative changes in tumour volume and vascularisation. These can be used to study tumour progression and angiogenesis. The complete eGFP tagged liver specific tumour spanning the entire width of the fish ($\sim$1 cm) has been successfully reconstructed, highlighting the ability of the CS-OPT platform to image whole adult zebrafish at the mesoscopic level. The vasculature has only been reconstructed up to 1.7 mm in depth within the tumour, which accounts for approximately a third of the tumour vasculature. The resolution of the CS-OPT images is 26 μm. As a result the CS-OPT imaging platform successfully bridges the 'mesoscopic imaging gap' and enables *in vivo* brightfield and fluorescence imaging of whole adult zebrafish. Additionally, this capability is achievable at a cost comparable to a widefield microscope. Therefore, the platform is advantageous to other imaging techniques that are described in Section 1.4.

CS-OPT does not account for scattering or aberrations of the emitted fluorescence and so the imaging performance is reduced towards the centre of adult zebrafish. Thus

the ability of the CS-OPT image reconstruction and subsequent image segmentation can vary throughout individual fish due to variations in their optical properties. This property is seen in the tumour vasculature, and not the tumour itself, due to its finer structure. While this instrument does already provide a useful platform for studying cancer progression and the corresponding angiogenic changes, its capabilities and vascular penetration depth could be improved.

Previous *in vivo* studies of tumour progression and corresponding vascularisation within zebrafish were studied qualitatively through observing the fluorescence levels and 2-D coverage. Quantitative measures were only provided with regards to tumour progression using histopathological, transcriptomic and protein analysis (Li et al., 2012; Nguyen et al., 2012; Li et al., 2013; Sun et al., 2015). This is also true of other adult model organisms, where quantitative analysis usually required sacrifice for subsequent processing. The CS-OPT quantifications are advantageous as they provide 3-D measures of tumour volume and the corresponding vascular properties *in vivo* within adult organisms. The additional dimension can enable greater information and consequently provide improved accuracy as the entire physiology can be analysed. As a result robust quantitative measurements of tumour progression, regression and angiogenesis can be detected and analysed with greater accuracy, with the added benefit of potential longitudinal imaging. This highlights the capability of CS-OPT imaging as a platform for both mechanistic and drug development studies.

CHAPTER 5

Longitudinal Imaging with CS-OPT

5.1 Introduction

The developed compressive sensing optical projection tomography (CS-OPT) platform facilitates 3-D mesoscopic fluorescence imaging of live, transparent zebrafish with the ability for quantitative analysis. Within Chapter 4 I have highlighted this capability through utilising the TraNac *Tg (KDR:mCherry:Fabp10-rtTA:TREeGFPKRAS^{V12})* zebrafish model (as described in Section 1.3.2.2) to quantify tumour volume and vascularisation. Coupled with benefits of low phototoxicity and quick acquisition times, as shown in Chapter 3, CS-OPT has the potential to be a powerful modality for longitudinal studies of tumorigenesis and angiogenesis, with respect to both mechanistic and drug development studies.

To achieve longitudinal imaging it is necessary that the CS-OPT platform is minimally invasive so that repetitive imaging will not impact on the viability of the zebrafish. It is also important that zebrafish reach a deep level of anaesthesia, where they have no response to external stimuli (Table 1.1), for prolonged periods of time without resulting in detrimental or lethal side effects (McFarland, 1959; Ross and Ross, 2008). This is due to the 3-D reconstruction algorithms being reliant upon motionless specimens and any slight movement during acquisition introduces errors in the reconstructed images and resulting quantifications (Correia et al., 2015; Kak and Slaney, 1988; Sharpe et al., 2002). CS-OPT imaging of adult tumour burdened fish requires approximately 3.5 minutes to acquire signals for both the tumour and vasculature. When including specimen positioning on the CS-OPT system this translates to an average time of approximately 10 minutes of required deep anaesthesia.

The anaesthetic regime widely used by the zebrafish community is 4.2% (168 parts per million (ppm)) MS-222 (tricaine methanesulfonate), based upon its reliability and consistency compared to other agents (Westerfield, 2000; Collymore et al., 2014). However, with prolonged exposure zebrafish experience respiratory and cardiac failure leading to higher mortality rates (Matthews and Varga, 2012; Sun et al., 2009). I had noticed on

multiple occasions that TraNac *Tg (KDR:mCherry:Fabp10-rtTA:TREeGFPKRAS^{V12})* fish require longer exposure to MS-222 to reach deep anaesthesia than wild-type (AB) zebrafish. Furthermore, these fish are unable to maintain deep anaesthesia for prolonged periods of time and are seen to moving during image acquisition, as previously mentioned in Section 4.3.1. It has been reported that a combination of MS-222 with isoflurane reduces cardiac failure and prolongs time under deep anaesthesia before reaching respiratory arrest and medullary collapse (Huang et al., 2010). The recovery period when using the combined anaesthesia is also reduced when compared to MS-222 alone.

The TraNac *Tg (KDR:mCherry:Fabp10-rtTA:TREeGFPKRAS^{V12})* model zebrafish expresses kras^{V12} within hepatocytes in a dosage dependent manner as described in Section 1.3.2.2 (Nguyen et al., 2012). Therefore, it is crucial to determine the optimal inducer concentration to achieve desired tumour onset and growth rates prior to longitudinal studies of tumorigenic and angiogenic progression. This it particularly true for drug development studies, whereby the optimal point to administer the therapeutic agent needs to be considered. Previously a concentration of 10 mg/L has been used, as in Chapters 3 and 4, but it is not known whether this dose is optimal or how tumour progression is affected after 3 weeks of treatment. The affect of adult zebrafish age on tumour onset and progression is also unknown. Therefore, this is another variable that needs to be better understood for accuracy in future studies.

Within this Chapter I address these points. I have performed longitudinal imaging of an individual zebrafish over a period of 5 months and analysed vasculature progression and remodelling in the context of development. I have also optimised a regime combining doses of MS-222 and isoflurane to repeatedly enable deep anaesthesia for prolonged periods of time and have analysed the effect of inducer concentration and zebrafish age on tumour onset and progression.

5.2 Experimental Summary

To demonstrate that CS-OPT is a minimally invasive imaging technique a single TraNac *Tg (KDR:mCherry)* zebrafish has been repeatedly imaged from 2 weeks post fertilisation (wpf) to 26 wpf as described in Section 2.8. Imaging was performed on the single arm OPT platform, as shown in Figure 2.3, whilst the fish was less than 5 wpf due to the organism size. After this point, during the juvenile and adult life stage, imaging was performed using the dual projection channel multispectral OPT system, as shown in

Figure 1.9.

Optimisation of anaesthesia for CS-OPT imaging of TraNac *Tg (KDR:mCherry:Fabp10-rtTA:TREeGFPKRAS^{V12})* involved using both MS-222 alone and in combination with Isoflurane. Fish lines used were Wild-Type (AB), TraNac, Casper, TraNac *Tg (KDR:mCherry:Fabp10-rtTA:TREeGFPKRAS^{V12})* and *Tg (KDRmCherry:cmlc2GFP)*, described in Sections 1.3.1 and 2.1.4. All fish used were between 6-9 months. Fish were anaesthetised with prescribed concentration and deep anaesthesia was determined as described in Table 1.1. All fish were continuously monitored whilst anaesthetised as described within Section 2.1.3. The external stimuli was tapping on the bench, which is a greater stimulus than that experienced during CS-OPT acqusition. The time taken for each fish to reach and to maintain deep anaesthesia were recorded, as well as the recovery time. For repetitive anaesthesia experiments the fish were anaesthetised once a week for a period of 4 weeks. Statistical analysis was performed as described in Section 2.9.

For the optimisation of doxycycline concentration studies were performed on TraNac *Tg (KDR:mCherry:Fabp10-rtTA:TREeGFPKRAS^{V12})* at ages 425 days post fertilisation (dpf) and 150 dpf, which are termed old and young, respectively. For each doxycycline concentration n$\geq$4. The required dose of doxycycline was added to the system water directly from within UCL fish facility, which is described in Section 2.1.1. Fish were kept in isolation, where they were fed and subsequently given fresh doxycycline water every other day. Imaging and quantification of tumour progression was performed twice a week using the widefield fluorescence microscope described in Section 2.7, where the fish were deeply anaesthetised (Table 1.1) prior to imaging.

5.3 Results

5.3.1 Demonstrating the minimally invasive nature of CS-OPT

To emphasise the minimally invasive nature of the CS-OPT platform an individual zebrafish with a red fluorescent vasculature was longitudinally imaged. Imaging began during the larval lifestage at 2 wpf and continued fortnightly through to adulthood at 12 wpf, with an additional final imaging session at 26 wpf. A subset of these have been reconstructed and are shown in Figure 5.1. The zebrafish recovered from all imaging sessions and its viability was not affected. Furthermore this zebrafish was able to breed and produce healthy, fertilised offspring after imaging was complete.

Qualitative changes are apparent when observing the zebrafish vasculature develop, Figure 5.1 and Video 5. Dramatic changes occur between 4 and 8 wpf as a result of the zebrafish size and vascular network developing and becoming increasingly dense. At 4 wpf some of the primitive embryonic vessels can clearly be seen, such as the intersegmental vessels, Figure 5.1. However, the dorsal aorta and posterior cardinal vein that are also obvious within zebrafish embryo images, Figure 1.6a, are hidden by further vessels that have developed. Smaller, finer vessels are depicted within the 4 wpf image, compared to the other images within Figure 5.1. This is due to both the higher magnification of the single axis OPT imaging system and zebrafish larvae itself. The larvae has reduced scatter as a result of its smaller size and greater transparency, where key organ systems and remaining pigmentation cells are still developing within the fish. From 8 wpf greater vascular detail can be observed and key vessels such as the lateral cutaneous artery (insert box within Figure 5.1) can be depicted. As the zebrafish continues to grow the density and complexity of the vasculature increases, where a greater degree of branching can be seen. The gaps in the vasculature apparent within the 8 wpf image are gradually filled through 12 wpf and up to 26 wpf, Figure 5.1 .

Quantitative analysis of developmental angiogenesis can be drawn from these longitudinal images. To demonstrate this ability the lateral cutaneous artery (insert boxes within Figure 5.1) has been analysed, Table 5.1. Due to the use of a different OPT imaging system for zebrafish larvae, analysis has been performed from 8 wpf onwards. As previously demonstrated within Section 4.3.2, Amira was used to extract the information required after image segmentation in MATLAB. The image was skeletonised so the remaining voxels represented the centre of each vessel and had a value corresponding to the diameter of the vessel at that point. From this skeleton the lateral cutaneous artery was selected and analysed. The key angiogenic characteristics of vessel length, mean vessel diameter and number of branches emanating were extracted from Amira for the 8, 12 and 24 wpf images shown in Figure 5.1. Vessel length was the total number of voxels within the skeleton for the particular vessel, the mean vessel diameter was the average of the voxel values within the vessel and the number of branches was calculated as the number of voxels that had three non-zero adjoining voxels. It is clear that each of these traits increases overtime and plateaus towards 26 wpf, as you would expect as the organism is growing and maturing towards a fully developed adult, Table 5.1.

Once again movement was seen from the zebrafish during image acquisition. Consequently, these datasets were not of use and particular time points were lost as CS

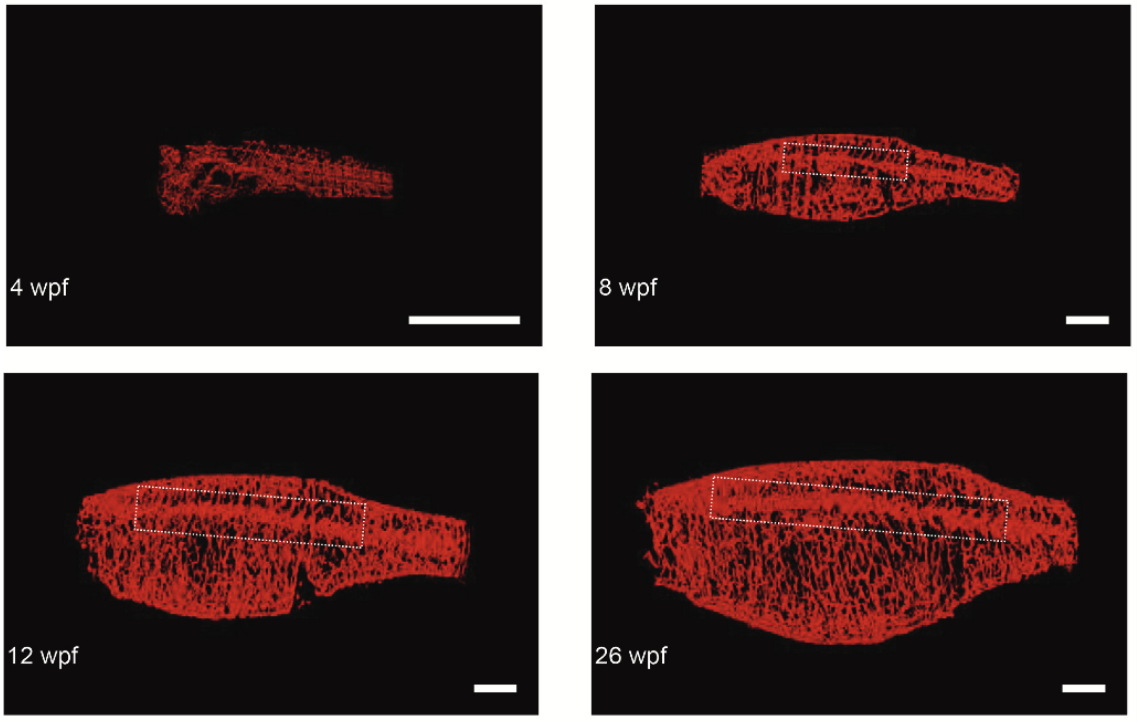

Figure 5.1: Reconstructed CS-OPT images from a longitudinal study of an individual TraNac Tg *(KDR:mCherry)* zebrafish repeatedly imaged at 4, 8, 12 and 26 weeks post fertilisation (wpf). Insert boxes define the vascular region containing the lateral cutaneous artery and Table 5.1 summarises the vascular quantification of this vessel. Scale bar = 2 mm. See Video 5 for corresponding 3-D animations.

	8 wpf	**12 wpf**	**24 wpf**
Length (mm)	7.09	11.00	16.01
Mean Diameter (μm)	159.82	253.22	265.24
Number of Branchpoints	36	57	65

Table 5.1: Vascular quantification of the lateral cutaneous artery in a TraNac Tg *(KDR:mCherry)* zebrafish longitudinally imaged using CS-OPT at 8,12 and 26 weeks post fertilisation (wpf).

reconstruction is reliant upon motionless specimens. The 2 wpf time point experienced significant motion, which was a result of their small size causing slipping and rotational movement within the FEP imaging tubing during acquisition. Movement within other time points during image acquisition was a result of a lack of maintained deep anaesthesia, where zebrafish exhibited traits of light anaesthesia such as response to external stimuli (Table 1.1).

5.3.2 Optimising the anaesthetic regime

5.3.2.1 Anaesthetising TraNac zebrafish using MS-222

As I had previously observed TraNac *Tg (KDR:mCherry:Fabp10-rtTA:TREeGFP KRAS^{V12})* fish require longer exposure to MS-222 to reach deep anaesthesia than wild-type (AB) zebrafish it was beneficial to clarify and elucidate this phenomenon. To do so the time to reach deep anaesthesia using 168 ppm MS-222 (4.2%) in these fish was compared to other zebrafish genotypes. The genotypes used for comparison included wild-type (AB), another double transgenic line (*Tg (KDRmCherry:cmlc2GFP)*) and two non-pigmented zebrafish lines, Casper and TraNac. As described in Section 1.3.1, Casper zebrafish are identical in appearance to TraNac and share the loss of functional *nacre*, however they lack both functional copies of the gene *roy* opposed to *transparent (tra)*.

The time taken to reach deep anaesthesia in the wild-type (AB) fish was not significantly different to that of the *Tg (KDRmCherry:cmlc2GFP)* or Casper lines, however a significant increase was seen in the TraNac *Tg (KDR:mCherry:Fabp10-rtTA:TREeGFPKRAS^{V12})* and the TraNac zebrafish, Figure 5.2. There was also a significantly larger variation within the TraNac *Tg (KDR:mCherry:Fabp10-rtTA:TREeGFPKRAS^{V12})* and the TraNac groups when compared to the pigmented lines, where $P<0.001$ using the Bartlett method. Therefore, it can be determined that these differences in response to MS-222 were not due to the expression of fluorescent transgenes or the non-pigmented phenotype, but a result of the TraNac genotype and likely as a result of loss of the *tra* gene.

Fish, of all genotypes, were also found to respond to external stimuli. Therefore, despite the use of 168 ppm MS-222 allowing deep anaesthesia to initially be reached, it was not maintained.

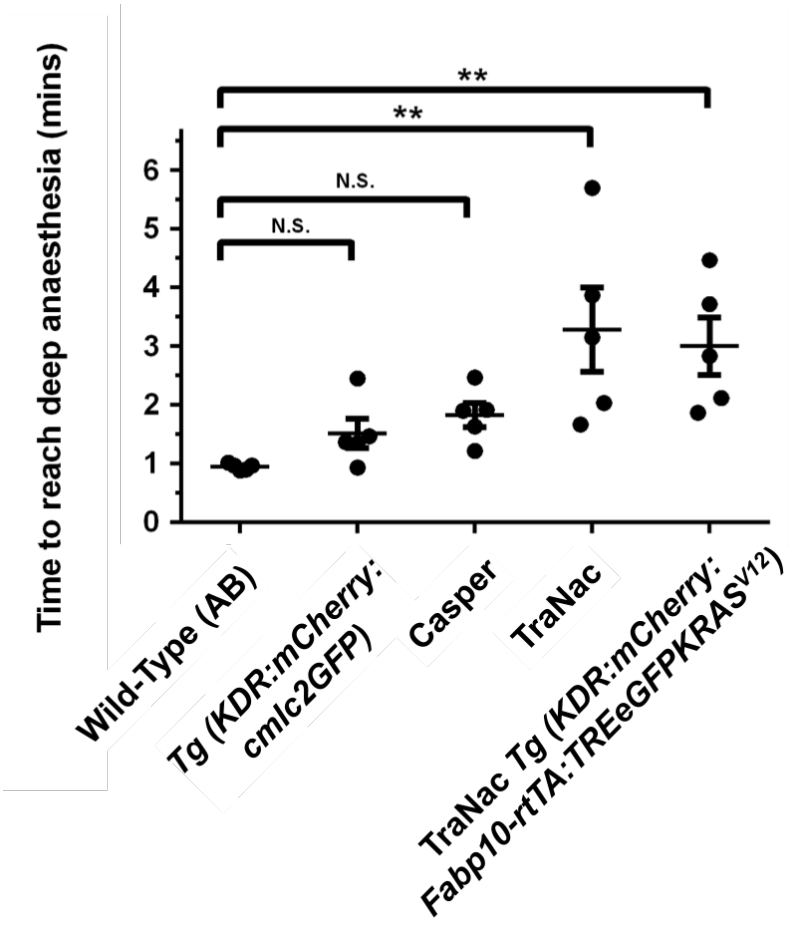

Figure 5.2: Analysis of the time to reach deep anaesthesia within different zebrafish lines using 168 ppm MS-222. The groups of zebrafish tested were as described in Section 5.2. Within each group n=5 and the error bars represent the standard error of the mean (SEM). **p< 0.01 and N.S. indicates not significant.

5.3.2.2 Using combined doses of MS-222 and Isoflurane to improve deep anaesthesia

Based upon a previously reported study by Huang et al. (2010) TraNac *Tg (KDR:mCherry:Fabp10-rtTA:TREeGFPKRAS^{V12})* zebrafish were anaesthetised with combined doses of MS-222 and isoflurane, in the hope to achieve and maintain longer periods of deep anaesthesia, Figure 5.3. In line with Huang et al. (2010) I began with equal anaesthetic concentrations as low as 50/50 ppm (MS-222/isoflurane), however all fish exhibited only light anaesthesia (Table 1.1) after 15 minutes of exposure. A dose escalation was then performed with equal amounts of each anaesthetic. The minimum concentration of MS-222 and isoflurane required for 100% of fish to reach deep anaesthesia within 15 minutes was found to be 150/150 ppm. However, despite reaching deep anaesthesia 75% of fish maintained in 150/150 ppm awoke within 5 minutes of treatment, Figure 5.3a. Using a dose of 165/165 ppm resulted in all fish staying under anaesthesia, yet 60% were seen to respond to external stimuli suggesting a state of light anaesthesia (Table 1.1). This was significantly improved when using doses of 170/170 or 175/175 ppm, where greater than 80% of fish were maintained under deep anaesthesia with no response to external stimuli, Figure 5.3a.

To determine whether longer periods of deep anaesthesia could be achieved and maintained the amount of isoflurane with a constant 175 ppm MS-222 was varied. It was reasoned that MS-222 doses higher than 175 ppm would be detrimental to zebrafish due to a concentration of 200 ppm being routinely used as an overdose for zebrafish euthanasia (Matthews and Varga, 2012). Using a dose of 175/200 ppm had little effect on the time under deep anaesthesia compared to 175/175 ppm, while the combination of 175/250 started to trend towards a reduced time. Using a regime of 175 ppm MS-222 alone resulted in a reduced time under deep anaesthesia, with a corresponding increase in response to external stimuli as had previously observed for 168 ppm MS-222, Figure 5.3b. Importantly, no significant differences in recovery time were observed using the combined regimes described Figure 5.3b when compared to MS-222 alone, Table 5.2.

5.3.2.3 Repeatedly using combined doses of MS-222 and Isoflurane

To implement longitudinal studies repeated anaesthesia is necessary. For CS-OPT analysis one imaging session per week is sufficient to see significant changes in tumour progression and vascularisation (Chapter 4). Based on results from Figure 5.3b, groups of TraNac *Tg (KDR:mCherry:Fabp10-rtTA:TREeGFPKRAS^{V12})* fish were subjected to the combined doses of 175/175 ppm or 175/200 ppm of isoflurane with MS-222, once a week

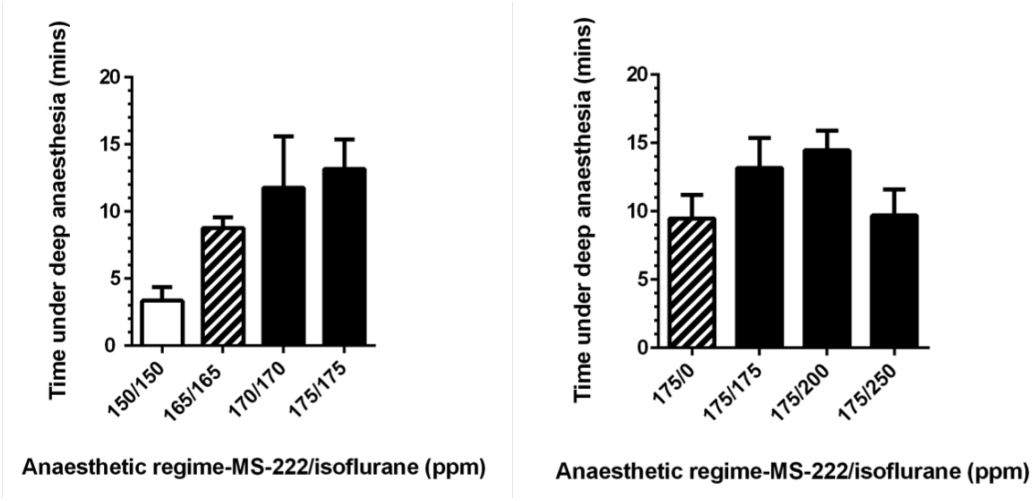

(a) **(b)**

Figure 5.3: Analysing time under deep anaesthesia using combinations of MS-222 and isoflurane (MS-222 ppm/isoflurane ppm) on TraNac *Tg (KDR:mCherry:Fabp10-rtTA:TRE- eGFPKRAS^{V12})* zebrafish. Equal doses of the anaesthetics (a) and variations of isoflurane concentration with 175ppm of MS-222 (b) were analysed. The data presented for each group is the mean with error bars representing the standard error of the mean (SEM), where n $\geq$ 4 for each group. Solid white bars represent > 50% of fish awakening, hatched bars represent > 50% fish experiencing light anaesthesia and solid black bars represent > 80% of fish remaining under deep anaesthesia.

Anaesthetic Regime MS-222/ Isoflurane (ppm)	Recovery Time (Mean (sec) $\pm$ SEM)
175/0	121 $\pm$ 9.3
175/175	99 $\pm$ 13.2
175/200	155 $\pm$ 7.1
175/250	202 $\pm$ 27.7

Table 5.2: The recovery time of TraNac *Tg (KDR:mCherry:Fabp10-rtTA:TRE-eGFPKRAS^{V12})* zebrafish after anaesthesia with regimes varying in isoflurane concentration (ppm) with 175 ppm of MS-222. The data presented is the mean recovery time (s) and error bars represent the standard error of the mean (SEM), where n $\geq$ 4 for each group.

for four weeks, Figure 5.4. The time under deep anaesthesia varied over the four week study when using a dose of 175/200, which was not seen when using 175/175 ppm, Figure 5.4. Therefore it was determined that the 175/175 ppm combined anaesthetic regime would be optimal for motionless 3-D image acquisition during longitudinal studies. Importantly, repeated exposure to these combined doses of MS-222 and isoflurane did not impact the health, fitness or viability of the zebrafish. All fish experienced rapid recoveries, did not have reduced viability or appear under any stress, Table 5.3.

5.3.2.4 Reducing the time to reach deep anaesthesia in TraNac zebrafish using both MS-222 and Isoflurane

The combined 175/175 ppm of MS-222 and isoflurane doses were tested on Wild-Type (AB), TraNac and TraNac *Tg (KDR:mCherry:Fabp10-rtTA:TREeGFPKRAS^{V12})* fish. This was to determine whether the time to reach deep anaesthesia compared to standard MS-222 alone in different genetic backgrounds was affected, Figure 5.5.

All fish were found to reach deep anaesthesia in less than 3 minutes. TraNac and TraNac *Tg (KDR:mCherry:Fabp10-rtTA:TREeGFPKRAS^{V12})* fish have a reduction in both the time taken to reach deep anaesthesia and the variation between individual fish ($P<0.01$ using Bartlett method) when using the 175/175 ppm combined regime compared to standard MS-222 used in Figure 5.2. A significant difference is still observed between the Wild-Type (AB) group and the TraNac fish, indicating a similar role effect as observed in Figure 5.2, Figure 5.5.

5.3.3 Optimising doxycycline treatment for tumour onset and progression

It is important to determine the optimal doxycycline concentration within the zebrafish tumour model prior to mechanistic and drug development studies. Furthermore, it is of interest to ascertain whether the models dose dependency is variable with age. Both old and young zebrafish were initially treated with low concentrations of doxycycline, 1 mg/L and 2 mg/L, and monitored over two weeks. Tumours did not develop in any of the fish at either concentration, highlighted with the higher dose in Figure 5.6.

Subsequently higher doses of doxycycline were required and 5 mg/L was analysed. All young zebrafish developed tumours over the 22 day period analysed, compared to only 75% of old fish. Of the fish that did develop tumours during the course of the

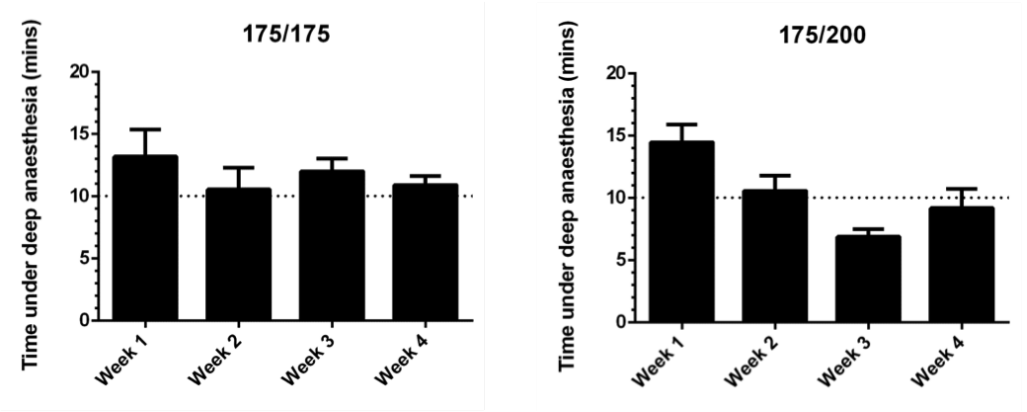

Figure 5.4: Time under deep anaesthesia with repeated use of MS-222 and isoflurane combinations 175/175 and 175/200 (MS-222 ppm/isoflurane ppm) on TraNac *Tg (KDR:mCherry:Fabp10-rtTA:TRE- eGFPKRAS^{VI2})* zebrafish. Each anaesthetic regime was tested over 4 weeks. The data presented for each group is the mean with error bars representing the standard error of the mean (SEM), where n $\geq$ 3 for each group. The horizontal dotted line at 10 minutes represents the average time required for CS-OPT image acquisition.

Anaesthetic Regime MS-222/ Isoflurane (ppm)	**Recovery Time (Mean (sec) $\pm$ SEM)**			
	Week 1	Week 2	Week 3	Week 4
175/175	155 $\pm$ 7	149 $\pm$ 22	137 $\pm$ 18	113 $\pm$ 15
175/200	202 $\pm$ 45	117 $\pm$ 24	132 $\pm$ 28	123 $\pm$ 28

Table 5.3: The recovery time after anaesthesia with repeated use of combined MS-222 and isoflurane concentrations 175/175 and 175/200 (MS-222 ppm/isoflurane ppm) on TraNac *Tg (KDR:mCherry:Fabp10-rtTA:TRE- eGFPKRAS^{VI2})* zebrafish. The data presented is the mean recovery time (s) and error bars represent the standard error of the mean (SEM), where n $\geq$ 3 for each group.

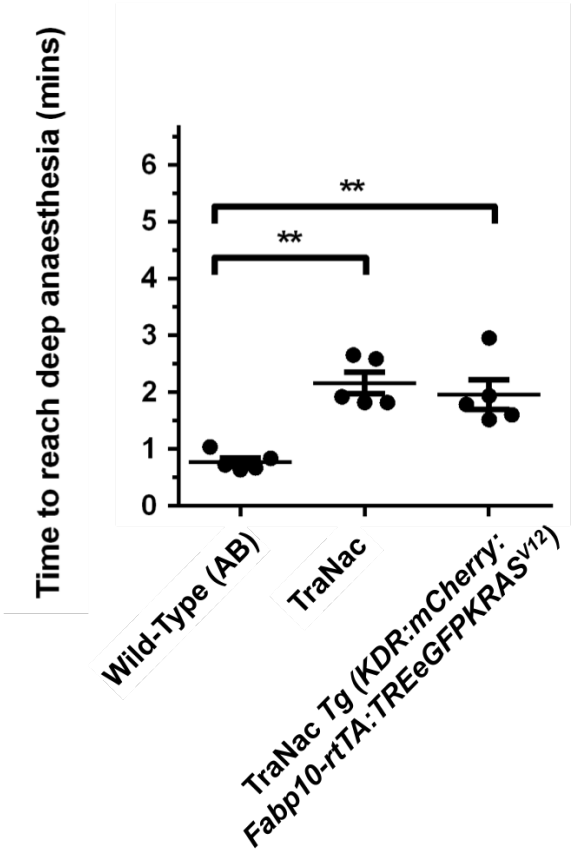

Figure 5.5: Analysis of the time to reach deep anaesthesia within different zebrafish lines using 175 ppm of both MS-222 and isoflurane. Within each group n=5 and the error bars represent the standard error of the mean (SEM). **p<0.01.

study differences were apparent with respect to age for both tumour onset and tumour progression, Figure 5.7. Tumours were apparent at 4 days post induction (dpi) in young zebrafish, but were not seen until imaging at 9 dpi in the older fish. Furthermore, the tumour area was consistently larger in younger fish and so the tumour progression was more advanced, Figure 5.7b. Linear regression analysis was performed on the quantifications shown in Figure 5.7b. When fitting linear functions to each of these datasets the the r^2 values were both greater than 0.95 and the tumour growth rate was significantly higher in younger fish when compared to old, at 2.085 ± 0.176 opposed to 1.187 ± 0.1086.

Induction of the young fish was continued with 5 mg/L in an attempt to understand the dynamics of the tumour progression and to identify the optimal point for therapeutic administration during drug development studies. The rate of tumour growth began to

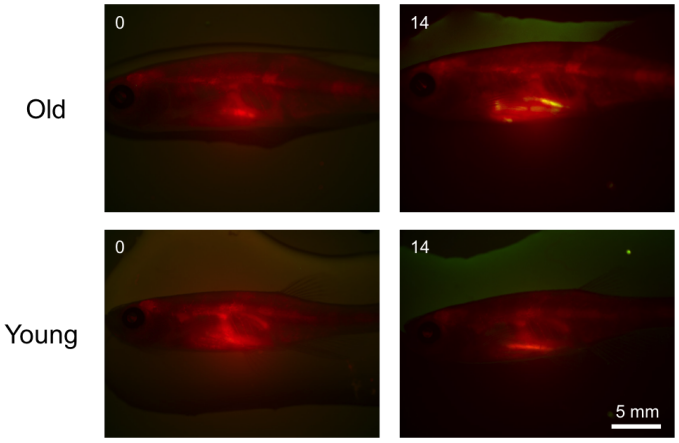

Figure 5.6: Representative TraNac *Tg (KDR:mCherry:Fabp10-rtTA:TRE-eGFPKRAS^{V12})* zebrafish from a cohort of 4 zebrafish per group induced with 2mg/L doxycycline. Widefield images of Old (425 dpf) and Young (150 dpf) zebrafish are shown at Day 0 and Day 14, as indicated in the top left of each image.

plateau after the initial 22 days of tumour induction, but surprisingly tumours were seen to regress after imaging on 26 dpi, as seen between 26 and 33 dpi in Figure 5.8. The inducer concentration of 5 mg/L did not appear to be sufficient to maintain tumours of this size. It was hypothesised that this was through too few reverse tetracycline-dependent transactivator (rtTA) proteins being able to bind to tetracycline response element (TRE) sequences within the hepatocytes and drive oncogene expression. With this in mind the inducer dose was raised to 7.5 mg/L after imaging on 33 dpi and the tumours began increasing in size again, Figure 5.8. After 44 dpi the same phenomena occurred once more with a dramatic drop in tumour size being observed at 47 dpi and so at this point the dose was escalated further to 10 mg/L, Figure 5.8.

Once again, the increase in doxycycline concentration temporarily resulted in tumour growth, before regression occurred after 51 dpi, Figure 5.8. This concentration had been used in previous studies, as shown in Chapters 3 and 4, and larger tumours had been seen, for example the representative fish after 3 weeks of tumour induction within Figure 4.2. Therefore, this finding was unusual. Using 10 mg/L of doxycycline a colour change was observed within the zebrafish water over the 48 hours used before a fresh water change. Doxycycline is known to be light sensitive and degrade overtime to give a yellow colour, but with a light/ dark cycle of 14/10 hours (as described in Section 2.1.1) a water change is only required every other day (personal communication with Zhiyuan Gong, The National University of Singapore). However, the colour change observed was to a shade of red. Upon this observation a water study was performed to determine whether

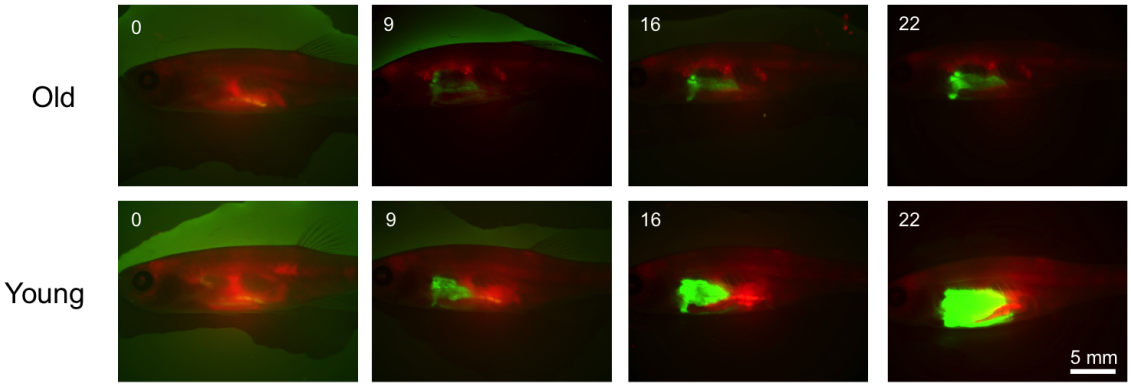

(a)

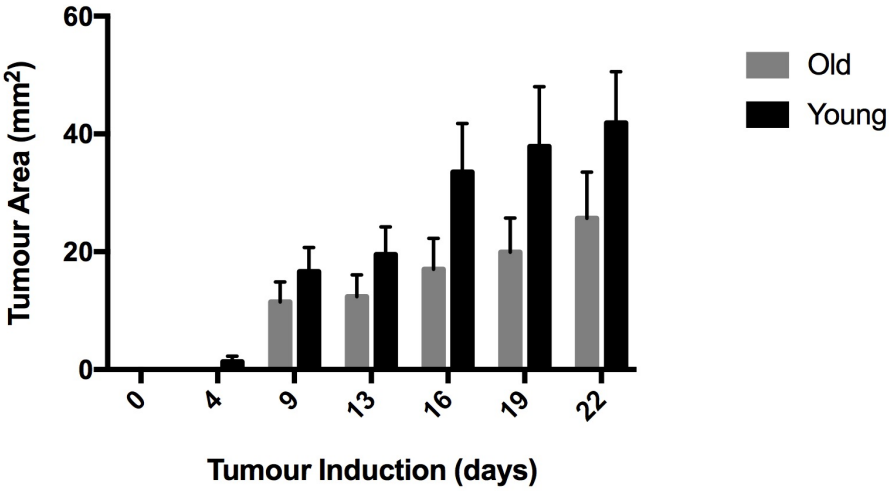

(b)

Figure 5.7: Longitudinal widefield imaging of Old (425 dpf) and Young (150 dpf) TraNac *Tg (KDR:mCherry:Fabp10-rtTA:TRE- eGFPKRAS^{V12})* zebrafish induced with 5 mg/L doxycycline for 22 days. Images show an eGFP labelled tumour and mCherry labelled vasculature. a) shows widefield images for a representative zebrafish from each group at selected time points, as indicated in the top left of each image. b) is the corresponding quantitative analysis of tumour area from all tumour burdened zebrafish within each group (n $\geq$ 3). The graph plots the mean tumour area and error bars represent the standard error of the mean (SEM).

the system water or the lighting within the room being used was causing an unusual degradation of doxycycline and reducing its potency. System water from the UCL fish facility and Tropic Marin® water made from 68mg/L of Tropic Marin® Sea Salt with deionised water were used with 10 mg/L doxycycline water. Fish tanks containing 100 mls of each water type were placed in two different rooms within the UCL fish facility, including the room the longitudinal study was being performed in. After 24 hours the system water had changed colour to the red shade in both locations, but the Tropic Marin® water had not. Therefore, 10 mg/L Tropic Marin® doxycycline water was then used after imaging on Day 58. This water change resulted in tumour growth at a similar rate to previous points within the study prior to regression, Figure 5.8b. The pH was tested for both waters and they were not significantly different, the system water was 7.01 and the Tropic Marin® water was 7.38.

5.4 Discussion

5.4.1 CS-OPT is a minimally invasive platform for longitudinal imaging

Longitudinal studies of tumour progression and the accompanying vascular changes would be beneficial to provide additional temporal information and improved accuracy when compared to cross-sectional studies (Ntziachristos et al., 2005). Furthermore the number of animals required for research would be reduced. There are limited imaging modalities capable of live mesoscopic imaging, which is desirable for *in vivo* studies of model organisms. CS-OPT achieves accurate quantitative mesoscopic imaging of whole organisms, as shown in Chapter 4, and the zebrafish simply require anaesthetising to satisfy the requirement of motionless imaging. The rapid acquisition time also minimises light dose and anaesthesia time experienced by the zebrafish. Therefore, CS-OPT has the potential to be a powerful platform for quantitative longitudinal studies if the viability of the imaged zebrafish is not affected through repeated imaging sessions.

Through longitudinal imaging of vascular progression and remodelling in the context of development the minimally invasive nature of this platform has been demonstrated. Repetitive imaging of individual zebrafish occurred every fortnight from 2 wpf up until 12 wpf, which spans the larvae, juvenile and adult life stages, with an additional imaging session at 26 wpf. The recovery and fitness of the zebrafish were not affected. 3-D quantitative imaging of whole organisms was achievable throughout the longitudinal

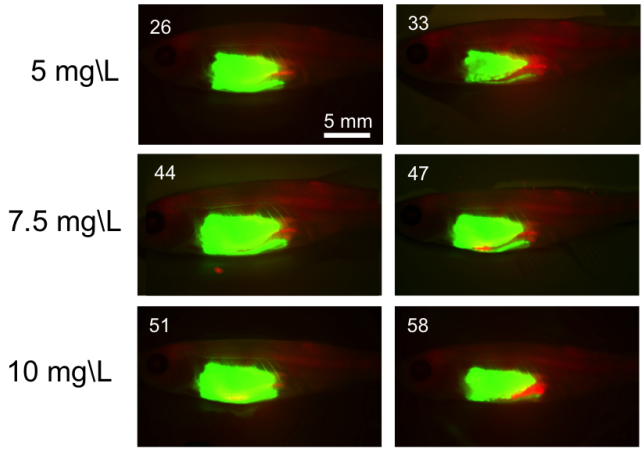

(a)

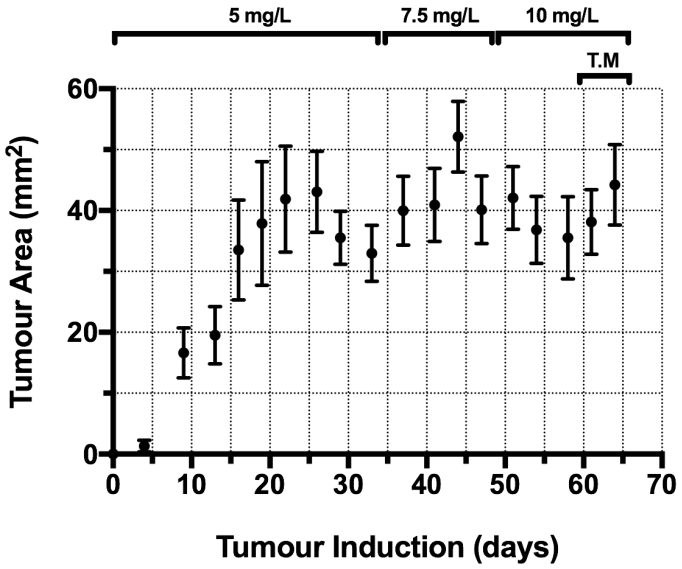

(b)

Figure 5.8: A longitudinal study to understand the relationship between dose dependency and tumour progression within TraNac *Tg (KDR:mCherry:Fabp10-rtTA:TRE-eGFPKRAS^{V12})* zebrafish at 150 dpf. Doxycycline concentration was initially 5 mg/L, before being increased to 7.5 mg/L and 10 mg/L after imaging on Day 33 and Day 47, respectively. a) shows widefield images of a representative zebrafish with the mCherry fluorescent vasculature and eGFP fluorescent tumour at selected time points, as indicated in the top left of each image. Doxycycline concentration is indicated on the left of each row. b) is the corresponding quantitative analysis plotting mean tumour area from all tumour burdened zebrafish throughout the study, for which n=4, and error bars represent the standard error of the mean (SEM). Bars indicate the doxycycline concentration used and when Tropic Marin® (T.M) was used in place of system water.

study without the need for invasive procedures such as chronic transparent window preparation. Therefore, CS-OPT provides advantages compared to other techniques frequently used such as 2-D imaging with widefield microscopy, surface imaging with confocal microscopy and the invasive nature of intravital imaging (Jain et al., 2002; Huisken and Stainier, 2009; Conway et al., 2014).

Quantitative analysis revealed the rate of angiogenesis and vascular growth for the lateral cutaneous artery was reducing during the 24 week study. It is important to note that there was greater detail and resolution of vasculature obtainable from the larvae fish at 2 wpf and 4 wpf, where primitive embryonic vessels could still be seen (Isogai et al., 2001). This is a result of both the organism physical features, such as size and transparency, and the use of a different, higher magnification imaging system. For these reasons these datasets were omitted from quantitative analysis of the lateral cutaneous artery. To minimise the noise sensitivity within the quantitative analysis filters were applied both before and after segmentation in MATLAB and before skeletonisation within Amira. However, this will not completely eliminate artefacts within the subsequent skeletons or quantifications. As I have previously discussed within Chapter 3, it is well known that the adult zebrafish is prone to light scatter, and therefore limits the depth of penetration achievable. Due to this physical constraint it is also likely that level of image noise would be greater towards the centre of the organism. Performing longitudinal studies of individual zebrafish would enable clarification between artefact and true signal within the reconstructions, as the noise should differ within repeated imaging sessions.

For CS-OPT to be accurately used within longitudinal studies it is crucial that the system is calibrated prior to use. This is to ensure that drift of the system does not influence subsequent quantifications when directly comparing individual organisms over time. There are two crucial operations involved in doing so, these are aligning the two imaging arms used within the multiplex system and registering them both with respect to each other. In order to do so an L-shaped bent needed positioned outside the axis of rotation is imaged by the system at 0° and 180°. The system is perfectly aligned if the mirror image of the 180° projection exactly overlaps that of the 0° projection. If perfect alignment cannot be achieved and an exact alignment is possible with a lateral translation only, then it is sufficient. Once the individual arms have been aligned the data from each can be combined and registered with respect to each other, which is currently a manual process performed by eye.

As previously mentioned CS-OPT imaging requires motionless specimens, otherwise reconstructions contain artefacts resulting in inaccurate or useless images (Kak and Slaney, 1988; Sharpe et al., 2002). Within the longitudinal study of vascular development movement was once again seen, with significant motion experienced in the 2 wpf imaging session. The zebrafish larvae experienced movement as a result of the imaging chambers rotational pull during acquisition. Previous 3-D imaging studies of small specimens, such as zebrafish embryos, have achieved immobilisation through embedding the specimens in low melt agarose (McGinty et al., 2011; Correia et al., 2015; Andrews et al., 2016). As I discussed within Section 4.4.1 the use of agarose or other materials to hold the fish within the imaging apparatus would require substantial research due to the increased complexity of the zebrafish larvae compared to the embryo. For example, gill function could be affected, which is essential for ionoregulation and oxygen uptake in zebrafish from 7 dpf (Rombough, 2002). Movement was also seen due to zebrafish responding to external stimuli, which was previously observed in Section 4.3.1. As defined in Table 1.1 deep anaesthesia results in no response to external stimuli, and despite initially reaching deep anaesthesia this is not maintained during imaging. This further highlights the need of an optimised anaesthetic regime for motionless 3-D imaging.

5.4.2 An optimised anaesthetic regime for motionless 3-D image acquisition

TraNac *Tg (KDR:mCherry:Fabp10-rtTA:TREeGFPKRAS^{V12})* zebrafish have been repeatedly anaesthetised using a combined dose of MS-222 and isoflurane to quickly reach and maintain a deep level of anaesthesia for extended periods of time. This overcomes the shortfalls encountered when using MS-222 alone for 3-D imaging of live, non-pigmented adult zebrafish.

It is known that using MS-222 alone for prolonged anaesthesia zebrafish are susceptible to both respiratory and cardiac failure (Sun et al., 2009; Matthews and Varga, 2012). It has previously been reported (Huang et al., 2010) that a combined dose of 65 ppm of both MS-222 and isoflurane in adult wild type zebrafish is optimal to improve the time under deep anaesthesia without impacting upon survival. The results presented here show that this dose was not sufficient to induce deep anaesthesia in either wild type zebrafish or in the TraNac *Tg (KDR:mCherry:Fabp10-rtTA:TREeGFPKRAS^{V12})* fish within 15 minutes. Using a combination of both MS-222 and isoflurane did improve

anaesthesia, however the minimal dose required for deep anaesthesia to be reached was 150 ppm of both MS-222 and isoflurane.

The combination of isoflurane with MS-222 improves the maintenance of deep anaesthesia within TraNac *Tg (KDR:mCherry:Fabp10-rtTA:TREeGFPKRAS^{V12})* zebrafish at doses higher than 170 ppm of each anaesthetic. This was determined through the response to an external stimulus greater than that experienced during CS-OPT image acquisition. Achieving this is an important advancement for imaging live zebrafish, whereby accurate images and quantifications are dependent upon completely motionless animals during acquisition. Furthermore, there was an increase in the time under deep anaesthesia before loss of opercula movement was observed, where the 175/175 ppm dose was optimal. The extended time under deep anaesthesia could open up additional avenues for imaging. Spatial and temporal readouts of protein activity have previously been achieved using Förster Resonance Energy Transfer (FRET) biosensors through Fluorescence Lifetime Imaging Microscopy (FLIM) OPT in zebrafish embryos (McGinty et al., 2011; Andrews et al., 2016). Providing a greater period of deep anaesthesia could enable FLIM OPT in live adult zebrafish, providing additional information in physiological and pathophysiological contexts. Importantly this anaesthetic regime can be repeated, and does not affect the viability of the adult zebrafish. Again a combined dose of 175/175 ppm of each anaesthetic was shown to be optimal, where it consistently achieved an average time under deep anaesthesia of greater than 10 minutes with little variation throughout. This highlights its potential use for longitudinal imaging studies.

It was also apparent that both TraNac and TraNac *Tg (KDR:mCherry:Fabp10-rtTA:TREeGFPKRAS^{V12})* fish require prolonged exposure to MS-222 to reach deep anaesthesia compared to Wild-Type (AB) zebrafish. This difference is not seen in Casper or other double transgenic fish suggesting a role for the *tra* gene in regulating the MS-222 response. The mutation present in the *tra* gene results in a truncated form of the mitochondrial protein mpv17, which leads to a reduction in iridophores, as discussed in Section 1.3.1. It has previously been proposed that the loss of mpv17 function could result in alterations in metabolism so it is possible that this could account for the differences in response to MS-222 (Krauss et al., 2013). It would be of great interest to further investigate this. The combined use of 175 ppm of both MS-222 and isoflurane reduces the time to reach deep anaesthesia and does not increase the recovery period when anaesthetising the TraNac and TraNac *Tg (KDR:mCherry:Fabp10-rtTA:TREeGFPKRAS^{V12})* fish. Therefore the zebrafish will experience less stress as a

result. However, it is important to note a difference in time to reach deep anaesthesia is still observed when compared to the wild-type (AB) fish. Due to differences between zebrafish lines there may be a need to perform additional adjustments to the 175/175 ppm anaesthetic regime. However, it is clear that using a combination of MS-222 and isoflurane is superior to the widely used 4.2% (168ppm) MS-222 regime.

Thus incorporating the combined anaesthetic dose of 175 ppm of both MS-222 and isoflurane can provide prolonged periods of deep anaesthesia required for 3-D imaging of adult non-pigmented zebrafish, without impacting upon recovery. Additionally, the ability to perform repeated treatments will significantly improve the accuracy and information achievable from imaging live adult zebrafish in longitudinal studies.

5.4.3 Investigating dose dependency within the tumour angiogenesis zebrafish model

For longitudinal studies of tumour progression and vascularisation using the tumour angiogenesis zebrafish model TraNac *Tg (KDR:mCherry:Fabp10-rtTA:TREeGFPKRAS^{V12})* it is important to understand the relationship between the inducer, doxycycline, and the tumour growth rate. This is especially the case for drug development studies, where optimal points of tumour progression should be identified for administering therapeutics. It would also be of benefit when planning mechanistic studies, where inducer concentration could be chosen to complement the predicted effect and provide sufficient time to observe differences. For example, if the study is hypothesised to increase tumour progression it may be desirable to reduce the rate for quantifications and comparisons to be drawn.

It is known that the hepatocellular carcinoma (HCC) model is dependent on the dose of doxycycline, whereby lower inducer concentrations reduce the frequency of tumour onset and the rate of progression (Nguyen et al., 2012). This has been seen within the performed longitudinal studies. A doxycycline concentration of 2 mg/L or lower was not adequate to induce tumour development within 14 dpi but with 5 mg/L doxycycline tumours were visible as early as 4 dpi in some individuals and in all by 9 dpi.

Prior to this longitudinal study it was unknown whether age affected tumour progression and initiation. It appears that older zebrafish have a reduced incidence of tumour growth, a delayed onset and a reduced growth rate compared to the younger fish. It is possible that the transgene is not being expressed as highly within older organisms or defensive protective mechanisms are involved. Further investigation would be required

to understand the cause of this observed reduction in tumorigenesis. However, it is clear that the model organism age should be considered within future studies.

Within this study continued treatment of doxycycline surprisingly caused tumour regression, even with a dose escalation up to the previously used concentration of 10 mg/L. It became clear that this is a result of using system water, as the use of Tropic Marin® Sea Salts dissolved in deionised water resulted in tumour growth when the doxycycline concentration was not altered from 10 mg/L. The pH of the two water types was not significantly different and system water (as described in Section 2.1.1) is also made from Tropic Marin® Sea Salts. Therefore it can be speculated that doxycycline degradation is caused by an additional component within the circulating system water, such as zebrafish waste products, pheromones or microorganisms. Future experiments using the TraNac *Tg (KDR:mCherry:Fabp10-rtTA:TREeGFPKRAS^{V12})* zebrafish model will use Tropic Marin® water. Consequently, optimisation is still required prior to initiating longitudinal studies as this longitudinal study of doxycycline dose was not performed within Tropic Marin® water.

The degradation of doxycycline has highlighted an important issue regarding compound stability. For future drug development studies the therapeutic stability within the zebrafish water would need to be determined, as if the therapeutic was degraded it could significantly impact upon efficacy.

CHAPTER 6

Mechanistic Studies of Tumour Progression and Vascularisation

6.1 Introduction

As shown within Chapter 4 the developed CS-OPT imaging modality is capable of whole organism, quantitative imaging of tumour progression and vascularisation using the TraNac *Tg (KDR:mCherry:Fabp10-rtTA:TREeGFPKRAS^{V12})* zebrafish model (as described in Section 1.3.2.2). Coupled with its ability for longitudinal imaging, as shown in Chapter 5, CS-OPT can be a powerful platform for researching key proteins and biological interactions of interest through mechanistic studies.

The tumours within the TraNac *Tg (KDR:mCherry:Fabp10-rtTA:TREeGFPKRAS^{V12})* zebrafish model are driven through an overexpression of oncogenic kras^{V12} and recapitulate human hepatocellular carcinoma (HCC) (Nguyen et al., 2011). However, this kras^{V12} driven model only achieves local metastasis. p53 is a tumour suppressor (seen in Figure 1.3) found frequently mutated or deleted in many cancers including HCC and it has been shown that its absence is critical for metastasis in a HCC mouse model (Lewis et al., 2005). It was recently shown that the metastatic potential was not increased when the zebrafish tumour model lacked functional p53, but there was an increase in tumour onset (Nguyen et al., 2011). As previously described (Section 1.2.2) several studies have shown that an increase in activity of the Ras pathway coupled with a decrease in PTEN expression results in more aggressive and metastatic tumours (Dankort et al., 2009; Nogueira et al., 2010; Wang et al., 2012). Furthermore, PTEN is highly mutated and deleted within human HCC, where a reduced PTEN expression correlates with the progression of the disease and an increase in metastasis (Dong-Dong et al., 2003; Hu et al., 2003). Therefore, it is of interest to determine whether a reduced PTEN expression within the zebrafish would increase the metastatic potential of the tumours and as a result better reflect the human pathology.

Due to the well known gene duplication events that commonly occur in the ze-

brafish genome there are two homologs to human PTEN within the zebrafish (Taylor et al., 2003). These are *ptena* on Chromosome 17 and *ptenb* on Chromosome 12. Both are highly similar to the human form and contain a N-terminal phosphatase domain and a C2 domain that targets the protein to the cell membrane (Faucherre et al., 2008). These lipid phosphatases are essential for development, as double knockouts of both ptena and ptenb ($ptena^{-/-}$ $ptenb^{-/-}$) are lethal (Faucherre et al., 2008). They exhibit hypervascularisation and enhanced angiogenesis throughout the zebrafish, as well as a significantly increased level of the zebrafish homolog for VEGF, vegfaa (Faucherre et al., 2008; Choorapoikayil et al., 2013). Haploinsufficient zebrafish, $ptena^{+/-}$ $ptenb^{-/-}$ or $ptena^{-/-}$ $ptenb^{+/-}$, develop normally but are prone to hemangiosarcomas with an increased vegfaa expression in the vascularised tissue connected to the eye bulb (Choorapoikayil et al., 2013). Also, Faucherre et al. (2008) reported that after 18 months $ptenb^{-/-}$ zebrafish had a 33% incidence rate of spontaneous eye tumours with an increased Akt phosphorylation, despite functional ptena expression. Tumours were not observed in WT or $ptena^{-/-}$ zebrafish.

It is of importance to understand the downstream signalling pathways required for tumour progression. Many groups, including our lab, have previously shown an important role for the protein p130Cas within tumorigenesis (Barrett et al., 2013). p130Cas is an adapter protein known to associate with multiple proteins through its phosphorylation sites and various interaction domains. These include a Src-homology 3 (SH3) domain, substrate domain and C-terminal domain, as shown within Figure 6.1. It is triggered through numerous receptor tyrosine kinases (RTKs) increasing p130Cas tyrosine phosphorylation, which is mediated by Src kinase. This results in the formation of signalling complexes that are required for several key cellular functions including cell cycle progression, cell survival, migration and invasion, Figure 6.1 (Barrett et al., 2013).

Deregulation and overexpression of p130Cas is found in many cancers, where its presence is often correlated with the advancement of the disease (Barrett et al., 2013). This is true of HCC, where greater p130Cas expressing tumours have reduced expression of adhesion molecules, increased metastasis and worse prognosis (Guo et al., 2008). Silencing p130Cas expression has found to block tumour growth and progression in lung, breast and ovarian cancer (Cabodi et al., 2010; Nick et al., 2011). Therefore it is a potential therapeutic target. p130Cas is also involved in endothelial cell migration and proliferation, whereby the pro angiogenic factor VEGF is known to induce its phosphorylation (Barrett et al., 2013). Its loss of function during development is lethal

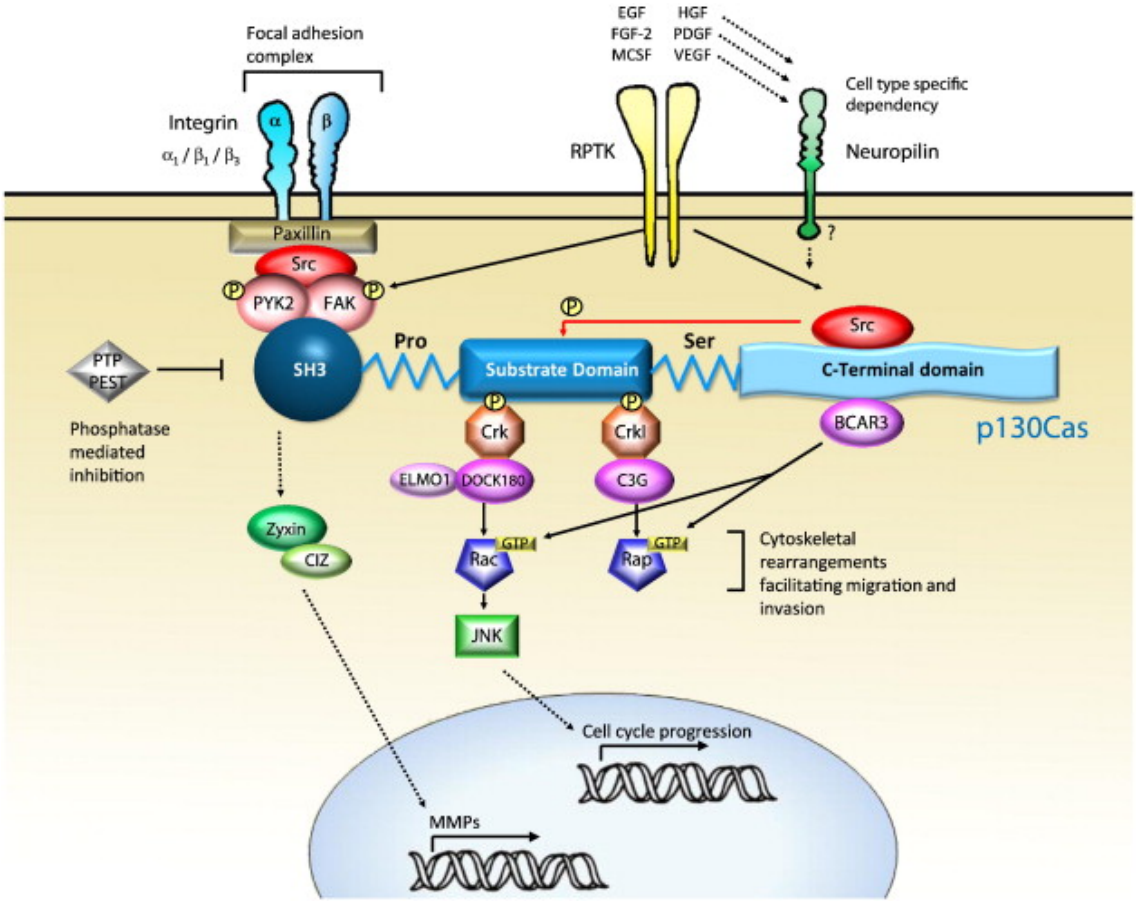

Figure 6.1: The structure and signalling pathways of adapter protein p130Cas. The protein consists of a N-terminal SH3 domain, a proline-rich domain, a substrate domain, a serine-rich domain and a C-terminal domain. Upstream regulation occurs through receptor tyrosine kinase phosphorylation mediated through Src kinase, indicated by the yellow 'P' symbols on the protein. Signalling complexes can then be formed that drive cell cycle progression, invasion, migration and survival. Figure from Barrett et al. (2013).

within mice, where the embryos have an underdeveloped cardiovascular system with dilated blood vessels and impaired integrity (Honda et al., 1998). This supports its critical role for developmental angiogenesis. However, the role of the zebrafish homolog *bcar1* has yet to be determined within tumour progression or angiogenesis.

For these reasons mechanistic studies relating to *ptena, ptenb* and *bcar1* are of interest within the tumour angiogenesis zebrafish model TraNac *Tg (KDR:mCherry:Fabp10-rtTA:TREeGFPKRAS^{V12})*. A non-functional mutant of *ptenb* was available from the Zebrafish International Resource Center (ZIRC) (`zebrafish.org`). This mutant, *ptenb^{hu1435}* henceforth referred to as *ptenb^{-}*, was created by Faucherre et al. (2008) and has a single point mutation from C to A within exon 3 that translates to a premature stop codon at position 65. This subsequently produces a non-functional protein as it is truncated before the catalytic site of the phosphatase domain, Figure 6.2. There were no *bcar1* or *ptena* non-functional mutants available at the start of the project. However the genome editing techniques transcription activator-like effector nucleases (TALENs) and clustered regularly interspaced short palindromic repeats (CRISPRs), as described in Section 1.3.3, could be used.

Due to the embryonic lethality of *ptena$^{-/-}$ ptenb$^{-/-}$* zebrafish an inducible knock out would be advantageous to produce a complete loss of ptena and ptenb within the adult tumour burdened zebrafish. TALENs and CRISPRs have recently been used for targeted knock-in gene editing, as described within Section 1.3.3 (Bedell et al., 2012; Chang et al., 2013; Auer and Del Bene, 2014). Therefore it is possible that genes of interest can be genetically modified through the insertion of LoxP sites within intronic regions surrounding a key exon of interest. The resulting mutant gene will produce a functional protein until Cre recombinase is present, causing a recombination event that removes the entire crucial exon, resulting in a loss of function mutation.

Within this Chapter I have performed a preliminary longitudinal mechanistic study of the available *ptenb^{-}* mutant within the TraNac *Tg (KDR:mCherry:Fabp10-rtTA:TREeGFPKRAS^{V12})* zebrafish line using widefield microscopy. I also describe efforts towards creating ptena and bcar1 non-functional mutant lines as well as a ptena inducible knock out line that could subsequently be used in combination with the *ptenb^{-}* mutant. Development of these mutant lines will lead to using the CS-OPT imaging platform for mechanistic studies to provide novel insights into tumour progression and vascularisation through longitudinal, 3-D quantifications.

6.2 Experimental Summary

To verify zebrafish genotype DNA extraction was performed using the methods stated in Section 2.1.8 and DNA amplification was performed through polymerase chain reactions (PCRs) as described in Section 2.2.3 with the primers and conditions listed in Table 2.1. When fluorescent screening was not possible (as described in Section 2.1.6) presence of the eGFPKRAS^{V12} transgene was determined through amplicon detection by gel electrophoresis, Section 2.2.4. The forward primer for the eGFPKRAS^{V12} transgene lies within the eGFP region of the construct and the reverse within the zebrafish KRAS^{V12} sequence. Therefore, PCR reactions will only amplify the transgenic DNA, and not the wild type zebrafish RAS within the fish. Sanger sequencing, deep sequencing or high resolution melting analysis (HRMA) was performed using the primers stated in Tables 2.3 and 2.4 and the Poly Peak Parser software was used to identify specific insertions or deletions (indels), all described within Section 2.4. Unless otherwise stated, 3 uninjected controls and 22 injected samples were used for each HRMA. The ptenb loss of function mutant genotype was identified from the sequencing chromatograms, as shown in Figure 6.3.

For longitudinal mechanistic studies of ptenb the zebrafish line TraNac:ptenb *Tg (KDR:mCherry:Fabp10-rtTA:TREeGFPKRAS^{V12})* was generated and genotyped. The zebrafish used were 174 days post fertilisation (dpf) and for each genotype examined n=8. The inducer concentration at the start of the study was 5 mg/L of doxycycline, which was added directly to system water from UCL fish facility. Fish were kept in isolation, where they were fed and subsequently given fresh doxycycline water every other day. Imaging of tumour progression was performed twice a week using the widefield fluorescence microscope described in Section 2.7. At the end of the study the zebrafish were euthanised with an overdose of anaesthesia resulting in medullary collapse (Table 1.1). Fin clips were taken for genotyping and the tumours were dissected and either fixed in 10% formalin (Fischer Scientific, P/0840/53) or were snap frozen in liquid nitrogen for subsequent protein or RNA analysis.

In an attempt to create new loss of function and inducible knock-out mutants the gene editing tools TALENs and CRISPRs were designed and created as described in Section 2.3. All TALEN arms were microinjected into single cell embryos at 300 ng/μl and CRISPR gRNAs at 70 ng/μl with 150 ng/μl of Cas9 nuclease. The concept for producing an inducible knockout was devised by Leo Valdivia Alvarez (Wilson

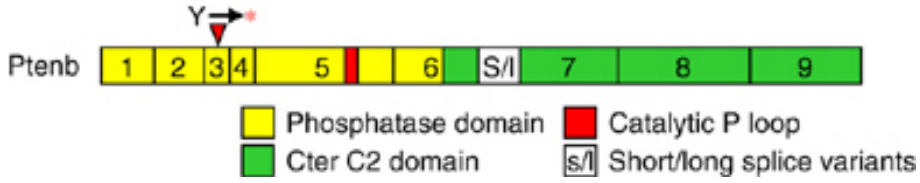

Figure 6.2: Schematic of the *ptenb*$^{-}$ mutant created by Faucherre et al. (2008), showing the structural domains, exon organisation and site of the point mutation within exon 3, where tyrosine 65 (Y) changes to a stop codon (*) before the catalytic P loop. Figure from Faucherre et al. (2008).

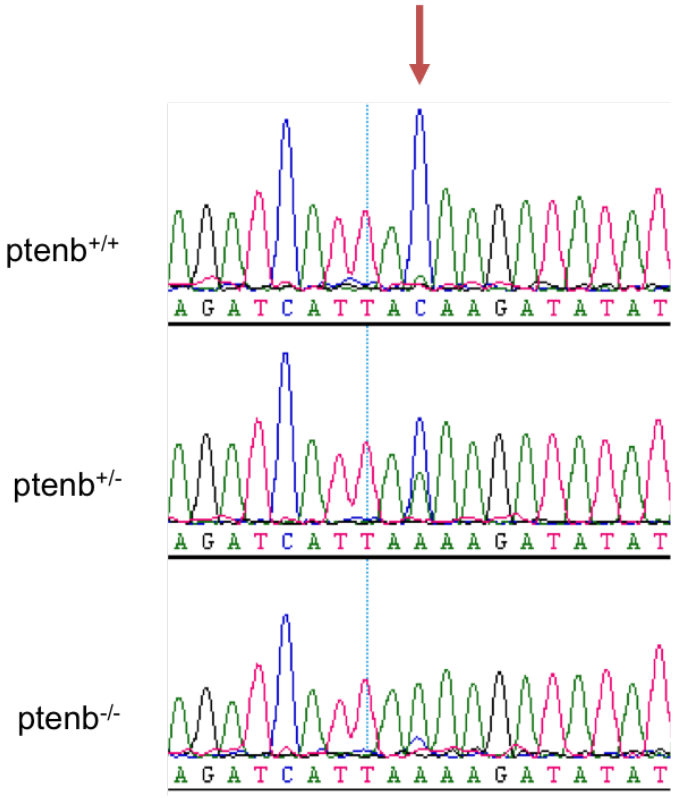

Figure 6.3: Sequencing chromatograms of the different ptenb^{-} genotypes. Figure shows the wild type ptenb (ptenb$^{+/+}$), the heterozygous(ptenb$^{+/-}$) and the homozygous (ptenb$^{-/-}$) loss of function mutant. The red arrow indicates the position of the C>A point mutation in the non-functional mutant gene.

Group, UCL). The approach used either TALENs or CRISPRs to target intronic regions surrounding a key exon of interest, rather than the conventional exonic regions. The aim was then to incorporate LoxP sites in a head to tail orientation through homology directed repair (HDR) of the TALEN or CRISPR mediated double strand break (DSB). This would occur by co-injecting synthetic DNA containing a modified LoxP (mLoxP) site, shown to function in zebrafish by (Hans et al., 2009), surrounded by complementary sequence to the DSB site, Figure 6.4. For TALEN mediated insertion the synthetic DNA is a single stranded oligonucleotide that corresponds to that published by Bedell et al. (2012). This oligonucleotide has 27 bases of sequence homology to the TALEN left arm recognition sequence and the start of the spacer region, the mLoxP sequence, and then 27 bases of homology to DNA 10bp downstream from the TALEN right arm recognition site. The TALEN specific synthetic DNA is microinjected at a concentration of 50 ng/μl. For CRISPR mediated insertion the synthetic DNA is based upon the design by Chang et al. (2013), where insertion of the mLoxP sequence is targeted to 3bp from the end of the gRNA target site. The synthetic DNA has the mLoxP sequence surrounded by 25bp of sequence homology upstream and 20bp homology downstream of the target region and is microinjected at 75 ng/μl.

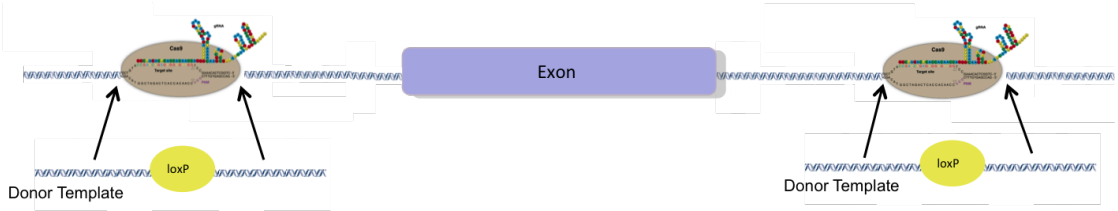

Figure 6.4: The novel genome editing approach using TALENs or CRISPRs to create inducible knockout zebrafish models. TALENs and CRISPRs are targeted to intronic regions surrounding a key exon. Upon eliciting a DSB the aim is to incorporate a mLoxP site through homology directed repair. Synthetic DNA containing a mLoxP site surrounded by donor templates of complementary sequence to the TALEN or CRISPR target site is coinjected with TALENs or CRISPRs. Includes figures from Auer and Del Bene (2014).

6.3 Results

6.3.1 Studying the ptenb loss of function mutant

6.3.1.1 Generating the line

The ptenb loss of function line was imported from ZIRC and fish were genotyped when they reached adulthood to identify heterozygotes, ptenb$^{+/-}$. These were subsequently bred with the tumour angiogenesis line, TraNac *Tg(KDR: mCherry:Fabp10-rtTA: TRE-eGFPKRAS^{V12})*. Embryos were selected for KDR:mCherry and eGFPKRAS^{V12} transgenes and for ptenb$^{+/-}$ once they reached adulthood. The identified zebrafish were heterozygous for all of the following genes and trangenes; *transparent, nacre, KDR:mCherry, eGFPKRAS^{V12}* and the *ptenb* loss of function mutant. Therefore, these were incrossed, and selected for fluorescence once more. When this generation reached adulthood the zebrafish had one of four pigmentation phenotypes due to different *tra* and *nacre* genotypes. They were either wild type, lacking melanocytes, lacking iridophores or lacking both, the TraNac phenotype, as shown within Figures 1.4 and 1.5. To generate a transparent line the TraNac phenotype fish with either the ptenb$^{+/-}$ or ptenb$^{-/-}$ genotype were incrossed and the clutch of embryos screened for fluorescence again. The resulting adult fish were transparent with a mCherry labelled vasculature, an inducible, liver specific cancer tagged with eGFP and had different ptenb genotypes. From this generation the ptenb$^{+/-}$ and ptenb$^{-/-}$ genotyped zebrafish were incrossed and once again the embryos were selected for fluorescence. The identified ptenb$^{+/-}$ zebrafish from this generation, which were confirmed to be homozygous for KDRmCherry and eGFPKRAS^{V12}, became the established line TraNac:ptenb$^{+/-}$*Tg(KDR: mCherry:Fabp10-rtTA:TRE-eGFPKRAS^{V12})*. Incrosses of this line provided ptenb$^{+/+}$, ptenb$^{+/-}$ and ptenb$^{-/-}$ zebrafish for studies of ptenb function within tumour progression.

6.3.1.2 Longitudinal mechanistic study of ptenb during tumorigenesis

An initial widefield fluorescence study of ptenb within tumour progression was performed prior to CS-OPT studies using the TraNac:ptenb:*Tg(KDR:mCherry:Fabp10-rtTA:TRE-eGFPKRAS^{V12})* zebrafish. Homozygous and heterozygous ptenb mutant zebrafish were used alongside a ptenb wild type (ptenb$^{+/+}$) control. All zebrafish used were genotyped offspring of the aforementioned established line with the ptenb$^{+/-}$ genotype.

The study began using an inducer concentration of 5 mg/L. After 4 days post induction (dpi) tumours were visible within the ptenb$^{+/-}$ and ptenb$^{+/+}$ zebrafish, which

had increased by 8 dpi, Figure 6.5. Conversely, no tumours were seen in any of the 8 ptenb$^{-/-}$ zebrafish, Figure 6.5. Due to this unexpected finding the inducer concentration was raised to 7.5 mg/L for all of the groups, in an attempt to see tumour onset within the ptenb$^{-/-}$ zebrafish. The ptenb$^{+/-}$ and ptenb$^{+/+}$ tumours continued to progress and increase in size. Not until 18 dpi were tumours observed within ptenb$^{-/-}$ group and this was only in 25% of the zebrafish, Figure 6.5b. Therefore, there was a significant delay ($p<0.01$) in tumour onset and progression when zebrafish had no functional copies of ptenb.

Metastasis was not observed in any of the zebrafish. However, non-functional ptenb heterozygous expression had a contrasting effect to the homozygous loss of function phenotype, where a trend towards greater tumour progression compared to wild type was seen, Figure 6.5. It is important to note that the ptenb$^{+/-}$ zebrafish with the largest tumour at 15 dpi, 57.03 mm^2, died prior to imaging on 18 dpi. Therefore, it is likely that the quantifications for 18 dpi are negatively skewed in comparison to other time points, but despite this the trend was still apparent. The next largest tumour within the ptenb$^{+/-}$ group died at 19 dpi, where the last recorded tumour area at 18 dpi was 131.84 mm^2. No wild type controls were this heavily tumour burdened, the largest being 53.14 mm^2, and 100% of the group survived. This again indicates the increased tumour progression experienced within the heterozygous group. As a result of losing the two largest samples within one group the study was terminated and the zebrafish were sacrificed for further studies to understand the underlying phenomena.

Due to the striking ptenb$^{-/-}$ phenotype it was important to confirm the genotype of these zebrafish, with respect to both ptenb and eGFPKRAS^{V12}. Sequencing verified all eight of the zebrafish were homozygous for the ptenb non-functional mutant and PCR proved the eGFPKRAS^{V12} transgene was also present within all fish, Figure A.6. Therefore, the genotype was verified and did not contribute to this unexpected result.

6.3.2 Creating a ptena loss of function mutant

The zebrafish *ptena* gene was studied to determine the gRNA target site for disrupting gene function through CRISPR mediated gene editing. Exon 2 was chosen as it is the first exon present within all splicing variants, excluding the polymerase binding site, and it is upstream of the catalytic site of the phosphatase domain. This target is also in line with the non-functional ptena mutant reported by Faucherre et al. (2008). Two gRNA's were designed to target this exon as shown in Table 6.1.

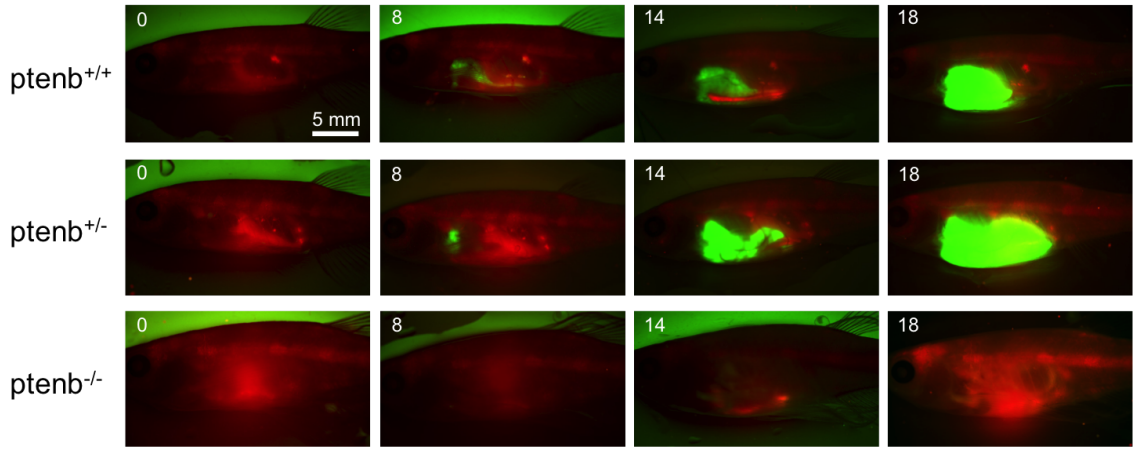

(a)

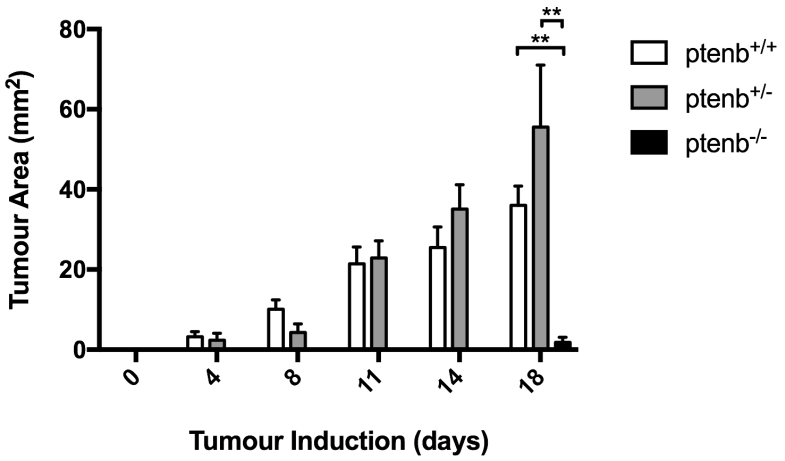

(b)

Figure 6.5: Longitudinal mechanistic study of ptenb during tumorigenesis using TraNac:ptenb *Tg (KDR:mCherry:Fabp10-rtTA:TRE- eGFPKRAS^{V12})* zebrafish, where homozygous (ptenb$^{-/-}$) and heterozygous (ptenb$^{+/-}$) expression of the non-functional ptenb mutant zebrafish were studied alongside a ptenb wild type control (ptenb$^{+/+}$). Zebrafish (174 dpf) were initially induced with 5 mg/L of doxycycline, which was raised to 7.5 mg/L after imaging on day 8. a) shows widefield images for a representative zebrafish with an eGFP labelled tumour and an mCherry labelled vasculature from each group at selected time points, indicated in the top left of each image. b) is the corresponding quantitative analysis of tumour area for all fish within the study (n $\geq$ 7). The graph plots the mean tumour area and error bars represent the standard error of the mean (SEM). **p<0.01 when using the Kruskal-Wallis test.

gRNA	gRNA Sequence ($5' \rightarrow 3'$)	Strand	HRMA Primers
ptena-1	AAGGCAGGCAAAGGTCG-CAC	Coding	ptena Forward 1 & Reverse 1
ptena-2	TCTGCGAGGATCTCGACCAG	Coding	ptena Forward 2 & Reverse 2

Table 6.1: Designed CRISPR gRNAs for zebrafish *ptena* exon 2. Information includes the gRNA DNA sequence, the strand of DNA being targeted and the primers (described in Table 2.4) used for testing for CRISPR function through High Resolution Melt Analysis (HRMA).

Initially oligonucleotides were designed as described in Gagnon et al. (2014) to create the gRNA. Therefore the forward oligonucleotide template was ATTTAGGTGACACTATA-N_{20}- GTTTTAGAGCTAGAAATAGCAAG, where the N_{20} corresponded to the gRNA sequence shown in Table 6.1. In all cases the dsDNA was successfully created, however subsequent transcription reactions failed to produce any RNA in contrast to successful positive controls. Upon further research it was discovered that the T7 RNA polymerase promoter stated and used by Gagnon et al. (2014) was 3 bases (AGG) shorter than recommended elsewhere. The forward oligonucleotide template was modified to include the additional 3 bases, ATTTAGGTGACACTATAAGG-N_{20}- GTTTTAGAGCTA-GAAATAGCAAG. This alteration rectified the encountered problem and transcriptions yielded approximately 9 μg of each gRNA.

Unfortunately neither of the ptena exon 2 gRNAs introduced indels within the targeted DNA region, as shown by the clean melting peaks within Figure A.7.

6.3.3 Creating an inducible knockout of ptena

6.3.3.1 Determining the target region of *ptena*

Due to possessing ptenb$^-$ zebrafish an inducible knock out of the zebrafish *ptena* gene would be attempted, which could be used upon the ptenb deficient background. Once again exon 2 was chosen for the aforementioned reasons.

It was essential to verify the DNA sequence of the intronic regions surrounding exon 2, to ensure the gene editing tools targeted a region with no single nucleotide polymorphisms (SNPs) that could affect the efficiency. Fin clips from 10 zebrafish were amplified and sequenced using primers ptena-LHS and ptena-RHS from Table 2.1.

6.3.3.2 Using TALENs to produce a ptena inducible knockout

Based upon the confirmed intronic sequence a TALEN pair was designed for each side of *ptena* exon 2, termed ptenaL and ptenaR, where each TALEN arm is referred to as either left or right. This is shown in Table 6.2, where the left and right arm binding sites, TALE repeat sequences and corresponding HRMA primers are presented. Full DNA sequences of each TALE subunit are available in Supplementary Table 1 of Reyon et al. (2012).

A low efficiency was observed when analysing TALEN construction through colony PCR. Gel electrophoresis revealed DNA bands that were clearly a variation of distinct sizes ranging from 0.5 to 2.1kb, Figure A.8. This indicated that the serial ligation reactions involved in the FLASH high throughput assembly of the TALEN had only been successful in a subset of reactions within each repetition. Therefore, the likelihood of a positive colony being produced was reduced. However, two possible candidates were identified for ptenaL-right and one for ptenaL-left, as indicated by the asterisks in Figure A.8. Sequencing confirmed these colonies were positive, therefore establishing a TALEN pair for ptenaL. It is important to note that for both identified TALEN arms over 100 colonies were screened for two attempts using the FLASH protocol. A positive colony for ptenaR-left of ptenaR-right during the two FLASH attempts could not be identified. To prevent wasting additional time and resources the construction of the designed ptenaR TALEN was outsourced to Genetic Service, Inc (Boston, USA). Interestingly, they encountered similar problems and were never able to create the TALEN.

The ptenaL TALEN created was verified through microinjection followed by HRMA using the tested primers stated within Table 6.2, Figure 6.6. The uninjected controls in Figure 6.6a show clean, single peak melt curves compared to the TALEN injections in Figure 6.6b, which have a shifted, noisy left tail. As a result it can be concluded that the ptenaL TALEN is functioning to elicit a DSB and indels are occurring during the DNA repair process as desired.

To test whether the TALEN mediated knock-in strategy would work synthetic single stranded DNA (ssDNA) containing the mLoxP site was designed and created for the ptenaL TALEN, as shown Figure 6.7. Co-injection of the TALEN and synthetic DNA was attempted on 3 occasions but LoxP insertion was never observed when genotyping with deep sequencing.

TALEN	DNA Target Sequence (5' → 3')	TALE repeats left arm	TALE repeats right arm	HRMA Primers
ptenaL	TTTTGCTTAATGTTAACC TGGTGTACAGTGCACA TTAAAGAAAAAGATCATA	TAL/010/015/020/024/ 027/015/020/021/ 026/015/019/025/ 030/011/016/022	TAL/010/011/016/021 /029/011/016/021/ 026/011/019/021/ 030/012/016/025	ptena-L Forward 1 & Reverse 1
ptenaR	TGTTTTAATGGATTACAC ATGTTTGAACTAGTATT TGTCCAATACCACACAGC	TAL/009/015/020/025/ 030/011/016/025/ 029/014/016/025/ 030/011/017/021	TAL/009/015/017/022/ 026/011/020/021/ 027/012/016/022/ 026/012/016/024	ptena-R Forward 1 & Reverse 1

Table 6.2: Designed TALENs to target and cleave either side of *ptena* exon 2. The TALEN DNA target sequence is shown in the following order; left arm, spacer region (underlined), right arm. Also presented are the TALE repeats for each arm, for DNA sequences of TALE repeats see Supplementary Table 1 of Reyon et al. (2012), and primers (described in Table 2.4) used for testing for TALEN function through High Resolution Melt Analysis (HRMA).

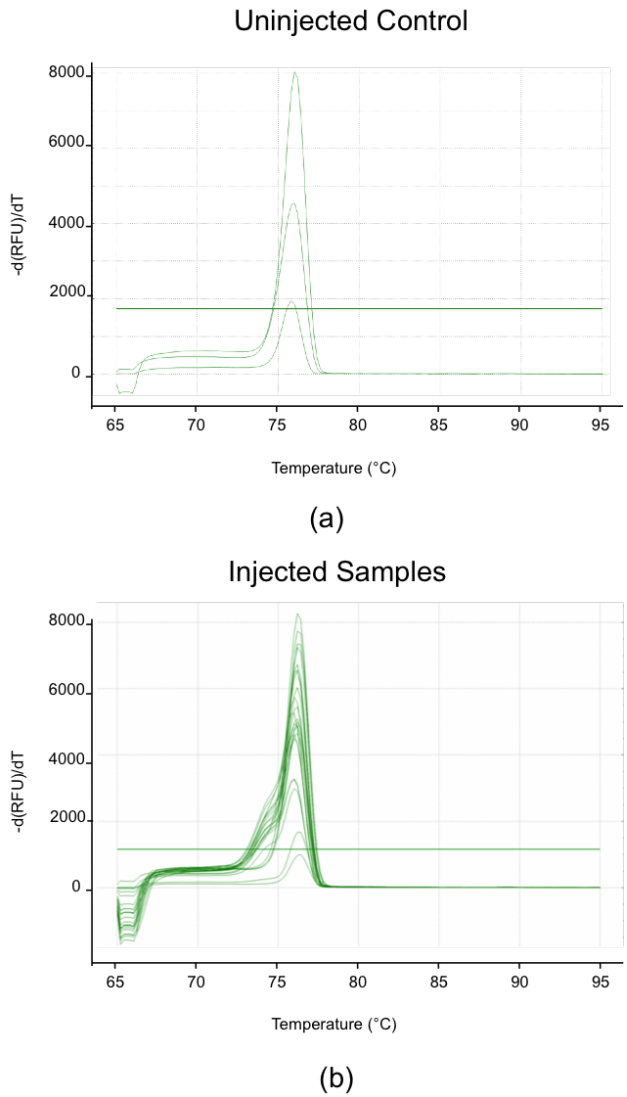

Figure 6.6: HRMA validating the functional activity of TALEN ptenaL using primers ptena-L Forward 1 and Reverse 1. Single cell embyros were injected with 300 ng/μl of both ptenaL-left and ptenaL-right TALEN arms. (a) shows the uninjected controls and (b) the TALEN injected samples.

TTTATTTTGCTTAATGTTAACCTGGTGATAACTTCGTATAATGTATGCTATACGAAGTTATCAGACATATACCCTAACATCATTGCCA

Figure 6.7: Synthetic single stranded DNA designed and created for TALEN ptenaL (described in Table 6.2) containing the mLoxP sequence. The synthetic DNA contains 27 bases of sequence homology, blue, surrounding the mLoxP sequence, red.

6.3.3.3 Using CRISPRs to produce a ptena inducible knockout

Initially four possible CRISPRs were designed and constructed for the right hand side of *ptena* exon 2 and only two for the left, due to already possessing a functioning gene editing tool for that side. The details of these are shown in Table 6.3. Their function was analysed by microinjection and HRMA using the tested primers stated within Table 6.3. HRMA of each of the six CRISPRs produced clean, single peaks that mimicked the uninjected controls and therefore they had failed to function and elicit gene editing, Figure A.9.

Due to having no success 8 further gRNAs were designed and created, 2 of which were for ptenaL and 6 for ptenaR, Table 6.4. Once again there was a greater effort towards creating a functional CRISPR for the right hand side of *ptena* exon 2. For ptenaR intronic regions further downstream than previous attempts were targeted incase an unknown factor, such as secondary structure, was inhibiting CRISPR function. Synthetic DNA fragments containing the mLoxP sequence to be inserted by HDR at each gRNA target site were also designed, Figure 6.8. Therefore these could be co-injected with the gRNA and Cas9, enabling both verification of CRISPR function and mLoxP site insertion simultaneously through deep sequencing.

gRNA	**Sequences 5' → 3'**	Strand	**HRMA Primers**
ptenaL-1	ACAATGCTACTGGCTAGAGC	Non-coding	ptena-L Forward 2 & Reverse 2
ptenaL-2	GTGCACAGAAAGTAAGGTCC	Coding	ptena-L Forward 3 & Reverse 3
ptenaR-1	TCGTCATTCTATTTTCAAAC	Coding	ptena-R Forward 2 & Reverse 2
ptenaR-2	TAGTATTGTGTATCGACGAT	Coding	ptena-R Forward 3 & Reverse 3
ptenaR-3	ATCGTCTTTAAAATCGTCAC	Non-coding	ptena-R Forward 3 & Reverse 3
ptenaR-4	GAAAAAAAGGACTGGGTGTA	Coding	ptena-R Forward 4 & Reverse 4

Table 6.3: Designed CRISPR gRNAs to target and cleave either side of zebrafish *ptena* exon 2. Information includes the gRNA DNA sequence, the strand of DNA being targeted and the primers (described in Table 2.4) used for testing for CRISPR function through High Resolution Melt Analysis (HRMA).

gRNA	Sequences 5' → 3'	Strand	MiSeq Primers
ptenaL-3	CCCCGGTTGATTACTC AAATT	Coding	ptena-L MiSeq Forward 2 & Reverse 2
ptenaL-4	CCCAAATTTGAGTAAT CAA	Non-coding	ptena-L MiSeq Forward 2 & Reverse 2
ptenaR-5	ACATGACTGTTTCTAT GCGGTGG	Non-coding	ptena-R MiSeq Forward 1 & Reverse 1
ptenaR-6	ACTGTTTCTATGCGGT GGCGCGG	Non-coding	ptena-R MiSeq Forward 1 & Reverse 1
ptenaR-7	CTATGCGGTGGCGCGG CTTCAGG	Non-coding	ptena-R MiSeq Forward 1 & Reverse 1
ptenaR-8	CGCATTAAGGTCCAAA CAGGAGG	Non-coding	ptena-R MiSeq Forward 2 & Reverse 2
ptenaR-9	ATTAAGGTCCAAACA GGAGGCGG	Non-coding	ptena-R MiSeq Forward 2 & Reverse 2
ptenaR-10	TCCTCCATCCGCCTCC TGTTTGG	Coding	ptena-R MiSeq Forward 2 & Reverse 2

Table 6.4: Additional designed CRISPR gRNAs to target and cleave either side of zebrafish *ptena* exon 2. Information includes the gRNA DNA sequence, the strand of DNA being targeted and the primers (described in Table 2.3) used for testing for CRISPR function through deep sequencing with MiSeq.

Figure 6.8: Synthetic single stranded DNA containing the mLoxP sequence for each additional CRISPR described in Table 6.4. Each piece of DNA contains 25 bases of sequence homology upstream and 20 bases downstream, blue, of the mLoxP sequence, red. The mLoxP sequence is designed to insert 3bp from the end of the gRNA target site, which is underlined in each case.

Deep sequencing revealed that all of the designed CRISPRs had failed to elicit a DSB and therefore neither indels or the mLoxP site were incorporated, Figure A.10. Unfortunately there was inadequate time to pursue this project further.

6.3.4 Creating a bcar1 loss of function mutant

6.3.4.1 Using CRISPRs for *bcar1* gene editing

The zebrafish *bcar1* gene was studied to determine the target site for gene disruption. There are two splicing variants within zebrafish and exon 1, which consists of only 4 amino acids, differs. Both variants have exon 2 and so this was targeted. Two CRISPRs were designed and created as shown in Table 6.5. The HRMA of injected samples clearly showed bcar1-1 failed to produce indels within the target sequence due to single, clean peaks mimicking the uninjected controls being produced, Figure 6.9. However, the bcar1-2 melt peak has a slightly disrupted left tail where a few small double peaks were observed, Figure 6.9c. This HRMA was promising, but not conclusive.

PCR amplification was performed on the bcar1-2 injections followed by Sanger sequencing, using the bcar1 primers within Table 2.1, to determine whether insertions and deletions were occurring. Sequencing was performed with the reverse primer, Table 2.1, due to having greater quality and reliability. Therefore, if indels had occurred at the gRNA target site there would be a single clean sequence downstream of this point and several sequences overlapping, with a shorter peak height, upstream. This was the case, as shown in Figure A.11, where 3bp from the end of the gRNA target site there is a change from a single sequence to multiple. Therefore bcar1-2 has successfully elicited a DSB and subsequently indels had been incorporated through DNA repair.

gRNA	gRNA Sequence ($5' \rightarrow 3'$)	Strand	HRMA Primers
bcar1-1	GCCGGCCATGCAGC-GAACAGAGCC	Non-coding	bcar1 Forward 2 & Reverse 2
bcar1-2	GTGCTGGAGCGGGA-CACGCA	Coding	bcar1 Forward 2 & Reverse 2

Table 6.5: Designed CRISPR gRNAs for zebrafish *bcar1* exon 2. Information includes the gRNA DNA sequence, the strand of DNA being targeted and the primers (described in Table 2.4) used for testing for CRISPR function through High Resolution Melt Analysis (HRMA).

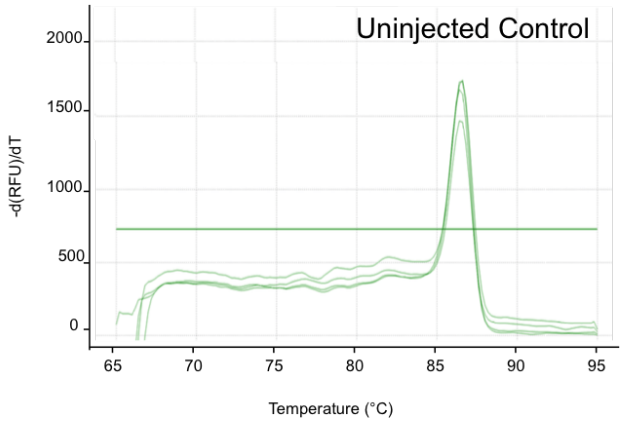

(a)

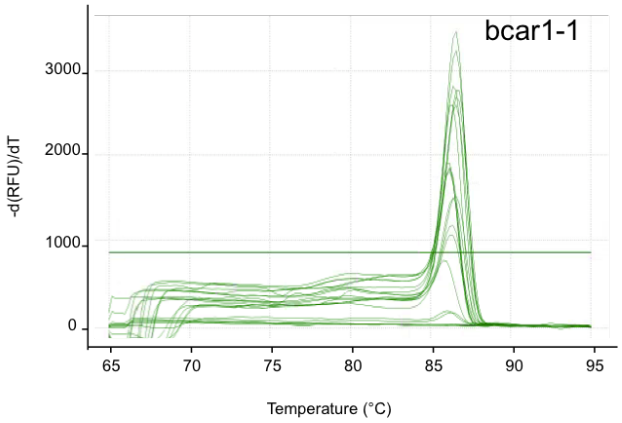

(b)

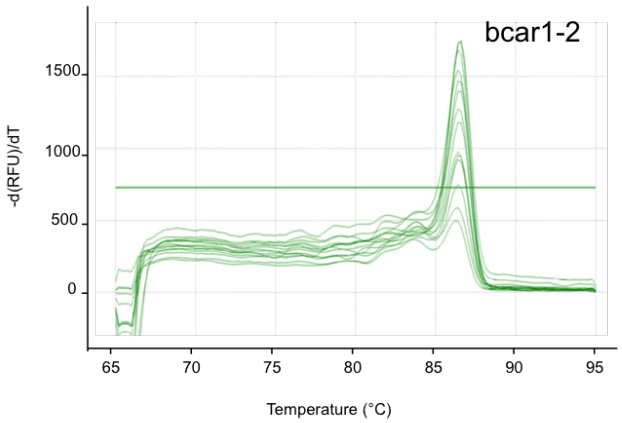

(c)

Figure 6.9: HRMA validating the functional activity of the bcar1 CRISPRs using primers bcar1 Forward 1 and Reverse 1. Single cell embyros were injected with 70 ng/μl with 150 ng/μl of Cas9. (a) shows the uninjected controls and (b) the bcar1-1 CRISPR injected samples and (c) the bcar1-2 CRISPR injected samples. (c) indicates function of bcar1-2 due to small double peaks being observed compared to the single, clean peaks as observed in (a) and (b).

The remaining injected embryos were raised to adulthood, where they were screened for germline transmission through outcrossing to wild type and performing HRMA once more. Only ten zebrafish were screened, as within these three positive fish were identified through disrupted melt peaks, which are referred to as bcar1-2-Fish1, bcar1-2-Fish2 and bcar1-2-Fish3, Figure 6.10. At this point deep sequencing was performed upon a clutch of 10 embryos per outcross to determine whether any of the mutations being transmitted were of use. This step could help to save time if the mutations present within the embryos did not disrupt gene function, rather than determining this after waiting for the zebrafish to develop and screening adults. Deep sequencing found that bcar1-2-Fish1 produced < 5% of reads with frame-shift mutations, Figure 6.11, where most indels created in-frame mutations of 3bp or 9bp that did not result in a premature stop codon, Figure A.12. As a result this fish, and its offspring, were of no use. Conversely, bcar1-2-Fish2 and bcar1-2-Fish3 both produced frame-shift mutations at the gRNA target site, as shown in Figures 6.11 and A.12. A frame shift of either one or two bases produces a premature stop codon within exon 2, so both of these germline transmitting zebrafish were of use. In an attempt to save time these fish were then also outcrossed to the tumour angiogenesis zebrafish line, TraNac *Tg(KDR: mCherry:Fabp10-rtTA:TRE-eGFPKRAS^{V12})*. Therefore, identification of founders within these offspring would reduce the number of additional crosses to establish the line, where a non-pigmented background with homozygous expression of both fluorescent transgenes is required.

Once the offspring from the bcar1-2-Fish2 and bcar1-2-Fish3 outcrosses reached adulthood genotyping was required to identify founder fish with bcar1 loss of function mutations. From this the bcar1 mutant lines could be established. Initially 40 of the wild-type background zebrafish were screened, where only two fish were found to have a frame-shift mutation. These fish were of opposite sex and had the same mutation consisting of a 1bp deletion and a 3bp insertion. This mutation is shown within Figure 6.12, as well as the amino acid sequence for both wild type bcar1 and the bcar1 mutant, where the SH3 domain is annotated as described by the NCBI (`http://www.ncbi.nlm.nih.gov`) - accession code NP_001128605.1. The indel mutation produces a different sequence from position 38 and a premature stop codon at position 61. This disrupts the SH3 domain, through altering conserved amino acids (# within Figure 6.12), and truncates the protein part way through the SH3 encoding region. Therefore, this should be a bcar1 loss of function mutation, hence forth referred to as bcar1^{-}, as no functional domains are translated. These two identified zebrafish create a breeding pair within a wild type background.

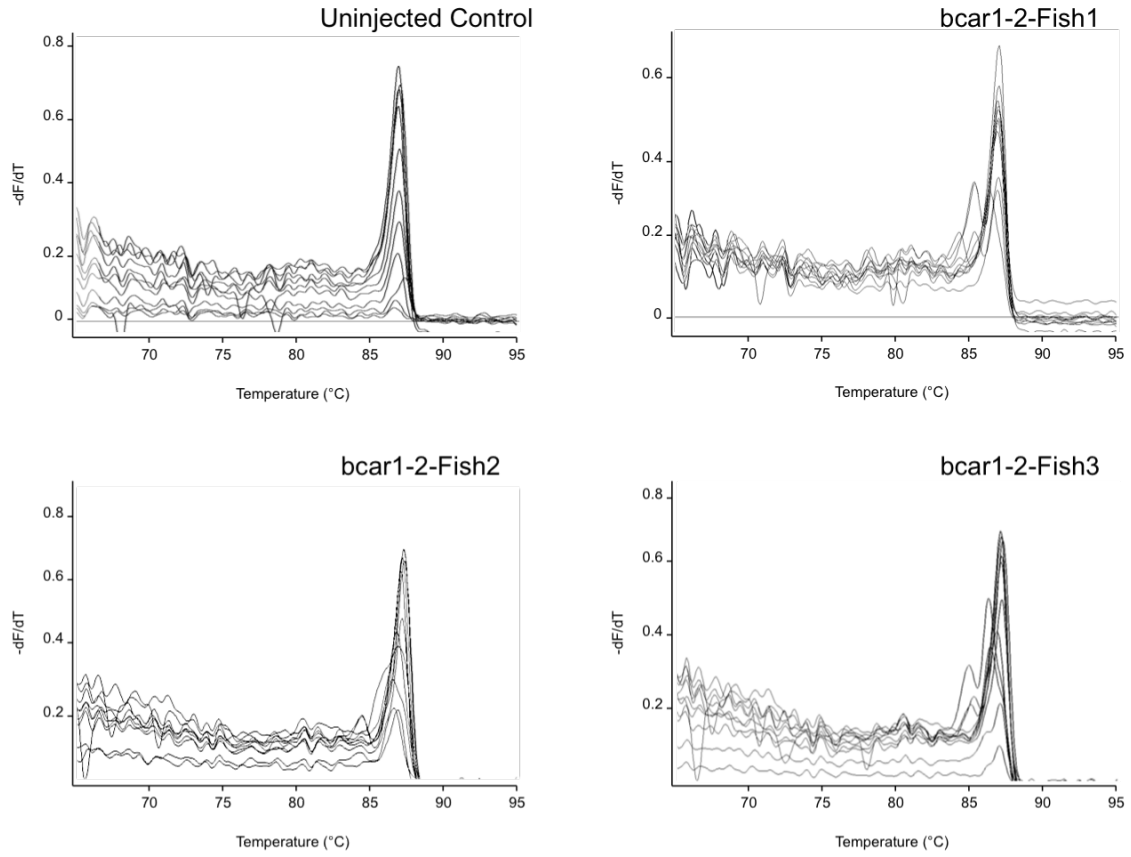

Figure 6.10: HRMA identifying germline transmission of the bcar1 mutations produced by gRNA bcar1-2, using primers bcar1 Forward 1 and Reverse 1. The HRMA melt peaks are shown for the uninjected control and identified zebrafish with germline transmission, bcar1-2-Fish1, bcar1-2-Fish2 and bcar1-2-Fish3, as labelled in the top right. HRMA was performed and analysed using the Rotor-gene 6000 (Corbett Life Science).

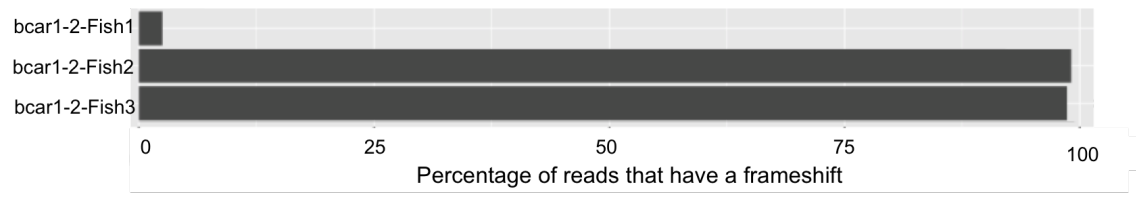

Figure 6.11: Deep sequencing results of the three bcar1 mutant germline transmitting zebrafish that were created using the gRNA bcar1-2, named bcar1-2-Fish1, bcar1-2-Fish2 and bcar1-2-Fish3. The bar graph shows the percentage of deep sequencing reads that resulted in frameshift mutations for each of these fish.

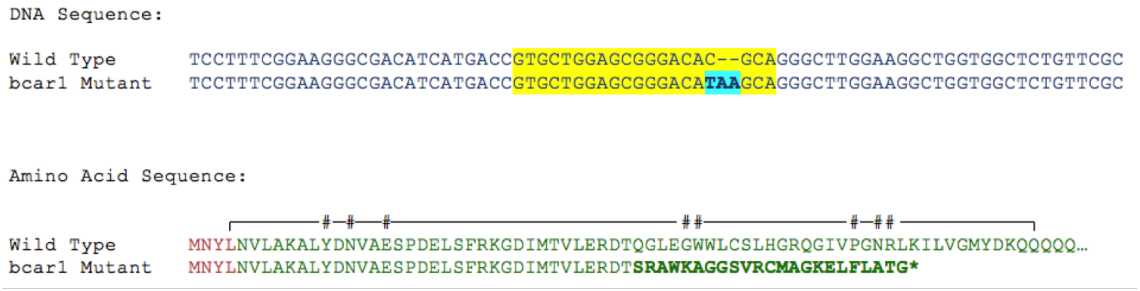

Figure 6.12: The bcar1 loss of function mutation identified from the wild type zebrafish cross. The DNA sequence of zebrafish bcar1 wild type (WT) and the bcar1 identified mutant are shown on top, where the gRNA target site is highlighted yellow and the insertion and deletion resulting in a 2bp frameshift is highlighted blue. Beneath is the amino acid sequence of the zebrafish bcar1 WT and identified mutant. The red text refers to the whole of exon 1 and the green text to exon 2. Bold residues within the mutant highlight where differences in the amino acid code lie and the asterisk (*) indicates a stop codon. The black square bracket shows the DNA within the WT encoding the SH3 domain, and the hash marks (#) indicate conserved residues, as reported by the NCBI, accession code NP_001128605.1.

A breeding pair of useful bcar1 loss of function mutants were not as easily identified within the offspring bred from the tumour angiogenesis model line. 6 different useful frameshift mutations were identified from 144 screened zebrafish, Table 6.6, however a male and a female with the same mutation were not identified. One zebrafish had the same mutation as the wild type background fish described in Figure 6.12, this was Mutation 5 within Table 6.6. Therefore, breeding could be performed between these to establish the line for mechanistic studies of bcar1 within the context of tumour progression.

6.3.4.2 Assessing the viability of bcar1$^{-/-}$ zebrafish

The two identified bcar1$^{+/-}$ zebrafish within the wild type background were bred to identify whether the bcar1$^{-/-}$ genotype was viable. During development no defects, delays or lethality were observed and 84% of the offspring reached adulthood, which is the usual survival rate of wild type fish. A subset of the zebrafish were genotyped and bcar1$^{+/+}$ and bcar1$^{+/-}$ were identified, along with one bcar1$^{-/-}$.

Mutation	Indel	Exon 2 Amino Acid Sequence
1	10bp del	NVLAKALYDNVAESPDELSFRKGDIMTVLER **AWKAGGSVRCMAGKELFLATG***
2	1bp ins	NVLAKALYDNVAESPDELSFRKGDIMTVLER **DTPGLGRLVALFAAWPARNCSWQPAEDSRWHV***
3	4bp del & 6bp ins	NVLAKALYDNVAESPDELSFRKGDIMTVLER **VISRAWKAGGSVRCMAGKELFLATG***
4	2bp ins	NVLAKALYDNVAESPDELSFRKGDIMTVLER **DIRRAWKAGGSVRCMAGKELFLATG***
5	1bp del & 3bp ins	NVLAKALYDNVAESPDELSFRKGDIMTVLER **DTSRAWKAGGSVRCMAGKELFLATG***
6	4bp del	NVLAKALYDNVAESPDELSFRKGDIMTVLER **DRAWKAGGSVRCMAGKELFLATG***

Table 6.6: The different identified bcar1 loss of function mutations within the tumour angiogenesis model offspring. The table shows the insertions (ins) and deletions (dels) identified and the resulting amino acid sequence of the truncated exon 2, where the bold residues show differences in the amino acid code compared to the wild type sequence and asterisks (*) indicates premature stop codons.

6.4 Discussion

6.4.1 Mechanistic studies of ptena and ptenb during tumour progression

Due to PTEN loss of function or deletion within human HCC increasing tumour progression and metastatic potential mechanistic studies of this protein are of interest. Globally researching this protein using the CS-OPT platform within a live adult organism would complement previous *in vitro* and cross-sectional studies and potentially improve the current zebrafish model to better reflect human HCC.

The zebrafish homolog ptenb was longitudinally studied within the context of tumour progression using the TraNac *Tg(KDR: mCherry:Fabp10-rtTA:TRE-eGFPKRAS^{V12})* zebrafish line, which can be imaged using CS-OPT to provide accurate tumour and vasculature quantifications, as shown in Chapter 4. It was hypothesised that a deficiency of this homolog could increase the rate of tumour formation and drive metastasis. This was reasoned due to the known effect of Pten loss in other model organisms and the formation of spontaneous eye tumours within ptenb deficient zebrafish (Di Cristofano et al., 1998; Faucherre et al., 2008; Choorapoikayil et al., 2013). Within the ptenb

heterozygous zebrafish a trend towards greater tumour progression was apparent and two heavily tumour burdened zebrafish died by 19 dpi. However, no metastases were observed. This mimics the findings in the study by Nguyen et al. (2011) when the zebrafish tumour model driven by eGFPKRAS^{V12} expression was studied upon a p53 absent background.

Surprisingly a contrasting effect was seen for ptenb$^{-/-}$ zebrafish, where there was a significantly delayed tumour onset and 75% of the fish were unable to develop tumours over an 18 day induction period. The ptenb and eGFPKRAS^{V12} genotype were confirmed and so an unexpected, underlying factor must be producing this effect. One possible explanation is that there could be an over compensation for complete loss of functional ptenb through an increased ptena expression. However, it was previously shown that ptena did not compensate within the spontaneous eye tumours developed in ptenb$^{-/-}$ zebrafish (Faucherre et al., 2008). The relative expression of ptena and ptenb within zebrafish may vary between tissues, which has yet to be determined, and so it is possible that the liver does not mimic what was observed in the eye. Livers and DNA samples from all of the zebrafish within the study have been preserved for further research to determine the cause. Immunohistochemistry (IHC) could be performed to determine relative levels of phosphoinositide 3-kinase (PI3K) downstream effectors, such as phospho-AKT/PKB and phospho-ERK (Figure 1.3), as well as TUNEL staining to determine levels of apoptosis within the samples. Quantification of protein expression can be achieved through both Western Blots and quantitative polymerase chain reaction (qPCR), the latter being required to determine distinct levels of ptena and ptenb as there are no homolog specific antibodies.

6.4.2 Generating ptena loss of function mutants

To complement the ptenb^{-} mutant available the development of a ptena^{-} mutant was attempted through CRISPR mediated genome editing. Only two ptena specific gRNAs were trialled and both failed to function. This is not uncommon, it could be due to the specific DNA target containing epigenetic changes for example. However, the ptena^{-} mutant described by Faucherre et al. (2008) is now available from ZIRC. This could be imported and the mutant could be expressed within the tumour angiogenesis line as achieved with the ptenb^{-} zebrafish.

Due to complete loss of both ptena and ptenb being lethal during development an inducible knock out could be advantageous to study its role in tumourigenesis and po-

tentially increase the metastatic potential of the zebrafish tumour model. To complement the ptenb^{-} zebrafish lines exon 2 of the *ptena* gene was targeted for removal to create the inducible knockout phenotype. Using TALENs for gene editing was inefficient and time consuming. After two separate attempts, with approximately 100 colonies per TALEN arm screened in each, one TALEN pair was identified for ptenaL. The lack of production success is likely due to inefficient ligations during the FLASH protocol by Reyon et al. (2012), as the colony PCR amplicons are a variety of different sizes that correspond to a distinct number of TAL subunits. This protocol could be optimised, but it is a laborious and time consuming method. Genetic Services Inc would not disclose the method they use to produce TALEN arms, however they were unable to produce the designed TALEN also. The main advantage of gene editing using TALENs over CRISPRs was the reduced likelihood of off target effects. This is due to their functioning being dependent on the orientation and sequence of two 20 nucleotide specific DNA sequences. However, online design tools for gRNAs consider the likelihood off target effects and score each possible gRNA in order to minimise this, such as the CRISPR Design tool developed by Hsu et al. (2013) used within these studies. CRISPR gRNA production is very fast and simple and they are known to elicit gene editing at a similar efficiency to TALENs (Hwang et al., 2013). Based upon these findings CRISPR mediated gene editing is preferable.

The one constructed TALEN was shown to function *in vivo*, but incorporation of the mLoxP DNA sequence by HDR at this DSB was not achieved on three separate occasions. Previously TALEN mediated insertion of the mLoxP site through HDR had a 10.3% efficiency, but this was targeted to an exon (Bedell et al., 2012). This efficiency is low and methods are currently being developed in an attempt to improve this in both TALEN and CRISPR mediated insertions. Research regarding different sizes of insert, sizes of sequence homology, insertion methods and different DNA structures, such as linear or circular donor DNA, is being performed by many groups (Bedell et al., 2012; Irion et al., 2014; Boel et al., 2016; Hoshijima et al., 2016). There are contrasting results and the zebrafish community has no optimal technique as of yet. However, circular donor DNA and CRISPR injections with Cas9 protein, rather than mRNA, do currently appear to have greater success (Genome Editing Session Workshop- Zebrafish Platform, The Allied Genetics Conference 2016).

Problems were also encountered when using CRISPRs to target the intronic regions surrounding exon 2 of *ptena*. Four gRNAs were trialled for the left hand side of the exon and ten for the right. Whilst performing analysis of the gRNAs positive

controls were included, such as the validated bcar1 CRISPR also described within this chapter. Therefore, the gRNA design tool, Cas9 mRNA and injection concentrations were all proven to work as required. It is possible that targeting intronic regions of DNA is the primary cause for the lack of both TALEN and CRISPR function. Due to a TALEN on the left hand side of the target exon being shown to elicit DSBs a functioning gRNA should be possible. Furthermore research since the start of this project has shown CRISPR mediated gene editing within an intron was possible with ∼83% efficiency (Li et al., 2015). It is feasible that the intron between exon 2 and 3 has an unknown element preventing gRNA and Cas9 binding within these studies and subsequently inhibiting a DSB. This could be an unknown secondary structure or epigenetic modifications, for example. It should not be due to SNPs in the target sequence as the intronic regions were sequenced prior to CRISPR design. However, sequencing did reveal that this intronic region was AT rich. This has not been previously reported to implicate CRISPR binding, but it may be involved. Therefore, if the production of an inducible knock out of ptena were to be pursued an intronic region further downstream could be targeted, such as the intron after exon 3. Incorporating a mLoxP site here would still enable an inducible knock out to be formed, where two exons are removed rather that just one.

6.4.3 Generating a bcar1 loss of function zebrafish line

There is a known correlation between p130Cas over expression and advancement of cancer progression within humans and its function is known to be triggered through the pro angiogenic factor VEGF (Guo et al., 2008; Barrett et al., 2013). Therapeutically targeting p130Cas could also be beneficial on account of tumour growth being blocked when it has been silenced (Cabodi et al., 2010; Nick et al., 2011). Due to this the zebrafish homolog bcar1 was of interest. Two CRISPRs were generated to target exon 2 of the *bcar1* gene and one, bcar1-2, was proven to incorporate indels through producing a DSB. 20% of the tested bcar1-2 injected embryos were shown to transmit a high proportion of frame-shift mutations through their germline.

Frame-shift mutations were found within both the wild type and tumour angiogenesis model outcrosses. By chance the first two frameshift mutations identified within the wild type background were the same and within different sex zebrafish, therefore a breeding pair was identified with ease. Breeding pairs were not easily identified within the tumour angiogenesis model background. 6 different mutations were found, one of which matching that found on the wild type background. These could be bred to establish a line to study bcar1 function within tumour progression, where accurate quantitative

imaging could be performed with CS-OPT.

The identified mutation results in a 2bp frameshift that produces a disrupted amino acid sequence from position 38 until a premature stop codon is encountered at position 61. Consequently this will produce a truncated form of the protein, which is usually 919 amino acids in length. This truncation prevents the translation of the entire proline-rich linker, substrate domain, serine-rich linker and the C-terminal domain. The SH3 domain is also disrupted and only partially translated. Crucially the disruption within the identified mutant results in 4 of the 7 conserved amino acids of the SH3 domain being altered. This is likely to affect the binding affinity to its ligands, which are known to bind with low affinity through 3 shallow hydrophobic pockets, (Mayer, 2001). Therefore, the 61 amino acids translated within the CRISPR generated bcar1^{-} mutant should not function as an adapter protein. Importantly, the previously reported knock out within mice by Honda et al. (1998) also disrupted and truncated p130Cas within the SH3 domain.

The breeding pair identified within the wild type background were incrossed. No defects were observed during development and there was a normal survival rate to adulthood. Genotyping identified a bcar1^{-} zebrafish and so it appears that homozygous expression of the bcar1^{-} mutant is not lethal. Only a small subset of the fish were genotyped, due to encountering issues with the Sanger sequencing reactions. Once these problems have been rectified it is important that further fish are screened, to find additional bcar1^{-} zebrafish and elucidate whether there is a mendelian ratio within the offspring. If this is the case it indicates that zebrafish development is not affected by homozygous expression of the bcar1^{-} mutant.

Further studies are required upon this bcar1^{-} mutant line. Firstly, it is important to determine whether the mutation has resulted in a loss of function and no wild type bcar1 is present within the zebrafish. This can be performed through assays such as Western blot, where antibodies specific for bcar1 and its downstream effectors can be used alongside wild type controls in both unstimulated and stimulated contexts. Also, qPCR can be used to confirm that both alleles produce the predicted truncated mRNA sequence. If the mutation is proven to result in a loss of function then mechanistic studies of both the bcar1$^{-/-}$ and bcar1$^{+/-}$ genotypes within tumourigenesis would be of interest.

CHAPTER 7

Discussion

7.1 Discussion

Angiogenesis is a crucial biological process throughout development and in select adult mechanisms, such as wound healing (Risau and Flamme, 1995). It acts to provide oxygen and metabolites to all cells, whilst removing any waste products. Strict control and coordination is provided through the expression of pro and anti angiogenic factors, however when these are deregulated pathologies arise due to either unrequired or inadequate vascularisation (Papetti and Herman, 2002; Carmeliet, 2003, 2005). A key example of when this occurs is within the context of cancer. Angiogenesis is a fundamental requirement for tumour progression (Gimbrone et al., 1972; Hanahan and Weinberg, 2011). As tumours begin to increase in size the distance between the cancer cells and the established vasculature exceeds the maximum oxygen diffusion distance and regions become hypoxic (Thomlinson and Gray, 1955; Semenza, 2000). As a result angiogenesis is stimulated through tumours expressing pro angiogenic factors (Semenza, 2002; Pugh and Ratcliffe, 2003). The resulting neovascularisation enables the tumours to survive and grow and also provides a possible route for metastasis. Metastasis is the primary cause for cancer death as a result of malignancy, therefore therapeutically preventing angiogenesis is a key target (Ferrara and Kerbel, 2005; Carmeliet and Jain, 2011).

It is becoming increasingly accepted that *in vitro* studies of biological processes may significantly differ from what occurs *in vivo*. This is due to the absence of global systems and true cellular environments. Zebrafish have become a popular model organism for studies due to their numerous beneficial features (Serbedzija et al., 1999; Stoletov and Klemke, 2008). One such benefit is the optical transparency of non-pigmented mutant lines such as TraNac, which enables the use of non-invasive imaging techniques including optical projection tomography (OPT). Therefore, adult organisms can be studied to accurately represent pathologies such as cancer, where a fully formed vasculature and mature immune system are crucial limitations in embryonic studies (Hanahan and Weinberg, 2011).

The research aim was to develop a 3-D imaging modality that was capable of quantifying tumour progression and vascularisation within live adult zebrafish. Consequently this platform could be used to provide novel insights into tumorigenesis and the accompanying angiogenesis through subsequent mechanistic studies. Furthermore, it could be used as a platform for drug development. Within this thesis the compressive sensing optical projection tomography (CS-OPT) platform was developed and validated, the accompanying protocols were optimised and novel zebrafish models were developed to address this.

7.1.1 Experimental Findings

7.1.1.1 Using CS-OPT to reduce the acquisition time when imaging adult zebrafish

When performing live, *in vivo* imaging acquisition time is important, whereby prolonged periods can result in detrimental effects being experienced by the zebrafish. This is particularly true when using OPT as the organisms require deep anaesthesia (Table 1.1) to enable motionless imaging and extended durations reduce zebrafish viability. Using conventional reconstruction methods, such as filtered back projection (FBP), a minimum of 360 projections are usually required (McGinty et al., 2008, 2011). Compressive sensing (CS) algorithms were applied to adult imaging due to their previous success in OPT reconstruction of zebrafish embryos (Correia et al., 2015). Parameters within the CS algorithm were optimised and the number of projections required to maintain image quality were reduced more than 5-fold, to just 64. As a result the OPT acquisition time was less than 3.5 minutes when imaging an eGFP-tagged liver tumour and a mCherry labelled vasculature within an adult zebrafish. This significant reduction resolves the anaesthesia viability issue and also provides further imaging time if required. For example, it may be beneficial to incorporate additional fluorescent markers or utilise Förster Resonance Energy Transfer (FRET) based biosensors to provide readouts of physiological interactions through Fluorescence Lifetime Imaging Microscopy (FLIM) OPT (McGinty et al., 2011; Andrews et al., 2016).

7.1.1.2 Accurate 3-D quantifications of tumour volume and vascularisation using CS-OPT

Quantifications are of importance to confidently determine the relationships within biological processes, enabling accurate conclusions. CS-OPT provides 3-D qualitative images from which quantifications could be drawn. In order to establish these quantifications I firstly determined the performance of the system with the tumour angiogenesis

zebrafish model, TraNac *Tg (KDR:mCherry:Fabp10-rtTA:TREeGFPKRAS^{V12})*. I concluded that starved, male zebrafish with homozygous expression of mCherry within the zebrafish vasculature would be optimal for imaging. Through performing an *in vivo* cross-sectional study quantifications of tumour volume and vascularisation were extracted. These revealed statistically significant differences throughout the course of the study, where inducer presence caused tumour progression with increased vascularisation and upon inducer removal tumours regressed with reduced vascularisation. Hematoxylin and Eosin (H&E) staining confirmed what had previously been shown by Nguyen et al. (2012) with regards to tumour growth and vascular quantifications were validated with the well established technique of immunohistochemistry (IHC).

The CS-OPT images reconstructed from this study demonstrated the mesoscopic imaging capability of the platform. The entire tumour was captured within the 1 cm wide zebrafish and its corresponding vasculature was reconstructed up to 1.7 mm in depth, which accounts for approximately a third of the tumour vasculature. The limited depth of penetration achievable for the vasculature using CS-OPT is a result of scattering, as the zebrafish liver tumours do not have a homogenous refractive index with regards to the rest of the fish. This is an area that could be improved. Despite this, CS-OPT is favourable to other mesoscopic imaging techniques. Greater penetration depths are achieved than with intravital imaging and no invasive procedures are required that could limit studies or affect results (Conway et al., 2014). Furthermore, live fluorescence and brightfield imaging are possible, the system is simple and the cost of implementation is comparable to a widefield microscope. These are all benefits over microMRI, microCT and light sheet microscopy (Sharpe, 2003; Cheng et al., 2011; Mayer et al., 2014). Therefore, CS-OPT is an advantageous imaging platform that enables accurate 3-D quantifications of physiological processes, such as tumour progression and vascularisation, to be acquired through non-invasive *in vivo* imaging of adult organisms.

7.1.1.3 Performing and optimising longitudinal imaging with CS-OPT

Longitudinal studies provide greater accuracy and additional temporal information than achievable through cross-sectional studies. Consequently, fewer animals are also required for research. In order to perform longitudinal studies of tumour progression and angiogenesis with the CS-OPT platform demonstration of its minimally invasive nature and optimisation of the accompanying protocols were required. Through repeatedly imaging a single zebrafish from the larvae stage through to adulthood CS-OPT was shown to have no impact upon zebrafish viability.

Motionless organisms are vital during OPT acquisition, due to any movement causing reconstruction artefacts that result in inaccurate images and quantifications. This can be achieved through deeply anaesthetising model zebrafish, where they have no movement or response to external stimuli, Table 1.1. It is known that prolonged exposure to 4.2% (168 parts per million (ppm)) MS-222, the regime widely used within the zebrafish community, results in respiratory and cardiac failure (Sun et al., 2009; Matthews and Varga, 2012). Furthermore, I have reported that this is insufficient for maintaining deep anaesthesia. Using a combined dose of 175 ppm of both MS-222 and isoflurane the maintenance of deep anaesthesia has been improved, which was determined using an external stimulus greater than experienced during CS-OPT imaging. Importantly this regime was repeatable without impacting upon the viability of the fish and the time under deep anaesthesia before loss of opercula movement was also increased. During these studies the *transparent* gene was found to be involved in the response to anaesthesia. This was evident due to non-pigmented TraNac fish, which lack functional copies of the *transparent* gene, taking longer to anaesthetise. However, using the combination of 175 ppm of both MS-222 and isoflurane the time taken to reach deep anaesthesia, and consequently the stress experienced by the fish, was reduced. Therefore, incorporating this combined anaesthetic regime will enable longitudinal imaging of non-pigmented adult zebrafish to be performed using CS-OPT with an improved efficiency.

For future mechanistic and drug development studies it was important to understand the dose dependency of the TraNac *Tg (KDR:mCherry:Fabp10-rtTA:TREeGFPKRAS^{V12})* zebrafish model with respect to doxycycline concentration and tumour progression. Therefore the inducer concentration could be chosen to achieve the desired rate of tumour progression and the point of drug administration could be determined. Through performing a longitudinal study to examine doxycycline concentration it was clear that the dynamics of tumour progression were different within older and younger zebrafish. The older zebrafish (425 dpf) had a delayed onset and also reduced growth rate compared to the younger (150 dpf) group. Therefore, age should always be considered in future studies with this zebrafish model. Unfortunately no conclusions were made with regards to optimal doxycycline dose for future longitudinal studies. It was noticed that doxycycline degradation was occurring in the fish facility system water being used, which was affecting the rate of tumour progression. This was resolved through using Tropic Marin® water as an alternative. Consequently, this longitudinal doxycycline study would require repeating to accurately determine the dynamics of tumour progression when doxycycline degradation is not occurring.

7.1.1.4 Mechanistic studies of ptena, ptenb and bcar1 within tumour progression

The CS-OPT platform can be used to provide accurate 3-D readouts regarding tumour progression and vascularisation of longitudinal mechanistic studies. With this in mind additional zebrafish models were applied.

The lipid phosphatase PTEN is frequently mutated and deleted within human cancer and its expression within hepatocellular carcinoma (HCC) has a negative correlation with tumour progression and metastasis (Dong-Dong et al., 2003; Hu et al., 2003). Both zebrafish homologs, ptena and ptenb, were studied. An initial longitudinal study of ptenb function within tumour progression using the TraNac *Tg (KDR:mCherry:Fabp10-rtTA:TREeGFPKRAS^{V12})* zebrafish model revealed unexpected results. Most surprisingly the ptenb$^{-/-}$ genotype resulted in a significantly delayed tumour onset. This was in contrast to the ptenb$^{+/-}$ zebrafish, where a trend towards an increase in tumour progression was seen compared to the ptenb wild type control. No metastasis was observed throughout the study. The reasons behind the unanticipated phenomenon of the delayed tumour onset are yet to be determined, but it is possible the other zebrafish homolog, ptena, is involved. To further understand the function of ptena gene editing was attempted to create a non-functional mutant. This was unsuccessful and abandoned due to a model now being available by ZIRC.

Due to a loss of both ptena and ptenb being embryonic lethal it was believed an inducible knock out would be required to increase the metastatic potential of the tumour angiogenesis zebrafish model. This would better reflect the human pathology. The intronic regions around *ptena* exon 2 were targeted. The designed TALEN for the left hand side successfully produced a DSB and indels, but was not able to incorporate donor DNA encoding a LoxP site. No TALEN or CRISPR successfully functioned when targeting the intron between exon 2 and 3. It is possible there is an unknown factor preventing nuclease binding and cleaving. Unfortunately, an inducible knockout of ptena was not created and a significant amount of work is still required in order to do so.

The adapter protein p130Cas is overexpressed in many cancers and silencing its expression has been seen to block tumour growth and progression in some contexts (Cabodi et al., 2010; Nick et al., 2011; Barrett et al., 2013). The zebrafish homolog, bcar1, was of interest and is currently uncharacterised. Therefore a non-functional form of the protein was desirable to study its function within the tumour angiogenesis model using CS-OPT. Using CRISPR mediated gene editing a frameshift mutant was seen

that is expected to result in a non-functional protein. The mutant results in a truncation at amino acid position 61, which is before the end of the SH3 domain. Prior to this truncation conserved residues are also disrupted. The homozygous loss of bcar1 does not appear to be lethal, unlike in other model organisms (Honda et al., 1998). It is critical that the loss of function of this mutant is confirmed, prior to mechanistic studies.

7.1.2 Future Directions

7.1.2.1 Further improving reconstruction of undersampled datasets

Sparsity has been assessed within CS reconstruction through applying the fixed transform of total variation and then minimising the gradient coefficients of the image. It has been shown previously that a greater level of sparsity can be achieved through using adaptive techniques that learn a sparsifying transform, termed dictionary, from overcomplete training datasets (Elad and Aharon, 2006; Liu et al., 2013). This method is known as dictionary learning (DL) and has been applied to many applications including image denoising and compressive sensing to optimise the subsequent image reconstruction (Tosic and Frossard, 2011). It has been seen that dictionaries learnt from the gradient domain directly give sparser representations and subsequently provide reconstructions with a greater accuracy and improved convergence (Liu et al., 2013). Therefore DL could be incorporated into CS-OPT reconstructions to enable faster acquisition and 3-D images with improved quality, allowing biological conclusions to be obtained with a greater accuracy. However, it is likely that reconstruction time would increase incorporating DL into Equation 1.3 and so it may only be worthwhile for particular applications.

7.1.2.2 Improving the depth of penetration

Within Chapter 4 I discussed the mesoscopic imaging capability of the CS-OPT platform. Despite being an improvement on previous non-invasive techniques for live *in vivo* organisms, vasculature imaging is limited to a penetration depth of $\sim$1.7 mm into the zebrafish liver tumour. As eluded to within Section 4.4.4 this is a result of the emitted fluorescence scattering, causing a reduced imaging performance towards the centre of the adult zebrafish. As previously mentioned (Section 1.4.3) accurate images from OPT are reliant upon transparent specimens with homogeneous refractive indexes. The non-pigmented zebrafish are sufficiently transparent to allow imaging, but they only lack melanocyte and iridophore production. Therefore, their organs and other internal structures are still visible. It is important to note that the liver is one of the organs most clearly observed within the non-pigmented mutants. This is seen in Figures 1.4 and 1.5,

where the liver is the tan coloured organ to the lower right of the visible eggs. As the inducible liver tumours within our chosen tumour angiogenesis model progress the livers increase in size and the cells become more densely packed. As a result these internal structures, organs and the tumour itself cause light scatter.

The capabilities and depth of penetration achievable when using CS-OPT to image non-pigmented adult zebrafish could be improved. The odds of scattering occurring when a photon is traveling through a uniform medium increase exponentially as the distance travelled increases. Consequently, small improvements in scatter length, the distance achievable before scatter of a photon occurs, can lead to substantial improvements in imaging capabilities (Lecoq and Schnitzer, 2011). Figure 7.1 shows the improved scatter length of infrared fluorescent protein (iRFP) in comparison to mCherry, which is used within the tumour angiogenesis zebrafish model. Therefore altering the zebrafish models to include fluorophores with greater wavelengths such as iRFP could give an improved CS-OPT depth of penetration. As well as this additional advanced reconstruction algorithms could be developed and incorporated that could predict the behaviour of the scattered, non-ballistic light.

7.1.2.3 Mechanistic studies of ptena, ptenb and bcar1 using CS-OPT

One of the aims of my PhD was to perform mechanistic studies by developing novel zebrafish models. This was partially achieved within Chapter 6, where a mechanistic study of ptenb was performed. It is still desirable to produce the inducible knock out of zebrafish ptena upon this background, as it could increase the metastatic potential of, and therefore improve, the tumour angiogenesis zebrafish model. Since the start of my PhD CRISPR technology has improved significantly and the zebrafish community are using it increasingly. Many groups are attempting different knock-ins through CRISPR gene editing (Bedell et al., 2012; Chang et al., 2013; Auer and Del Bene, 2014) and discoveries to improve the success of this are rapidly occurring (Genome Editing Session Workshop- Zebrafish Platform, The Allied Genetics Conference 2016). Therefore, with perseverance, there is no reason why the ptena inducible knock out zebrafish should not be possible as the technology develops. Once this has been achieved inducible knockouts could also be applied to other proteins of interest.

The bcar1 mutant I have created requires verification of loss of function. Once this has been performed the mutant can be expressed upon the tumour angiogenesis line for mechanistic studies using CS-OPT.

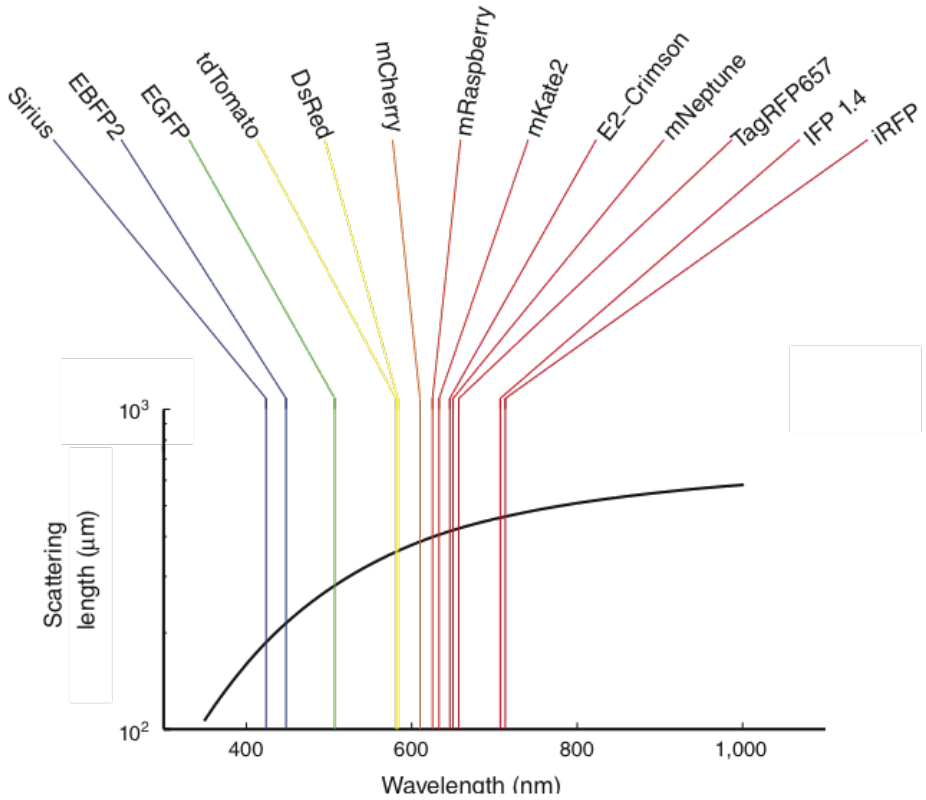

Figure 7.1: Scattering length of different fluorophores, where the length is longer for infrared fluorescent protein (iRFP) compared to proteins emitting visible light, such as mCherry. The black trace corresponds to a tissue sample of human skin as an example. Figure adapted from Lecoq and Schnitzer (2011).

7.1.2.4 Longitudinal drug development study for tumour progression and angiogenesis using CS-OPT

The research performed within my PhD developed the CS-OPT platform and the accompanying zebrafish models and protocols. This was to enable a longitudinal drug development study of tumour progression and angiogenesis. Zebrafish have been favourably used for small molecule drug screens as a result of their known advantages. These include their genetic and histological similarity to humans, broad range of disease associated phenotypes, applicability to high-throughput large scale studies and the ability to screen a whole intact organism (Serbedzija et al., 1999; Zon and Peterson, 2005; MacRae and Peterson, 2015). Screens have previously been performed in embryos due to their transparency enabling functional and morphological changes to be detected without organism sacrifice (Zon and Peterson, 2005). Therefore, the developed CS-OPT platform will enable adult zebrafish to be studied, providing an increased accuracy due to assessing the drug efficacy within a mature, developed organism.

Consequently, preparations for such a study were made with the intention to perform and complete it prior to the end of my PhD. There were two therapeutics of interest to be trialled, these being a tumorigenic inhibitor that targets Ras, deltarasin, and an angiogenesis inhibitor that targets VEGFRs, Vatalanib (PTK787). Ras inhibitors are of interest due to Ras being the most commonly mutated oncogene and its activity being increased in the majority of human cancers (Downward, 2003), however no previous attempts have been effective enough to make it into the clinic (Baines et al., 2011). The small molecule deltarasin is promising as it has been shown to reduce the growth rate of tumours *in vivo* through KRAS delocalisation (Zimmermann et al., 2013). Oncogenic KRAS activity is dependent upon its membrane association once it has been farnesylated, which is regulated by a protein called PDEδ. Deltarasin successfully binds to the farnesyl-binding pocket of PDEδ with nanomolar affinity and consequently inhibits KRAS oncogenic activity through delocalisation (Zimmermann et al., 2013). Vatalanib binds the protein kinase domain of the VEGFRs and inhibits autophosphorylation and subsequent activation, where it is most potent against KDR (Wood et al., 2000). This anti-angiogenic has been successfully used within zebrafish where angiogenesis was inhibited during caudal fin regeneration (Bayliss et al., 2006).

The CS-OPT platform and tumour angiogenesis model zebrafish, TraNac *Tg (KDR:mCherry:Fabp10-rtTA:TREeGFPKRAS^{V12})*, were to be used to study tumour progression and angiogenesis, through quantifying tumour volume and vascularisation as described within Chapter 4. The optimised anaesthetic regime determined within Section 5.3.2 would have also been incorporated to increase the efficiency of imaging and reduce the stress upon the zebrafish. Based upon the results of the longitudinal doxycycline study within Section 5.3.3 younger zebrafish (less than 6 months of age) would have been used. Within the study a minimum of 30 zebrafish were to be induced with doxycycline and at the point of drug administration they were to be divided into three groups, each with ten fish. Within these groups the zebrafish would have been distributed as equally as possible to avoid bias. In order to do this each group would have been chosen to have a Gaussian distribution with approximately the same mean and standard deviation with respect to tumour size. At this point all groups would have been continually treated with the same doxycycline concentration and additionally one group would have been treated with Vatalanib and another one with deltarasin. The doxycycline alone would act as a control group.

Unfortunately the longitudinal study has not yet been performed. This is due to

awaiting licensing approval from the Home Office to enable the zebrafish to be held over weekends within CS-OPT room at Imperial College London. This is a crucial requirement as frequently moving the fish to and from different rooms will incur stress. In the meantime another longitudinal doxycycline study can be performed using Tropic Marin® water. This study would consist of tumour angiogenesis model zebrafish being induced with different concentrations of doxycycline within Tropic Marin® water. Each group would consist of $n \geq 8$ fish and the tumour progression would be monitored in each group. This would allow the level of inducer treatment to be optimised and the optimal point for drug administration within the model to be determined.

7.1.3 Conclusion

The research presented within this thesis shows the development of CS-OPT, a novel 3-D mesoscopic imaging platform that can provide accurate quantifications of both tumour growth and vascularisation in live adult zebrafish. Furthermore, I have demonstrated the use of this platform to quantitatively measure vascular development in longitudinal studies. This is an advancement on currently available mesoscopic imaging techniques due to the depth of penetration achieved, the longitudinal capability, using a mature adult organism and also providing 3-D quantifications. The anaesthetic regime has been optimised to improve the efficiency of the CS-OPT system, through enabling prolonged periods of maintained deep anaesthesia that could be repeatedly used without impacting upon zebrafish viability. Novel zebrafish models of key proteins implicated in tumour progression and angiogenesis have been developed. These include the generation of a bcar1 loss of function line, a ptenb loss of function tumour model line and the attempt of an inducible knock out ptena line. As a result, CS-OPT will be of great use in future mechanistic and drug development studies of tumour progression and angiogenesis. In addition, the platform should be of interest to the wider zebrafish community for further developmental and pathophysiological applications.

Bibliography

Allan, C., Burel, J.-M., Moore, J., Blackburn, C., Linkert, M., Loynton, S., Macdonald, D., Moore, W. J., Neves, C., Patterson, A., Porter, M., Tarkowska, A., Loranger, B., Avondo, J., Lagerstedt, I., Lianas, L., Leo, S., Hands, K., Hay, R. T., Patwardhan, A., Best, C., Kleywegt, G. J., Zanetti, G., and Swedlow, J. R. OMERO: flexible, model-driven data management for experimental biology. *Nature methods*, 9(3):245–53, 2012.

Amatruda, J. F., Shepard, J. L., Stern, H. M., and Zon, L. I. Zebrafish as a cancer model system. *Cancer Cell*, 1(3):229–231, apr 2002.

Andrews, N., Ramel, M.-C., Kumar, S., Alexandrov, Y., Kelly, D. J., Warren, S. C., Kerry, L., Lockwood, N., Frolov, A., Frankel, P., Bugeon, L., McGinty, J., Dallman, M. J., and French, P. M. W. Visualising apoptosis in live zebrafish using fluorescence lifetime imaging with optical projection tomography to map FRET biosensor activity in space and time. *Journal of biophotonics*, 9(4):414–24, jan 2016.

Auer, T. O. and Del Bene, F. CRISPR/Cas9 and TALEN-mediated knock-in approaches in zebrafish. *Methods (San Diego, Calif.)*, 69(2):142–150, apr 2014.

Auerbach, R., Lewis, R., Shinners, B., Kubai, L., and Akhtar, N. Angiogenesis assays: A critical overview, 2003.

Baines, A. T., Xu, D., and Der, C. J. Inhibition of Ras for cancer treatment: the search continues. *Future medicinal chemistry*, 3(14):1787–808, oct 2011.

Barrett, A., Pellet-Many, C., Zachary, I. C., Evans, I. M., and Frankel, P. P130Cas: A key signalling node in health and disease, 2013.

Barriuso, J., Nagaraju, R., and Hurlstone, A. Zebrafish: A new companion for translational research in oncology. *Clinical Cancer Research*, 21(5):969–975, 2015.

Bassi, A., Fieramonti, L., D'Andrea, C., Mione, M., and Valentini, G. In vivo label-free three-dimensional imaging of zebrafish vasculature with optical projection tomography. *J Biomed Opt*, 16(10):100502, oct 2011.

Bayliss, P. E., Bellavance, K. L., Whitehead, G. G., Abrams, J. M., Aegerter, S., Robbins, H. S., Cowan, D. B., Keating, M. T., O'Reilly, T., Wood, J. M., Roberts, T. M., and Chan, J. Chemical modulation of receptor signaling inhibits regenerative angiogenesis in adult zebrafish. *Nature chemical biology*, 2(5):265–73, may 2006.

Bedell, V. M., Wang, Y., Campbell, J. M., Poshusta, T. L., Starker, C. G., Krug II, R. G., Tan, W., Penheiter, S. G., Ma, A. C., Leung, A. Y. H., Fahrenkrug, S. C., Carlson, D. F., Voytas, D. F., Clark, K. J., Essner, J. J., and Ekker, S. C. In vivo genome editing using a high-efficiency TALEN system. *Nature*, 491(7422):114–8, nov 2012.

Beery, A. K. and Zucker, I. Sex bias in neuroscience and biomedical research. *Neuroscience and biobehavioral reviews*, 35(3):565–72, jan 2011.

Betz, O., Wegst, U., Weide, D., Heethoff, M., Helfen, L., Lee, W.-K., and Cloetens, P. Imaging applications of synchrotron X-ray phase-contrast microtomography in biological morphology and biomaterials science. I. General aspects of the technique and its advantages in the analysis of millimetre-sized arthropod structure. *Journal of Microscopy*, 227(1):51–71, jul 2007.

Bioucas-Dias, J. M. and Figueiredo, M. A. A new twIst: two-step iterative shrinkage/thresholding algorithms for image restoration. *IEEE Trans Image Process*, 16(12): 2992–3004, dec 2007.

Bockamp, E., Maringer, M., Spangenberg, C., Fees, S., Fraser, S., Eshkind, L., Oesch, F., and Zabel, B. Of mice and models: improved animal models for biomedical research. *Physiol Genomics Am J Physiol Lung Cell Mol Physiol*, 11:115–132, 2002.

Boel, A., Steyaert, W., De Rocker, N., Menten, B., Callewaert, B., De Paepe, A., Coucke, P., and Willaert, A. BATCH-GE: Batch analysis of Next-Generation Sequencing data for genome editing assessment. *Scientific reports*, 6:30330, 2016.

Burri, P. H. and Tarek, M. R. A novel mechanism of capillary growth in the rat pulmonary microcirculation. *Anatomical Record*, 228(1):35–45, 1990.

Burri, P. H., Hlushchuk, R., and Djonov, V. Intussusceptive angiogenesis: Its emergence, its characteristics, and its significance. *Developmental Dynamics*, 231(3):474–488, 2004.

Cabodi, S., Tinnirello, A., Bisaro, B., Tornillo, G., Camacho-Leal, M. D. P., Forni, G., Cojoca, R., Iezzi, M., Amici, A., Montani, M., Eva, A., Di Stefano, P., Muthuswamy, S. K., Tarone, G., Turco, E., and Defilippi, P. p130Cas is an essential transducer element in ErbB2 transformation. *FASEB Journal*, 24(10):3796–3808, 2010.

Candès, E. J. and Wakin, M. B. An Introduction To Compressive Sampling. *IEEE Signal Processing Magazine*, V.21, 2008.

Candes, E., Romberg, J., and Tao, T. Stable Signal Recovery from Incomplete and Inaccurate Measurements. *Comm. Pure Appl. Math*, 40698:1–15, 2005.

Carmeliet, P., Ferreira, V., Breier, G., Pollefeyt, S., Kieckens, L., Gertsenstein, M., Fahrig, M., Vandenhoeck, A., Harpal, K., Eberhardt, C., Declercq, C., Pawling, J., Moons, L., Collen, D., Risau, W., and Nagy, A. Abnormal blood vessel development and lethality in embryos lacking a single VEGF allele. *Nature*, 380(6573):435–9, apr 1996.

Carmeliet, P. Angiogenesis in health and disease. *Nature medicine*, 9(6):653–60, jun 2003.

Carmeliet, P. Angiogenesis in life, disease and medicine. *Nature*, 438(7070):932–6, dec 2005.

Carmeliet, P. and Jain, R. K. Molecular mechanisms and clinical applications of angiogenesis. *Nature*, 473(7347):298–307, 2011.

Chakraborty, A. An efficient algorithm for compressed MR imaging using total variation and wavelets. In *2008 IEEE Conference on Computer Vision and Pattern Recognition*, pages 1–8. IEEE, jun 2008. ISBN 978-1-4244-2242-5.

Chan, T., Esedoglu, S., Park, F., and Yip, a. Recent developments in total variation image restoration. *Mathematical Models of . . .* , pages 1–18, 2005.

Chang, N., Sun, C., Gao, L., Zhu, D., Xu, X., Zhu, X., Xiong, J.-W., and Xi, J. J. Genome editing with RNA-guided Cas9 nuclease in Zebrafish embryos. *Cell Research*, 23(4): 465–472, apr 2013.

Chen, L., Andrews, N., Kumar, S., Frankel, P., McGinty, J., and French, P. M. W. Simultaneous angular multiplexing optical projection tomography at shifted focal planes. *Optics Letters*, 38(6):851, mar 2013.

Cheng, K. C., Xin, X., Clark, D. P., and La Riviere, P. Whole-animal imaging, gene function, and the Zebrafish Phenome Project. *Current opinion in genetics & development*, 21(5):620–9, oct 2011.

Chesler, D. A. and Riederer, S. J. Ripple suppression during reconstruction in transverse tomography. *Physics in Medicine and Biology*, 20(4):632–636, jul 1975.

Choorapoikayil, S., Weijts, B., Kers, R., de Bruin, A., and den Hertog, J. Loss of Pten promotes angiogenesis and enhanced vegfaa expression in zebrafish. *Disease models & mechanisms*, 6(5):1159–66, sep 2013.

Clegg, R. M. Fluorescence resonance energy transfer. *Current opinion in biotechnology*, 6(1):103–10, feb 1995.

Collymore, C., Tolwani, A., Lieggi, C., and Rasmussen, S. Efficacy and safety of 5 anesthetics in adult zebrafish (Danio rerio). *Journal of the American Association for Laboratory Animal Science : JAALAS*, 53(2):198–203, mar 2014.

Conway, J. R. W., Carragher, N. O., and Timpson, P. Developments in preclinical cancer imaging: innovating the discovery of therapeutics. *Nature reviews. Cancer*, 14(5):314–28, 2014.

Correia, T., Lockwood, N., Kumar, S., Yin, J., Ramel, M. C., Andrews, N., Katan, M., Bugeon, L., Dallman, M. J., McGinty, J., Frankel, P., French, P. M. W., and Arridge, S. Accelerated optical projection tomography applied to in vivo imaging of zebrafish. *PLoS ONE*, 10(8), 2015.

Cully, M., You, H., Levine, A. J., and Mak, T. W. Beyond PTEN mutations: the PI3K pathway as an integrator of multiple inputs during tumorigenesis. *Nature reviews. Cancer*, 6(3):184–92, mar 2006.

Dahlem, T. J., Hoshijima, K., Jurynec, M. J., Gunther, D., Starker, C. G., Locke, A. S., Weis, A. M., Voytas, D. F., and Grunwald, D. J. Simple methods for generating and detecting locus-specific mutations induced with TALENs in the zebrafish genome. *PLoS genetics*, 8(8):e1002861, jan 2012.

Dankort, D., Curley, D. P., Cartlidge, R. A., Nelson, B., Karnezis, A. N., Damsky, W. E., You, M. J., DePinho, R. A., McMahon, M., and Bosenberg, M. Braf(V600E) cooperates with Pten loss to induce metastatic melanoma. *Nature genetics*, 41(5):544–52, may 2009.

Davies, H., Bignell, G. R., Cox, C., Stephens, P., Edkins, S., Clegg, S., Teague, J., Woffendin, H., Garnett, M. J., Bottomley, W., Davis, N., Dicks, E., Ewing, R., Floyd, Y., Gray, K., Hall, S., Hawes, R., Hughes, J., Kosmidou, V., Menzies, A., Mould, C., Parker, A., Stevens, C., Watt, S., Hooper, S., Wilson, R., Jayatilake, H., Gusterson, B. A., Cooper, C., Shipley, J., Hargrave, D., Pritchard-Jones, K., Maitland, N., Chenevix-Trench, G., Riggins, G. J., Bigner, D. D., Palmieri, G., Cossu, A., Flanagan, A., Nicholson, A., Ho, J. W. C., Leung, S. Y., Yuen, S. T., Weber, B. L., Seigler, H. F., Darrow, T. L., Paterson, H., Marais, R., Marshall, C. J., Wooster, R., Stratton, M. R., and Futreal, P. A. Mutations of the BRAF gene in human cancer. *Nature*, 417(6892): 949–954, jun 2002.

Di Cristofano, A., Pesce, B., Cordon-Cardo, C., and Pandolfi, P. P. Pten is essential for embryonic development and tumour suppression. *Nature genetics*, 19(4):348–55, aug 1998.

Dong-Dong, L., Xi-Ran, Z., and Xiang-Rong, C. Expression and significance of new tumor suppressor gene PTEN in primary liver cancer. *Journal of cellular and molecular medicine*, 7(1):67–71, 2003.

Donoho, D. L. Compressed sensing. *Information Theory, IEEE Transactions*, pages 1289–1306, 2006.

Downward, J. Targeting RAS signalling pathways in cancer therapy. *Nature Reviews Cancer*, 3(1):11–22, jan 2003.

Elad, M. and Aharon, M. Image denoising via sparse and redundant representations over learned dictionaries. *IEEE transactions on image processing : a publication of the IEEE Signal Processing Society*, 15(12):3736–45, dec 2006.

Faucherre, a., Taylor, G. S., Overvoorde, J., Dixon, J. E., and Hertog, J. D. Zebrafish pten genes have overlapping and non-redundant functions in tumorigenesis and embryonic development. *Oncogene*, 27(8):1079–1086, 2008.

Ferlay, J., Soerjomataram, I., Ervik, M., Dikshit, R., Eser, S., Mathers, C., Rebelo, M., Parkin, D., Forman, D., Bray, F., and V1.0, F. G [Internet]. Lyon, F. I. A. f. R. o. C. . GLOBOCAN 2012 v1.0. *Cancer Incidence and Mortality Worldwide: IARC CancerBase No. 11 [Internet].*, 2012.

Ferrara, N. and Henzel, W. J. Pituitary follicular cells secrete a novel heparin-binding growth factor specific for vascular endothelial cells. *Biochemical and biophysical research communications*, 161(2):851–8, jun 1989.

Ferrara, N., Carver-Moore, K., Chen, H., Dowd, M., Lu, L., O'Shea, K. S., Powell-Braxton, L., Hillan, K. J., and Moore, M. W. Heterozygous embryonic lethality induced by targeted inactivation of the VEGF gene. *Nature*, 380(6573):439–42, apr 1996.

Ferrara, N. VEGF and the quest for tumour angiogenesis factors. *Nature reviews. Cancer*, 2(10):795–803, oct 2002.

Ferrara, N. and Davis-Smyth, T. The Biology of Vascular Endothelial Growth Factor. *Endocrine Reviews*, 18(1), jul 1997.

Ferrara, N. and Kerbel, R. S. Angiogenesis as a therapeutic target. *Nature*, 438(7070): 967–974, dec 2005.

Ferrara, N., Gerber, H.-P., and LeCouter, J. The biology of VEGF and its receptors. *Nature medicine*, 9(6):669–76, jun 2003.

Fieramonti, L., Bassi, A., Foglia, E. A., Pistocchi, A., D'Andrea, C., Valentini, G., Cubeddu, R., De Silvestri, S., Cerullo, G., and Cotelli, F. Time-gated optical projection tomography allows visualization of adult zebrafish internal structures. *PLoS One*, 7(11), 2012.

Fong, G. H., Rossant, J., Gertsenstein, M., and Breitman, M. L. Role of the Flt-1 receptor tyrosine kinase in regulating the assembly of vascular endothelium. *Nature*, 376(6535): 66–70, jul 1995.

Frangi, A. F., Niessen, W. J., Vincken, K. L., and Viergever, M. A. Multiscale vessel enhancement filtering. *Medical Image Computing and Computer-Assisted Interventation*, 1496:130–137, 2006.

Gagnon, J. A., Valen, E., Thyme, S. B., Huang, P., Ahkmetova, L., Pauli, A., Montague, T. G., Zimmerman, S., Richter, C., and Schier, A. F. Efficient mutagenesis by Cas9 protein-mediated oligonucleotide insertion and large-scale assessment of single-guide RNAs. *PloS one*, 9(5):e98186, jan 2014.

Gimbrone, M. A., Leapman, S. B., Cotran, R. S., and Folkman, J. Tumor dormancy in vivo by prevention of neovascularization. *The Journal of experimental medicine*, 136 (2):261–76, aug 1972.

Guo, C., Liu, Q. G., Yang, W., Zhang, Z. L., and Yao, Y. M. Relation among p130Cas, E-cadherin and β-catenin expression, clinicopathologic significance and prognosis in human hepatocellular carcinoma. *Hepatobiliary and Pancreatic Diseases International*, 7(5):490–496, 2008.

Hanahan, D. and Weinberg, R. A. The Hallmarks of Cancer. *Cell*, 100(1):57–70, jan 2000.

Hanahan, D. and Weinberg, R. A. Hallmarks of cancer: The next generation, 2011.

Hans, S., Kaslin, J., Freudenreich, D., and Brand, M. Temporally-controlled site-specific recombination in zebrafish. *PloS one*, 4(2):e4640, jan 2009.

Heilmann, S., Ratnakumar, K., Langdon, E. M., Kansler, E. R., Kim, I. S., Campbell, N. R., Perry, E. B., McMahon, A. J., Kaufman, C. K., van Rooijen, E., Lee, W., Iacobuzio-Donahue, C. A., Hynes, R. O., Zon, L. I., Xavier, J. B., and White, R. M. A Quantitative System for Studying Metastasis Using Transparent Zebrafish. *Cancer research*, 75(20):4272–82, oct 2015.

Hill, J. T., Demarest, B. L., Bisgrove, B. W., Su, Y. C., Smith, M., and Yost, H. J. Poly peak parser: Method and software for identification of unknown indels using sanger sequencing of polymerase chain reaction products. *Developmental Dynamics*, 243(12): 1632–1636, 2014.

Hiratsuka, S., Minowa, O., Kuno, J., Noda, T., and Shibuya, M. Flt-1 lacking the tyrosine kinase domain is sufficient for normal development and angiogenesis in mice. *Proceedings of the National Academy of Sciences of the United States of America*, 95(16): 9349–54, aug 1998.

Hisano, Y., Ota, S., and Kawahara, A. Genome editing using artificial site-specific nucleases in zebrafish. *Development, growth & differentiation*, 56(1):26–33, jan 2014.

Honda, H., Oda, H., Nakamoto, T., Honda, Z., Sakai, R., Suzuki, T., Saito, T., Nakamura, K., Nakao, K., Ishikawa, T., Katsuki, M., Yazaki, Y., and Hirai, H. Cardiovascular anomaly, impaired actin bundling and resistance to Src-induced transformation in mice lacking p130Cas. *Nature genetics*, 19(4):361–5, aug 1998.

Hoshijima, K., Jurynec, M. J., and Grunwald, D. J. Precise Editing of the Zebrafish Genome Made Simple and Efficient. *Developmental Cell*, 36(6):654–667, mar 2016.

Hsu, P. D., Scott, D. A., Weinstein, J. A., Ran, F. A., Konermann, S., Agarwala, V., Li, Y., Fine, E. J., Wu, X., Shalem, O., Cradick, T. J., Marraffini, L. A., Bao, G., and Zhang, F. DNA targeting specificity of RNA-guided Cas9 nucleases. *Nature biotechnology*, 31 (9):827–32, sep 2013.

Hu, T.-H., Huang, C.-C., Lin, P.-R., Chang, H.-W., Ger, L.-P., Lin, Y.-W., Changchien, C.-S., Lee, C.-M., and Tai, M.-H. Expression and prognostic role of tumor suppressor gene PTEN/MMAC1/TEP1 in hepatocellular carcinoma. *Cancer*, 97(8):1929–1940, apr 2003.

Huang, W.-C., Hsieh, Y.-S., Chen, I.-H., Wang, C.-H., Chang, H.-W., Yang, C.-C., Ku, T.-H., Yeh, S.-R., and Chuang, Y.-J. Combined use of MS-222 (tricaine) and isoflurane extends anesthesia time and minimizes cardiac rhythm side effects in adult zebrafish. *Zebrafish*, 7(3):297–304, sep 2010.

Huisken, J. and Stainier, D. Y. R. Selective plane illumination microscopy techniques in developmental biology. *Development (Cambridge, England)*, 136(12):1963–75, jun 2009.

Hwang, W. Y., Fu, Y., Reyon, D., Maeder, M. L., Tsai, S. Q., Sander, J. D., Peterson, R. T., Yeh, J.-R. J., and Joung, J. K. Efficient genome editing in zebrafish using a CRISPR-Cas system. *Nature biotechnology*, 31(3):227–9, mar 2013.

Irion, U., Krauss, J., and Nüsslein-Volhard, C. Precise and efficient genome editing in zebrafish using the CRISPR/Cas9 system. *Development (Cambridge, England)*, 141 (24):4827–30, dec 2014.

Isogai, S., Horiguchi, M., and Weinstein, B. The vascular anatomy of the developing zebrafish: an atlas of embryonic and early larval development. - PubMed - NCBI. *Developmental Biology*, 20(2):278–301, 2001.

Ivy, S. P., Wick, J. Y., and Kaufman, B. M. An overview of small-molecule inhibitors of VEGFR signaling. *Nature reviews. Clinical oncology*, 6(10):569–579, 2009.

Iyer, N. V., Kotch, L. E., Agani, F., Leung, S. W., Laughner, E., Wenger, R. H., Gassmann, M., Gearhart, J. D., Lawler, A. M., Yu, A. Y., and Semenza, G. L. Cellular and developmental control of O2 homeostasis by hypoxia-inducible factor 1 alapha. *Genes & development*, 12(2):149–62, jan 1998.

Jain, R. K., Munn, L. L., and Fukumura, D. DISSECTING TUMOUR PATHOPHYSIOLOGY USING INTRAVITAL MICROSCOPY. *Nature Reviews Cancer*, 2(4):266–276, apr 2002.

Jao, L.-E., Wente, S. R., and Chen, W. Efficient multiplex biallelic zebrafish genome editing using a CRISPR nuclease system. *Proceedings of the National Academy of Sciences of the United States of America*, 110(34):13904–9, aug 2013.

Jopling, C., Suñé, G., Faucherre, A., Fabregat, C., and Izpisua Belmonte, J. C. Hypoxia Induces Myocardial Regeneration in Zebrafish. *Circulation*, 126(25), 2012.

Joung, J. K. and Sander, J. D. TALENs: a widely applicable technology for targeted genome editing. *Nature reviews. Molecular cell biology*, 14(1):49–55, jan 2013.

Kak, A. C. and Slaney, M. *Principles of computerized tomographic imaging*. IEEE Press, 1988.

Kearse, M., Moir, R., Wilson, A., Stones-Havas, S., Cheung, M., Sturrock, S., Buxton, S., Cooper, A., Markowitz, S., Duran, C., Thierer, T., Ashton, B., Meintjes, P., and Drummond, A. Geneious Basic: An integrated and extendable desktop software platform for the organization and analysis of sequence data. *Bioinformatics*, 28(12):1647–1649, 2012.

Kerschnitzki, M., Kollmannsberger, P., Burghammer, M., Duda, G. N., Weinkamer, R., Wagermaier, W., and Fratzl, P. Architecture of the osteocyte network correlates with bone material quality. *Journal of Bone and Mineral Research*, 28(8):1837–1845, 2013.

Kim, K. J., Li, B., Winer, J., Armanini, M., Gillett, N., Phillips, H. S., and Ferrara, N. Inhibition of vascular endothelial growth factor-induced angiogenesis suppresses tumour growth in vivo. *Nature*, 362(6423):841–844, apr 1993.

Kimmel, C. B., Ballard, W. W., Kimmel, S. R., Ullmann, B., and Schilling, T. F. Stages of embryonic development of the zebrafish. *Developmental dynamics : an official publication of the American Association of Anatomists*, 203(3):253–310, jul 1995.

Kiyokawa, E., Hara, S., Nakamura, T., and Matsuda, M. Fluorescence (F{ö}rster) resonance energy transfer imaging of oncogene activity in living cells. *Cancer Sci*, 97(1): 8–15, jan 2006.

Konantz, M., Balci, T. B., Hartwig, U. F., Dellaire, G., André, M. C., Berman, J. N., and Lengerke, C. Zebrafish xenografts as a tool for in vivo studies on human cancer. *Annals of the New York Academy of Sciences*, 1266(1):124–137, aug 2012.

Konerding, M. A., Malkusch, W., Klapthor, B., van Ackern, C., Fait, E., Hill, S. A., Parkins, C., Chaplin, D. J., Presta, M., and Denekamp, J. Evidence for characteristic vascular patterns in solid tumours: quantitative studies using corrosion casts. *British journal of cancer*, 80(5-6):724–32, may 1999.

Krauss, J., Astrinides, P., Frohnhofer, H. J., Walderich, B., and C, N.-V. transparent, a gene affecting stripe formation in Zebrafish, encodes the mitochondrial protein Mpv17 that is required for iridophore survival. *Biology Open*, 0:1–8, may 2013.

Lecoq, J. and Schnitzer, M. J. An infrared fluorescent protein for deeper imaging. *Nature Publishing Group*, 29, 2011.

Lewis, B. C., Klimstra, D. S., Socci, N. D., Xu, S., Koutcher, J. A., and Varmus, H. E. The absence of p53 promotes metastasis in a novel somatic mouse model for hepatocellular carcinoma. *Molecular and cellular biology*, 25(4):1228–37, feb 2005.

Li, J., Zhang, B.-b., Ren, Y.-g., Gu, S.-y., Xiang, Y.-h., and Du, J.-l. Intron targeting-mediated and endogenous gene integrity-maintaining knockin in zebrafish using the CRISPR/Cas9 system. *Cell research*, 25(5):634–7, may 2015.

Li, Z., Huang, X., Zhan, H., Zeng, Z., Li, C., Spitsbergen, J. M., Meierjohann, S., Schartl, M., and Gong, Z. Inducible and repressable oncogene-addicted hepatocellular carcinoma in Tet-on xmrk transgenic zebrafish. *Journal of hepatology*, 56(2):419–25, feb 2012.

Li, Z., Zheng, W., Wang, Z., Zeng, Z., Zhan, H., Li, C., Zhou, L., Yan, C., Spitsbergen, J. M., and Gong, Z. A transgenic zebrafish liver tumor model with inducible Myc expression reveals conserved Myc signatures with mammalian liver tumors. *Disease models & mechanisms*, 6(2):414–23, mar 2013.

Lieschke, G. J. and Currie, P. D. Animal models of human disease: zebrafish swim into view. *Nature reviews. Genetics*, 8(5):353–67, may 2007.

Lister, J. A. Zebrafish Mitf-related gene nacre. *Development*, 126:3757–3767, 1999.

Liu, Q., Wang, S., Ying, L., Peng, X., Zhu, Y., and Liang, D. Adaptive dictionary learning in sparse gradient domain for image recovery. *IEEE Transactions on Image Processing*, 22(12):4652–4663, 2013.

Lu, J.-W., Ho, Y.-J., Yang, Y.-J., Liao, H.-A., Ciou, S.-C., Lin, L.-I., and Ou, D.-L. Zebrafish as a disease model for studying human hepatocellular carcinoma. *World journal of gastroenterology*, 21(42):12042–58, nov 2015.

Lustig, M., Donoho, D., and Pauly, J. M. Sparse MRI: The application of compressed sensing for rapid MR imaging. *Magnetic resonance in medicine : official journal of the Society of Magnetic Resonance in Medicine / Society of Magnetic Resonance in Medicine*, 58(6):1182–95, dec 2007.

MacRae, C. A. and Peterson, R. T. Zebrafish as tools for drug discovery. *Nature Reviews Drug Discovery*, 14(10):721–731, sep 2015.

Matthews, M. and Varga, Z. M. Anesthesia and euthanasia in zebrafish. *ILAR journal / National Research Council, Institute of Laboratory Animal Resources*, 53(2):192–204, jan 2012.

Maxwell, P. H., Wiesener, M. S., Chang, G. W., Clifford, S. C., Vaux, E. C., Cockman, M. E., Wykoff, C. C., Pugh, C. W., Maher, E. R., and Ratcliffe, P. J. The tumour suppressor protein VHL targets hypoxia-inducible factors for oxygen-dependent proteolysis. *Nature*, 399(6733):271–5, may 1999.

Maxwell, P. H., Pugh, C. W., and Ratcliffe, P. J. Activation of the HIF pathway in cancer. *Current opinion in genetics & development*, 11(3):293–9, jun 2001.

Mayer, B. J. SH3 domains: complexity in moderation. *Journal of cell science*, 114(Pt 7): 1253–63, apr 2001.

Mayer, J., Robert-Moreno, A., Danuser, R., Stein, J. V., Sharpe, J., and Swoger, J. OPTiSPIM: integrating optical projection tomography in light sheet microscopy extends specimen characterization to nonfluorescent contrasts. *Optics Letters*, 39:1053–1056, 2014.

McDonald, D. M. and Choyke, P. L. Imaging of angiogenesis: from microscope to clinic. *Nature medicine*, 9(6):713–725, 2003.

McFarland, W. N. A study of the effects of anaesthetics on the behaviour and physiology of fishes. *Publications of the Institute of Marine Sciences*, 6:22–55, 1959.

McGinty, J., Tahir, K. B., Laine, R., Talbot, C. B., Dunsby, C., Neil, M. A., Quintana, L., Swoger, J., Sharpe, J., and French, P. M. Fluorescence lifetime optical projection tomography. *J Biophotonics*, 1(5):390–394, oct 2008.

McGinty, J., Taylor, H. B., Chen, L., Bugeon, L., Lamb, J. R., Dallman, M. J., and French, P. M. In vivo fluorescence lifetime optical projection tomography. *Biomed Opt Express*, 2(5):1340–1350, 2011.

McMahon, G. a., Petitclerc, E., Stefansson, S., Smith, E., Wong, M. K., Westrick, R. J., Ginsburg, D., Brooks, P. C., and Lawrence, D. a. Plasminogen activator inhibitor-1 regulates tumor growth and angiogenesis. *The Journal of biological chemistry*, 276 (36):33964–33968, 2001.

Michailidou, C., Jones, M., Walker, P., Kamarashev, J., Kelly, A., and Hurlstone, A. F. L. Dissecting the roles of Raf- and PI3K-signalling pathways in melanoma formation and progression in a zebrafish model. *Disease models & mechanisms*, 2(7-8):399–411, 2009.

Michalska-Małecka, K., Kabiesz, A., Nowak, M., and Śpiewak, D. Age related macular degeneration – challenge for future: Pathogenesis and new perspectives for the treatment. *European Geriatric Medicine*, 6(1):69–75, feb 2015.

Miller, J. C., Tan, S., Qiao, G., Barlow, K. A., Wang, J., Xia, D. F., Meng, X., Paschon, D. E., Leung, E., Hinkley, S. J., Dulay, G. P., Hua, K. L., Ankoudinova, I., Cost, G. J., Urnov, F. D., Zhang, H. S., Holmes, M. C., Zhang, L., Gregory, P. D., and Rebar, E. J. A TALE nuclease architecture for efficient genome editing. *Nature biotechnology*, 29 (2):143–8, feb 2011.

Moy, A. J., White, S. M., Indrawan, E. S., Lotfi, J., Nudelman, M. J., Costantini, S. J., Agarwal, N., Jia, W., Kelly, K. M., Sorg, B. S., and Choi, B. Wide-field functional imaging of blood flow and hemoglobin oxygen saturation in the rodent dorsal window chamber. *Microvascular research*, 82(3):199–209, nov 2011.

Nguyen, A. T., Emelyanov, A., Koh, C. H. V., Spitsbergen, J. M., Lam, S. H., Mathavan, S., Parinov, S., and Gong, Z. A high level of liver-specific expression of oncogenic Kras(V12) drives robust liver tumorigenesis in transgenic zebrafish. *Disease models & mechanisms*, 4(6):801–13, nov 2011.

Nguyen, A. T., Emelyanov, A., Koh, C. H. V., Spitsbergen, J. M., Parinov, S., and Gong, Z. An inducible kras(V12) transgenic zebrafish model for liver tumorigenesis and chemical drug screening. *Disease models & mechanisms*, 5(1):63–72, jan 2012.

Nick, A. M., Stone, R. L., Armaiz-Pena, G., Ozpolat, B., Tekedereli, I., Graybill, W. S., Landen, C. N., Villares, G., Vivas-Mejia, P., Bottsford-Miller, J., Kim, H. S., Lee, J.-S., Kim, S. M., Baggerly, K. A., Ram, P. T., Deavers, M. T., Coleman, R. L., Lopez-Berestein, G., and Sood, A. K. Silencing of p130cas in ovarian carcinoma: a novel mechanism for tumor cell death. *Journal of the National Cancer Institute*, 103(21): 1596–612, nov 2011.

Nogueira, C., Kim, K.-H., Sung, H., Paraiso, K. H. T., Dannenberg, J.-H., Bosenberg, M., Chin, L., and Kim, M. Cooperative interactions of PTEN deficiency and RAS activation in melanoma metastasis. *Oncogene*, 29(47):6222–32, nov 2010.

Ntziachristos, V., Ripoll, J., Wang, L. V., and Weissleder, R. Looking and listening to light: the evolution of whole-body photonic imaging. *Nature biotechnology*, 23(3): 313–320, 2005.

Palmer, G. M., Fontanella, A. N., Shan, S., Hanna, G., Zhang, G., Fraser, C. L., and Dewhirst, M. W. In vivo optical molecular imaging and analysis in mice using dorsal window chamber models applied to hypoxia, vasculature and fluorescent reporters. *Nature Protocols*, 6(9):1355–1366, aug 2011.

Papetti, M. and Herman, I. M. Mechanisms of normal and tumor-derived angiogenesis. *American journal of physiology. Cell physiology*, 282(5):C947–70, 2002.

Patton, E. E., Widlund, H. R., Kutok, J. L., Kopani, K. R., Amatruda, J. F., Murphey, R. D., Berghmans, S., Mayhall, E. A., Traver, D., Fletcher, C. D. M., Aster, J. C., Granter, S. R., Look, A. T., Lee, C., Fisher, D. E., and Zon, L. I. BRAF mutations are sufficient to promote nevi formation and cooperate with p53 in the genesis of melanoma. *Current biology : CB*, 15(3):249–54, mar 2005.

Phelps, M. E. *PET: Physics, Instrumentation, and Scanners*. Springer Science & Business Media, 2006. ISBN 0387349464.

Potter, S. M., Pine, J., and Fraser, S. E. Neural transplant staining with DiI and vital imaging by 2-photon laser-scanning microscopy. *Scanning Microsc Suppl*, 10:189–199, 1996.

Pugh, C. W. and Ratcliffe, P. J. Regulation of angiogenesis by hypoxia: role of the HIF system. *Nature medicine*, 9(6):677–84, jun 2003.

Reyon, D., Tsai, S. Q., Khayter, C., Foden, J. a., Sander, J. D., and Joung, J. K. FLASH assembly of TALENs for high-throughput genome editing. *Nature Biotechnology*, 30 (5):460–465, may 2012.

Risau, W. Mechanisms of angiogenesis. *Nature*, 386(6626):671–674, 1997.

Risau, W. and Flamme, I. Vasculogenesis. *Annual review of cell and developmental biology*, 11:73–91, 1995.

Roberts, P. J. and Der, C. J. Targeting the Raf-MEK-ERK mitogen-activated protein kinase cascade for the treatment of cancer. *Oncogene*, 26(22):3291–310, may 2007.

Rombough, P. Gills are needed for ionoregulation before they are needed for O(2) uptake in developing zebrafish, Danio rerio. *The Journal of experimental biology*, 205(Pt 12): 1787–1794, 2002.

Ross, L. G. and Ross, B., editors. *Anaesthetic and Sedative Techniques for Aquatic Animals*. Blackwell Publishing Ltd., Oxford, UK, may 2008. ISBN 9781444302264.

Rudin, L. I., Osher, S., and Fatemi, E. Nonlinear total variation based noise removal algorithms. *PhysicaD*, 60:259–268, 1992.

Sander, J. D. and Joung, J. K. CRISPR-Cas systems for editing, regulating and targeting genomes. *Nature biotechnology*, 32(4):347–55, apr 2014.

Sang, N., Stiehl, D. P., Bohensky, J., Leshchinsky, I., Srinivas, V., and Caro, J. MAPK signaling up-regulates the activity of hypoxia-inducible factors by its effects on p300. *The Journal of biological chemistry*, 278(16):14013–9, apr 2003.

Santi, P. A. Light sheet fluorescence microscopy: a review. *The journal of histochemistry and cytochemistry : official journal of the Histochemistry Society*, 59(2):129–38, feb 2011.

Semela, D. and Dufour, J.-F. Angiogenesis and hepatocellular carcinoma. *Journal of hepatology*, 41(5):864–80, nov 2004.

Semenza, G. L. Hypoxia, clonal selection, and the role of HIF-1 in tumor progression. *Critical reviews in biochemistry and molecular biology*, 35(2):71–103, jan 2000.

Semenza, G. L. Signal transduction to hypoxia-inducible factor 1. *Biochemical Pharmacology*, 64(5-6):993–998, sep 2002.

Serbedzija, G. N., Flynn, E., and Willett, C. E. Zebrafish angiogenesis: A new model for drug screening. *Angiogenesis*, 3(4):353–359, dec 1999.

Shalaby, F., Rossant, J., Yamaguchi, T. P., Gertsenstein, M., Wu, X. F., Breitman, M. L., and Schuh, A. C. Failure of blood-island formation and vasculogenesis in Flk-1-deficient mice. *Nature*, 376(6535):62–6, jul 1995.

Sharpe, J. Optical projection tomography as a new tool for studying embryo anatomy. *J Anat*, 202(2):175–181, feb 2003.

Sharpe, J., Ahlgren, U., Perry, P., Hill, B., Ross, A., Hecksher-Sorensen, J., Baldock, R., and Davidson, D. Optical projection tomography as a tool for 3D microscopy and gene expression studies. *Science*, 296(5567):541–545, apr 2002.

Sidky, E. Y. and Pan, X. Image reconstruction in circular cone-beam computed tomography by constrained, total-variation minimization. *Physics in medicine and biology*, 53 (17):4777–807, sep 2008.

Sidky, E. Y., Kao, C.-M., and Pan, X. Accurate image reconstruction from few-views and limited-angle data in divergent-beam CT. *Journal of the Optical Society of America A. Optics, Image Sci ence and Vision.*, pages 119–139, apr 2009.

Sprague, J., Bayraktaroglu, L., Clements, D., Conlin, T., Fashena, D., Frazer, K., Haendel, M., Howe, D. G., Mani, P., Ramachandran, S., Schaper, K., Segerdell, E., Song, P., Sprunger, B., Taylor, S., Van Slyke, C. E., and Westerfield, M. The Zebrafish Information Network: the zebrafish model organism database. *Nucleic acids research*, 34 (Database issue):D581–5, 2006.

Staton, C. A., Reed, M. W. R., and Brown, N. J. A critical analysis of current in vitro and in vivo angiogenesis assays, 2009.

Stoletov, K. and Klemke, R. Catch of the day: zebrafish as a human cancer model. *Oncogene*, 27(33):4509–4520, jul 2008.

Stoletov, K., Montel, V., Lester, R. D., Gonias, S. L., and Klemke, R. High-resolution imaging of the dynamic tumor cell vascular interface in transparent zebrafish. *Proceedings of the National Academy of Sciences*, 104(44):17406–17411, oct 2007.

Sun, L., Nguyen, A. T., Spitsbergen, J. M., and Gong, Z. Myc-induced liver tumors in transgenic zebrafish can regress in tp53 null mutation. *PloS one*, 10(1):e0117249, 2015.

Sun, P., Zhang, Y., Yu, F., Parks, E., Lyman, A., Wu, Q., Ai, L., Hu, C.-H., Zhou, Q., Shung, K., Lien, C.-L., and Hsiai, T. K. Micro-electrocardiograms to study post-ventricular amputation of zebrafish heart. *Annals of biomedical engineering*, 37(5): 890–901, may 2009.

Talks, K. L., Turley, H., Gatter, K. C., Maxwell, P. H., Pugh, C. W., Ratcliffe, P. J., and Harris, A. L. The expression and distribution of the hypoxia-inducible factors HIF-1alpha and HIF-2alpha in normal human tissues, cancers, and tumor-associated macrophages. *The American journal of pathology*, 157(2):411–21, aug 2000.

Taylor, J. S., Braasch, I., Frickey, T., Meyer, A., and de Peer, Y. V. Genome Duplication, a Trait Shared by 22,000 Species of Ray-Finned Fish. *Genome Research*, 13(3):382–390, mar 2003.

Thomlinson, R. H. and Gray, L. H. The histological structure of some human lung cancers and the possible implications for radiotherapy. *British journal of cancer*, 9(4):539–49, dec 1955.

Tosic, I. and Frossard, P. Dictionary Learning, What is the right representation for my signal? *Signal Processing Magazine, IEEE*, 28(2):27–38, 2011.

Vakoc, B. J., Lanning, R. M., Tyrrell, J. A., Padera, T. P., Bartlett, L. A., Stylianopoulos, T., Munn, L. L., Tearney, G. J., Fukumura, D., Jain, R. K., and Bouma, B. E. Three-dimensional microscopy of the tumor microenvironment in vivo using optical frequency domain imaging. *Nature Medicine*, 15(10):1219–1223, oct 2009.

van Der Laak, J. A., Pahlplatz, M. M., Hanselaar, A. G., and de Wilde, P. C. Hue-saturation-density (HSD) model for stain recognition in digital images from transmitted light microscopy. *Cytometry*, 39(4):275–84, apr 2000.

Villanueva, A. and Llovet, J. M. Targeted therapies for hepatocellular carcinoma. *Gastroenterology*, 140(5):1410–26, may 2011.

Wang, J., Kobayashi, T., Floc'h, N., Kinkade, C. W., Aytes, A., Dankort, D., Lefebvre, C., Mitrofanova, A., Cardiff, R. D., McMahon, M., Califano, A., Shen, M. M., and Abate-Shen, C. B-Raf activation cooperates with PTEN loss to drive c-Myc expression in advanced prostate cancer. *Cancer research*, 72(18):4765–76, sep 2012.

Wang, Z., Bovik, A. C., Sheikh, H. R., and Simoncelli, E. P. Image quality assessment: from error visibility to structural similarity. *IEEE transactions on image processing : a publication of the IEEE Signal Processing Society*, 13(4):600–12, apr 2004.

Westerfield, M. *The zebrafish book: A guide for the laboratory use of zebrafish (Danio rerio)*. University of Oregon Press, Eugene, 4th ed. edition, 2000.

White, R. M., Sessa, A., Burke, C., Bowman, T., LeBlanc, J., Ceol, C., Bourque, C., Dovey, M., Goessling, W., Burns, C. E., and Zon, L. I. Transparent adult zebrafish as a tool for in vivo transplantation analysis. *Cell Stem Cell*, 2(2):183–189, feb 2008.

White, R., Rose, K., and Zon, L. Zebrafish cancer: the state of the art and the path forward. *Nature reviews. Cancer*, 13(9):624–36, sep 2013.

Witmer, A. N., Vrensen, G. F. J. M., Van Noorden, C. J. F., and Schlingemann, R. O. Vascular endothelial growth factors and angiogenesis in eye disease. *Progress in retinal and eye research*, 22(1):1–29, jan 2003.

Wood, J. M., Bold, G., Buchdunger, E., Cozens, R., Ferrari, S., Frei, J., Hofmann, F., Mestan, J., Mett, H., O'Reilly, T., Persohn, E., Rösel, J., Schnell, C., Stover, D., Theuer, A., Towbin, H., Wenger, F., Woods-Cook, K., Menrad, A., Siemeister, G., Schirner, M., Thierauch, K. H., Schneider, M. R., Drevs, J., Martiny-Baron, G., Totzke, F., and Marmé, D. PTK787/ZK 222584, a novel and potent inhibitor of vascular endothelial growth factor receptor tyrosine kinases, impairs vascular endothelial growth factor-induced responses and tumor growth after oral administration. *Cancer research*, 60(8): 2178–89, apr 2000.

World Health Organisation. Global estimates of visual impairment. *British Journal of Opthalmology Online*, 2010.

Yin, Y. and Shen, W. H. PTEN: a new guardian of the genome. *Oncogene*, 27(41): 5443–5453, sep 2008.

Zheng, W., Xu, H., Lam, S. H., Luo, H., Karuturi, R. K. M., and Gong, Z. Transcriptomic analyses of sexual dimorphism of the zebrafish liver and the effect of sex hormones. *PloS one*, 8(1):e53562, jan 2013.

Zheng, W., Li, Z., Nguyen, A. T., Li, C., Emelyanov, A., and Gong, Z. Xmrk, kras and myc transgenic zebrafish liver cancer models share molecular signatures with subsets of human hepatocellular carcinoma. *PloS one*, 9(3):e91179, jan 2014.

Zhong, H., Chiles, K., Feldser, D., Laughner, E., Hanrahan, C., Georgescu, M. M., Simons, J. W., and Semenza, G. L. Modulation of hypoxia-inducible factor 1alpha expression by the epidermal growth factor/phosphatidylinositol 3-kinase/PTEN/AKT/FRAP pathway in human prostate cancer cells: implications for tumor angiogenesis and therapeutics. *Cancer research*, 60(6):1541–5, mar 2000.

Zimmermann, G., Papke, B., Ismail, S., Vartak, N., Chandra, A., Hoffmann, M., Hahn, S. A., Triola, G., Wittinghofer, A., Bastiaens, P. I. H., and Waldmann, H. Small molecule inhibition of the KRAS-PDEδ interaction impairs oncogenic KRAS signalling. *Nature*, 497(7451):638–42, may 2013.

Zon, L. I. and Peterson, R. T. In vivo drug discovery in the zebrafish. *Nature Reviews Drug Discovery*, 4(1):35–44, jan 2005.

Appendix

Video Legends

Video 1. Reconstructed OPT images of adult TraNac *Tg (KDR:mCherry: Fabp10- rtTA: TRE-eGFPKRAS^{V12})* zebrafish expressing liver specific eGFP-labelled tumour (green) and mCherry-labelled vasculature (red). (a) and (b) show rendered 3-D FBP reconstructions computed with 512 and 64 projections, respectively. (c) shows a CS-OPT reconstruction from 64 projections using the TwIST algorithm. (d) shows the "vesselness" of (c) after Hessian-based analysis and (e) shows the "final" segmented CS-OPT reconstruction with segmented vasculature following skeletonisation and dilation. Scale bar 2.5 mm.

Video 2. Representative reconstructed CS-OPT videos of adult TraNac *Tg (KDR:mCherry: Fabp10- rtTA:TRE-eGFPKRAS^{V12})* zebrafish following tumour induction for (a) one week, (b) two weeks and (c) three weeks, with (d) imaged after three weeks of induction plus a further week after removal of inducer treatment. Scale bar 5 mm. Each group (n=8).

Video 3. Representative reconstructed CS-OPT videos of cropped tumour regions from adult TraNac *Tg (KDR:mCherry: Fabp10- rtTA:TRE-eGFPKRAS^{V12})* zebrafish following tumour induction for (a) one, (b) two and (c) three weeks with (d) imaged after three weeks of induction plus a further week after removal of inducer treatment. Scale bar 2 mm. Each group (n=8).

Video 4. Fly-through videos for the reconstructed CS-OPT cropped tumour regions from representative adult TraNac *Tg (KDR:mCherry: Fabp10- rtTA:TRE-eGFPKRAS^{V12})* zebrafish following tumour induction for (a) one, (b) two and (c) three weeks with (d) imaged after three weeks of induction plus a further week after removal of inducer treatment. Red indicates vasculature 'outside' the tumour, orange indicates vascular 'inside' the tumour and green is the tumour. Scale bar 2 mm. Each group (n=8).

Video 5. Representative reconstructed CS-OPT movies corresponding to Figure 5.1 showing reconstructed images from the CS-OPT data of TraNac *Tg (KDR:mCherry)* zebrafish imaged in longitudinal study over 26 weeks showing images acquired at (a) 4, (b) 8, (c) 12 and (d) 26 weeks post fertilisation (wpf). Scale bar 2 mm.

Figures

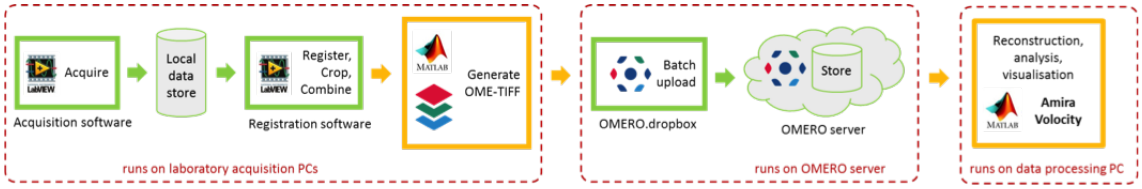

Figure A.1: Schematic of OPT data acquisition, registration, storage and reconstruction workflow.

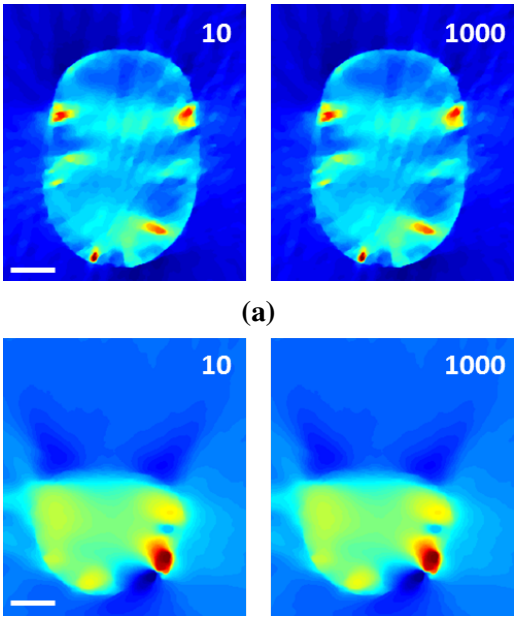

Figure A.2: Confirmation that the TwIST algorithm has converged during CS reconstruction when using only 10 iterations of the main algorithm (MaxiterA). The images show the cross-sectional reconstructions when MaxiterA is set to 10 or the default 1000 (value shown in top right hand corner of images) for both the vasculature (a) and tumour (b) channels. Scale bars 1 mm.

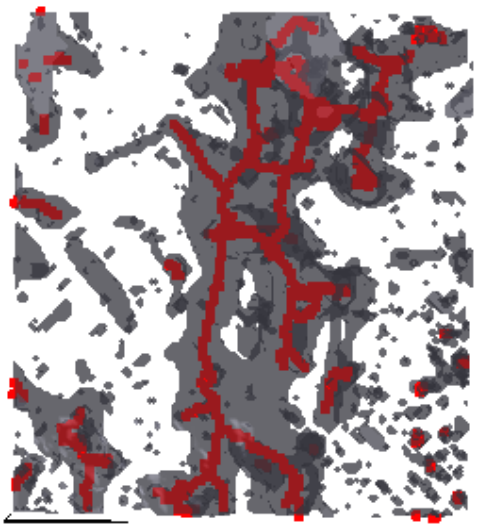

(a) Skeletonised

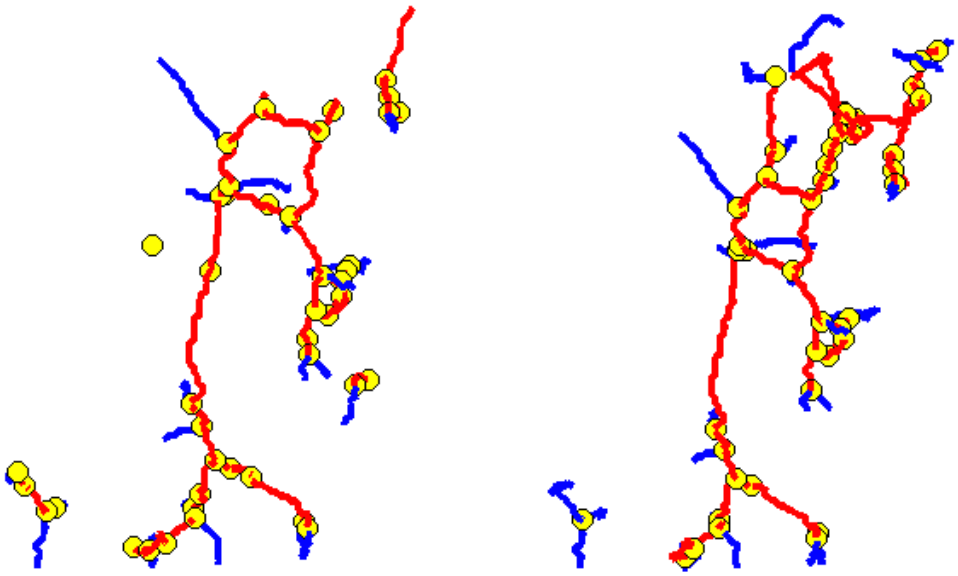

(b) Before Iterations **(c) After Iterations**

Figure A.3: Skeletonisation and vascular analysis of a region of the segmented tumour vasculature CS-OPT image using Matlab. (a) shows the segmented vasculature (grey) and the skeleton produced from the modified Matlab code Skeleton3D (red). (b) is the result from Skel2Graph3D, where connected vessels are in red, boundary vessels in blue and the branch points are yellow. This result is inaccurate and noisy, which is highlighted when comparing to (a) and also the iteratively cleaned skeleton using Graph2Skel3D (c).

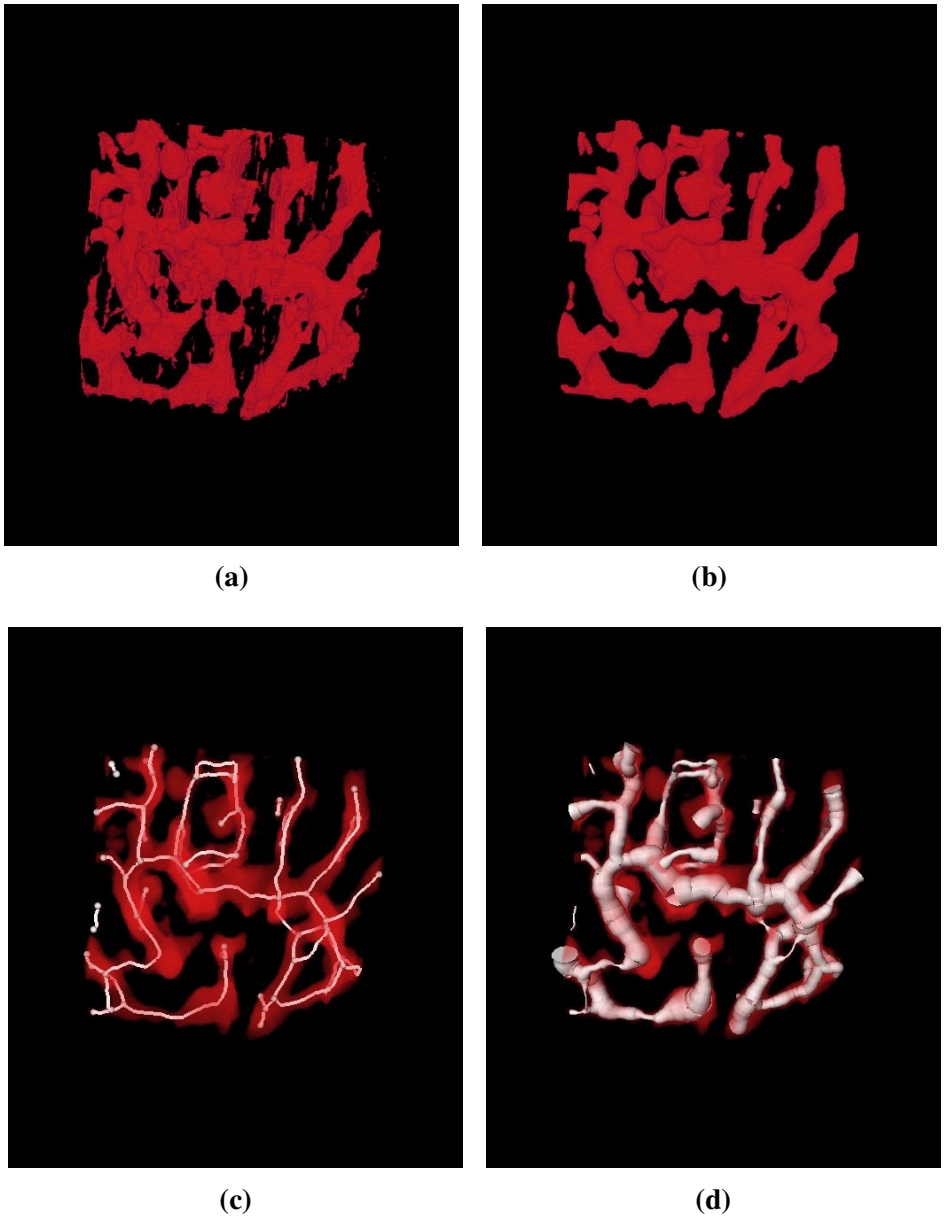

Figure A.4: Skeletonisation of a subregion of the segmented tumour vasculature CS-OPT image using Amira. (a) shows the segmented CS-OPT vasculature subregion imported into Amira and (b) is the subregion after the 3-dimensional median filter was applied to remove residual noise. (c) shows the extracted skeleton overlaid to the filtered CS-OPT image and (d) the skeleton dilated to correspond to the diameter value extracted from each vessel. These highlight the accuracy of the auto-skeleton tool.

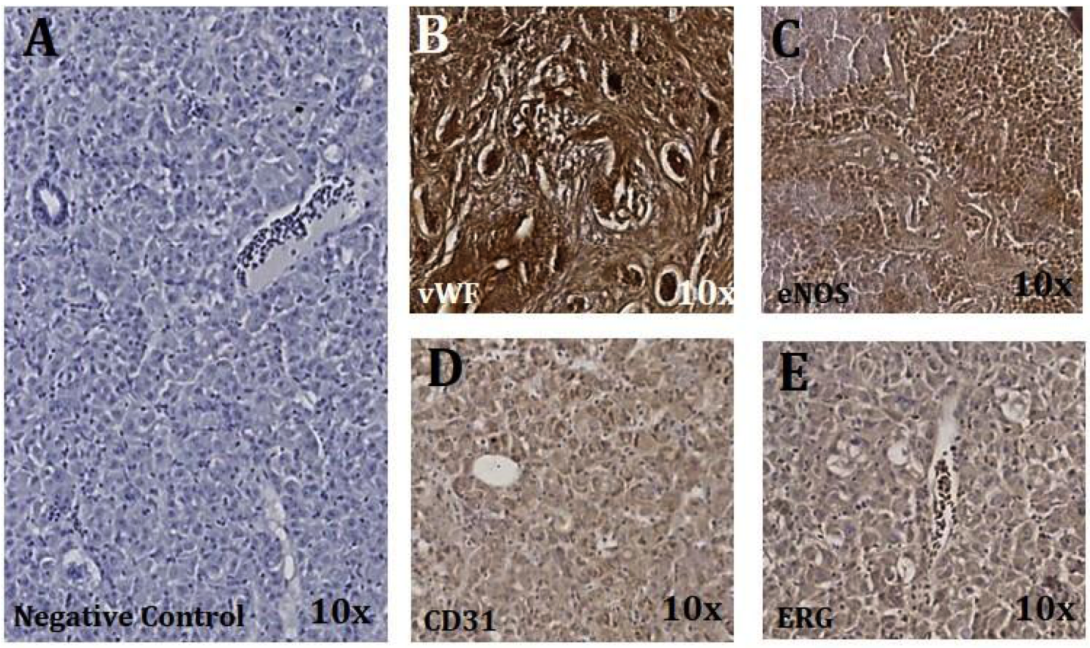

Figure A.5: Immunohistochemsitry of endothelial cells within the zebrafish liver using various marker antibodies to identify a specific stain with no cross- reaction. (A) is a negative control of a healthy liver, (B) vWF staining in healthy liver, (C) eNOS in healthy liver, (D) CD31 in liver tumour and (E) ERG in liver tumour. All tissues were subjected to antigen retrieval by citrate buffer and antibody concentrations of 1:100.

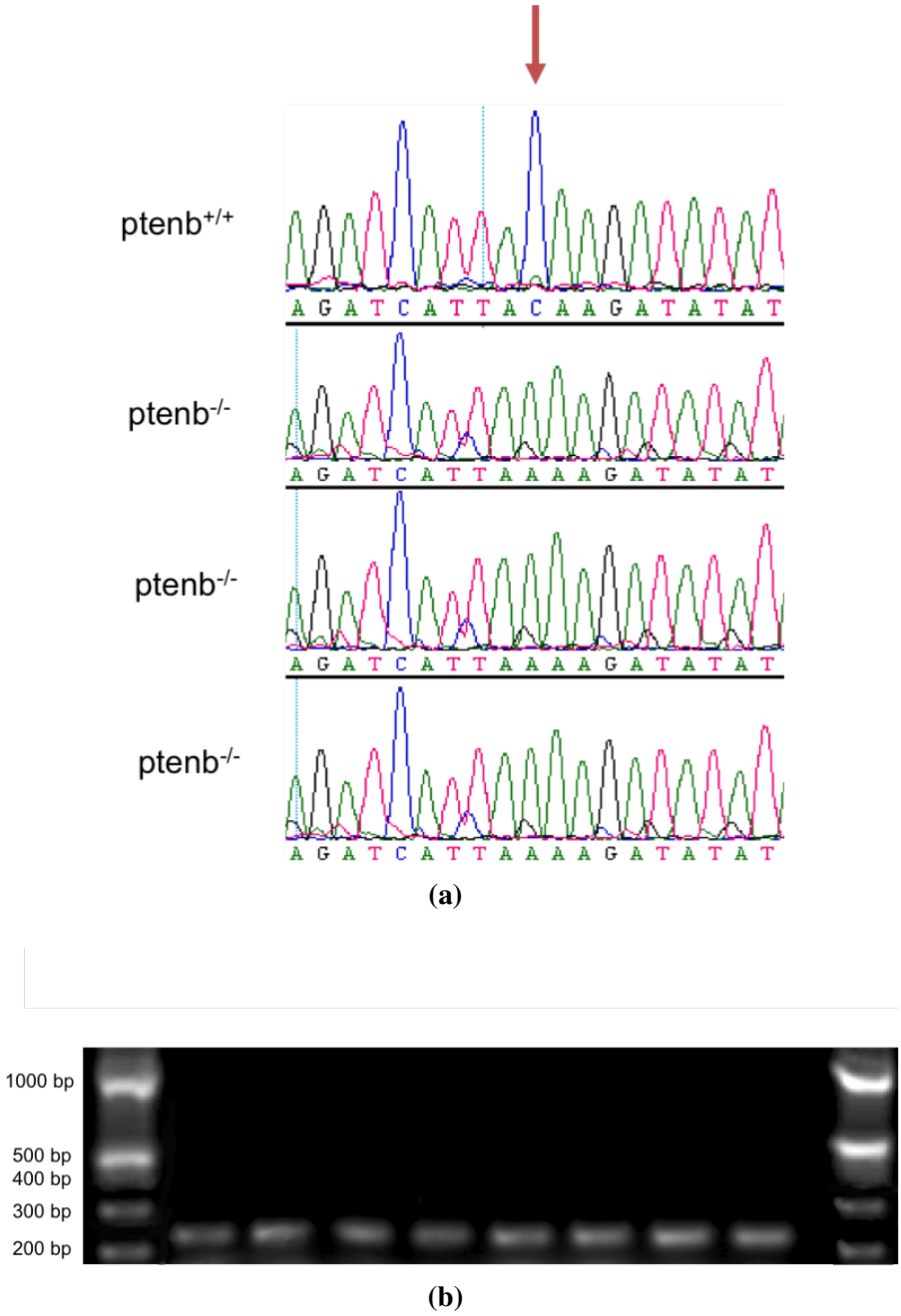

Figure A.6: Confirmation of the ptenb$^{-/-}$ zebrafish genotype. a) Shows sequencing chromatograms for the wild type control (ptenb$^{+/+}$) and 3 representative sequences for the 8 homozygous mutants (ptenb$^{-/-}$), where the red arrow indicates the position of the C>A point mutation within the mutant. b) is a verification of the eGFPKRAS^{V12} transgene presence through PCR followed by gel electrophoresis resulting in amplicons of ∼280 bp. All 8 zebrafish from the study are shown.

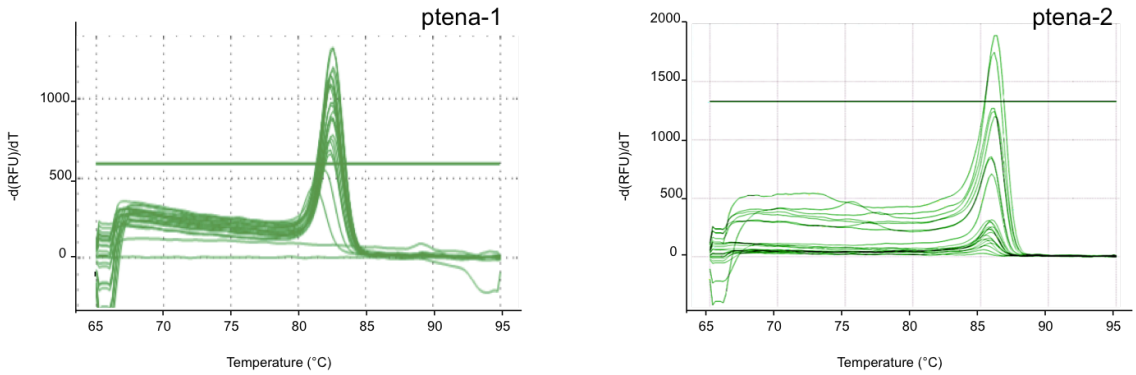

Figure A.7: HRMA to determine functional activity of CRISPRs for ptena using validated primers stated in Table 6.3. Melt peak graphs show both uninjected and injected samples for each gRNA, ptena-1 and ptena-2, as stated in the top right corner.

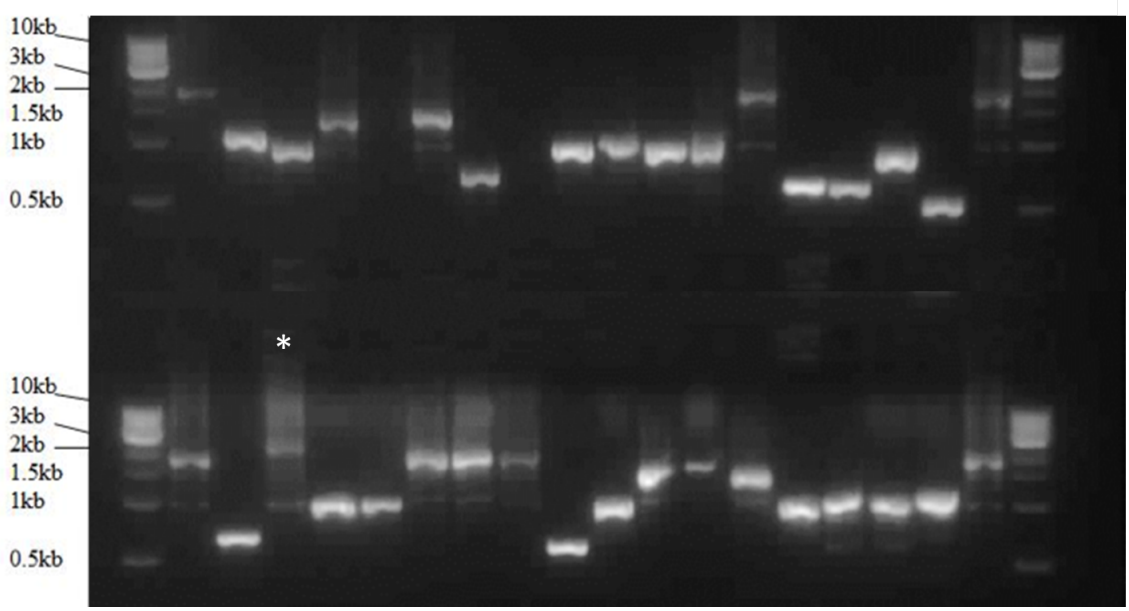

(a) ptenaL-left

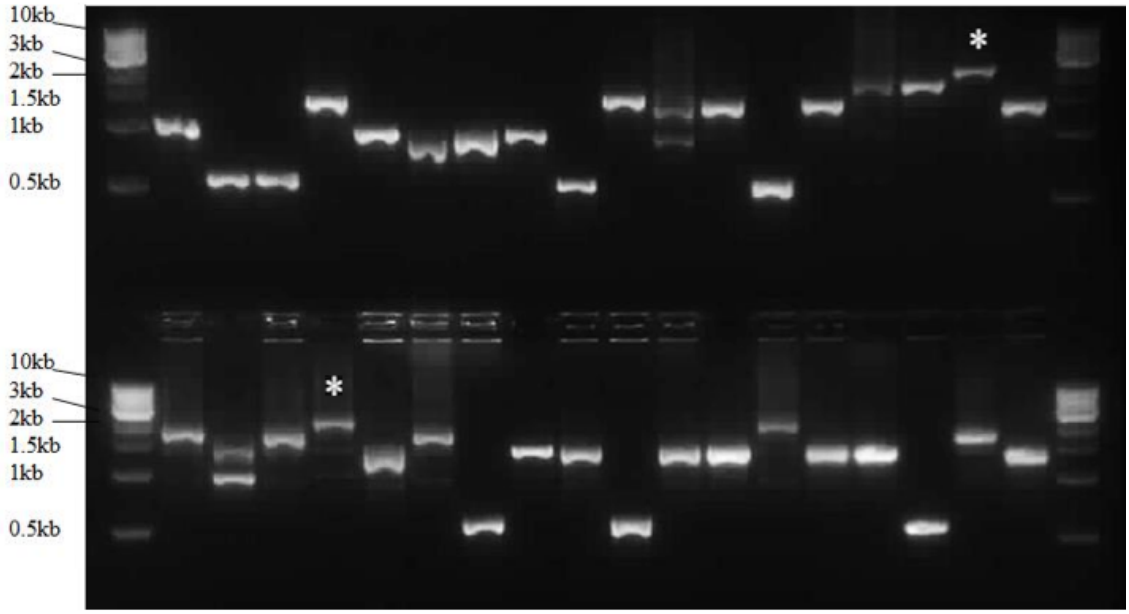

(b) ptenaL-right

Figure A.8: Verification of ptenaL-left (a) and ptenaL-right (b) colony PCR transcripts through 1.6% agarose gel electrophoresis, using a 1kb ladder. The 36 samples analysed show a clear variation in size, indicating a low efficiency in the FLASH TALENs protocol. However, one likely candidate for ptenaL-left (a) and two for ptenaL-right (b) are observed at approximately 2.1kb within these screen, labelled with asterisks. These were subsequently sequenced and verified as positive results.

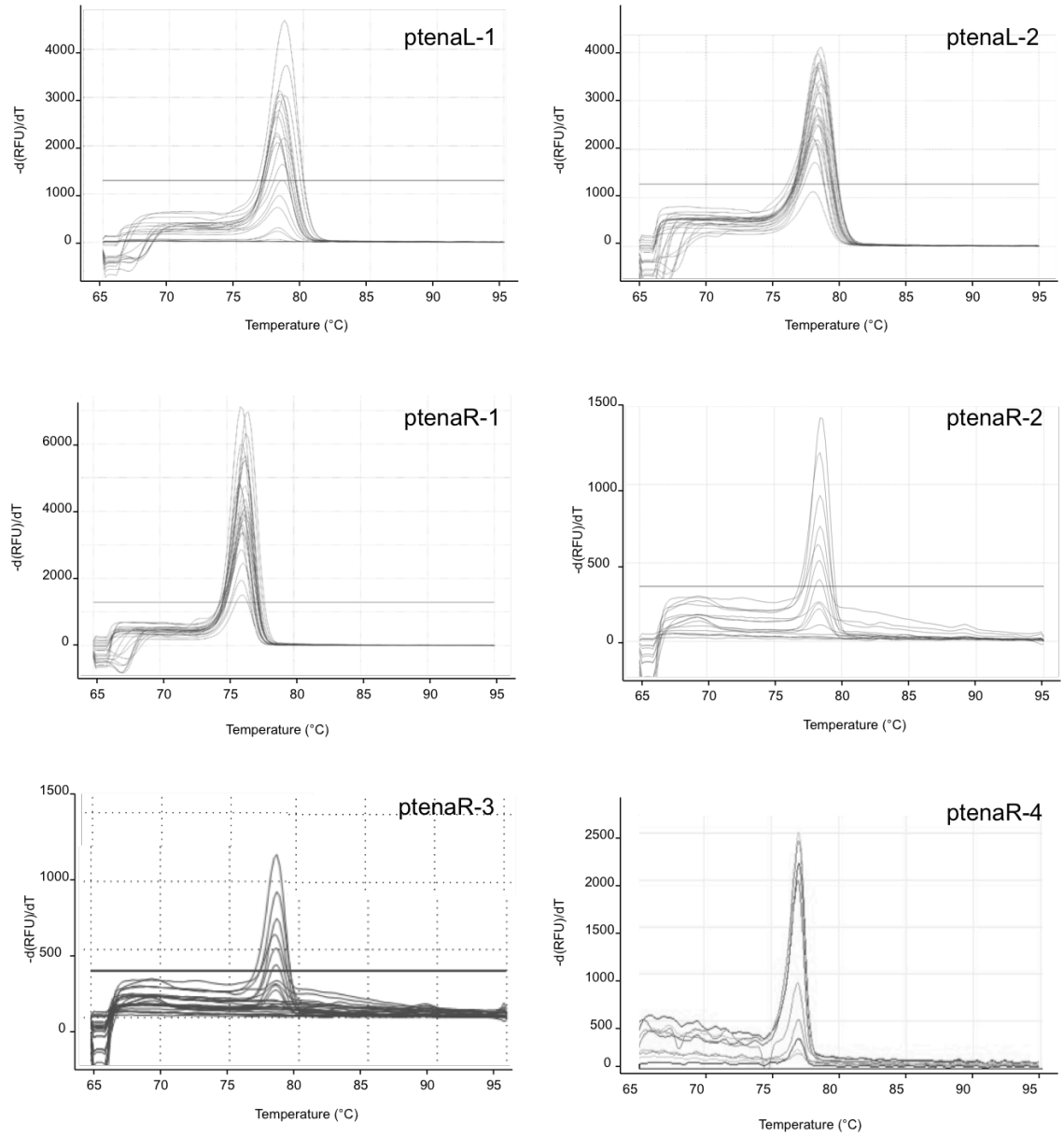

Figure A.9: HRMA to determine functional activity of initial CRISPRs for ptenaL and ptenaR using validated primers stated in Table 6.3. Melt peak graphs show both uninjected and injected samples for each gRNA, as stated in the top right corner.

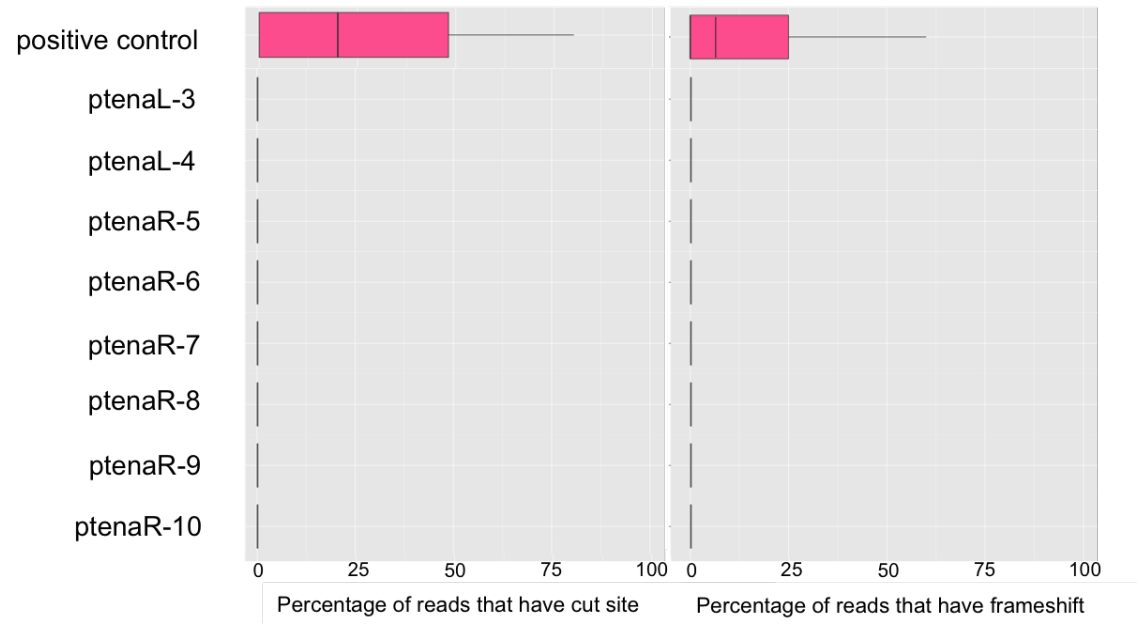

Figure A.10: Deep sequencing results of the attempted LoxP knock-in insertions using the additional CRISPRs, Table 6.4, and synthetic DNA, Figure 6.8, along with a positive CRISPR control from the Wilson Group (UCL). Percentage of reads that have a cut site and have a frameshift are shown, which do not include those reads marked as primer dimers. Results show box plots, with the median and interquartile range along with the extreme values.

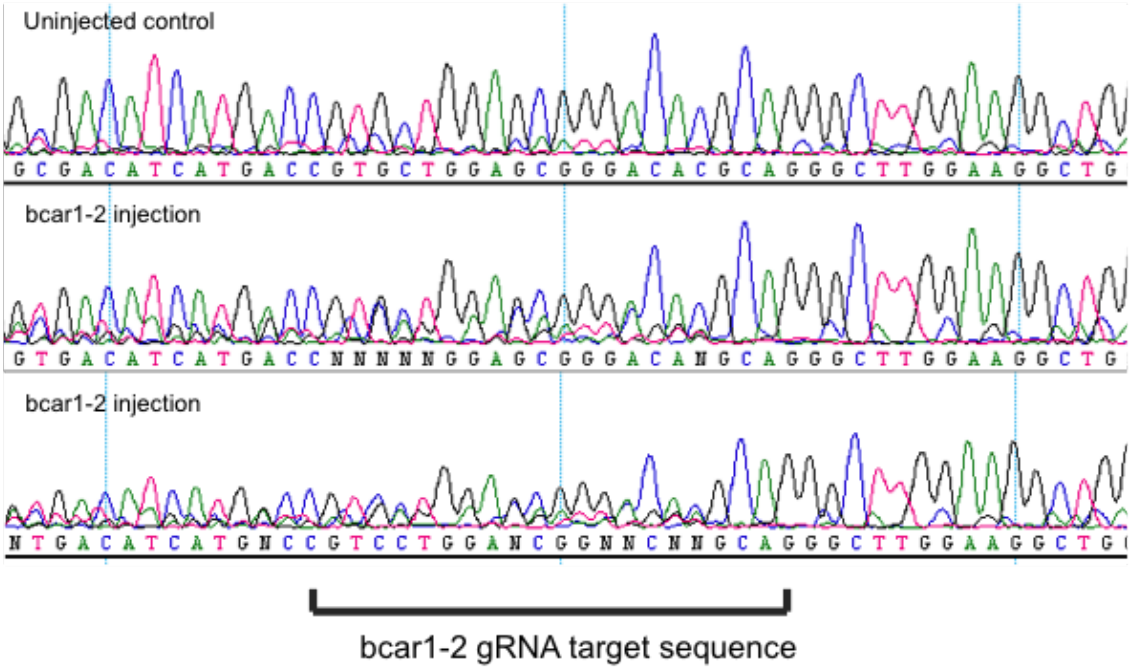

Figure A.11: Sequencing chromatogram of bcar1-2 injections to determine whether the CRISPR has functioned to elicit a DSB and indels through DNA repair mechanisms. The sequencing was performed with the bcar1 Reverse primer, Table 2.1 and the gRNA target site is highlighted. The top chromatogram shows a clean single sequence of the uninjected control sequence. The two chromatograms beneath are injected samples, where multiple sequences are seen once sequencing proceeds past the final 3 bases in the gRNA target site, indicating indels at this location.

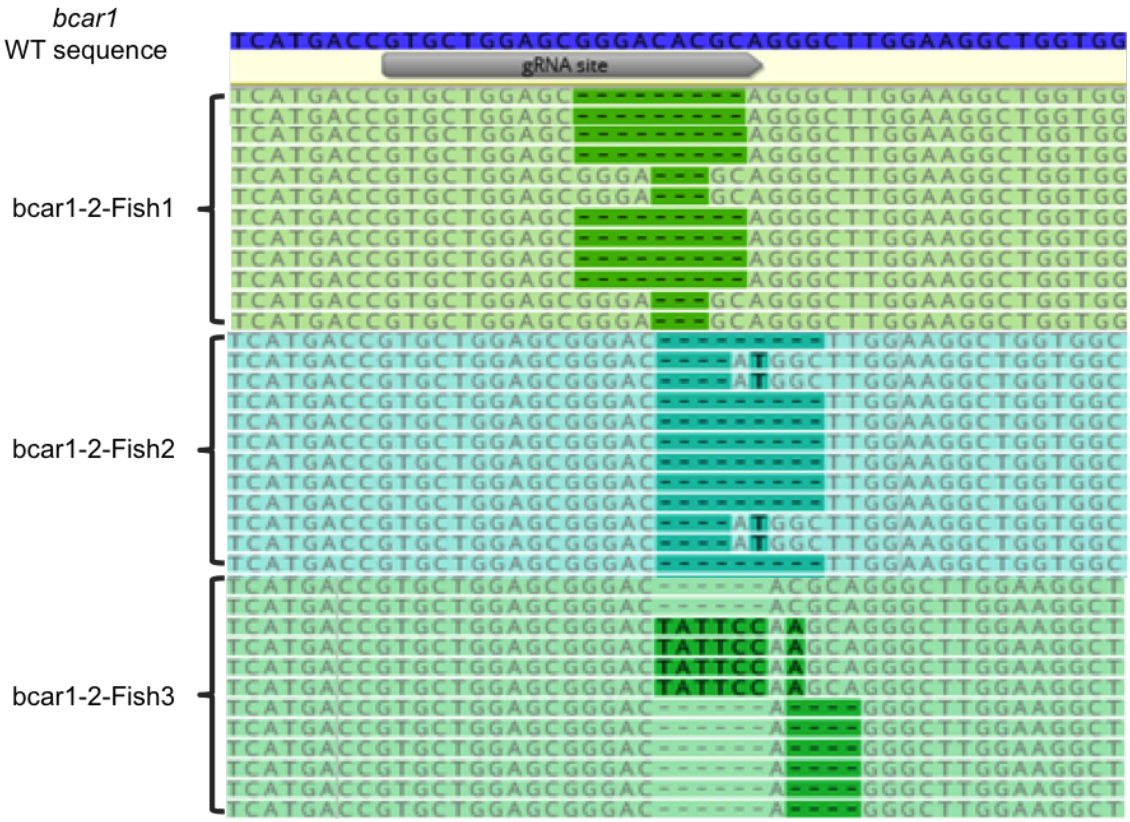

Figure A.12: Deep sequencing results of the bcar1 mutant germline transmitting zebrafish that were created using the gRNA bcar1-2. The *bcar1* wild type (WT) sequence is shown at the top along with the gRNA bcar1-2 target sequence. Twelve representative reads from the deep sequencing results are shown for each of the three germline transmitting zebrafish, bcar1-2-Fish1, bcar1-2-Fish2 and bcar1-2-Fish3, as indicated on the left hand side. Insertions (bold bases) and deletions (dashes) are highlighted.